

# Felsic melts in the oceanic crust: an experimental study on their generation, phase equilibria, and trace element partitioning

Von der Naturwissenschaftlichen Fakultät der  
Gottfried Wilhelm Leibniz Universität Hannover

et de

l'Université de Lorraine

zur Erlangung des Grades

Doktor der Naturwissenschaften (Dr. rer. nat.)

und

présentée et soutenue publiquement pour l'obtention du titre de

Docteur de l'Université de Lorraine Spécialité Géosciences

par

genehmigte Dissertation

von

Dipl.-Geow. Martin Erdmann

2017

Referenten: Prof. Dr. rer. nat. Jürgen Koepke

Prof. Dr. rer. nat. Etienne Deloule

Korreferenten: Dr. rer. nat. Lydéric France, Maître de conference

PD Dr. rer. nat. Andreas Klügel

Prof. Stephan Klemme, PhD

Tag der Promotion: 03.03.2017



## Acknowledgements

First, I would like to thank Prof. Dr. Jürgen Koepke who initiated this project. Thanks a lot for introducing me into the exciting topic of felsic melt generation in the oceanic crust, for your great support at any stage of the project and your patience during the last six years. This gratitude applies likewise for Prof. Dr. Lydéric France and Prof. Dr. Etienne Deloule for their technical and administrative support, the discussions of the results and the great time at the CRPG in Nancy. In addition, many thanks to all members of the CRPG for welcoming me during my stay in Nancy.

The project has greatly benefited from the collaboration with Prof. Dr. Karsten Haase and Dr. Sarah Freund, especially concerning the sampling campaign at the Oman ophiolite. Many thanks to you and all other participants of the fabulous field trip to Oman.

I would like to thank all people from the Institute of Mineralogy in Hannover. First, this thank is addressed to Lennart Fischer for the assistance with experiments and analyses as well as the extensive discussions of the results. Then, I like to thank Dr. Anika Husen and Torsten Bolte for a great time in our office. The technical support while conducting experiments by Dr. André Stechern and Dr. Adrian Fiege is deeply acknowledged as well as the reliable preparation of the samples by Otto Dietrich and Julian Feige. Even though not all colleagues are mentioned by name, I am grateful for the harmonic and stimulating working atmosphere at the Institute of Mineralogy in Hannover.

Special thanks go to my family, especially my parents, and my friends for supporting me all the time and allowing me to switch off during the free time.

Most important, I want to say “Thank you” to my lovely daughter Paulina and my gorgeous wife Svenja who love me as I am and accept all my moods. I love you! I am grateful to have such a wonderful family and, Paulina, now I finally have more time to play with you on the weekend.

Finally, I would like to thank the Deutsche Forschungsgemeinschaft (DFG) for giving financial support for this research (KO 1723/13).



## Abstract

Although in the majority basaltic, small but ubiquitous amounts of felsic rocks occur within the crust of modern oceans and in ophiolites. In the deep oceanic crust, they appear as late intrusions into the pre-existing gabbro sequence forming quartz diorites, tonalities, and trondhjemites, while in the upper oceanic crust felsic magmas form individual dikes within the basalts of the sheeted dikes or erupt as lava flows on the ocean floor. In general, two end-member processes are discussed regarding the formation of felsic magmas in the oceanic crust: fractional crystallization and partial melting of previously formed mafic rocks. In this study, these two end-member processes were tested experimentally by simulating (1) extensive crystallization in a dacitic system of the Pacific-Antarctic Rise (PAR) and (2) anatexis at the magma chamber roof by using different sheeted dike basalts as protolith, sampled from the core drilled at Site 1256 (eastern equatorial Pacific) by the Integrated Ocean Drilling Program (IODP).

Crystallization experiments using a natural dacitic glass from the PAR as starting material reproduced the phase assemblages of natural high-silica oceanic rocks only in a relatively small range of temperatures and melt-water contents ( $T \sim 950^\circ\text{C}$ ; melt  $\text{H}_2\text{O} < 1.5 \text{ wt}\%$ ) at redox conditions slightly below the quartz-fayalite-magnetite buffer. The relatively low water content is remarkable because high water activity due to distinct hydrothermal influence is generally regarded as key for producing silica-rich rocks in an oceanic environment. However, this finding is supported by mineral and bulk chemistry of naturally evolved rocks; these rocks are only congruent to the composition of those experimental phases that are produced under low water activity ( $a_{\text{H}_2\text{O}} < 0.4$ ). Low FeO contents under water-saturated conditions and the characteristic enrichment of  $\text{Al}_2\text{O}_3$  in high  $a_{\text{H}_2\text{O}}$  experiments, in particular, contradicts natural observations, while experiments with low  $a_{\text{H}_2\text{O}}$  match the natural trend.

The simulation of the complex igneous and metamorphic processes occurring at mid-ocean ridges (MORs) between the dynamic axial melt lens (AML) and the overlying sheeted dikes by partial melting experiments confirms that low  $a_{\text{H}_2\text{O}}$  is required to reproduce the low  $\text{Al}_2\text{O}_3$  contents as observed in natural silica rich rocks from the same location as the starting materials (IODP Site 1256). Moreover, experimental melts produced at  $a_{\text{H}_2\text{O}} < 0.5$  are highly enriched in trace elements despite relatively low  $\text{SiO}_2$ -contents (58.9 to 65.7 wt%). Low water activities put the importance of residual amphibole for anatectic processes into question, which is often used as an important phase for explaining trace element characteristics in relevant felsic rocks formed at MORs when modeling anatexis. Because amphibole is lacking in any experimental residue, which is in agreement with natural rocks from the dike/gabbro transition, partial melting within the AML roof rocks without the participation of amphibole as residual phase is likely. A comprehensive set of bulk and mineral/melt trace element partition coefficients was obtained from the amphibole free experiments for different potential protoliths and a large range of temperature and different water activities.

**Keywords:** *Experimental petrology, Phase equilibria, Differentiation, Fractional crystallization, Partial melting, Fast-spreading mid-ocean ridge, Oceanic plagiogranite, Granoblastic hornfels, Conductive boundary layer, contamination, Trace elements, Partition coefficients*

## Zusammenfassung

Obwohl rezente ozeanische Kruste und Ophiolite überwiegend basaltisch sind, treten häufig kleine Mengen von felsischen Gesteinen auf. Während sie in der tiefen ozeanischen Kruste als späte Intrusionen von Quarzdioriten, Tonaliten und Trondhjemiten in der bestehenden Gabbro-Sequenz vorkommen, bilden sie in der oberen ozeanischen Kruste einzelne felsische Gänge in den Basalten der Sheeted-Dike-Komplexe oder ergießen sich als Lavaströme auf den Ozeanboden. Im Prinzip werden zwei Prozesse für die Bildung von felsischer Magma in der ozeanischen Kruste diskutiert: Fraktionierte Kristallisation und Teilschmelzung von vorher gebildeten mafischen Gesteinen. In dieser Arbeit werden die beiden Prozesse experimentell getestet, indem zum einen (1) die extensive Kristallisation in einem dazitischen System von dem Pazifisch-Antarktischen Rücken (PAR) und zum anderen (2) die Anatexis an der Oberseite von Magmen-Kammern simuliert werden. Für die Experimente zur Anatexis werden verschiedene Basalte der Sheeted Dikes als Ausgangsgestein verwendet, die aus den Bohrkernen des Erkundungsortes 1256 vom „Integrated Ocean Drilling Program“ (IODP; östlicher äquatorial Pazifik) gewonnen wurden.

Kristallisationsexperimente mit natürlichem dazitischen Glas vom PAR als Ausgangsmaterial reproduzieren die Phasenzusammensetzung von natürlichen Silizium-reichen Gesteinen nur in einem relativ schmalen Temperaturbereich ( $\sim 950^\circ\text{C}$ ), bei geringem Wassergehalt der Schmelze ( $\text{H}_2\text{O} < 1,5 \text{ Gew.}\%$ ) und Redox-Bedingungen knapp unterhalb des Quarz-Fayalit-Magnetit-Puffers. Der relativ geringe Wassergehalt ist bemerkenswert, da im Allgemeinen eine hohe Wasseraktivität durch ausgeprägten hydrothermalen Einfluss als Schlüssel für die Entstehung von Silizium-reichen Gesteinen in einem ozeanischen Milieu angesehen wird. Diese Entdeckung wird allerdings von der chemischen Mineral- und Gesamtzusammensetzung der natürlichen entwickelten Gesteine gestützt; die Zusammensetzung dieser Gesteine stimmt nur mit den experimentellen Phasen überein, die bei geringer Wasseraktivität ( $a_{\text{H}_2\text{O}} < 0,4$ ) produziert wurden. Geringe FeO-Gehalte bei Wasser-gesättigten Bedingungen und insbesondere die charakteristische Anreicherung von  $\text{Al}_2\text{O}_3$  in Experimenten mit hoher  $a_{\text{H}_2\text{O}}$  stehen im Gegensatz zu Beobachtungen in natürlichen Proben, während Experimente mit geringer  $a_{\text{H}_2\text{O}}$  mit dem natürlichen Gegebenheiten übereinstimmen.

Mittels Teilschmelzexperimenten werden die komplexen intrusiven und metamorphen Prozessen, die am mittelozeanischen Rücken (MOR) zwischen der dynamischen axialen Schmelzlinse und dem darüber liegenden Sheeted-Dike-Komplex auftreten, nachgestellt. Sie bestätigen, dass geringe  $a_{\text{H}_2\text{O}}$  nötig ist, um die niedrigen  $\text{Al}_2\text{O}_3$ -Gehalte wie sie in den natürlichen Silizium-reichen Gesteinen, die von derselben Stelle wie das Ausgangsmaterial stammen (IODP Erkundungsort 1256), beobachtet werden. Darüber hinaus sind die bei geringer  $a_{\text{H}_2\text{O}}$  ( $< 0,5$ ) produzierten experimentellen Schmelzen trotz relativ niedrigen  $\text{SiO}_2$ -Gehalten (58,9 bis 65,7 Gew.%) stark an Spurenelementen angereichert. Diese geringen Wasseraktivitäten stellen die Bedeutung von residualen Amphibolen für die Anatexis in Frage. Amphibol wird bei der Modellierung von Anatexis häufig als wichtige Phase zur Beurteilung von Spurenelement-Charakteristika der felsischen Gesteine, die an MOR gebildet werden, herangezogen. Da es allerdings weder im experimentellen Residuum noch in natürlichen Gesteinen des Sheeted-Dike-

/ Gabbro-Überganges auftritt, ist es wahrscheinlich, dass Amphibol für die Teilschmelzprozesse an der Oberseite von axialen Schmelzlinsen keine Rolle spielt. Ein umfangreicher Satz von Gesamtgesteins- und Mineral/Schmelze-Verteilungskoeffizienten für Spurenelemente wurde aus den Amphibol-freien Experimenten für verschiedene potenzielle Ausgangsgesteine sowie einen umfassenden Bereich von Temperatur und  $a_{\text{H}_2\text{O}}$  gewonnen.

**Schlagwörter:** *Experimentelle Petrologie, Phasengleichgewichte, Differenzierung, Fraktionierte Kristallisation, Teilschmelzung, Schnell-spreizende mittelozeanische Rücken, Ozeanische Plagiogranite, Granoblastischer Hornfels, Grenzschicht der Wärmeleitung, Kontaminierung, Spurenelemente, Verteilungskoeffizienten*

## Resumé

Bien que majoritairement de composition basaltique, la croûte formant les fonds océaniques actuels et les ophiolites contient aussi toujours de faibles quantités de roches felsiques. Dans les portions de croûte profonde ces lithologies sont intrusives dans les gabbros, alors que dans les portions de croûte supérieure des petits dykes intrudent les basaltes du complexe filonien, ou sont émis sur les fonds océaniques sous forme de dacite ou rhyolites. Deux modèles principaux sont proposés pour expliquer la genèse de ces magmas felsiques: i. la cristallisation fractionnée poussée de liquides basaltiques, ou ii. la fusion partielle des roches basaltiques formant cette croûte océanique. Dans cette étude ces deux modèles ont été testés expérimentalement pour comprendre leur importance respective en simulant 1/ une cristallisation importante d'un système dacitique déjà évolué provenant de la dorsale Pacifique-Antarctique (PAR), et 2/ la fusion partielle des roches formant le toit de la chambre magmatique en utilisant différents protolithes échantillonnés proche de la base du complexe filonien au niveau du site de forage IODP 1256 (programme de forage international, Integrated Ocean Drilling Program), qui se situe dans la plaque Cocos (Pacifique équatorial).

Pour des conditions redox légèrement inférieures au tampon quartz-fayalite-magnétite, les expériences de cristallisation utilisant comme matériel de départ un verre dacitique de la PAR, reproduisent les assemblages de phases des lithologies océaniques riches en silice pour une faible gamme de température, et de contenus en eau ( $\sim 950^{\circ}\text{C}$ ;  $\text{H}_2\text{O}_{\text{Liquide}} < 1.5 \text{ \%}_{\text{poids}}$ ) apportant donc de nouvelles contraintes sur les conditions de formation de ces lithologies. La relativement faible concentration en eau est remarquable puisque des conditions hydratées à mettre en lien avec les circulations hydrothermales ont en général été considérées dans la genèse de ces roches acides. Ces résultats expérimentaux sont de plus renforcés par leur correspondance avec les lithologies naturelles, en particulier pour la composition chimique des différentes phases en présence; cette correspondance n'existe que pour les expériences conduites pour des activités en eau faibles ( $a_{\text{H}_2\text{O}} < 0.4$ ). Les expériences conduites à plus forte activité d'eau mènent en particulier à des concentrations en fer trop faibles, et à des concentrations en aluminium trop élevées dans les liquides expérimentaux en comparaison des roches naturelles.

La simulation expérimentale des processus magmatiques et métamorphiques complexes qui se produisent aux dorsales médio-océaniques lors d'interactions entre la lentille magmatique axiale qui est un système dynamique, et le complexe filonien sus-jacent, confirment que les processus anatectiques doivent se produire dans des conditions d'activité en eau réduite. En effet seules ces expériences ont le potentiel de reproduire les faibles concentrations en aluminium des roches naturelles. Les liquides anatectiques produits dans des conditions d'activité en eau faible, sont ceux qui contiennent les plus fortes quantités d'éléments trace pour des proportions de silice relativement faibles (58.9-65.7  $\text{ \%}_{\text{poids}}$ ). Ces conditions de faible activité en eau remettent en question la présence d'amphibole dans les résidus de fusion, présence qui est toujours considérée dans les modèles actuels de genèse visant à reproduire les concentrations en éléments trace des magmas océaniques riches en silice. De plus, nos résidus expérimentaux ainsi que les lithologies naturelles correspondantes au niveau du puits IODP 1256D (dykes granoblastiques) ne contiennent pas d'amphibole; nous considérons donc ici que le processus anatectique se déroule

sous des activités d'eau faible, et en l'absence d'amphibole avec par conséquent des conséquences fortes sur la composition en éléments trace des liquides anatectiques. Dans l'optique de permettre de mieux contraindre ces processus complexes dans notre zone d'étude et dans de futurs travaux, un jeu complet de coefficients de partage globaux, et minéral-liquide est fourni pour différents éléments trace, sous différentes températures, et activités en eau. Ces coefficients de partage représentent aujourd'hui les paramètres les plus adaptés pour modéliser la formation des liquides riches en silice observés au niveau des bordures des chambres magmatiques océaniques.

**Mots clés:** *Pétrologie expérimentale, Équilibre de phases, Différentiation; Cristallisation fractionnée, Fusion partielle, Dorsale médio-océanique à expansion rapide, Plagiogranite océanique, Cornéennes granoblastiques, Couche limite conductive, Contamination, Éléments en traces, Coefficients de partage*



# Table of contents

Introduction .....	15
Formation of felsic magmas in the oceanic crust .....	16
The role of chlorine at mid-crustal levels of fast-spreading ridges and felsic melts as a contaminator for MORB ....	19
Formation of felsic melts in the dike/gabbro transition of fast-spreading ridges .....	19
Previous experimental studies simulating felsic melt generation within the oceanic crust .....	20
Outline of the study .....	22
Chapter A .....	25
A.1. Silica-rich lavas in the oceanic crust: Experimental evidence for fractional crystallization under low water activity .....	25
A.1.1. Abstract .....	25
A.1.2. Introduction .....	25
A.1.3. Methods .....	27
A.1.3.1. Starting material from the PAR .....	27
A.1.3.2. Experimental methods .....	27
A.1.3.3. Analytical methods .....	29
A.1.4. Experimental results .....	32
A.1.4.1. Phase relations .....	32
A.1.4.2. Phase proportions .....	32
A.1.4.3. Phase chemistry .....	35
A.1.5. Discussion .....	41
A.1.5.1. Attainment of equilibrium .....	41
A.1.5.2. Partitioning of trace elements between melt and plagioclase .....	42
A.1.5.3. Comparison with other phase equilibria data in a dacitic/tonalitic system .....	43
A.1.5.4. Application to natural felsic lavas from mid-ocean ridges .....	44
A.1.6. Conclusion .....	51
Chapter B .....	53
B.1. Experimental temperature cycling as a powerful tool to enlarge melt pools and crystals at magma storage conditions .....	53
B.1.1. Abstract .....	53
B.1.2. Introduction .....	54
B.1.3. The apparatus .....	54
B.1.4. The starting material .....	56
B.1.5. Experimental methods .....	59
B.1.5.1. Experimental procedure to enlarge melt-pools and crystals .....	59
B.1.5.2. Analytical methods .....	61
B.1.6. Results and discussion .....	61
B.1.6.1. Achievement of equilibrium .....	61

B.1.6.2. Effect of temperature cycling on phase relation .....	62
B.1.6.3. Effect of temperature cycling on phase chemistry .....	66
B.1.7. Implications .....	67
Chapter C .....	69
C.1. Anatexis at the roof of an oceanic magma chamber at IODP Site 1256 (equatorial Pacific): An experimental study .....	69
C.1.1. Abstract .....	69
C.1.2. Introduction .....	70
C.1.3. Background .....	71
C.1.3.1. Oceanic plagiogranites and granoblastic hornfels .....	71
C.1.3.2. IODP Site 1256 stratigraphy .....	72
C.1.3.2. Previous experiments testing an anatectic origin of felsic melt in oceanic crust .....	73
C.1.4 Experimental and analytical techniques .....	74
C.1.4.1. Starting material .....	74
C.1.4.2. Felsic rocks from IODP Site 1256 .....	75
C.1.4.3. Experiments .....	77
C.1.4.4. Electron-probe micro analyzer (EPMA) .....	79
C.1.5. Results .....	79
C.1.5.1. Attainment of equilibrium .....	79
C.1.5.2. Phase relations .....	80
C.1.5.3. Composition of the anatectic melts .....	84
C.1.5.4. Compositions of newly-formed mineral phases .....	86
C.1.6. Discussion .....	89
C.1.6.1. Influence of the starting material composition on anatectic products .....	89
C.1.6.2. Temperature evolution through the sheeted dike complex root zone .....	92
C.1.6.3. Comparison of the experimental melts with felsic rocks from IODP Site 1256 .....	92
C.1.6.4. Comparison of the experimental residue with granoblastic hornfels from IODP Site 1256 .....	94
C.1.6.5. The role of water activity .....	95
C.1.6.6. The absence of amphibole-rich rocks as possible protoliths for felsic melt generation .....	96
C.1.7. Conclusion .....	98
C.2. Trace element evidence for anatexis at oceanic magma chamber roofs and the role of partial melts for contamination of fresh MORB .....	101
C.2.1. Abstract .....	101
C.2.2. Introduction .....	101
C.2.2.1. Felsic veins intruding granoblastic hornfels at IODP Site 1256 .....	102
C.2.2.2. Previous study .....	103
C.2.2.3. Trace element characteristics of felsic veins .....	106
C.2.3. Analytical technique .....	106
C.2.4. Results and discussion .....	108

C.2.4.1. Comparison: Natural felsic veins from IODP Site 1256 versus experimental melts .....	108
C.2.4.2. Comparison: Granoblastic hornfels versus experimental residues.....	108
C.2.4.3. Implications for the contamination of MOR basalts from fast-spreading ridges .....	109
C.2.5. Conclusion .....	113
C.3. Trace elements in anatectic products at the roof of mid-ocean ridge magma chambers: an experimental study .....	115
C.3.1. Abstract .....	115
C.3.2. Introduction.....	116
C.3.3. Methods.....	118
C.3.3.1. Experimental setup .....	118
C.3.3.2. Analytical methods .....	119
C.3.4. Results.....	120
C.3.4.1. Trace element characteristics of the starting material from IODP Site 1256.....	120
C.3.4.2. Trace element contents of experimental products.....	123
C.3.5. Discussion .....	124
C.3.5.1. Attainment of equilibrium .....	124
C.3.5.2. Comparison of experimental products to natural lithologies .....	126
C.3.5.3. Influence of the protolith on trace element enrichment of anatectic melt.....	127
C.3.5.4. Partitioning of trace elements between melt and residue.....	131
C.3.5.5. Implications for modeling anatectic processes, and for tracing MORB contamination.....	135
C.3.6. Conclusion .....	136
Chapter D .....	139
D.1. Constraints on the magmatic evolution of the oceanic crust from plagiogranite intrusion in the Oman ophiolite .....	139
D.1.1. Abstract.....	139
D.1.2. Introduction.....	139
D.1.3. Geological background .....	140
D.1.3.1. Geological overview.....	140
D.1.3.2. Geochemical overview .....	142
D.1.3.3. Ophiolite crust formation age and age of obduction.....	143
D.1.4. Sampling and analytical methods .....	143
D.1.4.1. Field observations and sampling .....	143
D.1.4.2. Analytical methods.....	143
D.1.5. Results.....	145
D.1.5.1. Petrology of the samples.....	145
D.1.5.2. Geochemistry and isotope composition.....	145
D.1.6. Discussion.....	150
D.1.6.1. Hydrothermal alteration of the plutonic rocks .....	150
D.1.6.2. The geochemical relationship between the plutonic and volcanic rocks .....	151

D.1.6.3. Formation of the felsic magmas .....	153
D.1.6.4. Anatectic processes at the dyke/gabbro transition of the Wadi Tayin block .....	154
D.1.6.5. Implications for the evolution of the oceanic crust.....	155
D.1.6.6. Constraints on the mantle source composition and the nature of the slab component .....	156
D.1.7. Conclusions .....	157
D.2. Melts of sediments in the mantle wedge of the Oman ophiolite .....	159
D.2.1. Abstract.....	159
D.2.2. Introduction .....	159
D.2.3. Geological overview .....	160
D.2.4. Results .....	160
D.2.5. Discussion.....	162
D.2.5.1. Origin of the felsic rocks by melting of sediments.....	162
D.2.5.2. Evidence for two-component mixing .....	163
D.2.5.3. Implications for sediment recycling in subduction zones.....	164
D.2.5.4. Implications for the formation of the Oman ophiolite .....	165
Concluding remarks .....	166
References .....	168
Curriculum Vitae.....	175
List of Publications.....	176

## Introduction

The outermost layer of the Earth lithosphere is divided in two different types of crust: (1) The overall basaltic oceanic crust, representing more than 60 % of the surface even though covered by the oceans (Fisher and Schmincke 1984; Wilson et al. 2006), and (2) the continental crust, mainly formed by SiO<sub>2</sub>-rich rocks (Taylor and McLennan 1985; Rudnick and Gao 2003). Consequently, felsic magmas occur most frequently on continents. These magmas have high viscosities and thus lead to explosive volcanic eruptions (Blake 1984). Moreover, SiO<sub>2</sub>-rich magmas can form ore deposits due to its enrichment in incompatible elements compared to more mafic magmas (Hedenquist and Lowenstern 1994).

Even though predominant on the continents, felsic rocks are also observed in different oceanic settings like mid-oceanic ridges (MORs; Byerly et al. 1976; Hékinian et al. 1999), oceanic intraplate volcanoes (Geist et al. 1995), or oceanic island arcs (Smith et al. 2003; Haase et al. 2006) as well as in ophiolites (Amri et al. 1996; Gillis and Coogan 2002; Rollinson 2009). In the deep oceanic crust these felsic rocks, often called oceanic plagiogranites, form late intrusions into the pre-existing gabbro sequence (Koepeke et al. 2007), while in the upper crust they form individual felsic dikes within the basalts of the sheeted dike sequence (Wilson et al. 2006) or specific lava flows (Perfit and Fornari 1983). Despite their low proportion in the oceanic crust, studies on felsic rocks are important because they may help to shed light on late differentiation processes during crustal accretion and on anatexis triggered by hydrothermal fluids. Moreover, the enrichment of felsic magmas in many incompatible elements has the potential to contaminate MOR basalts (MORBs) to a certain extend (France et al 2014).

The aim of this study is an experimental petrological simulation of the formation and differentiation of felsic magmas within the oceanic crust under various water activities which helps to understand (1) the phase relations in a typical felsic system from the oceanic crust; (2) the formation of felsic melts by partial melting of mafic rocks at the roof of mid-ocean ridge magma chambers with a focus on the influence of the starting material and their different grades of recrystallization and hydrothermal alteration. (3) A third aim is related to natural rocks of the Oman ophiolite and a focus on the role of assimilation-fractional crystallization processes versus partial melting on the formation of felsic melts in the Oman ophiolite. In this last theme, which was performed in close collaboration with the research group of Professor K. Haase (University of Erlangen, Germany), a large number of samples of intrusive felsic rocks, so called oceanic plagiogranite (for definition see below), were collected and geochemically analyzed in the Oman ophiolite, whose geodynamic setting and hence significance for mid-ocean ridge processes is controversial (e.g., MacLeod et al. 2013).

For the experimental simulation of crystal fractionation, natural dacitic glass from the Pacific-Antarctic Rise (PAR) was used as starting material. The PAR represents a fast-spreading ridge with abundant felsic volcanism. The experimental reproduction of the complex anatectic processes occurring at the roof of fast-spreading oceanic ridge magma chambers was performed by using six natural analogs recovered from Site 1256 (eastern equatorial Pacific) of the Integrated Ocean Drilling Program (IODP) Expeditions 312 and 335 as protoliths. For both scenarios (i.e., crystal fractionation processes and partial melting) the role of water on phase

chemistry was investigated. Special focus is on the major and trace element characteristics of the experimental phases and the comparison of those with their natural counterparts. The combination of experimental and natural rock studies can be regarded as key for establishing models of felsic melt generation. For this, in-situ trace element analyses of the experimental phases, especially of the melt phase, by secondary ion mass spectrometry (SIMS) have been included. Because experimental phases, especially in low temperature runs, are often too small, another aim of this study was to develop a new method that allows enlarging melt pools and crystals during experimental runs.

The combined experimental results – phase diagrams, trace element patterns of melts, distribution coefficients - provide a unique data base for modeling magmatic processes at ridges, especially for the evolution of felsic lithologies in the oceanic crust, in an, up to now, poorly investigated regime, where primary melts interact with previously hydrothermalized lithologies.

## **Formation of felsic magmas in the oceanic crust**

The formation of large portions of felsic magmas took place already in the Archean when continental crust, consisting of a tonalite-trondhjemite-granodiorite (TTG; e.g., Barker 1979) rock suite, was probably formed by a very effective transformation from mafic rocks or magmas composing the earliest crust of the Earth (Foley et al. 2002; Rollinson 2008; Smithies et al. 2009). In most models describing this transformation, amphibole and/or garnet residues are an important component, implying that the generation of felsic magmas is independent of the pre-existence of larger volumes of SiO<sub>2</sub>-rich material like pelitic sediments. The incompatible element compositions of Archean TTGs are similar to modern subduction-related magmas suggesting a formation in island arc settings (e.g., Foley et al. 2002). However, modern sodic felsic rocks can be also formed within the oceanic crust and geochemical studies of dacitic magmas from MOR settings have demonstrated that negative Nb and Ta anomalies, as required for early continental crust and typically occurring at subduction zones due to the fluid immobility of Nb and Ta relative to other elements (Foley et al. 2002), can be observed at MORs as well (Haase et al. 2005; Martin et al. 2008). Consequently, some parts of the Archean continental crust may have formed at oceanic ridges or plateaus rather than in island arc settings (Marsh et al. 1991; Martin et al. 2008).

Frequently, evolved rocks with SiO<sub>2</sub> contents between ~52 and 80 wt%, often called oceanic plagiogranites, are observed at various MOR sites. The term “oceanic plagiogranite”, once introduced by Thayer (1977), was described by Koepke et al. (2007) in detail, which is rather a typical field term for light-colored, felsic plutonic rocks (including [leucocratic] tonalite, trondhjemite, and [quartz] diorites) within an oceanic crust setting than an accurate definition based on the chemical or modal components of the corresponding rock. Some scientists avoid the use of the term “plagiogranite”, and use “felsic vein” instead. However, also the term “felsic vein” (e.g., used by Dick et al. 2002) does not exactly describe a SiO<sub>2</sub>-range and is sometimes used for intermediate compositions as well. Nevertheless, both expressions are established and used in this study. If necessary, the exact SiO<sub>2</sub>-content is given additionally.

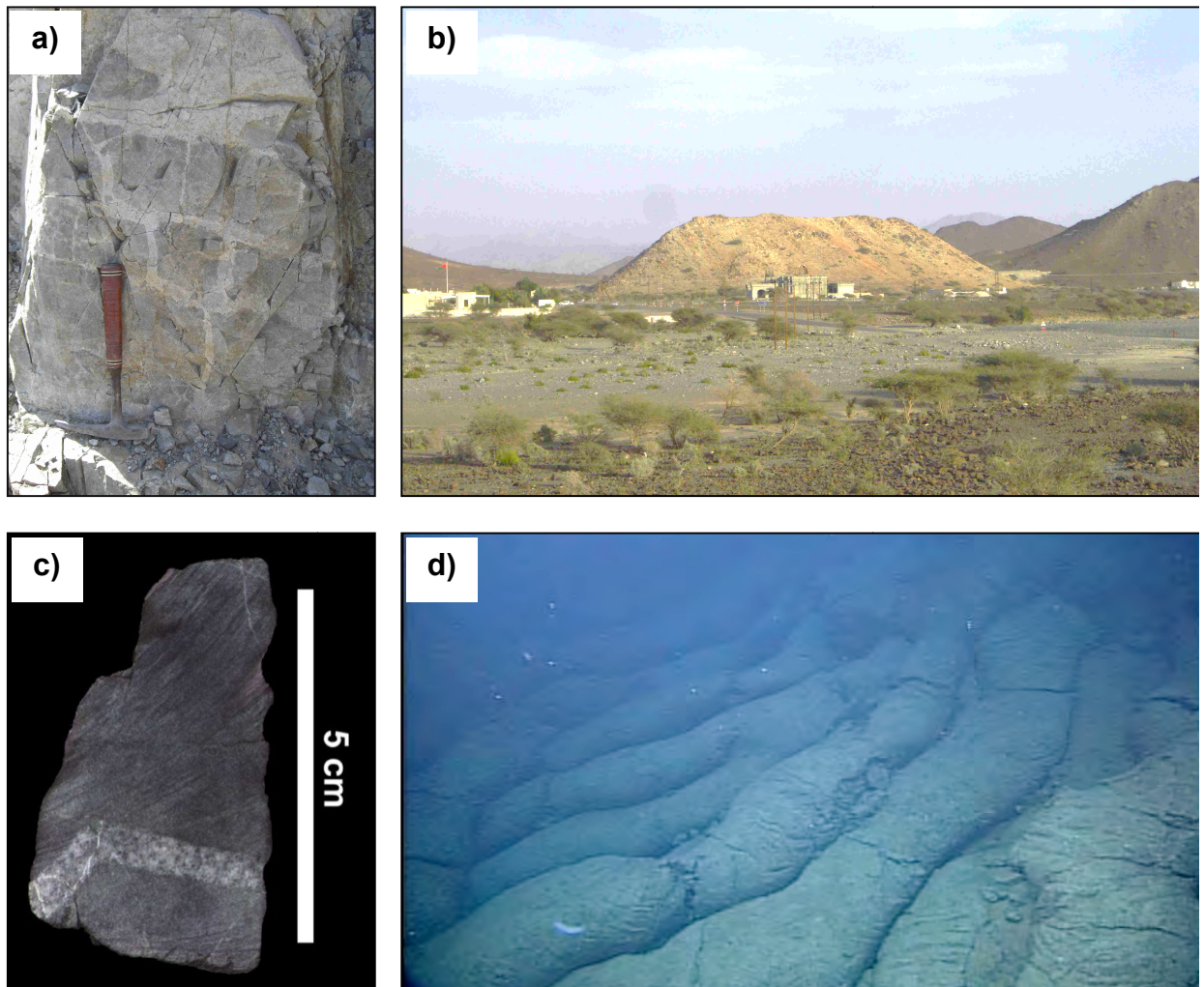


**Figure 1:** Felsic rocks in the oceanic crust. **a)** Granoblastic dikes netveined by a plagiogranite matrix within the sheeted dike rooting zone at the southern end of the Wadi Gideah, Semail ophiolite, Oman (see also Müller et al. accepted). **b)** Large plagiogranite intrusion near Samrah, Semail ophiolite, Oman. **c)** Core image from IODP sample 312-1256D-212R-1, 25–28 cm showing a tonalitic vein intruding granoblastic hornfels (from IODP Janus database Core Photos 312-1256D-212R). **d)** Erupted dacitic flows at the Juan de Fuca Ridge (Perfit et al. 2008; photos from MBARI Tiburon ROV Dive T735).

In the recent oceanic crust or in ophiolites small volumes of oceanic plagiogranites typically occur (1) as vein networks (Fig.1a) and/or discrete larger intrusive bodies at the dike/gabbro transition (Fig.1b; Amri et al. 1996; Gillis and Coogan 2002; Rollinson 2009; France et al. 2009; Müller et al. accepted), (2) as small veins, mainly at the dike/gabbro transition (Fig.1c; e.g., Dick et al. 2000; Blackman et al. 2004; Teagle et al. 2006; France et al. 2009, 2014) or as felsic veins within the plutonic crust of slow-spreading ridges (e.g., Dick et al. 2000, 2015), and (3) as silicic lavas erupted at the ocean floor close to a MOR (Fig.1d; e.g., Fornari et al. 1983; Haase et al. 2005). While plagiogranites in ophiolites are numerous, partly occurring as large bodies (up to a few hundred meters in width; e.g., Amri et al. 1996; Gillis and Coogan 2002) and erupted silicic lavas appear comparatively frequent at ocean floors (e.g., Galapagos Spreading Center, GSC; Fornari et al. 1983; PAR; Haase et al. 2005; Alarcón Rise; Dreyer et al. 2014), felsic veins within present oceanic crust are rarely sampled (e.g., at IODP Sites at the Southwest Indian Ridge, SWIR; Dick et al. 2002; or at the EPR). The dike/gabbro transition of present day oceanic crust, regarded as an important layer for anatexis processes due to the related axial melt lens (AML,

see below; e.g., France et al. 2010, 2014), has been sampled at only three locations (IOPD Site 1256, Pito Deep, and Hess Deep; all related to the EPR).

The generation of silica rich magmas in the ocean crust has been debated for decades, and different models are suggested: (1) Crystal fractionation processes from basaltic magmas resulting in highly differentiated melt (e.g., Coleman and Donato 1979; Juster et al. 1989; Berndt et al. 2005); (2) Re-melting of gabbroic rocks possibly containing amphibole in the deep oceanic crust (Flagler and Spray 1991; Beard 1995; Gillis and Coogan 2002; Koepke et al. 2004, 2008) or anatexis of hydrothermally altered crustal rocks in the shallow oceanic crust (Gillis and Coogan 2002; France et al. 2010, 2014); (3) liquid immiscibility in an evolved tholeiitic system (Sato 1978; Philpotts 1982; Veksler et al. 2007; Charlier et al. 2011). As pointed out in the detail review of the end-member processes by Koepke et al. (2007), a combination of the different processes is likely and hydrous conditions for the formation are expected. Brophy (2008) presented a summarizing chart for potential pathways of the evolution of fresh MORB to dacitic and rhyolitic lava by fractional crystallization, partial melting or combination of these processes (Fig. 2).

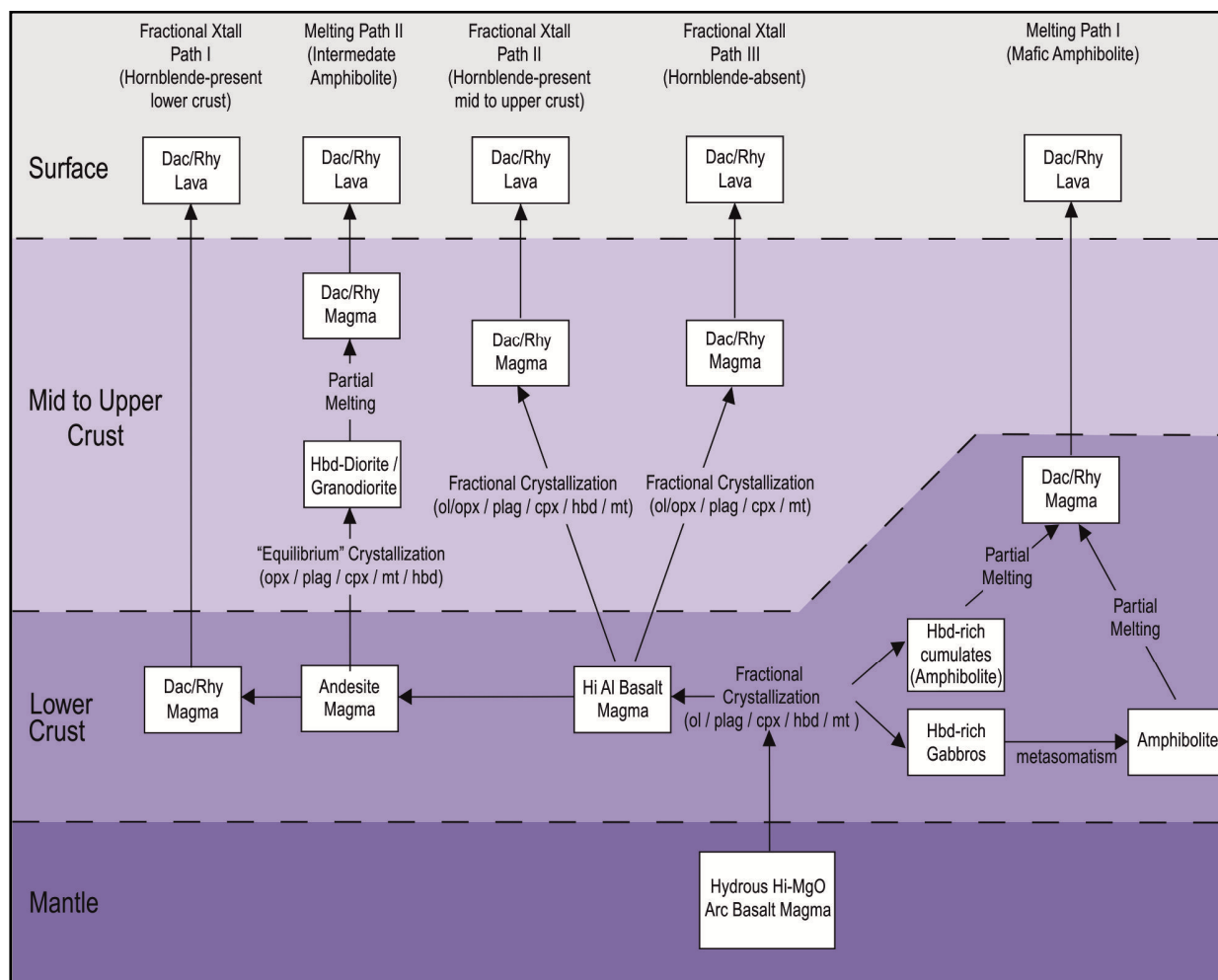


**Figure 2:** Schematic flow diagram showing five potential end-member paths that primitive mantle-derived basaltic magma may take to generate felsic magma (modified after Brophy 2008).



## The role of chlorine at mid-crustal levels of fast-spreading ridges and felsic melts as a contaminator for MORB

In general, chlorine plays an important role for MORB contamination (Michael and Schilling 1989; Jambon et al. 1995; Michael and Cornell 1998). For instance, Cl can strongly affect the partitioning of several elements and has a strong influence on the transport and reaction behavior of major and trace elements during the interaction between solid oceanic crust and seawater-derived fluids (Ayers and Eggler 1995; Keppler 1996). Moreover, Cl can significantly affect the phase relations and the composition of the phases in equilibrium with Cl-bearing fluids (Botcharnikov et al. 2004, 2007; Stelling et al. 2008). Plagiogranitic melts can have an important share in the contamination process. Increased Cl-contents and  $^{87}\text{Sr}/^{86}\text{Sr}$ -ratios in felsic melts generated at mid-crustal levels of fast-spreading ridges imply that assimilation and partial melting of hydrothermally altered oceanic crust is an important process in the formation of these  $\text{SiO}_2$ -rich melts (Haase et al. 2005). The presence of brines exsolved from seawater-derived hydrothermal fluids shows that considerable amounts of chlorine are available in the mid-crustal level (Coogan et al. 2003) that can be incorporated into newly formed felsic melts. Next to Cl-rich brines, amphibole has been suggested as reservoir for the high Cl contents and seawater-like Sr isotopes in the hydrothermally affected oceanic crust assimilated by the ascending melts. Thus, the interaction between hydrothermal circulation, amphibole-bearing hydrothermal metamorphic rocks, and ascending magmas might be strongly dependent on the dynamics of the AML under the ridge, for instance the up and down moving of the melt lens and related stoping and assimilation effects (Gillis and Coogan 2002; Coogan et al. 2003; Koepke et al. 2008; France et al. 2009, 2010, 2013, 2014).

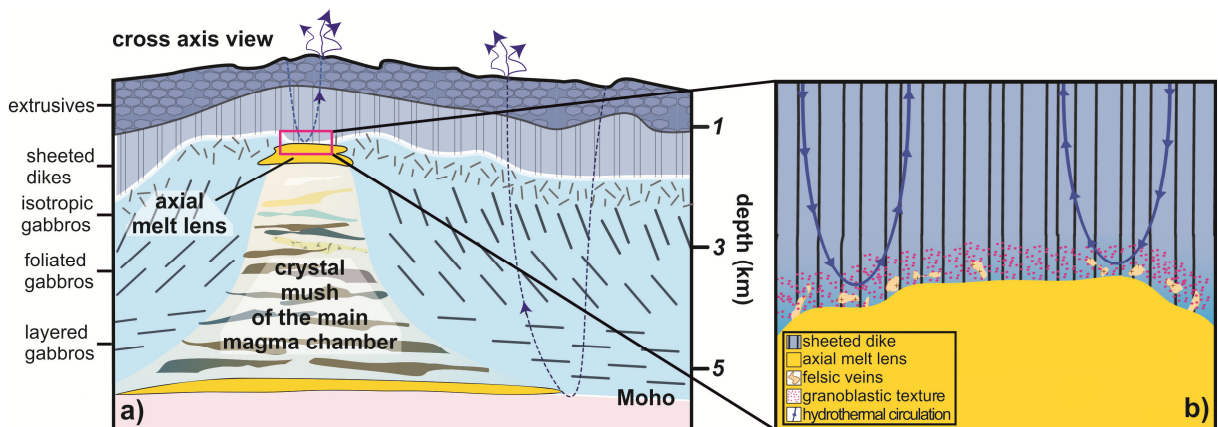


**Figure 3:** a) Schematic cross axis view of the magmatic system at fast spreading ridges. b) Focus on the axial melt lens roof where anatexis may generate felsic veins and residual granoblastic rocks are present (modified after France et al. 2010).

## Formation of felsic melts in the dike/gabbro transition of fast-spreading ridges

Below fast-spreading ridges, a small (~50-100 m thick and ~1000 m wide) steady-state AML at the top of the main magma chamber, composed of crystal mush with less than 20 % of melt and reaching down to the Moho (e.g., Caress et al. 1992; Crawford et al. 1999; Lamoureux et al. 1999; Dunn et al. 2000) has been discovered by vertical seismic reflection (e.g., Vera et al. 1990; Fig. 3). This discovery has raised the question of how it relates to the overlying sheeted dyke

complex. Theoretical models predict that heat is exchanged across a thin (<100 m), hot (>650 °C), impermeable conductive boundary layer (CBL) sandwiched between the AML and the sheeted dykes (e.g., Lowell and Burnell 1991). The CBL separates two convective systems: the AML filled with nearly pure basaltic magma at ~1200°C below, and the seawater hydrothermal cells operating at temperatures of max. 400-500°C. Seismic, structural, and geochemical studies from fast-spreading ridges imply that the AML and the overlying CBL are transient phenomena, moving up and down, likely related to the magmatic activity beneath the spreading segments.

The AML feeds the basalts of the upper crust and is assumed to be the place where the main stage of MORB differentiation occurs. Studies on the interaction of the melts with the surrounding altered rocks have been performed, for example in the Troodos ophiolite (Gillis and Coogan 2002), which is regarded to be formed in a supra-subduction environment, in a core drilled by IODP in ~15 Ma years old EPR crust at Site 1256 (Koepke et al. 2008), and in the Oman ophiolite (France et al. 2010, 2014). Most of these studies regarded amphibole as a major phase in the mid-crustal horizon above the AML. Therefore, the authors concluded that amphibole plays an important role in magmatic processes leading to the petrogenesis of felsic magmas because it contains water with the potential to lower the solidus of metamorphosed mafic crust during its breakdown.

There is only limited access to this complex horizon of fast-spreading ridges. Next to the Oman ophiolite, a fossil conductive boundary layer at recent oceanic crust was penetrated by drilling at IODP Hole 1256D, revealing that this horizon consists of metamorphosed, granoblastic hornfels (former hydrothermally altered sheeted dykes) sandwiched between gabbros and sheeted dykes (e.g., Koepke et al. 2008, 2011; Teagle et al. 2012). By using a diffusion-modelling approach based on CaAl-NaSi interdiffusion in zoned plagioclases from the granoblastic hornfels from Hole 1256D, Zhang et al. (2014) made the first estimation of cooling rates above the AML.

Investigations of the fossilized AML in the Oman ophiolite were performed for instance by MacLeod and Rothery (1992), MacLeod and Yaouancq (2000), and Coogan et al. 2002 with special focus on its formation by upstreaming melt flux. The complexity of magmatic processes involving both fractional crystallization of MORB and partial melting of altered dykes was investigated by Mueller et al. (2017). France et al. (2009) highlighted the close similarities between Oman and Hole 1256D with respect to the magmatic and metamorphic processes at the sheeted dike rooting zone.

## **Previous experimental studies simulating felsic melt generation within the oceanic crust**

The two major end-member models for the formation of felsic rocks within the ocean crust – (1) fractional crystallization of MORB and (2) partial melting of mid-crustal rocks (gabbros or hydrothermally altered basalts) – have been tested by numerous experimental studies. As a third model, (3) liquid immiscibility is also proposed as a potential process for the generation of felsic rocks.

- (1) Crystallization experiments for simulating differentiation of MORB performed, for instance, by Juster et al. (1989) and Toplis and Carroll (1995) showed that silica rich

melts can be produced due to fractionation of Fe-Ti oxides during late stage differentiation of a tholeiitic melt. However, these studies have been performed in a dry system without respecting the presence of amphibole in oceanic plagiogranites requiring high water activities during their formation. First phase-equilibria experiments in water-bearing systems under shallow pressure (<500 MPa), relevant for MOR processes, struggled with the formation of quench-crystals during cooling (e.g., Hamilton et al. 1964; Eggler and Burnham 1973; Dixon-Spulber and Rutherford 1983). With the development of a rapid-quench system for internally heated pressure vessels (Holloway et al. 1992; Roux and Lefevre 1992; Berndt et al. 2002) this problem is minimized. Applying the rapid-quench technique, Berndt et al. (2005) and Feig et al. (2006, 2010) conducted pressurized crystallization experiments (mainly at 200 MPa, also at 100 and 500 MPa) at various water activities and oxygen fugacities using primitive and evolved MORB as starting material. They showed that highly evolved melts with tonalitic composition ( $\text{SiO}_2$  contents up to 70 wt %) can be produced by fractionation processes. It has to be noted that felsic melt production at lower pressures and hydrous conditions has been simulated by crystallization experiments in various studies for volcanic systems using andesitic to dacitic starting material (e.g., Scaillet and Evans 1999; Costa et al. 2004; Holtz et al. 2005; Cadoux et al. 2014). These studies aim to study pre-eruptive conditions of Santorini, Unzen, San Pedro, and Pinatubo volcano and, thus, deviate from an oceanic setting. Nevertheless, these studies are well eligible for a comparison to results of experiments aiming to simulate crystallization processes in the lower oceanic crust because applied pressures, melt-water contents, redox conditions, and temperatures are at least partly in the same range as those predicted for the oceanic environment.

- (2) Several studies in the last decades demonstrated that partial melting of basic rocks can produce silicic melts (see compilation in Johannes and Koepke 2001). However, most of these studies used amphibolites and greenstones as starting material for the dehydration melting experiments in order to investigate the formation of Archean TTG rocks. Hydrous partial melting experiments with starting materials of (partly) basaltic composition were performed, for instance, by Holloway and Burnham (1972), Helz (1973), Beard and Lofgren (1991), and Kawamoto (1996). However, most of these experiments, as well as those using amphibolites and greenstones as starting material, aimed to simulate dehydration melting processes related to subduction zones or the deep continental basement. Thus, the applied pressures (> 300 MPa) are in general (except for one series of Beard and Lofgren (1991) at  $P = 100$  MPa) distinctly higher than those expected for felsic melt generation in the oceanic crust via partial melting of gabbro or hydrothermally altered basalt. Especially anatectic processes occurring at the AML roof are characterized by low pressures ( $\leq 100$  MPa) and high water activities (e.g., France et al. 2009). Experiments directly related to hydrous partial melting of MOR lithologies at shallow pressures ( $\leq 200$  MPa) were performed by Koepke et al. (2004) and Wolff et al. (2013) with primitive gabbro as starting material and from France et al. (2010, 2014) using hydrothermally altered basalt from the lower sheeted dike as protolith.
- (3) Liquid immiscibility as a potential process for the generation of felsic rocks in the tholeiitic system is proposed by different studies (e.g., McBirney and Nakamura 1974; Philpotts 1979; Veksler et al. 2007). However, these experiments were performed at

ambient pressure and do not model hydrous, shallow pressure conditions prevailing at MORs. Phase equilibria studies performed in hydrous tholeiitic systems under pressure (e.g.; Dixon-Spulber and Rutherford 1983; Koepke et al. 2004; Berndt et al. 2005; Feig et al. 2006) are lacking in evidence for immiscibility between two silicate melts (see also review in Koepke et al. 2007). Moreover, the study of Veksler et al. (2007) led to a controversial debate on the reliability of the experiments (McBirney 2008; Morse 2008). Nevertheless, new experiments conducted by Charlier and Grove (2012) show evidence for liquid immiscibility along tholeiitic liquid lines of descent. Thus, this process has to be kept in mind as a contributor to felsic melt generation.

In general, the previous partial melting experiments have been performed under water-saturated conditions. However, experimental studies simulating fractional crystallization (see above) demonstrated the impact of different water activities on phase equilibria and compositions (e.g., Feig et al. 2006). Since other fluids such as CO<sub>2</sub>, which have the potential to lower the water activity, are likely in anatectic processes, the influence of reduced water activity during partial melting should be considered. Moreover, most of these studies are dealing with major element composition of the experimental phases and only a few minor elements have been measured. Based on these data, it is difficult to discriminate between the two end-member models by applying the experimental results to natural felsic rocks from the oceanic crust. For this, it is necessary to measure the trace element composition of the experimental phases. France et al. (2014) presented a comprehensive dataset of trace elements measured in experimental hydrous partial melts. Their results suggest that a reproduction of the trace element pattern of natural felsic rocks by partial melting is possible. Nevertheless, France et al. (2014) used a fully altered basalt (greenschist facies conditions) from the Oman ophiolite as starting material lacking any primary mineral. Due to the subduction zone relation of the Oman ophiolite (e.g. MacLeod et al. 2013), these rocks are only minimally applicable to fast spreading ridges. Typical basalts from Oman are relatively enriched in SiO<sub>2</sub>, Al<sub>2</sub>O<sub>3</sub>, and K<sub>2</sub>O and depleted in TiO<sub>2</sub> for a given MgO. Such lithologies are uncommon at modern MORs.

Therefore, experiments using MOR related samples as starting material with special focus on trace element geochemistry of the involved experimental phases generated at shallow pressures are necessary. Moreover, the influence of reduced water activity on phase relations and compositions during partial melting and the important role of deep, seawater-derived, probably Na and Cl-rich fluids during the petrogenesis of felsic lithologies in oceanic crust (see above) has only been rarely studied up to now.

## **Outline of the study**

In total, this study consists of seven manuscripts (four with Martin Erdmann as first author) that can be divided in four sub-themes. In the following, the key-points of the corresponding chapters including a summary of the related field and lab work are given.

In **Chapter 1**, the experimental simulation of magma differentiation in the oceanic crust is presented. For this, a detailed phase equilibria study using a dacitic starting material sampled at the PAR was performed. Special focus is on the influence of water activity and redox conditions on the equilibrium crystallization path within an oceanic dacitic potassium-depleted system at

shallow pressure (i.e. 200 MPa). Moreover, trace element distribution coefficients between melt and plagioclase are presented. A remarkable outcome of this experimental investigation is the relatively low water content (< 1.5 wt%) required for the experimental reproduction of natural phase assemblages and compositions, while highly evolved experimental melts are relatively enriched in chlorine at the same time, implying a decoupling between these two volatiles during crustal contamination. This peer-reviewed paper was published in *Contributions to Mineralogy and Petrology* (Erdmann and Koepke 2016b).

**Chapter 2** introduces a new approach to enlarge melt pools and crystals in experiments which was developed during the experimental study presented in chapter 1. Large experimental phases are essential for in-situ analyses of trace elements, for instance with SIMS. Especially in the high silica range, experimental products are often very small (i.e. < 10  $\mu\text{m}$ ) preventing reliable trace element analyses. In order to approach this problem, a strategy to enlarge experimental phases, especially melt pools, was developed. In a first step, the possibility to enlarge melt pools in a partially molten oceanic gabbro by adding a synthetic glass of the assumed equilibrium composition was investigated. James G. Brophy (Department of Geological Sciences, Indiana University, Bloomington, IN, USA) has initiated this work based on an idea of the pioneering study from Nakajima and Arima (1998). The results of this study are summarized in a bachelor thesis (Fischer 2011) and in a conference abstract (Fischer et al. 2012). Against the expectations, no analyzable melt pools have been recognized in the experimental products. While the application of diamond traps in order to separate melt from other experimental phases (see Baker and Stolper 1994) was also without results for highly evolved systems, the temperature cycling technique was very successful. It could be shown for the first time in an evolved, water bearing system that periodic heating and cooling causes a significant enlargement of clinopyroxene and plagioclase crystals and dissolves tiny crystals in the matrix resulting in larger, undisturbed melt pools. This peer-reviewed methodical work was published in *American Mineralogist* (Erdmann and Koepke 2016a).

**Chapter 3** contains three different manuscripts, all aiming, with different focus, an experimental simulation of anatectic processes occurring at oceanic magma chamber roofs. While the paper of the first section concentrates on the major element compositions of the experimental phases obtained via partial melting experiments, manuscripts of sections two and three presents detailed trace element analyses. For all studies of this chapter, the same starting material, obtained from the sheeted dike complex of IODP Expeditions 312 and 335 at Site 1256 (eastern equatorial Pacific) was used. The protoliths span a lithological range from poorly to strongly altered basalts to partially or fully recrystallized granoblastic hornfels. Similar to the outcome of the experimental simulation of magma differentiation, major and trace element composition of natural felsic veins, sampled at the same location, could be only reproduced in the experimental series performed at low water activity. Additionally, bulk and mineral/melt trace element partition coefficients for different potential protoliths of anatectic processes are provided. Moreover, KD values are given for a large range of temperature and for different water activities. With these data, it is possible to decipher the different processes of felsic melt generation and to track MORB contamination by assimilation of highly evolved wall rocks. However, calculations of mixing and assimilation fractional crystallization using the experimental partial melts as

contaminant/assimilant showed that anatectic melts can only be a minor contributor to the contamination process. Two peer-review papers are published in *Contributions to Mineralogy and Petrology* (Erdmann et al. 2015) and *Lithos* (Fischer et al. 2016), the third manuscript (Erdmann et al. submitted) is submitted to *Chemical Geology*.

**Chapter 4** investigates natural felsic intrusions sampled in many massifs of the Oman ophiolite. While the geochemical analyses are the basis for another PhD thesis (Freund 2013) conducted by the research group of Professor K. Haase (University of Erlangen, Germany), the sampling campaign in Oman was mainly part of this PhD work. This included the preparation of the fieldwork with a review of the related geological maps in order to identify relevant outcrops of plagiogranites. The locations of these outcrops, obtained from geological maps, were merged with satellite images via the ArcGIS software package, which is crucial for locating the points of interest in the field. During the three weeks lasting fieldwork, more than 150 rock samples from 34 locations have been collected. Next to plagiogranites, numerous corresponding wall rocks have been sampled. After the field work thin sections of all relevant samples have been conducted and selected samples have been analyzed by microscope and electron probe micro analyzer (EPMA). Simultaneously, samples have been prepared for trace element analyses that were conducted by the research group of Professor K. Haase. Moreover, ~50 rock samples have been selected for  $\delta^{18}\text{O}$  SIMS analyses of zircons at the WISC-SIMS lab Madison, Wisconsin, USA that have been executed in collaboration with Craig B. Grimes (Department of Geological Sciences, Ohio University, Athens, Ohio, USA). Preliminary results were presented at the AGU Fall Meeting 2015 (Alberts et al. 2015). Results of the geochemical work published in *Contributions to Mineralogy and Petrology* by Haase et al. (2016) illustrate constraints on the magmatic evolution of the oceanic crust by interpreting major and trace element data of the plagiogranites. The data suggest that most of the felsic rocks of the plagiogranite intrusions from the Oman ophiolite formed by fractional crystallization processes from mafic melts. Next to plagiogranite intrusions into the sheeted dike section of the ophiolite, granitic intrusions in the mantle section have been sampled. Geochemical analyses including Nd-Hf isotope data indicate an origin by partial melting of pelagic sediments similar to leucogranites in continental collision zones. Thus, the work published in *Geology* by Haase et al. (2015) confirm the possible generation of the ophiolite above a subducting slab.

# Chapter A

## A.1. Silica-rich lavas in the oceanic crust: Experimental evidence for fractional crystallization under low water activity

*Martin Erdmann<sup>1,2</sup> and Jürgen Koepke<sup>1</sup>*

<sup>1</sup>*Institut für Mineralogie, Leibniz Universität Hannover, Callinstr. 3, 30167 Hannover, Germany*

<sup>2</sup>*CRPG, UMR 7358, CNRS, Université de Lorraine, 15 rue Notre Dame des Pauvres, 54501 Vandoeuvre-lès-Nancy, France*

*Contributions to Mineralogy and Petrology, Volume 171(10), pages 1-22, 2016*

*DOI: 10.1007/s00410-016-1294-0*

### A.1.1. Abstract

We experimentally investigated phase relations and phase compositions as well as the influence of water activity ( $a_{\text{H}_2\text{O}}$ ) and redox conditions on the equilibrium crystallization path within an oceanic dacitic potassium-depleted system at shallow pressure (200 MPa). Moreover, we measured the partitioning of trace elements between melt and plagioclase via secondary-ion mass spectrometry for a highly-evolved experiment ( $\text{SiO}_2 = 74.6 \text{ wt}\%$ ). As starting material we used a dacitic glass dredged at the Pacific-Antarctic Rise. Phase assemblages in natural high-silica systems reported from different locations of fast-spreading oceanic crust could be experimentally reproduced only in a relatively small range of temperature and melt-water content ( $T \sim 950^\circ\text{C}$ ; melt  $\text{H}_2\text{O} < 1.5 \text{ wt}\%$ ) at redox conditions slightly below the quartz-fayalite-magnetite buffer. The relatively low water content is remarkable, because distinct hydrothermal influence is generally regarded as key for producing silica-rich rocks in an oceanic environment. However, our conclusion is also supported by mineral and melt chemistry of natural evolved rocks; these rocks are only congruent to the composition of those experimental phases that are produced under low  $a_{\text{H}_2\text{O}}$ . Low FeO contents under water-saturated conditions and the characteristic enrichment of  $\text{Al}_2\text{O}_3$  in high  $a_{\text{H}_2\text{O}}$  experiments, in particular, contradicts natural observations, while experiments with low  $a_{\text{H}_2\text{O}}$  match the natural trend. Moreover, the observation that highly evolved experimental melts remain  $\text{H}_2\text{O}$ -poor while they are relatively enriched in chlorine, implies a decoupling between these two volatiles during crustal contamination.

**Keywords:** *Crystallization experiments, Phase equilibria, Differentiation, Dacite, Fast-spreading mid-ocean ridge, Oceanic plagiogranite*

### A.1.2. Introduction

Although the extrusive crust, which formed at oceanic spreading centers with intermediate- to fast-spreading ridges, is regarded as basaltic, at some places silicic rocks like andesites, dacites, and rhyodacites have erupted (e.g., Byerly et al. 1976; Fornari et al. 1983; Perfit and Fornari, 1983; Hekinian et al. 1999; Haase et al. 2005; Stakes et al. 2006; Wanless et al. 2010, 2011;

Freund et al. 2013). The total amount of these evolved rocks is small but they are widely distributed within the upper oceanic crust. In addition to evolved extrusive rocks, high-silica rocks also occur in the lower oceanic crust, mostly as small intrusions and veins, known from ophiolites (see compilation in Koepke et al. 2004) but also sampled in the recent oceanic crust (e.g., Dick et al. 2000; Wilson et al. 2006; Silantsev et al. 2014; Erdmann et al. 2015).

The generation of highly-evolved, silicic magmas within the oceanic crust has been attributed to various magmatic processes and is, in many cases, related to a complex mix of different formation processes. The question of whether partial melting (Koepke et al. 2007; Brophy, 2009; France et al. 2010, 2014; Erdmann et al. 2015), extensive fractional crystallization (Toplis and Carroll, 1996; Berndt et al. 2005; Brophy 2008), and/or accompanying assimilation of crustal material (Haase et al. 2005; Wanless et al. 2010, 2011; Freund et al. 2013) is the main process in felsic melt generation is discussed at length in the literature. Magma mixing (Sinton and Detrick 1992) and liquid immiscibility (Veksler et al. 2007; Charlier et al. 2013) are additional potential generation processes.

For the experimental simulation of felsic melt generation in the oceanic crust, it is useful to concentrate on one of the described magmatic processes. In previous experimental studies endmember processes for felsic melt generation within oceanic spreading centers under shallow pressures (< 200 MPa) were investigated by using basaltic or gabbroic starting material, for example by simulating partial melting (Beard and Lofgren, 1991; Koepke et al. 2004; France et al. 2010, 2014; Erdmann et al. 2015), crystallization processes (Juster et al. 1989; Berndt et al. 2005; Feig et al. 2006, 2010), and liquid immiscibility (Dixon-Spulber and Rutherford 1983; Charlier et al. 2013). Other studies focused on calc-alkaline differentiation trends (Sisson and Grove 1993) or phase relations in dry or hydrous ferrobalt (Toplis and Carroll 1995; Botcharnikov et al. 2008) via crystallization experiments.

Here, we simulate the process of equilibrium crystallization in a low potassium, oceanic dacitic system by investigating phase relations and phase compositions derived from crystallization experiments. Moreover, we investigate the influence of water activity ( $a_{\text{H}_2\text{O}}$ ) and redox conditions on the crystallization path within this system. As starting material we used a dacitic glass dredged at the Pacific-Antarctic Rise (PAR). The evolved lavas from the PAR, including the starting material of this study, are considered to be products of assimilation-fractional crystallization processes (Haase et al. 2005; Freund et al. 2013). With this experimental work we fill a gap in phase-relation studies on evolved rocks from the oceanic crust, which are characterized by formation under shallow pressure in a relatively dry, potassium-depleted system. Another purpose of this paper is to present coefficients for trace element distribution between crystals and a dacitic melt for modeling magmatic formation and evolutionary processes in such a special, shallow mid-oceanic ridge environment. Up to now, experimental phase relations studies in oceanic high-SiO<sub>2</sub> lavas have only existed for significantly higher pressure and more potassium-enriched systems (see references below).



### A.1.3. Methods

#### A.1.3.1. Starting material from the PAR

Submarine samples were dredged along the fast-spreading PAR between 36°S and 40.5°S in 2001, during the SO157 expedition with the German research vessel RV SONNE. These samples show a wide spectrum of lithologies, from basaltic to andesitic-dacitic composition (Haase et al. 2005). The PAR is intersected by the Foundation Seamount Chain at 37°S which probably formed above a mantle plume.

As starting material we used the sample SO157-3DS1 representing a dacitic, sparsely phyrlic glass, which can be regarded as an evolved end-member in the magmatic evolution of the PAR from mid-ocean ridge basalt (MORB) to felsic melts (analysis of the remelted glass is presented in Table A.1.1). The mineral assemblage in this sample consisted of small (~0.2 mm) plagioclase and clinopyroxene phenocrysts in a glassy matrix with accessory opaques. Detailed petrographical and geochemical information for sample 3DS1 and other characteristic evolved lavas from the PAR are presented by Haase et al. (2005) and Freund et al. (2013).

**Table A.1.1** Starting compositions in wt%

Sample	SiO <sub>2</sub>	TiO <sub>2</sub>	Al <sub>2</sub> O <sub>3</sub>	FeO	MnO	MgO	CaO	Na <sub>2</sub> O	K <sub>2</sub> O	P <sub>2</sub> O <sub>5</sub>	Cr <sub>2</sub> O <sub>3</sub>	SO <sub>2</sub>	Cl	Total
Freund et al. (2013)														
PAR-SO157-3DS1	61.95	1.02	13.54	7.97	0.12	1.57	4.47	4.49	1.27	0.29	0.03	0.06	0.96	97.74
Freund et al. (2013) normalized to 100 wt%														
PAR-SO157-3DS1	63.38	1.04	13.85	8.15	0.12	1.61	4.57	4.59	1.30	0.30	0.03	0.06	0.99	100.00
remelted sample PAR-SO157-3DS1 for this study, normalized to 100 wt%														
PAR-ME	65.00	0.95	14.20	7.87	b.d.	1.46	4.58	4.45	1.18	b.d.	n.a.	b.d.	0.32	100.00
Cadoux et al. (2014), normalized to 100 wt%														
Santorini - Cape Riva	67.58	0.68	15.43	4.35	0.13	1.09	3.00	4.90	2.61	0.23				100.00
Holtz et al. (2005), normalized to 100 wt%														
Unzen	64.58	0.70	15.84	5.04	0.09	2.65	4.86	3.60	2.50	0.14				100.00
Costa et al. (2004), normalized to 100 wt%														
San Pedro	66.33	0.52	16.25	3.90	0.10	1.71	4.05	4.21	2.76	0.16				100.00
Scaillet and Evans (1999), normalized to 100 wt%														
Pinatubo	65.03	0.53	16.42	4.35	2.38	0.10	5.20	4.47	1.53					100.00

b.d. - below detection limit of the electron microprobe

n.a. - not analyzed

#### A.1.3.2. Experimental methods

The experimental procedure is described in detail by Erdmann and Koepke (2016) who used the same starting material. Here, we give a brief summary of the applied procedure. The crushed and ground sample was fused twice at 1600°C and the homogeneity of the resulting glass was checked by electron microprobe. To ensure a minimal pore volume, the Au capsules were filled with 40 mg of glass powder consisting of two different fractions (<125 µm and 125-200 µm) and a defined amount of fluid. In order to study the influence of water,  $a_{\text{H}_2\text{O}}$  of the experiments was fixed via a mixture of (distilled) water and CO<sub>2</sub> (by using silver-oxalate, Ag<sub>2</sub>C<sub>2</sub>O<sub>4</sub>). Five experiments can be performed simultaneously during one run (at defined P, T,  $f_{\text{H}_2}$ ). Four experiments were fluid-saturated with different H<sub>2</sub>O-CO<sub>2</sub> compositions: pure H<sub>2</sub>O ( $X_{\text{H}_2\text{O}}=1$ ,

water saturated),  $X_{\text{H}_2\text{O}}=0.6$ ,  $X_{\text{H}_2\text{O}}=0.2$ , and pure  $\text{CO}_2$  ( $X_{\text{H}_2\text{O}}=0$ ). An additional experiment was performed in which the influence of seawater was simulated by adding a fluid composed of distilled water with 3.2 wt% NaCl (also fluid-saturated; all experiments with 5% total fluid).

All experiments in the high-temperature range (i.e. 1030 to 910°C) were performed in two different vertically-mounted internally heated pressure vessels (IHPVs) at the high pressure lab in Hannover; both IHPVs are equipped with a rapid quench system to prevent the formation of meta-stable quench phases (Berndt et al. 2002). One of these apparatuses is additionally equipped with a Shaw membrane for controlling  $f\text{O}_2$  via the defined addition of  $\text{H}_2$  (for details see Berndt et al. 2002).

The chosen pressure (pure Ar as pressure medium) for the experiments was 200 MPa, which is a typical value for magma storage conditions at the base of fast-spreading oceanic crust. Additionally, near-liquidus experiments were also performed at lower pressure (i.e. 100 and 50 MPa) in order to simulate magma ascent and to study the influence on pressure-sensitive phases. In order to consider the influence of  $f\text{O}_2$  on phase relations and compositions, especially on the stability of FeTi-oxides, two experimental series were performed. For this, different proportions of  $\text{H}_2$  were added to the pressure medium (Ar) corresponding to an  $f\text{O}_2$  of QFM+1 (QFM =  $\log f\text{O}_2$  buffered by the quartz-fayalite-magnetite assemblage; hereafter labeled as “reducing” conditions), and QFM+3.2 (“intrinsic” conditions of the vessel; hereafter labeled as “oxidizing” conditions) for the water-saturated condition. Since in water-undersaturated experiments  $f\text{H}_2\text{O}$  and, thus,  $f\text{O}_2$  decrease with  $a\text{H}_2\text{O}$ , and most of our experiments were water-undersaturated, the prevailing  $f\text{O}_2$  in our experiments was generally more reduced. To calculate  $f\text{O}_2$  under water-undersaturated conditions, we followed Berndt et al. (2005; see below). Considering the variation of  $a\text{H}_2\text{O}$  in our runs, the estimated values of  $f\text{O}_2$  in our experiments varied between  $\sim\text{QFM}-3.4$  and  $\sim\text{QFM}+3.2$ . Temperatures varied between 1030°C (hyper-liquidus for high-water-content/reducing conditions; near-liquidus for lower-water-content/reducing conditions and for high-water-content/oxidizing conditions) and 910°C (near-solidus/solidus) in steps of 40°C.

Near-solidus experiments (i.e.  $T \leq 850^\circ\text{C}$ ) were performed in cold sealed pressure vessels (CSPVs) at 200 MPa ( $\text{H}_2\text{O}$  as pressure medium). In these vessels, redox conditions are buffered by the steel-containing nickel autoclave material. The  $f\text{O}_2$  in the experiments corresponds to NNO (NNO =  $\log f\text{O}_2$  buffered by the nickel-nickeloxide transition) which is identical to  $\Delta\text{QFM}+0.7$ . Therefore, these experiments are in the same range as experiments performed under reducing conditions in the IHPV and, thus, directly comparable to each other.

For two experimental series at 950°C/high initial  $f\text{O}_2$  and 800°C/low initial  $f\text{O}_2$  the temperature-cycling technique was applied in order to generate larger crystals and melt pools (for details see Erdmann and Koepke 2016). Hence, for these conditions a larger data set is available and in-situ trace element analyses were enabled due to larger phases (see below).

The  $a\text{H}_2\text{O}$  was calculated following the thermodynamic model of Burnham (1979, 1994). It should be noted that the model of Burnham (1979) slightly overestimates  $a\text{H}_2\text{O}$  (e.g.,

Botcharnikov et al. 2005). Our experiments were performed with known  $f\text{H}_2$  but variable  $f\text{H}_2\text{O}$ . Therefore,  $f\text{O}_2$  is not strictly constant from one capsule to the other. Decreasing  $f\text{H}_2\text{O}$  along with decreasing  $X\text{H}_2\text{O}$  causes a lowering of  $f\text{O}_2$  (Scaillet et al. 1995; Botcharnikov et al. 2005). Knowing  $f\text{H}_2\text{O}$  (calculated from thermodynamically defined conditions at certain temperature) and  $f\text{H}_2$  ( $\text{pH}_2$  monitored during experiments),  $f\text{O}_2$  can be computed. Here  $f\text{H}_2$  is calculated using the set  $\Delta\text{QFM}$  value for water-saturated conditions of the IHPV. With given pressure, temperature, and intrinsic  $\text{pH}_2$  conditions measured by the Shaw membrane technique, we calculated  $\Delta\text{QFM}$  for water-saturated conditions using the models of Pitzer and Sterner (1995), Shaw and Wones (1964) and Schwab and Küstner (1981). All experimental conditions are summarized in the experimental protocol in Table A.1.2.

### **A.1.3.3. Analytical methods**

These analytical methods are the same as described by Erdmann and Koepke (2016) who used a small subset of experiments presented here for a methodological study. The run products (glass and minerals) were analyzed with the Cameca SX 100 electron microprobe at Leibniz Universität Hannover. To analyze the crystals, the following operating conditions were chosen: 15 kV high voltage, 15 nA beam current, 10 s counting time on peak and 10 s on background, focused beam. For the analysis of the remaining water-bearing glass, which is problematic due to “alkali-loss” effects, a special procedure was applied following Koepke et al. (2004). The beam current was set to 4 nA; the counting time varied for different elements and was 4 s for K, 8 s for Si, Al, Ti, and Fe, 10 s for Na and Zr, 12 s for Mg, 16 s for Ca and 30 s for Ba, P, S, Cl, and Mn. Background counting time was always same as the peak time. Whenever possible a defocused beam with a spot size of 5, 10, or 20  $\mu\text{m}$  was used, and Na loss was checked by comparing the results of measurements with different beam sizes on identical glasses of an experimental sample with larger melt pools. Standard glasses with compositions similar to the experimental glasses and with known water contents have been used for estimating the water contents in the experimental glasses by the “by-difference” method (Devine et al. 1995). When melt pools were large enough, melt-water contents were double checked by Karl-Fischer titration (KFT; for crystal-free samples) and Fourier transform infrared spectroscopy (FTIR; all samples with melt pools larger 30x30  $\mu\text{m}$ ).

For one experiment (#110) trace elements of melt and plagioclase were analyzed with a Cameca IMS-1270 secondary ion mass spectrometer (SIMS) at the Centre de Recherches Pétrographiques et Géochimiques in Nancy, France. An  $\text{O}^-$  primary beam with an intensity of 5-30 nA was used at an acceleration voltage of 13 kV. The secondary beam was accelerated with 10 kV, and we analyzed with a mass resolving power of 8000. The energy offset was set to 0 V with a 40 eV energy window. The beam size was between 20 and 30  $\mu\text{m}$  with a slightly oval shape. A reflected light microscope was used to seek the point of interest on the sample and points were checked after measurement using backscattered electron (BSE) images with an Electron Probe Micro-Analysis (EPMA). One analysis consists of six cycles, each starting from mass  $^{28}\text{Si}$  and increasing to  $^{30}\text{Si}$ ,  $^{47}\text{Ti}$ ,  $^{85}\text{Rb}$ ,  $^{88}\text{Sr}$ ,  $^{89}\text{Y}$ ,  $^{90}\text{Zr}$ ,  $^{93}\text{Nb}$ ,  $^{138}\text{Ba}$ ,  $^{139}\text{La}$ ,  $^{140}\text{Ce}$ ,  $^{142}\text{Ce}$ ,  $^{146}\text{Nd}$ ,  $^{147}\text{Sm}$ ,  $^{151}\text{Eu}$ ,  $^{152}\text{Sm}$ ,  $^{153}\text{Eu}$ , and finally  $^{181}\text{Ta}$  with mass 27.7 and 29.5 as background. For data processing  $^{30}\text{Si}$  was used as reference mass, and the Basalt, Hawaiian Volcano Observatory

(BHVO)-2-G standard (Wilson 1997; Ila and Frey 2000; Gao et al. 2002; Raczek et al. 2003; Strnad et al. 2005) was used for calibration. To provide high-quality data, standard measurements were performed between every analytical session. Data were corrected for oxide interferences following the principle of Fahey et al. (1987) and Hellebrand et al. (2002).

**Table A.1.2** Experimental conditions

Sample	P [MPa]	T [°C]	time [h] <sup>a</sup>	cH <sub>2</sub> O <sup>b</sup>	aH <sub>2</sub> O <sup>c</sup>	log f <sub>O<sub>2</sub></sub> <sup>d</sup>	ΔQFM <sup>e</sup>	phase assemblages and proportions
<b>ΔQFM nominal=+3.2 (at aH<sub>2</sub>O=1)</b>								
PAR-ME-51	200	1030	72	4.5 <sup>h</sup>	0.86	-7.08	+3.2	melt(98.6), Mt(1.4)
PAR-ME-52	200	1030	72	5.2	1.00	-6.96	+3.4	melt(99.0), Mt(1.0)
PAR-ME-53	200	1030	72	2.1	0.30	-8.00	+2.3	melt(98.1), Mt(1.9)
PAR-ME-55	200	1030	72	1.9	0.25	-8.28	+2.0	melt(73.3), Mt(1.3), Cpx-Opx(6.4), Pl(19.0)
PAR-ME-54	200	1030	72	1.4	0.15	-8.74	+1.6	melt(76.4), Mt(2.2), Cpx(3.9), Pl(17.5)
PAR-ME-86	100	1030	69	3.2 <sup>h</sup>	0.82	-6.78	+3.6	melt(98.4), Mt(1.6)
PAR-ME-87	100	1030	69	3.7	1.00	-6.66	+3.7	melt(98.4), Mt(1.6)
PAR-ME-88	100	1030	69	1.0	0.13	-8.41	+2.0	melt(91.5), Mt(1.4), Cpx(1.9), Pl(5.2)
PAR-ME-90	100	1030	69	0.5	0.03	-9.60	+0.8	melt(73.6), Mt(1.5), Cpx(4.3), Pl(20.6)
PAR-ME-89	100	1030	69	0.3	0.01	-10.58	-0.2	melt(78.8), Mt(1.6), Cpx(7.0), Pl(12.6)
PAR-ME-92	50	1030	72	1.9	0.60	-6.47	+4.0	melt(98.6), Mt(1.4)
PAR-ME-91	50	1030	72	1.8 <sup>h</sup>	0.56	-6.54	+3.9	melt(98.1), Mt(1.9)
PAR-ME-93	50	1030	72	0.3	0.02	-9.32	+1.1	melt(92.9), Mt(2.8), Cpx(1.0), Pl(3.3)
PAR-ME-94	50	1030	72	0.1	0.00	-11.17	-0.8	melt(87.2), Mt(0.7), Cpx(2.9), Pl(9.3)
PAR-ME-95	50	1030	72	0.1	0.00	-12.12	-1.7	melt(78.4), Mt(2.0), Cpx(3.1), Pl(16.5)
PAR-ME-36	200	990	115	4.4 <sup>h</sup>	0.84	-7.88	+3.0	melt(98.5), Mt(1.5)
PAR-ME-37	200	990	115	4.2	0.78	-7.94	+3.0	melt(98.4), Mt(1.6)
PAR-ME-38	200	990	115	2.3	0.34	-8.61	+2.3	melt(79.4), Mt(3.1), Cpx(7.7), Pl(9.8)
PAR-ME-39	200	990	115	2.0	0.28	-8.79	+2.1	melt(45.3), Mt(9.2), Cpx-Opx(4.1), Pl(41.4)
PAR-ME-40	200	990	115	1.9	0.26	-8.85	+2.1	melt(42.4), Mt(2.3), Cpx-Opx(21.6), Pl(33.8)
PAR-ME-57 <sup>f</sup>	200	950±20	120	5.1	1.00	-8.35	+3.2	melt(95.2), Mt(2.4), Cpx(0.9), Ap(1.5)
PAR-ME-42 <sup>f</sup>	200	950	120	5.1	0.98	-8.37	+3.2	melt(95.1), Mt(1.9), Cpx(1.2), Ap(1.8)
PAR-ME-62 <sup>f</sup>	200	950±20	120	4.9	1.00	-8.35	+3.2	melt(96.6), Mt(2.2), Cpx(0.5), Ap(0.7)
PAR-ME-41	200	950	120	4.8 <sup>h</sup>	0.92	-8.43	+3.1	melt(93.0), Mt(2.6), Cpx(2.6), Ap(1.7)
PAR-ME-43 <sup>f</sup>	200	950	120	2.6	0.39	-9.38	+2.2	melt(63.3), Mt(5.1), Cpx(6.0), Pl(25.6)
PAR-ME-44	200	950	120	2.3	0.34	-9.50	+2.0	melt(68.1), Mt(2.7), Cpx(7.1), Pl(21.4), Qz(0.8)
PAR-ME-58 <sup>f</sup>	200	950±20	120	2.0	0.26	-9.52	+2.0	melt(67.7), Mt(3.8), Cpx(4.4), Pl(24.1)
PAR-ME-63 <sup>f</sup>	200	950±20	120	1.8	0.22	-9.67	+1.9	melt(66.6), Mt(3.1), Cpx(3.9), Pl(26.5)
PAR-ME-66 <sup>f</sup>	200	950±20	120	0.8	0.06	-10.82	+0.7	melt(32.0), Mt(3.7), Cpx-Opx(15.2), Pl(47.5), Qz(1.6)
PAR-ME-45 <sup>f</sup>	200	950	120	0.5	0.02	-11.79	-0.3	melt(24.9), Mt(6.1), Cpx(20.9), Pl(44.1), Qz(4.0)
PAR-ME-65 <sup>f</sup>	200	950±20	120	0.5	0.02	-11.6	-0.1	melt(24.3), Mt(5.7), Cpx(12.9), Pl(53.0), Qz(4.2)
PAR-ME-46	200	910	144	5.3 <sup>h</sup>	0.99	-9.32	+2.9	melt(90.7), Mt-Ilm(2.3), Cpx(4.1), Ap(2.9)
PAR-ME-47	200	910	144	5.1	0.95	-9.35	+2.9	melt(90.9), Mt-Ilm(2.6), Cpx(3.8), Ap(2.7)
PAR-ME-49	200	910	144	2.2	0.31	-10.33	+1.9	melt(55.4), Mt(3.5), Cpx(4.8), Pl(32.4), Qz(3.9)
PAR-ME-50	200	910	144	1.6	0.16	-10.88	+1.3	melt(29.6), Mt(6.6), Cpx(21.8), Pl(35.0), Qz(7.1)

**Table A.1.2** *continued*

Sample	P [MPa]	T [°C]	time [h] <sup>a</sup>	cH <sub>2</sub> O <sub>b</sub>	aH <sub>2</sub> O <sub>c</sub>	log <i>f</i> O <sub>2</sub> <sup>d</sup>	ΔQFM <sub>e</sub>	phase assemblages and proportions
<b>ΔQFM nominal=+1 (at aH<sub>2</sub>O=1)</b>								
PAR-ME-27	210	1030	92	3.0	0.51	-9.27	+1.0	melt(100)
PAR-ME-28	210	1030	92	2.7	0.44	-9.41	+0.9	melt(100)
PAR-ME-26	210	1030	92	1.8 <sup>h</sup>	0.23	-9.95	+0.4	melt(98.5), Cpx(1.5)
PAR-ME-30	210	1030	92	1.3	0.14	-10.34	±0	melt(75.3), Cpx-Opx(4.2), Pl(20.5)
PAR-ME-29	210	1030	92	0.6	0.03	-11.59	-1.3	melt(73.4), Cpx-Opx(6.8), Pl(19.8)
PAR-ME-11	200	990	220	5.5 <sup>h</sup>	1.00	-10.03	+0.9	melt(100)
PAR-ME-12	200	990	220	5.3	1.00	-10.03	+0.9	melt(100)
PAR-ME-13	200	990	220	2.8	0.45	-10.73	+0.2	melt(96.2), Cpx(3.2), Pl(0.6)
PAR-ME-14	200	990	220	1.9	0.26	-11.20	-0.3	melt(73.8), Ilm(0.6), Cpx-Opx(6.0), Pl(19.6)
PAR-ME-15	200	990	220	1.0	0.08	-12.24	-1.3	melt(34.9), Ilm(2.8), Cpx-Opx(20.0), Pl(42.3)
PAR-ME-21	208	950	115	5.5 <sup>h</sup>	1.00	-10.79	+0.7	melt(100)
PAR-ME-22	208	950	115	5.2	1.00	-10.79	+0.7	melt(100)
PAR-ME-23	208	950	115	2.1	0.28	-11.93	-0.4	melt(77.6), Mt(1.3), Cpx-Opx(9.9), Pl(11.2)
PAR-ME-24	208	950	115	1.3	0.13	-12.62	-1.1	melt(46.0), Mt-Ilm(1.2), Cpx-Opx(11.6), Pl(41.3)
PAR-ME-25	208	950	115	0.3	0.01	-14.89	-3.4	melt(47.8), Ilm(1.3), Cpx-Opx(16.2), Pl(34.7)
PAR-ME-02	200	910	188	4.4	0.81	-11.06	+1.2	melt(90.2), Mt(2.8), Cpx(4.5), Ap(2.5)
PAR-ME-01	200	910	188	4.2 <sup>h</sup>	0.76	-11.11	+1.1	melt(89.4), Mt(2.8), Cpx(4.5), Ap(3.3)
PAR-ME-04	200	910	188	2.0	0.27	-12.01	+0.2	melt(26.7), Mt(4.0), Cpx(17.8), Pl(43.5), Qz(8.1)
PAR-ME-03	200	910	188	1.6	0.17	-12.39	-0.2	melt(28.3), Mt(2.7), Cpx-Opx(11.7), Pl(55.0), Qz(2.3)
PAR-ME-05	200	910	188	1.0	0.09	-13.01	-0.8	melt(21.6), Mt(3.7), Cpx-Opx(17.8), Pl(51.0), Qz(5.8)
PAR-ME-71	200	850	670 <sup>e</sup>	5.5 <sup>h</sup>	1.00	-12.01	+1.3	melt(85.4), Mt-Ilm(3.3), Cpx(5.5), Pl(4.1), Ap(1.7), Zrn
PAR-ME-72	200	850	670 <sup>e</sup>	5.1	0.92	-12.70	+0.6	melt(70.6), Mt-Ilm(3.7), Cpx(5.4), Pl(17.2), Ap(3.1), Zrn
PAR-ME-81 <sup>f</sup>	200	800	650 <sup>e</sup>	5.5 <sup>h</sup>	1.00	-13.73	+0.6	melt(72.5), Mt-Ilm(4.9), Cpx(8.2), Pl(14.4), Ap, Zrn
PAR-ME-101 <sup>f</sup>	200	800±20	336 <sup>e</sup>	5.5 <sup>h</sup>	1.00	-13.77	+0.5	melt(68.4), Mt-Ilm(5.7), Cpx(6.7), Pl(19.1), Zrn, Amp
PAR-ME-82	200	800	650 <sup>e</sup>	5.4	1.00	-13.73	+0.6	melt(70.2), Mt-Ilm(3.3), Cpx(6.6), Pl(18.3), Ap(1.6), Zrn
PAR-ME-110 <sup>f</sup>	200	800+5 0	336 <sup>e</sup>	5.4	1.00	-13.77	+0.5	melt(63.9), Mt-Ilm(3.0), Cpx(13.6), Pl(19.6)
PAR-ME-105 <sup>f</sup>	200	800	336 <sup>e</sup>	4.8 <sup>h</sup>	0.86	-13.89	+0.4	melt(75.9), Mt-Ilm(3.8), Cpx(6.6), Pl(13.7), Ap, Zrn, Amp
PAR-ME-107 <sup>f</sup>	200	800	336 <sup>e</sup>	3.5	0.62	-14.19	+0.1	melt(46.7), Mt-Ilm(5.7), Cpx(10.8), Pl(30.9), Qz(6.0)
PAR-ME-111 <sup>f</sup>	200	800+5 0	336 <sup>e</sup>	3.1	0.50	-14.37	-0.1	melt(49.5), Mt-Ilm(6.6), Cpx(9.0), Pl(28.0), Qz(7.0), Amp
PAR-ME-103 <sup>f</sup>	200	800±20	336 <sup>e</sup>	2.9	0.44	-14.48	-0.2	melt(39.8), Mt-Ilm(6.1), Cpx(8.2), Pl(33.1), Qz(12.9), Ap, Zrn
PAR-ME-97	200	750	666 <sup>e</sup>	5.1	1.00	-14.95	+0.5	melt(40.2), Ilm(7.0), Cpx(11.1), Pl(23.2), Qz(18.6), Ap, Zrn, Amp

*Mt* magnetite, *Ilm* ilmenite, *Cpx* clinopyroxene, *Opx* orthopyroxene, *Pl* plagioclase, *Qz* quartz, *Ap* apatite, *Zrn* zircon, *Amp* amphibole

<sup>a</sup> time between reaching desired temperature and rapid quench

<sup>b</sup> water content of the melt determined via by-difference with electron microprobe (KFT-calibrated)

<sup>c</sup> aH<sub>2</sub>O is calculated from the measured composition of the fluid phase after Burnham (1979)

<sup>d</sup> calculated following the procedure of Scaillet et al. (1995)

<sup>e</sup> ΔQFM indicates log *f*O<sub>2</sub> (experiment) - log *f*O<sub>2</sub> (QFM buffer) as estimated by Schwab and Küstner (1981)

<sup>f</sup> Data from Erdmann and Koepke (2016); if specified, temperature variations indicate temperature cycling

<sup>e</sup> experiments performed in CSPVs; intrinsic conditions in the CSPVs correspond to the NNO buffer (NNO ~ ΔQFM+1)

<sup>h</sup> seawater analog (distilled water + 3.2 wt% NaCl) was added as fluid phase instead of pure water

## A.1.4. Experimental results

### A.1.4.1. Phase relations

Phase relations were studied using IHPVs in the high-temperature range from 1030°C to 910°C under both oxidizing conditions (i.e.  $\Delta\text{QFM}+3.2$  at  $a\text{H}_2\text{O}=1$ ) and reducing conditions (i.e.  $\Delta\text{QFM}+1$  at  $a\text{H}_2\text{O}=1$ ). The latter case corresponds more closely to the natural system, in an environment where fractionated, MORB-derived melts interact with a hydrothermally altered oceanic crust. For the 850°C to 750°C temperature range only one set of experiments was performed using the CSPVs under  $f\text{O}_2$  corresponding to  $\sim \Delta\text{QFM}+1$  at  $a\text{H}_2\text{O}=1$  (see above). The phase relations are presented in Fig. A.1.1a and A.1.1b.

Clinopyroxene is the liquidus phase under reducing conditions and is the second mineral after magnetite to crystallize under oxidizing conditions. The clinopyroxene saturation curves are quite similar in both experimental series, except that under reducing conditions the saturation curve is slightly shifted to lower temperatures compared to oxidized conditions. The plagioclase saturation curves are also quite similar under both redox conditions, with a marked negative slope addressing the well-known effect of  $\text{H}_2\text{O}$  on the suppression of plagioclase crystallization (e.g., Gaetani et al. 1993, Berndt et al. 2005). Similar to observations of other experimental studies in various systems (e.g., Feig et al. 2006, 2010, primitive MORB system; Almeev et al. 2012, rhyolitic system), low-Ca pyroxene has a relatively small stability field, being restricted to low melt-water content and relatively high temperature. The amount of low-Ca pyroxene crystals in the run products is very low (only one analysis per run was possible; see electronic supplemental material A.1.ESM). The stability of quartz is directly correlated to low-Ca pyroxene stability based on the simplified peritectic reaction of enstatite to quartz (Ernst 1976). Here, in a non-ideal system with no end-member composition, a strict transition from one phase to the other does not exist and the stability fields of these two phases slightly overlap at reducing conditions. At higher  $f\text{O}_2$ , quartz is also stable at 950°C. Magnetite is liquidus phase under oxidizing conditions, while under reducing conditions, magnetite crystallizes at  $\sim 950^\circ\text{C}$  and becomes unstable at  $T \leq 750^\circ\text{C}$ . The only accessory mineral observed in the high-temperature range (i.e. 1030 to 910°C in IHPVs) is apatite, in both oxidizing and reducing experiments. Zircon, as a second accessory mineral, is stable in all runs with melt  $\text{H}_2\text{O} > 3.5$  wt%. Amphibole is the last crystallizing phase, only stable in experiments at high melt-water content ( $\geq 4.8$  wt%) and low temperature ( $\leq 800^\circ\text{C}$ ). The solidus is dramatically influenced by the water content, independent of redox conditions. It is shifted lower by more than 300°C when comparing the dry system (solidus at  $\sim 1000^\circ\text{C}$ ) with water-saturated conditions (solidus at  $\sim 700^\circ\text{C}$  at melt  $\text{H}_2\text{O} \approx 5.5$  wt%; data only available for reducing conditions; Fig. A.1.1b).

### A.1.4.2. Phase proportions

Proportions of all phases (determined via *ImageJ*; Schneider et al. 2012; <http://imagej.nih.gov/ij/>) are listed in Table A.1.2. The melt fraction in experiments with high  $a\text{H}_2\text{O}$  ( $> 0.8$ ) is relatively high over a large temperature range ( $\geq 64$  vol% at  $T \geq 800^\circ\text{C}$ ) and decreases rapidly at  $T = 750^\circ\text{C}$  to  $\leq 40$  vol% (Fig. A.1.2a). The melt fraction remains at a relatively high level ( $\geq 40$  vol%) in experiments with a moderate water content ( $a\text{H}_2\text{O} > 0.4$ ) at

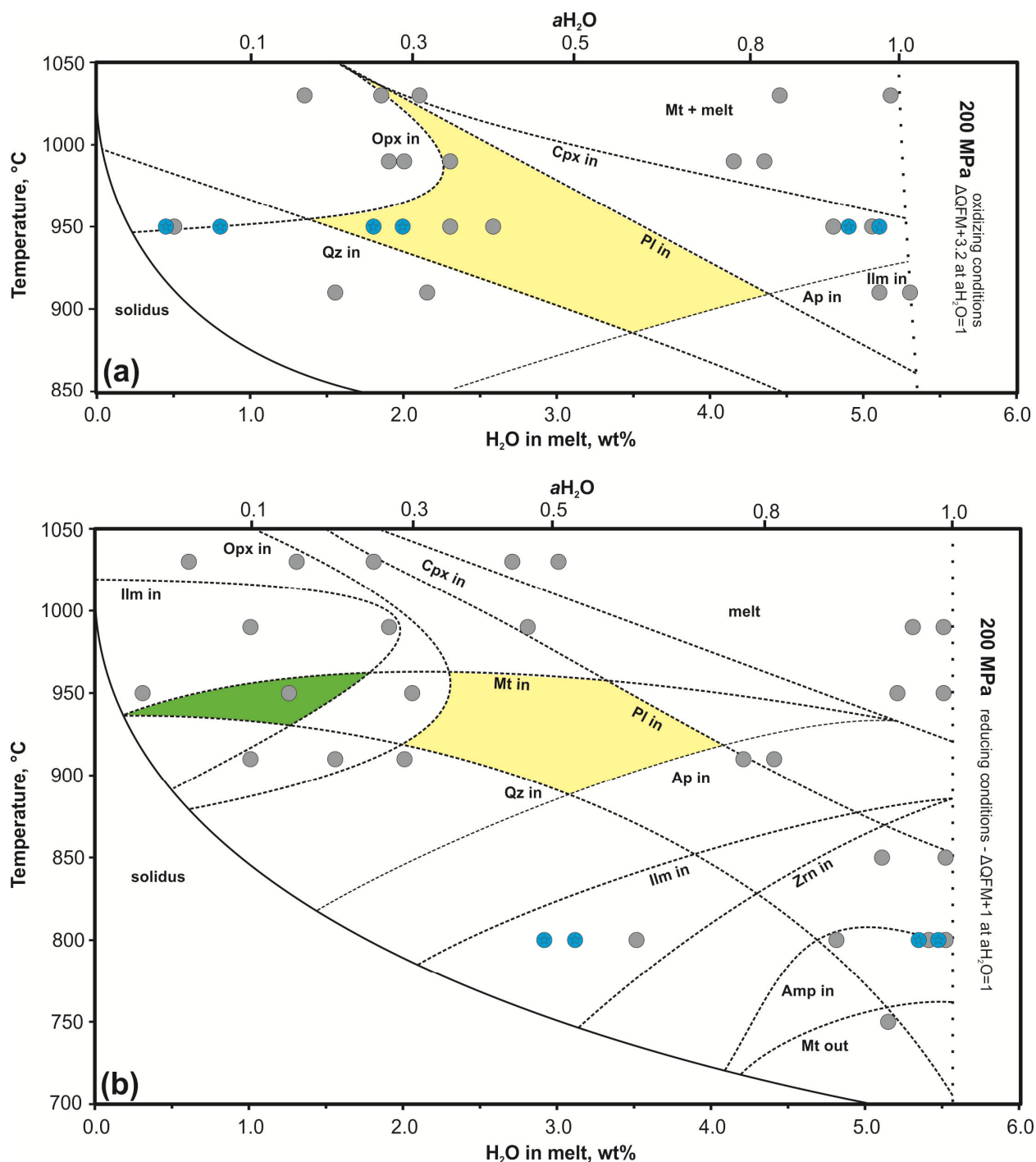


**Figure A.1.1:** Phase relations determined for the PAR 3DS1 sample (dacitic composition) as a function of temperature and water content in the melt (in wt%) at **a)** high initial  $fO_2$  ( $\Delta QFM+3.2$  at  $aH_2O=1$ ) and **b)** low initial  $fO_2$  ( $\Delta QFM+3.2$  at  $aH_2O=1$ ). Each grey dot represents an experimental run (dots marked with a star are cycling experiments; see Erdmann and Koepke 2016 for details). The green field highlights conditions with the best match to phase assemblages of natural systems, the yellow field indicates the mineral assemblage observed in the natural PAR silicic lavas (see text for details). The dashed vertical line marks water saturation in each system. The experimental data and mineral abbreviations are presented in Tab. A.1.2. Please note that given  $aH_2O$  values are only estimated and do not exhibit a linear relationship with the melt-water content. A greatly simplified version of this phase diagram was published by Erdmann and Koepke (2016).

temperatures (i.e.  $T = 800^\circ\text{C}$ ). However, slightly lower water contents ( $a_{\text{H}_2\text{O}} < 0.4$ ) dramatically decrease the melt fraction down to  $\sim 20$  vol% at  $910^\circ\text{C}$ . This pronounced difference between experiments with high and low  $a_{\text{H}_2\text{O}}$  also accounts for the steeply-sloping solidus curve (inversely proportional;  $y \sim 1/x$ ) in the phase diagram at low water contents with differences of about  $200^\circ\text{C}$  between dry conditions and 2 wt%  $\text{H}_2\text{O}$  and a moderate decrease at higher water contents (see Fig. A.1.1).

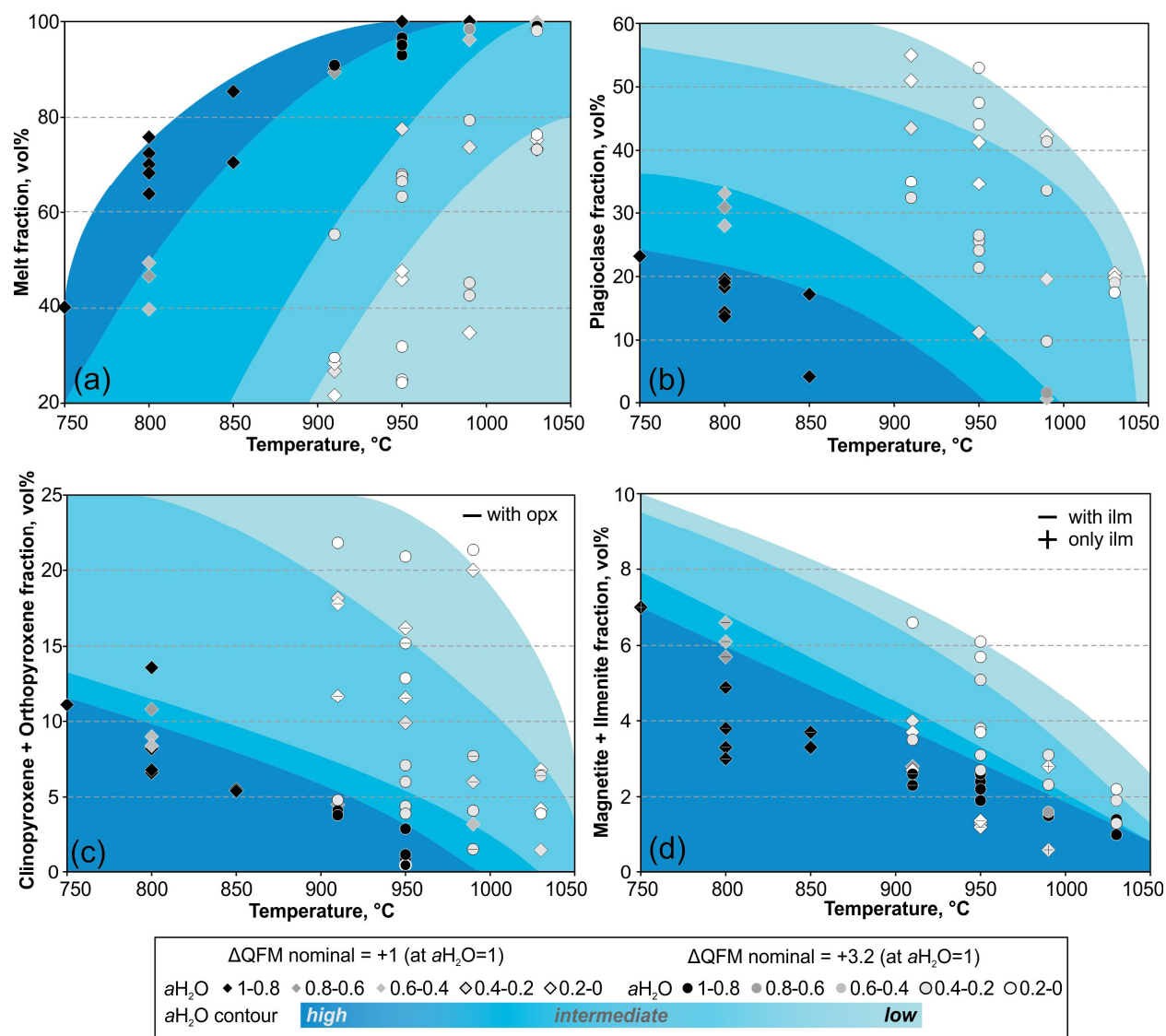


**Figure A.1.2:** Phase proportions (determined via *ImageJ*; Schneider et al. 2012; <http://imagej.nih.gov/ij/>) as a function of temperature,  $f_{\text{O}_2}$ , and  $a_{\text{H}_2\text{O}}$ . Experiments under oxidizing conditions at  $950^\circ\text{C}$  and reducing conditions at  $800^\circ\text{C}$  are from Erdmann and Koepke (2016).

The plagioclase fraction exhibits an inverse relationship to the trend of melt fraction, i.e. it increases with decreasing temperature. At high  $a_{\text{H}_2\text{O}}$ , low crystallization degree, and higher temperature, plagioclase is not stable (Fig. A.1.2b).

The fraction of pyroxenes is relatively low for  $a_{\text{H}_2\text{O}} > 0.4$  over the complete temperature range and also shows no significant increase close to the solidus. This is different for  $a_{\text{H}_2\text{O}} < 0.4$  where the pyroxene fraction spans a large range and the increase in pyroxene fraction with



decreasing temperature is much larger when compared to the wet system. The modal percentages of clinopyroxenes and orthopyroxenes are summed, as they are indistinguishable by BSE image analyses. Orthopyroxenes are, however, rare (only present as single crystals at  $T \geq 910^\circ\text{C}$  under reducing conditions,  $T \geq 950^\circ\text{C}$  at oxidizing conditions, and melt  $\text{H}_2\text{O} \leq 2 \text{ wt}\%$ ) and do not influence the phase proportion significantly (Fig. A.1.2c).

The fraction of FeTi-oxides remains at a relatively low level over the complete temperature range ( $\leq 7 \text{ vol}\%$ , except for one outlier at  $990^\circ\text{C}$ ); also, the influence of varying  $a\text{H}_2\text{O}$  is smaller than for the other phases (Fig. A.1.2d). A significant observation is the delayed crystallization of FeTi-oxides under reducing conditions and the absence of ilmenite in most experiments performed under oxidizing conditions (only present at  $910^\circ\text{C}$  and high  $a\text{H}_2\text{O}$ ). However, there is no observable influence on the total FeTi-oxide fraction in general if ilmenite is present.

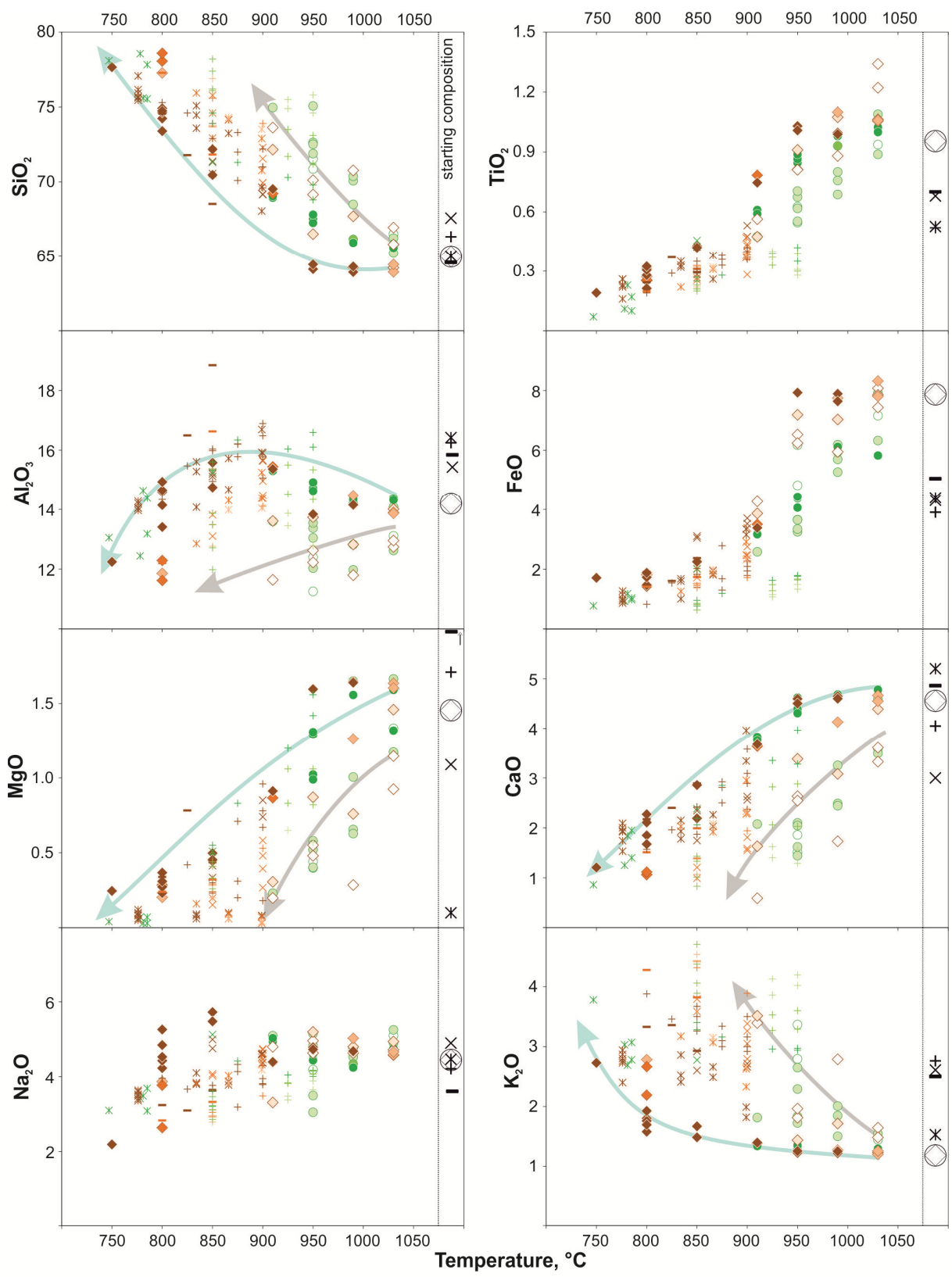
#### **A.1.4.3. Phase chemistry**

The major element compositions of all phases with respect to temperature are given in the electronic supplemental material A.1.ESM.

##### *Glass*

The chemical evolution of various element oxides with respect to temperature,  $a\text{H}_2\text{O}$ , and  $f\text{O}_2$  (for  $T \geq 910^\circ\text{C}$ ) is illustrated in Figure A.1.3. When comparing experiments performed at the same temperature, a shift to higher  $\text{SiO}_2$  values under oxidizing conditions is visible and is most pronounced at high  $a\text{H}_2\text{O}$ . This shift is mainly caused by the early crystallization of magnetite and, slightly delayed, clinopyroxene under oxidizing conditions, while the corresponding experiments under reducing conditions are crystal free (see also Fig. A.1.1).

Other than the indirect effect on  $\text{SiO}_2$ , the different applied redox conditions mainly influence the crystallization of FeTi-oxides and, thus, the concentration of FeO and, to a smaller extent,  $\text{TiO}_2$  in the melt. Most obvious is the shift of melt FeO content in less-evolved, water-saturated samples. While the FeO concentration in experiments performed under reducing conditions is close to the starting composition at higher temperature ( $\sim 8 \text{ wt}\%$ ) followed by a strong decrease in FeO between  $950^\circ\text{C}$  and  $910^\circ\text{C}$  with initiated FeTi-oxide crystallization, the content of FeO in experiments performed under oxidizing conditions is also distinctly lower at high temperature ( $\sim 6 \text{ wt}\%$ ). Under reducing conditions only at low  $a\text{H}_2\text{O}$ , a significant increase of  $\text{TiO}_2$  in the melt relative to the starting material is visible. This feature corresponds to a continuation of the tholeiitic trend well-known from typical basaltic systems (e.g., Toplis and Carroll, 1995; Berndt et al. 2005) to the more-evolved system investigated here. This significant increase in  $\text{TiO}_2$  is a consequence of the absence of FeTi-oxides under these conditions and contrasts with corresponding experiments under oxidizing conditions. There, the crystallization of magnetite occurs early and incorporates up to  $12.5 \text{ wt}\%$   $\text{TiO}_2$ , which is reflected by the decrease in melt  $\text{TiO}_2$  content.



reduced conditions ( $\Delta QFM$ nominal $\approx +1$ at $a_{H_2O}=1$ )	oxidized conditions ( $\Delta QFM$ nominal $\approx +3.2$ at $a_{H_2O}=1$ )
$a_{H_2O}$ $\blacklozenge$ 1-0.8 $\color{orange}\lozenge$ 0.8-0.6 $\color{lightorange}\lozenge$ 0.6-0.4 $\color{yellow}\lozenge$ 0.4-0.2 $\color{lightyellow}\lozenge$ 0.2-0	$a_{H_2O}$ $\bullet$ 1-0.8 $\color{green}\bullet$ 0.8-0.6 $\color{lightgreen}\bullet$ 0.6-0.4 $\color{yellowgreen}\bullet$ 0.4-0.2 $\color{lightyellow}\bullet$ 0.2-0
$\times$ Cadoux et al. (2014) $-$ Holtz et al. (2005) $+$ Costa et al. (2004) $\times$ Scaillet & Evans (1999)	
<i>literature data with same coloring for redox conditions and <math>a_{H_2O}</math> as used for experiments of this study</i>	
$\longrightarrow$ trend for low $a_{H_2O}$	$\longrightarrow$ trend for high $a_{H_2O}$

**Figure A.1.3:** (see previous page) Compositional evolution of experimental melts as a function of temperature,  $fO_2$ , and  $aH_2O$ . All compositions are in wt% and normalized to 100%. For comparison, we include selected experimental results from the literature (Scaillet and Evans 1999; Costa et al. 2004; Holtz et al. 2005; Cadoux et al. 2014) using dacitic starting material at similar experimental conditions in terms of temperature, pressure, water contents, and redox conditions (see text for details). Experiments under oxidizing conditions at 950°C and reducing conditions at 800°C are from Erdmann and Koepke (2016).

As expected, the  $Al_2O_3$  concentration is enriched in those experiments in which plagioclase crystallization is delayed (i.e. at high  $aH_2O$  and temperatures above 850°C). With initiation of plagioclase crystallization at high  $aH_2O$ ,  $Al_2O_3$  content in the melt decreases rapidly to the same level found under  $H_2O$ -undersaturated conditions. Samples with intermediate  $aH_2O$  contain less plagioclase than samples with low  $aH_2O$ , which is illustrated by a slower decrease in  $Al_2O_3$  (see also phase proportions in Table A.1.2).

The delay in plagioclase crystallization at high  $aH_2O$  also affects the CaO concentrations. However, with respect to CaO in melt, clinopyroxene crystallization has a more distinct effect due to the higher concentration of CaO in clinopyroxene compared to plagioclase. Hence, CaO content in melt decreases earlier in the crystallization sequence than does  $Al_2O_3$  content, since clinopyroxene crystallizes at a higher temperature than does plagioclase (Fig. A.1.3). At intermediate and low  $aH_2O$ , clinopyroxene crystallization dominates and leads to a linear decrease in CaO. This is also valid for the decrease of melt MgO since MgO is incorporated in significant amounts exclusively in pyroxenes.  $K_2O$  is not significantly enriched in any crystalline phase; thus, the trend of  $K_2O$  reflects the degree of pure fractional crystallization (determined with the modeling program MELTS; e.g., Wanless et al. 2010), which is more pronounced at low  $aH_2O$  than at lower higher water contents (Fig. A.1.3).

#### *Magnetite & ilmenite*

As expected from results of previous studies (e.g., Toplis and Carroll 1995; Bernd et al, 2005; Feig et al. 2010), the stability of FeTi-oxides is significantly influenced by changing redox conditions. Magnetite is the dominant FeTi-oxide and is stable in all samples, at least under oxidizing conditions. Figure A.1.4 shows the composition of the FeTi-oxides, recalculated following Stormer (1983). The magnetite (MT) – ulvöspinel (USP) solid solution ( $X_{MT}$ ) for all redox conditions varies from  $X_{MT}$  0.31 to 0.97 (Fig. A.1.4a). Ilmenite in the experiments performed under oxidizing conditions is rare and is characterized by a high hematite component ( $X_{ILM} < 0.4$ ; Fig. A.1.4b).

The MT-USP solid solution for experiments under oxidizing conditions with  $aH_2O > 0.4$  is relatively high ( $X_{MT} \geq 0.88$ ). As expected, MT crystallized at comparable  $aH_2O$  but under reducing conditions shows a higher USP component with values down to  $X_{MT} = 0.76$ . The results show a linear trend with lower  $X_{MT}$  accompanied by lower  $aH_2O$  and, thus, lower  $fO_2$ . Consequently, the  $X_{MT}$  in experiments with low  $aH_2O$  ( $< 0.4$ ) and under reducing conditions varies from  $X_{MT} = 0.31$  to a high of  $X_{MT} = 0.61$ , lower than in comparable experiments performed under oxidizing conditions ( $X_{MT} = 0.86-0.42$ ). However, the general trend observed under reducing conditions mirrors the trend observed under oxidizing conditions except for experiments with extremely low  $aH_2O$  (Fig. A.1.4a). Experimental MT compositions of

Botcharnikov et al. (2008), who performed a phase relation study using a ferrobasalt as starting material, follow a clear linear trend towards lower  $X_{MT}$  with decreasing  $\Delta QFM$ , even more pronounced than in our experimental results. However, Botcharnikov et al (2008) did not observe any correlation in terms of  $aH_2O$  and concluded that  $aH_2O$  has no effect. At least for the dacitic system presented here, our results show that the influence of  $aH_2O$  is obvious, irrespective of the applied initial redox condition.

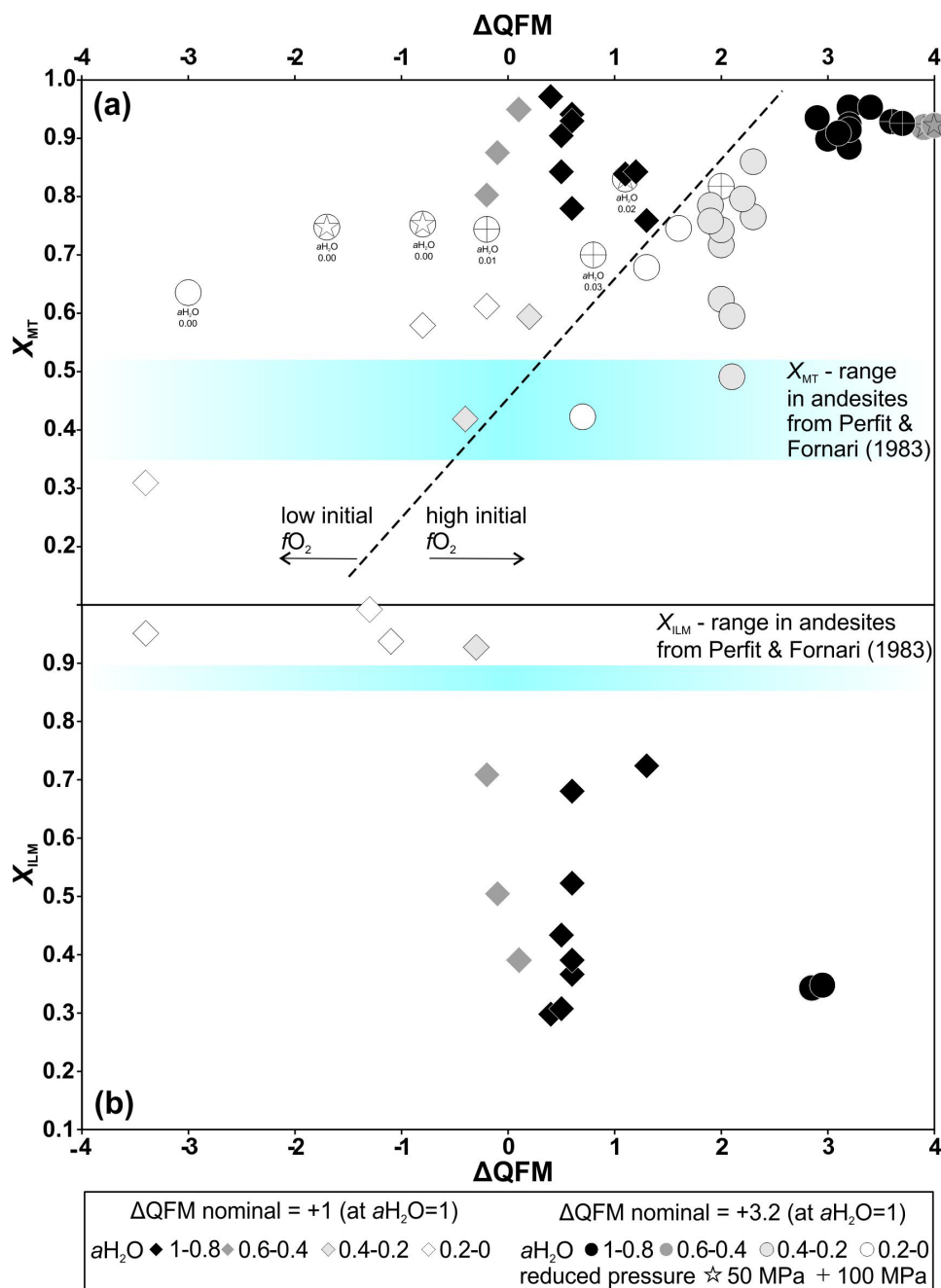


**Figure A.1.4:** Mole fractions of (a) MT in magnetite-ulvöspinel solid solution and (b) ILM in ilmenite-hematite solid solution, as a function of redox conditions (expressed as  $\Delta QFM$ ) and  $aH_2O$ . Dashed line in (a) separates experiments with high from those with low initial  $fO_2$ . The blue fields in (a) and (b) correspond to the composition of FeTi-oxides from eastern Galapagos rift andesites (Perfit and Fornari 1983). Experiments under oxidizing conditions at 950°C and reducing conditions at 800°C are from Erdmann and Koepke (2016).

With regard to the ILM-HM solid solution (Fig. A.1.4b), experiments performed under reducing conditions and high  $aH_2O$  produce ilmenites which are as hematite-rich as those produced under high  $aH_2O$  and oxidizing conditions ( $X_{ILM} < 0.4$ ). Lowering the  $aH_2O$  causes an increase in the ilmenite mole fraction, up to 0.99 at  $aH_2O < 0.1$ . This marked step towards high  $X_{ILM}$  values proceeds exactly at the  $fO_2$  of the fayalite-magnetite-quartz buffer ( $\Delta QFM=0$ ). Berndt et al.

(2005) stated that ilmenite crystallization is less dependent on melt oxidation state but is controlled mainly by melt  $\text{TiO}_2$  concentration, which increases with a higher degree of crystallization. Our experiments under two different redox conditions show that this conclusion has limited applicability for phase relations in a dacitic system. Since in both of our experimental series all conditions are the same except for  $f\text{O}_2$ , the absence of ilmenite at low melt-water content and high temperature in oxidizing experiments argues for an influence of varying redox conditions on ilmenite crystallization. This is supported by Botcharnikov et al. (2008) who showed that ilmenite is only stable in a tholeiitic system at  $f\text{O}_2$  corresponding to  $\Delta\text{QFM}+1$ . While generally in agreement with our experiments, Botcharnikov et al. (2008) observed HM-rich oxides (low  $X_{\text{ILM}}$ ) only under highly-oxidized conditions ( $\Delta\text{QFM} \gg 3$ ). Moreover, their experimental products are, in contrast to our study, independent of  $a\text{H}_2\text{O}$ ; they also detected water-saturated oxides at high ILM fractions. Here, as described already for  $X_{\text{MT}}$ , a correlation of  $X_{\text{ILM}}$  and  $a\text{H}_2\text{O}$  and, thus, redox conditions is detectable.

Seven experiments produced coexisting ilmenite and magnetite which were applied to the two-oxide geothermometer of Andersen and Lindsley (1985) using the calculation procedure of Stormer (1983). In general, the calculated temperatures are in the same range as experimental temperatures. Temperatures in experiments performed under reducing conditions are slightly overestimated by the calculation, with a larger deviation at lower temperatures ( $\Delta T \approx +50\text{K}$  at  $800^\circ\text{C}$ ) and better consistency at higher run temperatures ( $\Delta T \approx +30\text{K}$  at  $850^\circ\text{C}$  and  $\Delta T \approx +10\text{K}$  at  $950^\circ\text{C}$ ). In contrast, calculated temperatures for experiments performed under oxidizing conditions are slightly underestimated (Tab. A.1.3). Redox conditions obtained from the geothermometer of Andersen and Lindsley (1985) are consistent with those experiments that are performed above  $900^\circ\text{C}$  but out of the range at lower temperatures and reduced experimental conditions (Tab. A.1.3).

**Table A.1.3** Geothermometry of magnetite-ilmenite pairs

Sample	T [ $^\circ\text{C}$ ] exp.	T [ $^\circ\text{C}$ ] calc. <sup>a</sup>	log $f\text{O}_2$ <sup>b</sup> exp.	log $f\text{O}_2$ <sup>b</sup> calc. <sup>a</sup>
<b><math>\Delta\text{QFM nominal}=+3.2</math> (at <math>a\text{H}_2\text{O}=1</math>)</b>				
PAR-ME-46	910	893	-9.32	-9.26
PAR-ME-47	910	880	-9.35	-9.51
<b><math>\Delta\text{QFM nominal}=+1</math> (at <math>a\text{H}_2\text{O}=1</math>)</b>				
PAR-ME-24	950	959	-12.62	-12.30
PAR-ME-71	850	877	-12.01	-11.13
PAR-ME-72	850	878	-12.70	-10.95
PAR-ME-81 <sup>c</sup>	800	850	-13.73	-10.01
PAR-ME-82	800	857	-13.73	-10.03

<sup>a</sup> calculation of the equilibrium temperature and  $f\text{O}_2$  using the geothermobarometer of Andersen & Lindsley (1985);  $X^{\text{Usp}}$  &  $X^{\text{Ilm}}$  from Stormer (1983)

<sup>b</sup> calculated following the procedure of Scaillet et al. (1995)

<sup>c</sup> experiment from Erdmann and Koepke (2016)

*Pyroxene*

While pyroxenes in experiments with high  $a_{H_2O}$  are exclusively clinopyroxenes (mainly augites and few diopsides), experiments performed at lower  $a_{H_2O}$  often exhibit both clinopyroxenes and low-Ca pyroxenes (pigeonites). However, most pigeonites are relatively Ca rich. Thus, we assume that our obtained compositions are the result of accidental detection of a pigeonite and augite combination, caused by a tiny intergrowth as previously observed by Grove and Bence (1979). Grove and Bence’s (1979) experimental study interpreted pyroxenes with intermediate Ca content to be a result of microprobe analyses of overlapping clino- and orthopyroxenes. This applies to natural samples of PAR andesites, where single measurements of pyroxene are in the same range as experimental crystals. Freund et al. (2013) stated that the small (<0.2 mm) clinopyroxene minerals in the evolved lavas from the PAR are optically and chemically zoned. The same observation was made for pyroxene analyses in andesites from the eastern Galapagos rift (Perfit and Fornari 1983) and the southern Juan de Fuca Ridge (Perfit et al. 2008).

The Mg number ( $Mg\# = Mg/[Mg+Fe^{2+total}]*100$ , molar) of all experimentally-synthesized clinopyroxenes spans a wide range, from 39 to 75 (Fig. A.1.5). Most apparent is the influence of  $a_{H_2O}$  on Mg#. While Mg# in experiments with high  $a_{H_2O}$  is almost constant within a wide temperature range and decreases only in the run close to the solidus (i.e. 750°C), Mg# in experiments with lower  $a_{H_2O}$  decreases dramatically despite little temperature variation.

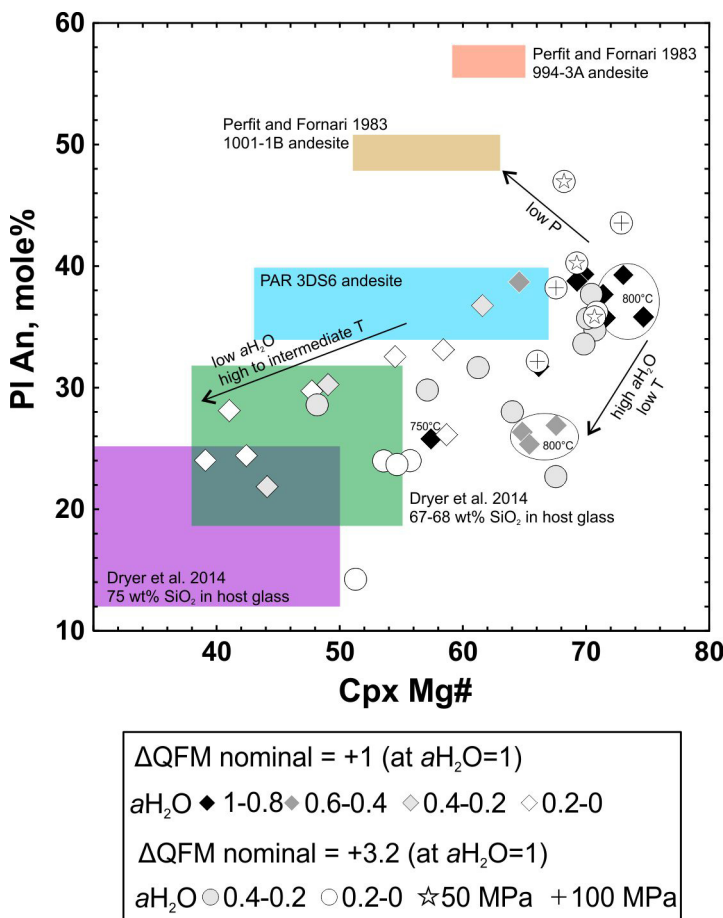


**Figure A.1.5:** An content in plagioclase versus Mg# in clinopyroxene as a function of  $a_{H_2O}$  and  $f_{O_2}$ . Shown as colored fields are the phenocryst ranges of relevant natural silica-rich rocks from the oceanic crust (sample PAR 3DS6 unpublished, the others from Perfit and Fornari 1983 and Dreyer et al. 2014). Experiments under oxidizing conditions at 950°C and reducing conditions at 800°C are from Erdmann and Koepke (2016).

## *Plagioclase*

Compositions of all plagioclases relative to the Mg# of clinopyroxenes are shown in Figure A.1.5 as a function of melt-water activity for experiments performed under both reducing and oxidizing redox conditions. As expected, the An content decreases with decreasing temperature and decreasing  $a_{\text{H}_2\text{O}}$ . Plagioclases from experiments with high  $a_{\text{H}_2\text{O}}$  (i.e.  $> 0.8$ ) are strongly enriched in An compared to those with lower  $a_{\text{H}_2\text{O}}$  (i.e.  $< 0.4$ ), which is in full agreement with previous studies (e.g., Botcharnikov et al. 2008; Feig et al. 2006; Koepke et al. 2004; Martel et al. 1998). The influence of pressure on plagioclase composition is illustrated in Figure A.1.5, but only for oxidizing conditions at 1030°C and low  $a_{\text{H}_2\text{O}}$  (i.e.  $< 0.2$ ), showing an apparent increase of An content with decreasing pressure. While the highest An content in a comparable experiment performed at 200 MPa is 38, the highest An content in plagioclases synthesized in experiments performed at 100 MPa is 43 and at 50 MPa is as high as 47. The An content is slightly influenced by varying  $f_{\text{O}_2}$ : Experiments performed under oxidizing conditions are systematically lower in An than comparable experiments (in terms of  $a_{\text{H}_2\text{O}}$ ) under reducing conditions.

## **A.1.5. Discussion**

### ***A.1.5.1. Attainment of equilibrium***

Our experiments performed in IHPVs extended from 72 to 220 h (depending on temperature; cf. Experimental protocol, Tab. A.1.2), which is much longer than needed to reach equilibrium conditions in a basaltic system (Berndt et al. 2005; Feig et al. 2010) and is in a time frame similar to that of experiments with rhyolitic starting material conducted in the same IHPVs (Almeev et al. 2012). Experiments performed in CSPVs lasted as long as 670 h. Almeev et al. (2012) and others (e.g., Pichavant et al. 2007) showed that near-equilibrium conditions can also be reached in a highly-evolved silicic system by using homogenized fine-grained ( $< 200\mu\text{m}$ ) glass as starting material and choosing an appropriate run duration with regard to the expected melt viscosity.

The following observations suggest that equilibrium was obtained: (1) Crystals and melt are distributed homogeneously along the capsule; (2) crystals are euhedral and chemically constant within one experimental run; (3) melt measurements are also constant within the analytical error; (4) the compositions of crystals and melt change systematically with the experimental conditions, following expected compositional trends; (5) static temperature cycling experiments were reproduced twice with the same total run duration and consistent melt and crystal chemistry; and (6) temperatures of magnetite-ilmenite pairs calculated using different geothermometers are close to the run temperature.

Additionally, since our experiments were performed twice under oxidizing and reducing conditions, the consistency and systematics of both series' results at the same temperature suggest that equilibrium was achieved in our experiments. Even though the duration time of experiments with an  $\text{H}_2$  control were generally longer due to slow diffusion of  $\text{H}_2$  into the Shaw

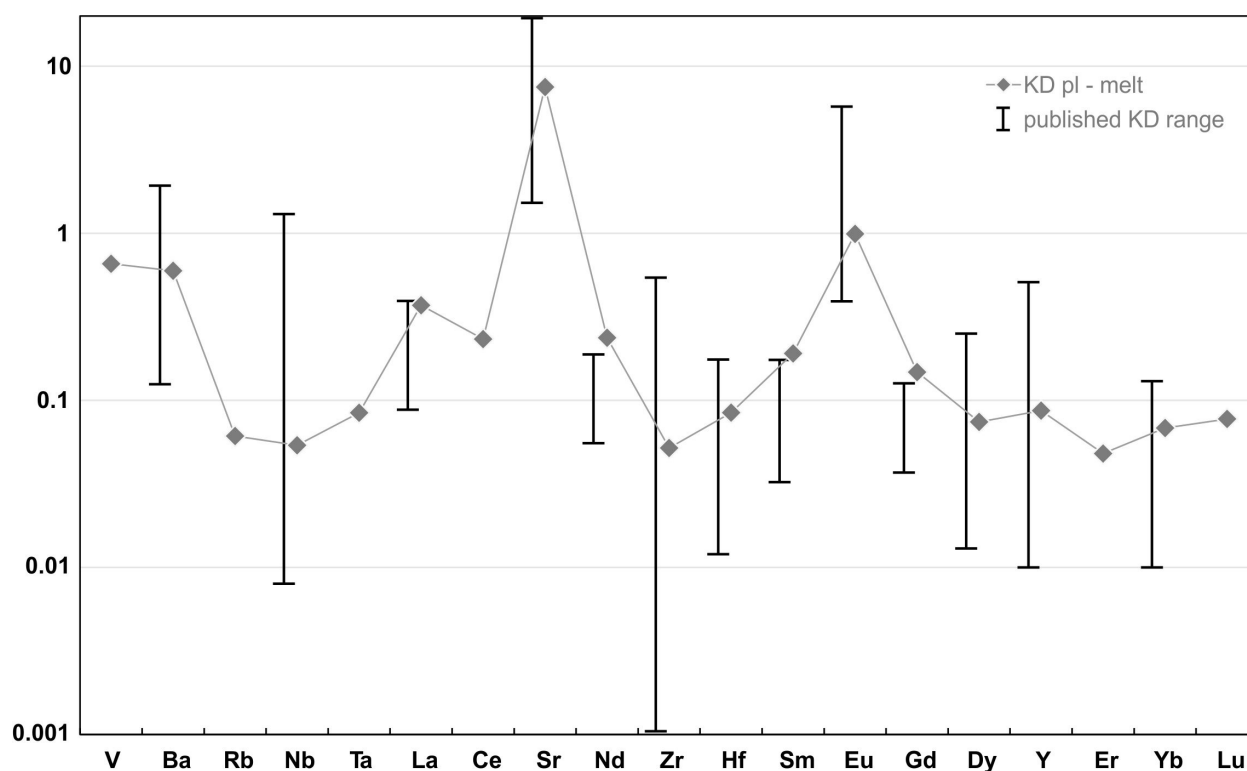
membrane, non-sensitive redox phases show identical stability curves (see below), suggesting that the chosen run times were sufficient for reaching equilibrium.

**Table A.1.4** Trace element melt composition of experiment #110 and partitioning (KD) to crystallized plagioclase

	V	Ba	Rb	Nb	Ta	La	Ce	Sr	Nd	Zr
<b>Melt [ppm]</b>	18.6	491	76.3	93.7	2.48	82.0	205	143	103	553
<b>SD</b>	2.09	0.27	2.12	0.98	0.19	0.08	0.09	0.55	0.84	7.03
<b>KD pl-melt</b>	0.658	0.597	0.061	0.054	0.084	0.371	0.233	7.510	0.237	0.052

	Hf	Sm	Eu	Gd	Dy	Y	Er	Yb	Lu
<b>Melt [ppm]</b>	80.2	24.7	5.30	42.6	35.7	112	77.2	58.6	8.57
<b>SD</b>	4.30	0.13	0.09	4.20	0.36	0.08	1.08	2.95	0.30
<b>KD pl-melt</b>	0.085	0.191	0.993	0.148	0.074	0.087	0.048	0.068	0.077



**Figure A.1.6:** Partition coefficients (KDs) for trace element partitioning between experimental melt and plagioclase of run #110 listed in Table A.1.4 compared to published values from Severs et al. 2009 and summarized references therein. The symbols represent the average partition coefficient determined in this study. The bold vertical line to the left of data from this study represents the complete range of partition coefficients reported in the literature.

#### **A.1.5.2. Partitioning of trace elements between melt and plagioclase**

The application of the temperature cycling technique in some of our experiments resulted in increased sizes of crystals and melt pools, thus enabling the possibility of in-situ trace element measurement of melt and crystals in highly-evolved experiments (see Erdmann and Koepke 2016 for details). The run #110 temperature (800°C equilibrium temperature) was periodically increased by 50 K, causing dissolution of tiny crystals in the melt and enormous growth of larger



crystals, especially plagioclase. Thus, we were able to measure 19 trace elements of melt and plagioclase via SIMS in order to provide partition coefficients useful for modeling fractional crystallization processes (Tab. A.1.4). The data on trace element partitioning between plagioclase ( $An = 39.3$ ) and coexisting melt ( $SiO_2 = 74.6$  wt%) of experiment #110 (see Tab. A.1.2 for experimental conditions) are plotted in Figure A.1.6 and compared to previously-published partition coefficients for plagioclase in andesitic to rhyodacitic melts (Severs et al. 2009 and summarized references therein). The partition coefficients determined experimentally in this study are comparable to published data with a slight tendency toward the upper limit of the range of literature values. As expected, most large ion lithophile elements (LILEs) and high field strength elements (HFSEs) behave incompatibly and are strongly enriched in the melt (Rb-Nb-Ta, Zr-Hf, Heavy Rare Earth Elements (HREEs)-Y). Significant KD-positive anomalies relative to neighbor elements are obtained for Sr and Eu.

### ***A.1.5.3. Comparison with other phase equilibria data in a dacitic/tonalitic system***

In Figure A.1.3 we include data from other experimental phase relation studies (Scaillet and Evans 1999; Costa et al. 2004; Holtz et al. 2005; Cadoux et al. 2014), using dacitic starting materials that are, in terms of major elements, similar to the PAR-dacite used in this study (Tab. A.1.1). Starting material of these studies were obtained from different volcanos (Santorini, Unzen, San Pedro, and Pinatubo) and, thus, from a different environment than the oceanic setting described in this study. Nevertheless, these studies are well eligible for comparison because applied pressures, melt water contents, redox conditions and temperatures are at least partly in the same range as those for experiments of this study. Moreover, phase assemblages as well as phase proportions of the experimental results are similar. For a better comparability we only used those experiments from literature performed at  $P=200$  MPa with dry glass as starting material (all experiments are fluid saturated).

When comparing the phase equilibria established on the Pinatubo dacite (Fig. 2 of Scaillet and Evans 1999) with the phase relations of this study (Fig. A.1.1), two major differences are obvious: (1) slightly larger ilmenite stability field in the phase diagram of Scaillet and Evans (1999), and (2) increase of orthopyroxene stability, also at high melt  $H_2O$  contents. Both can be attributed to slightly more reduced conditions in experiments of Scaillet and Evans (1999). Costa et al. (2004) also reported a larger orthopyroxene stability field for the San Pedro dacite, even at higher  $fO_2$ . Because experiments performed in the intermediate water content range (i.e. 2 – 4 wt%  $H_2O$  in the melt) at temperatures between 900 and 800°C are lacking, it is possible that the ilmenite stability field of the PAR dacite is larger in the experimental series performed at reduced conditions. However, due to one orthopyroxene-free experiment at 900°C and 2 wt%  $H_2O$ , the orthopyroxene stability curve was established at low melt  $H_2O$ . Other phase stability fields of both studies are in a similar range as those established for the PAR dacite.

Major element trends of most oxides presented by Scaillet and Evans (1999), Costa et al. (2004), Holtz et al. (2005), and Cadoux et al. (2014) are in general in the same range as experimental results of this study (Fig. A.1.3). Since most experiments from the cited literature were performed at  $aH_2O > 0.6$ , their melt compositions mainly follow the trend for high water activities (except for Costa et al. 2004, who conducted more experiments at low  $aH_2O \geq 0.4$ ).

Pronounced discrepancies are, as expected, visible when the corresponding oxide concentration is different in the starting compositions compared to the PAR-dacite of this study (e.g., MgO at Scaillet and Evans 1999, K<sub>2</sub>O in Costa et al. 2004, Holtz et al. 2005 and Cadoux et al. 2014 and FeO in all studies used for comparison). The higher K<sub>2</sub>O values reveal the different character of the volcanic starting materials in comparison to an oceanic environment, even though the K<sub>2</sub>O content in the PAR-dacite is already relatively high. However, most evolved samples are turning into a similar range at  $T \leq 800^\circ\text{C}$ . Even though only slightly higher in the starting compositions, literature data do not show the low Al<sub>2</sub>O<sub>3</sub> range at  $T \geq 900^\circ\text{C}$  as it is produced by low  $a_{\text{H}_2\text{O}}$  experiments of this study. While most experiments from the literature follow the trend for high  $a_{\text{H}_2\text{O}}$  or are slightly lower (Costa et al. 2004), results of Holtz et al. (2005) show a strong enrichment despite distinct plagioclase crystallization in the corresponding phase assemblages.

#### ***A.1.5.4. Application to natural felsic lavas from mid-ocean ridges***

When comparing an experimental phase equilibria study with a wide range of natural lithologies aiming to infer their pre-eruptive conditions, particular attention should be paid on the starting compositions. As demonstrated by Cadoux et al. (2014), small changes in whole rock compositions can affect phase relationships significantly and, hence, the inferred conditions of pre-eruptive temperature, pressure, water content and redox conditions. Cadoux et al. (2014) recommended “a case-by-case approach, whenever a precise estimate of pre-eruptive conditions is the chief objective of the experimental study”. However, our study do not primarily aims to reveal the exact pre-eruptive conditions of particular silicic magmas but rather to provide a general idea of the potential generation of felsic melts with special regard on prevailing water activities. Up to now, experimental phase relations studies in oceanic high-SiO<sub>2</sub> lavas have only existed for significantly higher pressures and more potassium-enriched systems. Thus, with the implication of the phase equilibria and compositions of this study, we can provide only a rough idea on formation conditions of high-silica lavas in a MOR-environment based on a starting composition typically for MOR-dacites (see Fig. A.1.7), even though exact P-T- $a_{\text{H}_2\text{O}}$  conditions should be handled with caution.

#### ***Phase equilibrium constrains on pre-eruptive conditions of PAR dacites***

As described by Freund et al. (2013), the mineral assemblage in the PAR silicic lavas consists of small (~0.2 mm) optical and chemical zoned plagioclase and clinopyroxene phenocrysts in a glassy matrix with accessory opaques (<10  $\mu\text{m}$ , mainly magnetite). This mineral assemblage is reproduced in the phase equilibria at oxidized conditions as well as at reduced conditions (as indicated by the yellow fields in Fig. A.1.1). While at oxidized conditions five experiments bear the corresponding mineral assemblage of clinopyroxene, plagioclase, and magnetite, the range of the potential pre-eruptive at reduced conditions can be only indirectly inferred. Nevertheless, water contents are in both cases in the intermediate range between 2.0 and 3.5 wt% H<sub>2</sub>O (corresponding to  $a_{\text{H}_2\text{O}}$  of 0.3 to 0.6). The indicated temperature range is slightly larger at oxidized conditions ( $T \sim 1000^\circ\text{C}$  to  $900^\circ\text{C}$ ) than at reduced conditions ( $T \sim 950^\circ\text{C}$  to  $900^\circ\text{C}$ ). At these inferred conditions, the predominant mineral phase is plagioclase with ~25 vol%, followed by lower amounts of clinopyroxene (~5 vol%) and magnetite (~4 vol%, Fig. A.1.2, Tab. A.1.2).

Melt proportion vary between 60 and 70 vol% which is in a comparable range to natural PAR dacites.

*Phase relations of felsic lavas from MORs and inferred pre-eruptive conditions*

Here, we compare our results on phase relations with other felsic lavas from actual mid-ocean ridges. For the natural evolved andesitic-to-rhyolitic system of the Alarcon Rise (northern extension of the East Pacific Rise (EPR) in the Gulf of California), a phase assemblage with dominantly plagioclase associated with titanomagnetite, ilmenite, clinopyroxene, and orthopyroxene is reported (Dreyer et al. 2014). This assemblage is only reproduced under reducing conditions in a small range of temperature and melt-water content indicated by the green field in Fig. A.1.1b. Dreyer et al. (2014) also observed fayalitic olivine, zircon, and rare accessories in their studied sample suite. While zircon is stable, at least in experiments performed under high  $a\text{H}_2\text{O}$  and low temperature, olivine is absent from all our experiments.

Cotsonika et al. (2005), Perfit et al. (2008) and Werts (2012) investigated dacites from the Juan de Fuca Ridge (JdFR) and reported clinopyroxene, pigeonite, magnetite, ilmenite, and plagioclase coexisting with a dacitic melt (see also Wanless et al. 2010). This phase occurrence also matches the green field in Figure A.1.1b, suggesting that the JdFR dacites formed under high temperatures ( $\sim 950^\circ\text{C}$ ) under reducing conditions at low  $a\text{H}_2\text{O}$ . The water content in basaltic andesites to dacites from the JdFR vary from 1.5 to 2.0 wt% (Werts 2012). However, the low amount of plagioclase in some JdFR dacites suggests a tendency to higher  $a\text{H}_2\text{O}$  resulting in plagioclase suppression. It is worth to mention that also JdFR dacitic lavas bear fayalite, apatite and zircon. Fayalite and hedenbergite are not in equilibrium with the host glass leading to the assumption that the dacite is a mixing product of ferrobasalt and rhyodacite (Perfit et al. 2008; Schmitt et al. 2011).

Perfit and Fornari (1983) describe Galápagos Spreading Center (GSC) andesites with rare phenocrysts and microphenocrysts of augite, ferroaugite, pigeonite, FeTi-oxides, and plagioclase. This phase assemblage also indicates formation under reducing conditions at low  $a\text{H}_2\text{O}$ , corresponding to the green field in Figure A.1.1b. Apatite crystals are also present in GSC andesites but are extremely rare. However, the observation of apatite by Perfit and Fornari (1983) and of zircon by Dreyer et al. (2014) accompanied by the low amount of plagioclase in some JdFR dacites reinforces the tendency to higher  $a\text{H}_2\text{O}$ . Alternatively, the crystallization of these accessories could also be a result of higher P concentration in Perfit and Fornari's (1983) system and higher Zr concentration in the system of Dreyer et al. (2014). In general, the presence of accessory minerals as apatite and zircon should be assigned a minor role, because their stabilities are potentially strongly dependent on the composition of the protolith. For silicic lavas from the PAR, Freund et al. (2013) reported only plagioclase, clinopyroxene, and accessory FeTi-oxides as mineral phases, supporting crystallization conditions under higher  $a\text{H}_2\text{O}$  due to the absence of low-Ca pyroxenes.

In summary, crystallized phenocrysts and microphenocrysts in high-silica lavas from different fast- to intermediate-spreading mid-ocean ridges are experimentally reproduced only in a small

range of temperature and melt-water content. The best conformity is given at a temperature of about 950°C and melt-water contents below 2 wt%. A relatively low  $a_{\text{H}_2\text{O}}$  is also indicated by the composition of the crystallized phases (see below). The observed accessory phases, apatite and zircon as well as the PAR phase assemblage where low-Ca pyroxene is absent (Freund et al. 2013), indicate a tendency to slightly higher  $a_{\text{H}_2\text{O}}$  even though accessory stability should not be overstated. It should be also noted that more reducing conditions would enlarge the stability fields of ilmenite and orthopyroxene to higher water contents (e.g., Dall’Agnol et al. 1999).

#### *Composition of the experimental phases in comparison to natural phenocrysts*

The comparison to natural FeTi-oxides of andesites from the eastern Galapagos rift (Perfit and Fornari 1983) reveals an agreement with our FeTi-oxides generated experimentally at low  $a_{\text{H}_2\text{O}}$  (i.e.  $a_{\text{H}_2\text{O}} < 0.4$ ; Fig. A.1.4a). Because all water-rich samples show  $X_{\text{MT}}$  values  $>0.75$  and a correlation of  $X_{\text{MT}}$  and  $X_{\text{ILM}}$  with  $a_{\text{H}_2\text{O}}$  exists, we can conclude that a high  $a_{\text{H}_2\text{O}}$  is an unlikely condition required for the formation of magnetite. The same conclusion can be drawn with regard to the ILM-HM solid solution, where natural ilmenites ( $X_{\text{ILM}} 0.86-0.90$ ) and those from water-poor experiments ( $X_{\text{ILM}} 0.93-0.99$ ) are in a similar high range, while the ILM fraction at higher  $a_{\text{H}_2\text{O}}$  is distinctly lower (Fig. A.1.4b).

To compare experimental plagioclases to phenocrysts observed in the glass of natural andesitic to rhyolitic lavas, we used the study of Perfit and Fornari (1983) as well as the study of Dreyer et al. (2014). Additionally, we show the single analysis ranges of an andesite similar to our starting material from the PAR (sample 3DS6; Fig. A.1.5). Generally, with increasing silica content of the natural sample host glasses (Perfit and Fornari 1983, with the lowest  $\text{SiO}_2$  content, Dryer et al. 2014, with the highest), An content in plagioclase and Mg# in clinopyroxene decreases consistently. This linear trend is also observable in this study’s experiments for crystals generated at low  $a_{\text{H}_2\text{O}}$  (i.e.  $<0.4$ ) and high to intermediate temperature (1030°C to 910°C). Experiments performed at lower temperature (i.e. 800°C) and higher melt-water content ( $a_{\text{H}_2\text{O}} >0.4$ ) show Cpx Mg# that changes only slightly at a relatively high level but Pl An contents that decrease significantly. Only one water-saturated experiment close to the solidus ( $T=750^\circ\text{C}$ ) plots near the natural range of Dreyer et al. (2014). In general, their phenocrysts from the Alarcon Rise mid-ocean ridge fit our experimental crystals. This was expected, because the Dryer et al. (2014) phenocrysts are from the most silica-rich host glasses. The high conformity with our experimental crystals generated at low  $a_{\text{H}_2\text{O}_{\text{melt}}}$  confirms the assumption that silica-rich lavas are generated at lower  $a_{\text{H}_2\text{O}}$  rather than under extensive hydrothermal influence.

A completely different trend can be observed for the limited number of experiments performed at lower lithostatic pressure (experiments at 50 and 100 MPa were only performed at 1030°C). At lower pressure the amount of water which can be incorporated into the melt is limited, and water-saturated conditions, under which plagioclase crystallization is suppressed, are rapidly reached. Thus, plagioclase only crystallizes at very low total water contents. Pressures of 100 and 50 MPa, and even lower are generally expected for the degassing history of erupted silica-rich lavas. The composition of phenocrysts in natural systems is potentially influenced by the

ascent prior to eruption and does not necessarily mirror the conditions of generation deeper in the crust.

### *Melt compositions*

In Figure A.1.7 we compare experimental results of this study in Harker plots for eight elements (given as their oxides) versus  $\text{SiO}_2$  with several natural systems of evolved lavas sampled in the oceanic crust (Byerly et al. 1976; Perfit et al. 1983, 1999; Wanless et al. 2011; Freund et al. 2013; Erdmann et al. 2015). The general trend of FeO and, to a lesser extent,  $\text{TiO}_2$  of all natural evolved lavas is congruent with those experiments performed at lower  $a\text{H}_2\text{O}$  (Fig. A.1.7).

This observation does not hold for the  $\text{K}_2\text{O}$  trend; the compositions of natural silica-rich lavas are reproduced only by experiments performed under high  $a\text{H}_2\text{O}$ , while water-undersaturated runs exhibit higher  $\text{K}_2\text{O}$  contents. However, the  $\text{K}_2\text{O}$  content of the starting composition is relatively high at 1.2 wt%, probably caused by the influence of the Foundation hotspot chain (Haase et al. 2005; Freund et al. 2013). Thus, a strong  $\text{K}_2\text{O}$  enrichment in our experiments with low water contents is expected and does not exclude the possibility of silica-rich rock generation at low  $a\text{H}_2\text{O}$ , provided that the basaltic protolith is not enriched in  $\text{K}_2\text{O}$  due to external influence.

A clear indication of low  $a\text{H}_2\text{O}$  during the generation of evolved lavas under mid-ocean ridges is given by the  $\text{Al}_2\text{O}_3$  content of the melts. Natural evolved systems from Byerly et al. (1976), Perfit et al. (1983, 1999), Wanless et al. (2011), Freund et al. (2013), and Erdmann et al. (2015) all follow the trend of low  $a\text{H}_2\text{O}$  ( $\leq 0.4$ ; Fig. A.1.7). This indicates a relatively high amount of plagioclase in the natural rocks preventing an enrichment in  $\text{Al}_2\text{O}_3$  as it is the case in the low  $a\text{H}_2\text{O}$  experiments of this study (see Fig. A.1.2b). The markedly different trend at high  $a\text{H}_2\text{O}$  ( $> 0.4$ ) shows that an increased  $\text{Al}_2\text{O}_3$  with progressive crystallization (until a melt  $\text{SiO}_2$  content of  $\sim 70$  wt% is reached) is not reproduced by any natural system. Erdmann et al. (2015) showed a similar observation for the natural system of the EPR, where drilled tonalites (the same as those shown in Fig. A.1.7) could be experimentally reproduced only via anatexis of a hydrothermally-altered basalt at low  $a\text{H}_2\text{O}$ . Irrespective of the dominant process responsible for felsic melt generation (i.e. anatexis or fractional crystallization) it is confirmed once again that excess water is unlikely.

The differences in MgO and  $\text{K}_2\text{O}$  of the tonalites drilled from the dike/gabbro EPR transition (Erdmann et al. 2015) are eye-catching. Those samples were, in contrast to the other natural samples shown in Figure A.1.7, crystallized in-situ within the crust and not after being erupted to the ocean floor. Thus, the influence of hydrothermal alteration is minor and the  $\text{K}_2\text{O}$  content, which can be enriched due to alteration by seawater circulation, remains low. However, Wanless et al. (2011) concluded that the high  $\text{K}_2\text{O}$  values of their natural samples from the mid-ocean ridge of the EPR are a result of partial melting and assimilation of altered oceanic crust. Here we show that  $\text{K}_2\text{O}$  values in the same range, and even higher, can be produced by extensive crystallization of an andesitic-to-dacitic rock (given that the protolith has a relatively high  $\text{K}_2\text{O}$  content; here 1.18 wt%).

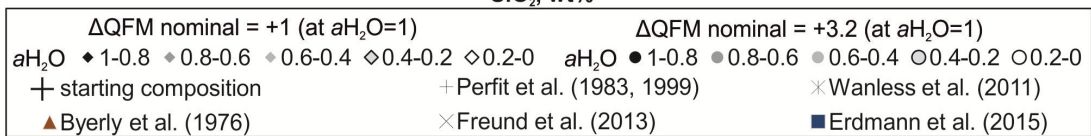
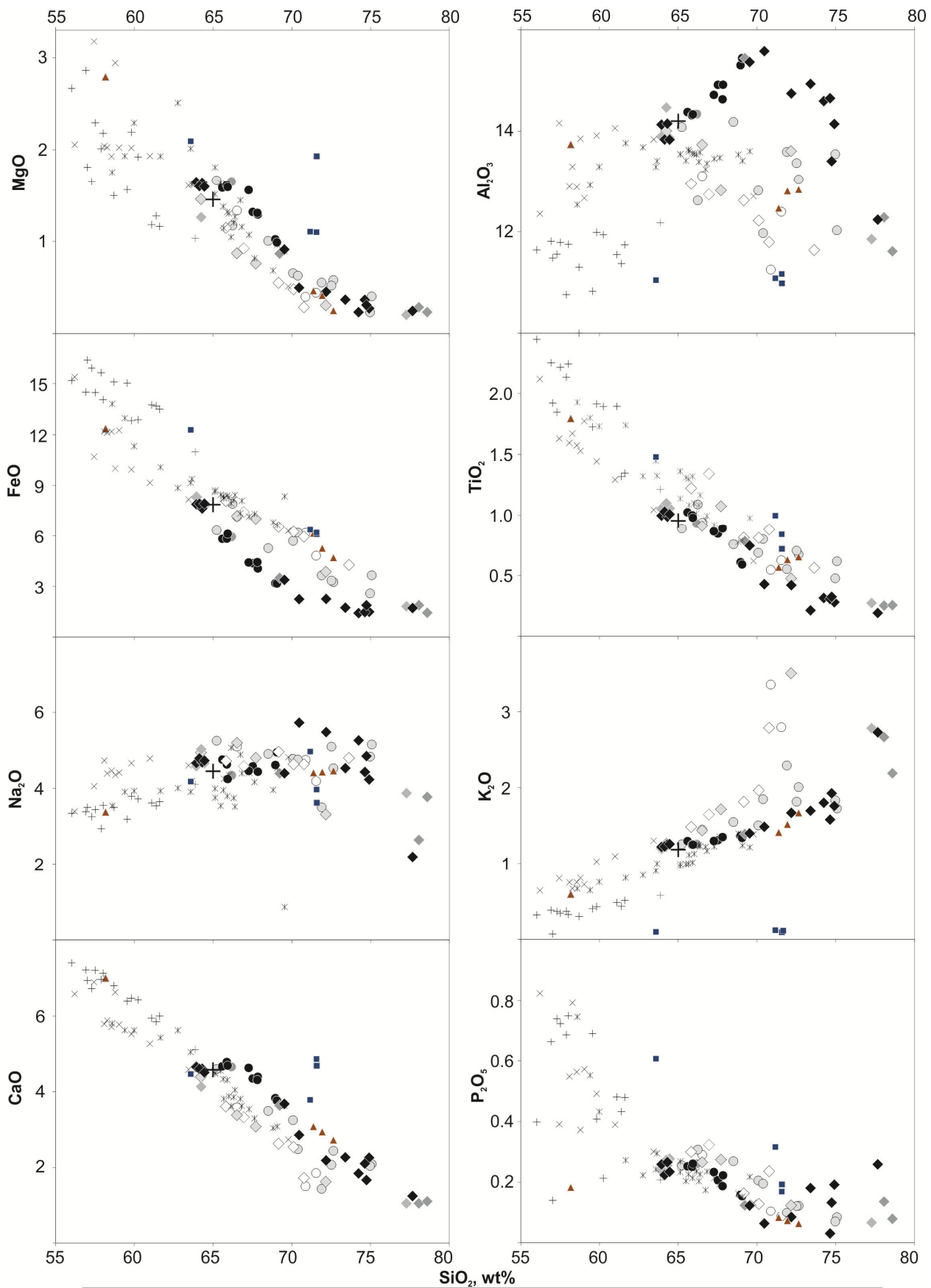


**Figure A.1.7:** (see previous page) Compositional evolution of experimental melts as a function of temperature,  $fO_2$ , and  $aH_2O$ . All compositions are in wt% and normalized to 100%. For comparison, we include data from natural silica-rich rocks from the oceanic crust published by Byerly et al. (1976), Perfit et al. (1983, 1999), Wanless et al. (2011), Freund et al. (2013), and Erdmann et al. (2015). Experiments under oxidizing conditions at 950°C and reducing conditions at 800°C are from Erdmann and Koepke (2016).

Despite the evolved character of the tonalites presented by Erdmann et al. (2015), the MgO content is relatively high and matches the water-saturated experiments of this study.

#### *Chlorine enrichment due to seawater influence*

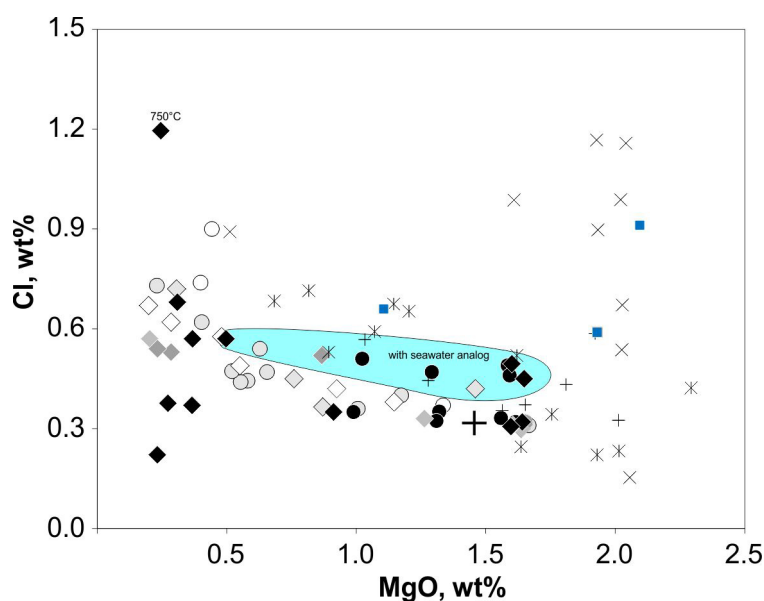


**Figure A.1.8:** Cl content (in wt%) as a function of MgO (in wt%),  $aH_2O$ , and  $fO_2$ . Data points of experiments within the blue fields represent those runs in which a seawater analog was added to the fluid phase (see text for details). For comparison, we include data from natural silica-rich lavas from fast- and intermediate-spreading mid-ocean ridges published by Perfit et al. (1983, 1999), Wanless et al. (2011), Freund et al. (2013), and Erdmann et al. (2015). Experiments under oxidizing conditions at 950°C and reducing conditions at 800°C are from Erdmann and Koepke (2016). For legend see Figure A.1.7.

The chlorine content in the natural dredged 3DS1 sample from the PAR used as starting material for this study is 1.0 wt% and after the required re-melting for homogenization of the starting glass for the experiments is still 0.3 wt%. This is distinctly higher than expected for dacitic lava from fast- to intermediate-spreading ridges containing 1.5 wt% MgO. Modeling the liquid line of descent in typical MORB with an average Cl content of 350 ppm using the MELTS program (Ghiorso and Sack 1995) leads to less than 0.1 wt% Cl in fractionated melts of dacitic composition (Wanless et al. 2010). Thus, following the arguments posed by Wanless et al. (2010), silica-rich lavas with Cl contents higher than ~0.1 wt%, as in our 3DS1 starting material, are not believed to be generated solely by extensive fractional crystallization, but are influenced by the assimilation of hydrothermally-altered wall rocks rocks, i.e. amphibole-bearing metabasalts or metagabbro in the lower- and mid-crust (Freund et al. 2013). Thus, here we experimentally continue the evolutionary process of fractional crystallization, and simultaneously study the chemical influence of an assimilant that existed early in the evolution history on extensively-evolved rocks with dacitic to rhyolitic composition. While elucidating the formation history of the starting material is beyond the aim of this study, we shed light on the Cl evolution in the experimental melts in our 3DS1 dacitic system with 0.32 wt% Cl (Fig. A.1.8). For MgO contents higher 1.0 wt%, Cl contents of natural silica-rich lavas (Perfit et al. 1983, 1999; Wanless et al. 2011; Freund et al. 2013; Erdmann et al. 2015) are reproduced only in those experiments in which a seawater analog was added as fluid phase instead of pure water (fluid composed of distilled water with 3.2 wt% NaCl; see A.1.3.2 for details) in order to simulate the

influence of seawater-derived hydrothermal activity. This again suggests that all known natural dacitic lavas are not formed by simple fractionation of an evolved MORB alone, but are influenced by intense Cl contamination, probably due to assimilation of hydrothermally-altered material (e.g., Haase et al. 2005; Wanless et al. 2011; Freund et al. 2013). Following Kendrick et al. (2013), who studied amongst others basaltic glasses from the GSC, Cl contamination is not just caused by seawater contamination but rather by brine assimilation.

As melt evolution proceeds with decreasing MgO contents, the influence of added NaCl in the fluid phase on Cl enrichment in the melt becomes marginal, and the elevated Cl contents ( $\leq 0.9$  wt%) of the most evolved natural sample from the PAR (Freund et al. 2013) could be reproduced in experiments with low  $a_{\text{H}_2\text{O}}$  and without extra NaCl addition (Fig. A.1.8). The melt with the highest Cl content (1.2 wt%, #97) formed in an experiment with water saturation close to the solidus without NaCl addition. This shows that during fractional crystallization hydrothermal influence is not necessarily required for enhanced Cl enrichment in a system in which Cl was already enriched in the protolith. The  $a_{\text{H}_2\text{O}}$  during the formation of silica-rich lava could be low, as demonstrated in our experiments, or it could initially be high (as in run #97), but  $\text{H}_2\text{O}$  degassed at eruption. In general, the eruptive potential is elevated due to pre-eruptive enrichments of volatiles in magmas and, thus, it controls whether the silica-rich lava erupts on the sea floor or crystallizes in-situ in the deeper part of the oceanic crust. As demonstrated here, due to low  $a_{\text{H}_2\text{O}}$ ,  $\text{CO}_2$  can be the dominant fluid phase. In erupted silica-rich rocks,  $\text{CO}_2$  is mainly degassed and only moderate amounts of water are detected (1.5 – 2.0 wt%), but, as concluded by Wanless et al. (2011),  $\text{CO}_2$  triggered the eruption. Hence, we propose a scenario where the water content in the fluid phase is low for evolutionary processes in the high-silica range. Hydrothermal alteration or assimilation of brine, if it occurs at all, influences primarily the basaltic protolith but plays a minor role in subsequent evolutionary processes. Thus, Cl over-enrichment is possible because Cl degassing is, in contrast to  $\text{H}_2\text{O}$  degassing, insignificant (Wanless et al. 2011). The potential decoupling between these two volatiles during crustal contamination can lead to the following hypothesis: Hydrothermally altered oceanic rocks that get assimilated during magmatic evolution are Cl-rich but  $\text{H}_2\text{O}$ -poor.

The mineral assemblage of the water-rich experiment #97 also contains amphibole which has the ability to incorporate Cl. However, the Cl content of the amphibole is only 0.18 wt% (see electronic supplementary data A.1.ESM), so the crystallization of amphibole in this experiment does not have the potential to significantly reduce the Cl content in the coexisting melt. In general, the Cl content of all analyzed amphiboles (four experiments, see electronic supplementary data A.1.ESM) is relatively low, varying only between 0.13 and 0.19 wt%; however, the coexisting melts are strongly enriched in Cl (0.6 - 1.2 wt%), implying that the potential for producing amphiboles strongly enriched in Cl, as is sometimes observed in oceanic plagiogranites (e.g., Vanko 1986; Silantyev et al. 2014), is low, and other processes are more important, like the interaction between amphibole and a high-saline fluid in the sub-solidus regime.



### **A.1.6. Conclusion**

We simulated crystallization processes in a dacitic system from fast- to intermediate-spreading rate mid-ocean ridges. Results on phase relations and phase compositions can be used to evaluate generation processes of highly-evolved rocks of the oceanic crust, either erupted to the ocean floor or crystallized in-situ in the mid and lower oceanic crust. With regard to the following results we conclude that influence by either assimilation or contamination by hydrothermally altered crust or brines is not necessarily required for felsic melt generation and relatively low  $a_{\text{H}_2\text{O}}$  can be sufficient:

- Mineral assemblages in high-silica lavas from fast- and intermediate-spreading ridges could be experimentally reproduced in a narrow range of temperature ( $\sim 950^\circ\text{C}$ ) and  $a_{\text{H}_2\text{O}}$  ( $< 0.3$ ) at redox conditions slightly below the QFM buffer. Even though accessory phases and the absence of low-Ca pyroxenes in some natural rocks indicate a tendency to slightly higher  $a_{\text{H}_2\text{O}}$ , as proposed here water-saturated conditions are unlikely to generate the observed natural phase assemblages.
- The glass and bulk composition of felsic rocks is best reproduced in the melt of those experiments performed under low  $a_{\text{H}_2\text{O}}$  ( $< 0.4$ ). The strong enrichment in  $\text{Al}_2\text{O}_3$  in high  $a_{\text{H}_2\text{O}}$  experiments, especially, contradicts natural observations.
- The strong decrease in FeO due to high water concentration as described in previous experimental studies (e.g., Feig et al. 2006; Botcharnikov et al. 2008) can be observed in the experimental melts as well. However, because natural rocks show a minor decrease in FeO, which is only reproduced in experiments at low  $a_{\text{H}_2\text{O}}$ , the presence of excess water is unlikely.
- Relatively high Cl contents, as observed in natural systems ( $\text{Cl} \leq 0.9$  wt%), can be reproduced in evolved melts of the crystallization experiments performed under low  $a_{\text{H}_2\text{O}}$ , given early-stage Cl enrichment in the protolith, probably due to contamination of hydrothermally altered crust or brines.
- FeTi-oxides, clinopyroxene, and plagioclase phenocrystic compositions of natural evolved systems are only reproduced in experiments with low  $a_{\text{H}_2\text{O}}$ . The presence of FeTi-oxides additionally confirms the assumption that redox conditions around QFM or slightly below are most likely for the formation of silica-rich rocks because natural trends are better reproduced by experiments performed under low initial  $f\text{O}_2$ .

### **Acknowledgements**

We thank Otto Dietrich and Julian Feige for their careful sample preparation. We also thank the Editor J. Hoefs and the reviewers M. Perfit and B. Scaillet for their constructive comments that considerably improved the quality of this work. We gratefully acknowledge the chief scientists of RV Sonne, especially K.M. Haase, for access to the sample 3DS1 used in this study. Funding for this research was provided by grants from the Deutsche Forschungsgemeinschaft (KO 1723/13). This is CRPG contribution number 2461.



## Chapter B

### B.1. Experimental temperature cycling as a powerful tool to enlarge melt pools and crystals at magma storage conditions

*Martin Erdmann<sup>1,2</sup> and Jürgen Koepke<sup>1</sup>*

<sup>1</sup>*Institut für Mineralogie, Leibniz Universität Hannover, Callinstr. 3, 30167 Hannover, Germany*

<sup>2</sup>*CRPG, UMR 7358, CNRS, Université de Lorraine, 15 rue Notre Dame des Pauvres, 54501 Vandoeuvre-lès-Nancy, France*

*American Mineralogist, Volume 101, pages 960-969, 2016*

*DOI: 10.2138/am-2016-5398*

#### B.1.1. Abstract

Experiments in high silica systems at temperatures close to the solidus often produce crystals and melt pools that are too small for in situ analysis. Oscillating the temperature during an experimental run speeds up recrystallization of magma by dissolving small and increasing the size of larger crystals, dramatically changing the crystal size distribution. This principle of periodic heating and cooling, caused for example by repeated injection of hot magma, is also a potential acceleration for the formation of phenocrystic textures in natural rocks.

Here we show that temperature cycling has the potential to significantly enlarge melt pools and crystals in a fluid saturated dacitic system. Using a natural dacite dredged from the Pacific-Antarctic Rise as starting material, we performed crystallization experiments applying temperature cycling systematically for two different temperatures and different water activities at 200 MPa. For experiments at 950°C (with  $a_{\text{H}_2\text{O}} \sim 1$ ,  $\sim 0.3$ , and  $< 0.1$ ) an internally heated pressure vessel was used, experiments at 800°C (with  $a_{\text{H}_2\text{O}} \sim 1$ ,  $\sim 0.5$ ) were performed in a cold seal pressure vessel. Comparative experiments at equilibrium conditions with constant temperature were performed for both approaches. For all other experiments temperature was cycled with amplitudes of 20K for different time intervals but constant total run duration after initial equilibration at constant temperature. Additionally, for one experiment at 800°C, the temperature was increased several times by 50 K to study the potential of dissolving tiny crystals in the matrix.

As a result of the temperature cycling, tiny crystals in the matrix were preferentially dissolved, leading to large melt pools with only rare mineral inclusions enabling microprobe analysis using a defocused beam. With regard to the area of the 10 largest crystals of each cycling experiment, clinopyroxene crystals were up to 19 times larger, and plagioclase crystals even up to 69 times when comparing to experiments performed at constant temperature. Grain sizes of FeTi-oxide phases are less influenced by this technique. Essential requirements for applying temperature cycling routinely are identical phase relations and compositions in runs with constant and cycled temperature. For all studied temperatures and water activities, the phase assemblage was the same and compositions of all phases are identical within the analytical error. Thus, the

temperature cycling technique opens interesting perspectives, especially in facilitating in situ analysis in near solidus systems.

**Keywords:** *Experimental petrology, Temperature cycling, Crystallization experiments, Dacite, Crystal growth, Phenocrysts*

### **B.1.2. Introduction**

*In-situ* analyses of experiments by thermal emission techniques in high-silica systems, especially at conditions close to the solidus, are challenging due to the generally very small size of crystals and melt pools. It is difficult to measure and identify phases with sizes around 1  $\mu\text{m}$  by electron microprobe, and analyses of melt pools  $< 5 \mu\text{m}$  by electron microprobe are challenging, due to the requirement of a defocused beam in order to avoid Na-loss (e.g., Morgan and London 2005). Moreover, trace element analyses of experimental phases  $< 20\mu\text{m}$ , for example with secondary ion mass spectroscopy (SIMS) or laser ablation ICP-MS, are virtually impossible for these samples. While the positive effect of oscillating temperature on nucleation and growth rates has been well known for decades from material (e.g., Randolph et al. 1971) and food sciences (e.g., Donhowe and Hartel 1996), Mills et al. (2011) showed that for magma analogues it is possible to generate larger phases in experimental run products under atmospheric conditions and at low temperature ( $47\pm 3^\circ\text{C}$ ) via a process of dissolution/recrystallization. In addition, Mills and Glazner (2013) presented a detailed experimental study on the effects of temperature cycling on coarsening of crystals (plagioclase and olivine) in an alkali basalt at ambient pressure.

Previous experimental and petrological studies concentrated less on temperature cycling but rather on effects of decompression and/or cooling rates on crystal size distribution (CSD) in order to understand the formation of phenocrystic textures (e.g., Kirkpatrick 1977; Pupier et al. 2008; Brugger and Hammer 2010). As all of them mainly investigated crystal growth rates and crystal orientation, potential effects on phase chemistry caused by varying temperature remain unconsidered. Moreover, up to now, temperature cycling was rarely studied under pressurized fluid saturated magma storage conditions (Mills and Glazner 2011a).

Here we show that temperature cycling also substantially increases the grain size of the phases (mainly plagioclase, clinopyroxene and melt pools) in a fluid-saturated dacitic system under pressure with varying water activities at magma storage conditions. Particular attention was paid to potential variations of phase chemistry in experiments with temperature cycling compared to static ones. Some experiments were performed in a cold-seal pressure vessel (CSPV) in which run durations of up to 4 weeks are generally required to generate measureable crystals. This long time duration often causes nickel (the main constituent of the vessel) contamination of the sample due to in-diffusion of Ni through the Au-capsule (Schier and Schmidbaur 1996). Additionally, if the temperature is relatively high (i.e.,  $> 700^\circ\text{C}$ ), long run durations causes the vessel to deform. Thus, a further aim of this study was to test the option of reducing the total run duration by applying the temperature cycling technique in this device.

### **B.1.3. The apparatus**

The experiments at  $950\pm 20^\circ\text{C}$  were performed in a vertically mounted internally heated pressure vessel (IHPV) using pure argon as pressure medium in the high pressure lab of Hannover,

equipped with a rapid quench system to prevent the formation of metastable quench phases (Berndt et al. 2002). The temperature during the experiments was programmed and monitored with a Eurotherm 906 EPC controller. Near-solidus experiments (i.e.,  $T = 800 \pm 20^\circ\text{C}$  and  $+50^\circ\text{C}$ , respectively) were performed in a CSPV with  $\text{H}_2\text{O}$  as pressure medium and external cooling via compressed air. Temperature cycling in the CSPV was programmed by a RKC instrument program controller REX-P24.

**Table B.1.1** Experimental protocol

Run no.	cycling type	P (MPa)	Temp. ( $^\circ\text{C}$ )	Time (h)	TC (h)	$\text{H}_2\text{O}^a$ by-diff	$a\text{H}_2\text{O}^b$ exp	$\Delta\text{QFM}^c$ exp	Phase assemblages (proportions <sup>d</sup> )
42	static	200	950	120	-	5.1	0.98	+3.2	Melt(95.1), Mag(1.9), Cpx(1.2), Ap(1.8)
62	TC	200	950 $\pm$ 20	120	40	4.9	1.00	+3.2	Melt(96.6), Mag(2.2), Cpx(0.5), Ap(0.7)
57	TC	200	950 $\pm$ 20	120	72	5.1	1.00	+3.2	Melt(95.2), Mag(2.4), Cpx(0.9), Ap(1.5)
43	static	200	950	120	-	2.6	0.39	+2.2	Melt(63.3), Mag(5.1), Cpx(6.0), Pl(25.6)
63	TC	200	950 $\pm$ 20	120	40	1.8	0.22	+1.9	Melt(66.6), Mag(3.1), Cpx(3.9), Pl(26.5)
58	TC	200	950 $\pm$ 20	120	72	2.0	0.26	+2.0	Melt(67.7), Mag(3.8), Cpx(4.4), Pl(24.1)
45	static	200	950	120	-	0.5	0.02	-0.3	Melt(24.9), Mag(6.1), Cpx(20.9), Pl(44.1), Qz(4.0)
65	TC	200	950 $\pm$ 20	120	40	0.5	0.02	-0.1	Melt(24.3), Mag(5.7), Cpx(12.9), Pl(53.0), Qz(4.2)
66	TC	200	950 $\pm$ 20	120	72	0.8	0.06	+0.7	Melt(32.0), Mag(3.7), Cpx(15.2), Pl(47.5), Qz(1.6), Opx
81	static	200	800	650	-	5.5	1.00	+0.6	Melt(72.5), Mag/Ilm(4.9), Cpx(8.2), Pl(14.4), Ap, Zrn
105	static	200	800	336	-	4.8	0.86	+0.4	Melt(75.9), Mag/Ilm(3.8), Cpx(6.6), Pl(13.7), Ap, Zrn, Amp
101	TC	200	800 $\pm$ 20	336	192	5.5	1.00	+0.5	Melt(68.4), Mag/Ilm(5.7), Cpx(6.7), Pl(19.1), Ap, Zrn, Amp
110	peak	200	800+50	336	192	5.4	1.00	+0.5	Melt(63.9), Mag/Ilm(3.0), Cpx(13.6), Pl(19.6), Ap, Zrn, Amp
107	static	200	800	336	-	3.5	0.62	+0.1	Melt(46.7), Mag/Ilm(5.7), Cpx(10.8), Pl(30.9), Qz(6.0), Ap
103	TC	200	800 $\pm$ 20	336	192	2.8	0.43	-0.2	Melt(39.8), Mag/Ilm(6.1), Cpx(8.2), Pl(33.1), Qz(12.9), Ap, Zrn
111	peak	200	800+50	336	192	3.1	0.50	-0.1	Melt(49.5), Mag/Ilm(6.6), Cpx(9.0), Pl(28.0), Qz(7.0), Ap

*Mag* magnetite, *Ilm* ilmenite, *Cpx* clinopyroxene, *Opx* orthopyroxene, *Pl* plagioclase, *Qz* quartz, *Ap* apatite, *Amp* amphibole, *Zrn* zircon

<sup>a</sup> determination via by-difference (following Devine et al. 1995) with electron microprobe (KFT-calibrated)

<sup>b</sup> water activity is calculated from the measured composition of the fluid phase

<sup>c</sup>  $\Delta\text{QFM}$  indicates  $\log f\text{O}_2$  (experiment) -  $\log f\text{O}_2$  (QFM buffer) as estimated by Schwab and Küstner (1981)

<sup>d</sup> phase proportions in vol% (<0.5 vol % if not specified); determined via *ImageJ* (see text for details)

The water activity ( $a\text{H}_2\text{O}$ ) of the experimental run products was calculated following the thermodynamic model of Burnham (1979, 1994). It should be noted that the model of Burnham (1979) slightly overestimates water activity (e.g., Botcharnikov et al. 2005). The experiments were performed with known hydrogen fugacity ( $f\text{H}_2$ ) corresponding to the intrinsic conditions of the vessels but variable water fugacity ( $f\text{H}_2\text{O}$ ). Therefore, the oxygen fugacity ( $f\text{O}_2$ ) is not strictly constant from one capsule to the other. Decreasing  $f\text{H}_2\text{O}$  (accompanied with decreasing initial  $\text{H}_2\text{O}$  in the capsule) causes a lowering of  $f\text{O}_2$  (Scaillet et al. 1995). Knowing  $f\text{H}_2\text{O}$  (calculated after Pitzer and Sterner (1994) from thermodynamically conditions at certain temperature) and  $f\text{H}_2$ ,  $f\text{O}_2$  can be computed. Here  $f\text{H}_2$  is calculated by the set  $\Delta\text{QFM}$  value for water-saturated

conditions of the vessel (QFM = the quartz-fayalite-magnetite buffer; intrinsic conditions of the IHPV (measured with Ni-Pd solid sensors; Taylor et al. 1992): 3.2 log units above  $fO_2$  of QFM, hereafter labeled  $\Delta QFM+3.2$ ; intrinsic condition of the CSPV:  $\Delta QFM+1$  corresponding to the Ni-NiO buffer). With given pressure, temperature, and intrinsic  $pH_2$  conditions,  $\Delta QFM$  for water saturated conditions was calculated following models of Pitzer and Sterner (1994), Shaw and Wones (1964), and Schwab and Küstner (1981). Considering the variation of  $aH_2O$  in our runs, the estimated values of  $fO_2$  of our experiments vary between  $\Delta QFM-0.4$  and  $\Delta QFM+3.2$  (Tab. B.1.1). With regard to natural systems, this is generally more oxidizing than in typical MORB magmas (Bézos and Humler 2005). However, since we expect a higher  $aH_2O$  prevailing during the corresponding late-stage magmatic processes, and since water has an oxidizing effect (e.g., Botcharnikov et al. 2005), we expect generally a higher  $fO_2$  for the formation of silicic melts compared to primary MORB processes.

The chosen pressure for the experiments was 200 MPa, which is a typical value for magma storage conditions at the base of fast-spreading oceanic crust. Moreover, at this pressure several phase equilibria studies have been performed for more primitive tholeiitic systems, which make our results directly comparable to experimental data of those studies (e.g., Berndt et al. 2005; Botcharnikov et al. 2008; Feig et al. 2006, 2010).

#### **B.1.4. The starting material**

As starting material for the temperature cycling study, we used a remelted natural glass from the Pacific-Antarctic Rise (PAR) with dacitic composition (Tab. B.1.2; sample 3DS1 from Haase et al. 2005). The study presented here was performed in the framework of a phase relation study which aims to experimentally simulate the generation of felsic melts in oceanic crust. The natural sample is analytically well characterized (major and trace elements, selected isotopes) and can be regarded as an evolved end-member in the magmatic evolution of the PAR from MORB to felsic melts. The mineral assemblage in this sample consist of small (~0.2 mm) plagioclase and clinopyroxene phenocrysts in a glassy matrix with accessory oxides (< 10  $\mu m$ ). Detailed petrographical and geochemical information for sample 3DS1 and other characteristic evolved lavas are presented by Freund et al. (2013). Phase equilibria in this system were estimated in a companion study (preliminary results in Erdmann et al. 2012).

For the preparation of the starting glass we followed Feig et al. (2006). The sample was crushed and ground in a rotary mortar. The powder was fused twice at 1600°C in a platinum crucible at 1 atm (so at highly oxidizing conditions, where Fe diffusion into the capsule material is negligible) and quenched by placing the crucible in water. Between the two fusing steps, the glass was ground again. The homogeneity of the glass was checked by electron microprobe on pieces from the top, middle, and bottom of the crucible. Fe and Na loss of the fused glass compared to the whole rock analysis of the natural starting material (water free sample PAR-SO157-3DS1 of Freund et al. 2013 normalized to 100 wt%) is minimal (FeO 7.87 wt%/8.15 wt%, 4.45 wt%/4.59 wt%). The starting material for the experimental runs was produced by grinding the glass in two different fractions (<125  $\mu m$  and 125-200  $\mu m$ ). These two fractions were mixed together in a ratio ~1:1 to reduce the free volume between grains.

**Table B.1.2** Experimental results

Run	Phase	<i>n</i> <sup>a</sup>	SiO <sub>2</sub>	TiO <sub>2</sub>	Al <sub>2</sub> O <sub>3</sub>	Fe <sub>2</sub> O <sub>3</sub>	FeO	MnO	MgO	CaO	Na <sub>2</sub> O	K <sub>2</sub> O	P <sub>2</sub> O <sub>5</sub>	Cl	ZrO <sub>2</sub>	Total
Starting composition		60	65.00 <i>0.51</i>	0.95 <i>0.05</i>	14.20 <i>0.21</i>		7.87 <i>0.36</i>	b.d.	1.46 <i>0.14</i>	4.58 <i>0.20</i>	4.45 <i>0.26</i>	1.18 <i>0.05</i>	b.d.	0.32 <i>0.02</i>	b.d.	100.00
42	Mag	3	0.08 <i>0.07</i>	3.20 <i>0.04</i>	1.77 <i>0.07</i>	60.72 <i>0.45</i>	28.48 <i>0.15</i>	0.52 <i>0.06</i>	3.04 <i>0.04</i>	0.10 <i>0.01</i>	b.d.	b.d.				98.01
62		7	0.13 <i>0.04</i>	3.08 <i>0.05</i>	1.64 <i>0.06</i>	61.96 <i>0.44</i>	27.97 <i>0.30</i>	0.50 <i>0.09</i>	3.51 <i>0.08</i>	0.10 <i>0.05</i>	b.d.	0.01 <i>0.02</i>				98.95
57		2	0.06 <i>0.08</i>	4.28 <i>0.02</i>	1.77 <i>0.01</i>	58.22 <i>0.64</i>	29.84 <i>0.01</i>	0.44 <i>0.00</i>	2.76 <i>0.09</i>	0.07 <i>0.10</i>	b.d.	b.d.				97.44
42	Cpx	5	51.84 <i>1.09</i>	0.64 <i>0.11</i>	2.89 <i>0.65</i>		7.74 <i>0.65</i>	0.33 <i>0.05</i>	14.01 <i>0.64</i>	21.51 <i>0.86</i>	0.60 <i>0.10</i>	0.09 <i>0.05</i>				99.64
62		3	51.12 <i>0.24</i>	0.71 <i>0.01</i>	2.25 <i>0.17</i>		7.83 <i>0.10</i>	0.37 <i>0.04</i>	14.82 <i>0.54</i>	21.87 <i>0.41</i>	0.47 <i>0.04</i>	0.04 <i>0.02</i>				99.48
57		2	52.38 <i>0.27</i>	0.40 <i>0.01</i>	1.28 <i>0.06</i>		7.28 <i>0.04</i>	0.33 <i>0.01</i>	15.48 <i>0.19</i>	22.78 <i>0.33</i>	0.44 <i>0.01</i>	0.02 <i>0.01</i>				100.37
42	Melt	5	67.81 <i>0.30</i>	0.89 <i>0.05</i>	14.63 <i>0.12</i>		4.43 <i>0.23</i>	0.15 <i>0.02</i>	1.31 <i>0.07</i>	4.31 <i>0.08</i>	4.61 <i>0.19</i>	1.35 <i>0.06</i>	0.19 <i>0.01</i>	0.32 <i>0.00</i>	b.d.	100.00
62		5	67.26 <i>0.27</i>	0.86 <i>0.08</i>	14.72 <i>0.33</i>		4.41 <i>0.21</i>	0.12 <i>0.01</i>	1.56 <i>0.09</i>	4.62 <i>0.07</i>	4.46 <i>0.19</i>	1.30 <i>0.12</i>	0.23 <i>0.01</i>	0.33 <i>0.00</i>	0.11 <i>0.02</i>	100.00
57		4	67.52 <i>0.21</i>	0.85 <i>0.05</i>	14.92 <i>0.38</i>		4.37 <i>0.15</i>	0.13 <i>0.03</i>	1.32 <i>0.04</i>	4.34 <i>0.04</i>	4.58 <i>0.22</i>	1.31 <i>0.03</i>	0.21 <i>0.03</i>	0.35 <i>0.00</i>	0.11 <i>0.02</i>	100.00
43	Mag	4	0.36 <i>0.18</i>	7.11 <i>0.24</i>	1.91 <i>0.06</i>	51.49 <i>1.20</i>	33.29 <i>0.58</i>	0.55 <i>0.03</i>	2.24 <i>0.11</i>	0.21 <i>0.10</i>	b.d.	0.01 <i>0.02</i>				97.18
63		5	0.52 <i>0.26</i>	7.48 <i>0.07</i>	1.91 <i>0.06</i>	51.23 <i>0.28</i>	34.30 <i>0.26</i>	0.58 <i>0.04</i>	2.11 <i>0.09</i>	0.18 <i>0.06</i>	0.03 <i>0.06</i>	0.02 <i>0.02</i>				98.36
58		3	0.58 <i>0.60</i>	8.75 <i>0.05</i>	1.93 <i>0.02</i>	47.84 <i>1.08</i>	35.53 <i>0.45</i>	0.51 <i>0.05</i>	2.00 <i>0.12</i>	0.28 <i>0.25</i>	b.d.	0.01 <i>0.02</i>				97.44
43	Cpx	2	51.77 <i>0.14</i>	0.75 <i>0.14</i>	3.64 <i>0.71</i>		9.68 <i>0.38</i>	0.51 <i>0.08</i>	13.11 <i>0.71</i>	19.62 <i>0.37</i>	0.93 <i>0.13</i>	0.11 <i>0.08</i>				100.12
63		7	51.42 <i>0.92</i>	0.70 <i>0.07</i>	2.48 <i>0.52</i>		10.47 <i>0.67</i>	0.54 <i>0.10</i>	13.59 <i>0.35</i>	19.85 <i>0.37</i>	0.74 <i>0.19</i>	0.08 <i>0.05</i>				99.86
58		3	51.85 <i>0.82</i>	0.53 <i>0.08</i>	2.12 <i>0.32</i>		10.52 <i>0.66</i>	0.54 <i>0.11</i>	13.85 <i>0.56</i>	19.62 <i>1.28</i>	0.64 <i>0.07</i>	0.08 <i>0.07</i>				99.76
43	Pl	5	60.11 <i>0.77</i>	0.30 <i>0.08</i>	21.95 <i>0.70</i>		3.23 <i>0.98</i>	b.d.	0.72 <i>0.33</i>	6.73 <i>0.30</i>	6.73 <i>0.13</i>	0.38 <i>0.03</i>				100.15
63		5	61.37 <i>1.09</i>	0.23 <i>0.03</i>	22.63 <i>0.65</i>		2.04 <i>0.37</i>	b.d.	0.36 <i>0.18</i>	6.40 <i>0.54</i>	6.70 <i>0.37</i>	0.44 <i>0.10</i>				100.18
58		3	59.74 <i>0.26</i>	0.19 <i>0.07</i>	23.21 <i>1.19</i>		2.15 <i>0.76</i>	b.d.	0.46 <i>0.39</i>	7.05 <i>0.16</i>	6.81 <i>0.37</i>	0.31 <i>0.06</i>				99.92
43	Melt	3	72.64 <i>0.59</i>	0.67 <i>0.05</i>	13.04 <i>0.52</i>		3.25 <i>0.12</i>	0.10 <i>0.00</i>	0.58 <i>0.08</i>	2.10 <i>0.30</i>	5.15 <i>0.04</i>	1.73 <i>0.13</i>	0.12 <i>0.02</i>	0.44 <i>0.02</i>	0.17 <i>0.01</i>	100.00
63		3	72.51 <i>0.47</i>	0.70 <i>0.02</i>	13.37 <i>0.09</i>		3.34 <i>0.22</i>	0.09 <i>0.01</i>	0.52 <i>0.06</i>	2.05 <i>0.01</i>	4.83 <i>0.18</i>	1.83 <i>0.07</i>	0.12 <i>0.00</i>	0.47 <i>0.00</i>	0.15 <i>0.01</i>	100.00
58		3	71.89 <i>0.92</i>	0.55 <i>0.01</i>	13.59 <i>0.47</i>		3.65 <i>0.21</i>	0.11 <i>0.01</i>	0.55 <i>0.08</i>	2.07 <i>0.25</i>	5.10 <i>0.44</i>	1.82 <i>0.17</i>	0.10 <i>0.01</i>	0.44 <i>0.02</i>	0.13 <i>0.02</i>	100.00
45	Mag	3	0.74 <i>0.48</i>	12.03 <i>0.40</i>	1.58 <i>0.11</i>	41.39 <i>1.57</i>	40.19 <i>0.61</i>	0.42 <i>0.05</i>	1.25 <i>0.02</i>	0.25 <i>0.12</i>	b.d.	b.d.				97.84
65		3	1.84 <i>1.06</i>	12.62 <i>0.78</i>	1.86 <i>0.43</i>	38.70 <i>1.65</i>	40.22 <i>0.96</i>	0.40 <i>0.05</i>	0.96 <i>0.50</i>	0.59 <i>0.52</i>	0.43 <i>0.40</i>	0.06 <i>0.03</i>				97.69
66		2	2.76 <i>0.49</i>	17.45 <i>0.03</i>	1.22 <i>0.07</i>	28.00 <i>1.48</i>	47.05 <i>1.07</i>	0.43 <i>0.03</i>	0.62 <i>0.02</i>	0.42 <i>0.10</i>	0.32 <i>0.08</i>	0.12 <i>0.01</i>				98.38
45	Cpx	4	50.99 <i>0.49</i>	0.58 <i>0.12</i>	2.01 <i>0.48</i>		17.38 <i>0.66</i>	0.65 <i>0.09</i>	11.25 <i>0.44</i>	16.30 <i>0.49</i>	0.72 <i>0.13</i>	0.12 <i>0.08</i>				100.00
65		3	50.98 <i>1.00</i>	0.56 <i>0.01</i>	1.75 <i>0.65</i>		16.85 <i>0.51</i>	0.61 <i>0.05</i>	11.39 <i>0.55</i>	17.13 <i>1.13</i>	0.59 <i>0.16</i>	0.12 <i>0.13</i>				99.99
66		7	51.06 <i>0.92</i>	0.63 <i>0.08</i>	1.96 <i>0.76</i>		16.02 <i>1.01</i>	0.56 <i>0.05</i>	9.46 <i>0.77</i>	18.73 <i>0.96</i>	1.13 <i>0.42</i>	0.14 <i>0.08</i>				99.69
45	Pl	(3)	69.19 <i>1.80</i>	0.45 <i>0.06</i>	16.65 <i>1.25</i>		2.90 <i>0.17</i>	b.d.	0.38 <i>0.21</i>	3.74 <i>0.42</i>	6.04 <i>0.37</i>	0.78 <i>0.13</i>				100.14
65		3	64.80 <i>0.73</i>	0.36 <i>0.02</i>	19.03 <i>0.37</i>		3.04 <i>0.42</i>	b.d.	0.33 <i>0.13</i>	4.19 <i>0.46</i>	6.62 <i>0.17</i>	1.28 <i>0.13</i>				99.64
66		7	64.84 <i>0.94</i>	0.25 <i>0.22</i>	19.59 <i>1.09</i>		2.41 <i>0.80</i>	b.d.	0.14 <i>0.05</i>	2.83 <i>0.58</i>	8.56 <i>0.79</i>	1.30 <i>0.33</i>				99.92
45	Melt	(1)	76.14	1.35	11.08		3.20	0.00	0.92	2.71	3.94	0.55	0.06	0.05	b.d.	100.00
65		2	71.54 <i>0.95</i>	0.63 <i>0.04</i>	12.40 <i>0.18</i>		4.82 <i>0.21</i>	0.13 <i>0.02</i>	0.44 <i>0.22</i>	1.86 <i>0.37</i>	4.19 <i>0.39</i>	2.80 <i>0.02</i>	0.09 <i>0.01</i>	0.90 <i>0.01</i>	0.22 <i>0.01</i>	100.00
66		3	70.87 <i>0.42</i>	0.55 <i>0.08</i>	11.25 <i>0.88</i>		6.17 <i>0.98</i>	0.08 <i>0.02</i>	0.40 <i>0.21</i>	1.51 <i>0.38</i>	4.75 <i>0.64</i>	3.37 <i>0.15</i>	0.10 <i>0.03</i>	0.74 <i>0.14</i>	0.21 <i>0.08</i>	100.00

**Table B.1.2** *continued*

Run	Phase	<i>n</i> <sup>a</sup>	SiO <sub>2</sub>	TiO <sub>2</sub>	Al <sub>2</sub> O <sub>3</sub>	Fe <sub>2</sub> O <sub>3</sub>	FeO	MnO	MgO	CaO	Na <sub>2</sub> O	K <sub>2</sub> O	P <sub>2</sub> O <sub>5</sub>	Cl	ZrO <sub>2</sub>	Total
81	Mag	2	0.19 <i>0.01</i>	2.09 <i>0.00</i>	1.27 <i>0.01</i>	61.53 <i>0.17</i>	29.22 <i>0.12</i>	0.70 <i>0.02</i>	1.40 <i>0.00</i>	0.28 <i>0.00</i>	b.d.	b.d.				96.67
105		3	1.81 <i>0.56</i>	1.03 <i>0.01</i>	1.63 <i>0.10</i>	60.89 <i>1.03</i>	28.76 <i>0.44</i>	0.85 <i>0.09</i>	2.44 <i>0.19</i>	0.42 <i>0.30</i>	b.d.	0.06 <i>0.02</i>				97.89
101		6	0.94 <i>0.64</i>	5.36 <i>0.08</i>	1.53 <i>0.04</i>	53.54 <i>1.52</i>	32.93 <i>0.50</i>	0.59 <i>0.05</i>	1.67 <i>0.16</i>	0.35 <i>0.18</i>	b.d.	0.02 <i>0.02</i>				96.95
110		3	0.37 <i>0.12</i>	3.28 <i>0.30</i>	1.83 <i>0.08</i>	57.60 <i>1.00</i>	29.62 <i>0.67</i>	0.64 <i>0.04</i>	1.76 <i>0.10</i>	0.18 <i>0.08</i>	b.d.	b.d.				95.28
81	Ilm	2	0.16 <i>0.01</i>	18.61 <i>0.21</i>	0.35 <i>0.02</i>	60.61 <i>0.06</i>	14.85 <i>0.27</i>	0.25 <i>0.05</i>	0.87 <i>0.04</i>	0.22 <i>0.09</i>	b.d.	b.d.				95.93
105		5	0.19 <i>0.09</i>	15.67 <i>0.53</i>	0.51 <i>0.04</i>	67.67 <i>0.89</i>	11.77 <i>0.42</i>	0.26 <i>0.04</i>	1.13 <i>0.05</i>	0.16 <i>0.02</i>	b.d.	b.d.				97.36
101		4	0.55 <i>0.35</i>	26.53 <i>0.31</i>	0.39 <i>0.07</i>	46.05 <i>0.66</i>	21.30 <i>0.41</i>	0.33 <i>0.03</i>	1.26 <i>0.07</i>	0.41 <i>0.17</i>	b.d.	0.04 <i>0.00</i>				96.86
110		2	0.85 <i>1.01</i>	21.94 <i>0.67</i>	0.45 <i>0.01</i>	53.97 <i>0.89</i>	17.42 <i>0.20</i>	0.32 <i>0.01</i>	1.76 <i>0.10</i>	0.18 <i>0.08</i>	b.d.	b.d.				95.28
81	Cpx	3	52.30 <i>0.15</i>	0.44 <i>0.06</i>	2.61 <i>0.28</i>		8.34 <i>0.24</i>	0.50 <i>0.06</i>	13.79 <i>0.35</i>	21.96 <i>0.17</i>	0.60 <i>0.02</i>	0.06 <i>0.00</i>				100.59
105		3	51.15 <i>1.00</i>	0.71 <i>0.10</i>	3.40 <i>0.29</i>		8.95 <i>0.17</i>	0.44 <i>0.06</i>	12.52 <i>0.24</i>	21.96 <i>0.44</i>	0.62 <i>0.08</i>	0.06 <i>0.02</i>				99.80
101		4	50.19 <i>0.87</i>	0.75 <i>0.09</i>	3.03 <i>0.79</i>		11.45 <i>1.01</i>	0.52 <i>0.07</i>	12.56 <i>0.72</i>	19.55 <i>0.45</i>	0.76 <i>0.18</i>	0.08 <i>0.02</i>				98.90
110		9	50.36 <i>1.35</i>	0.64 <i>0.13</i>	2.96 <i>0.74</i>		8.77 <i>1.26</i>	0.46 <i>0.06</i>	13.32 <i>0.64</i>	22.15 <i>0.75</i>	0.61 <i>0.16</i>	0.04 <i>0.01</i>				99.32
81	Pl	3	59.58 <i>0.96</i>	0.07 <i>0.02</i>	24.79 <i>0.76</i>		1.20 <i>0.40</i>	b.d.	b.d.	7.09 <i>0.49</i>	6.86 <i>0.45</i>	0.23 <i>0.05</i>				99.84
105		5	60.34 <i>0.87</i>	0.11 <i>0.03</i>	24.51 <i>0.56</i>		1.06 <i>0.25</i>	b.d.	0.12 <i>0.04</i>	7.27 <i>0.52</i>	6.48 <i>0.44</i>	0.26 <i>0.07</i>				100.16
101		8	60.86 <i>1.17</i>	0.21 <i>0.15</i>	24.05 <i>0.89</i>		1.42 <i>0.40</i>	b.d.	0.24 <i>0.27</i>	6.36 <i>0.70</i>	7.38 <i>0.28</i>	0.27 <i>0.09</i>				100.79
110		10	58.18 <i>1.21</i>	0.04 <i>0.03</i>	27.60 <i>0.58</i>		0.76 <i>0.32</i>	b.d.	0.03 <i>0.02</i>	8.10 <i>0.81</i>	6.83 <i>0.51</i>	0.14 <i>0.02</i>				101.60
81	Melt	12	74.25 <i>0.57</i>	0.31 <i>0.05</i>	14.59 <i>0.18</i>		1.41 <i>0.18</i>	0.08 <i>0.01</i>	0.23 <i>0.04</i>	1.85 <i>0.15</i>	5.26 <i>0.43</i>	1.80 <i>0.08</i>	b.d. <i>0.01</i>	0.22 <i>0.01</i>	b.d.	100.00
105		5	73.42 <i>0.27</i>	0.21 <i>0.04</i>	14.95 <i>0.29</i>		1.70 <i>0.28</i>	0.10 <i>0.03</i>	0.37 <i>0.05</i>	2.27 <i>0.20</i>	4.53 <i>0.42</i>	1.70 <i>0.04</i>	0.18 <i>0.15</i>	0.57 <i>0.05</i>	b.d.	100.00
101		20	74.74 <i>0.41</i>	0.32 <i>0.04</i>	13.41 <i>0.27</i>		1.88 <i>0.21</i>	0.08 <i>0.02</i>	0.31 <i>0.06</i>	1.67 <i>0.16</i>	4.85 <i>0.24</i>	1.93 <i>0.11</i>	0.13 <i>0.13</i>	0.68 <i>0.01</i>	b.d.	100.00
110		14	74.62 <i>0.41</i>	0.31 <i>0.05</i>	14.63 <i>0.27</i>		1.47 <i>0.25</i>	0.09 <i>0.01</i>	0.37 <i>0.05</i>	2.11 <i>0.09</i>	4.42 <i>0.30</i>	1.58 <i>0.08</i>	0.03 <i>0.03</i>	0.37 <i>0.01</i>	b.d.	100.00
107	Mag	2	0.80 <i>0.65</i>	1.87 <i>0.14</i>	1.33 <i>0.12</i>	62.53 <i>1.57</i>	29.15 <i>0.38</i>	0.79 <i>0.01</i>	2.04 <i>0.13</i>	0.15 <i>0.04</i>	0.07 <i>0.10</i>	0.04 <i>0.02</i>				98.77
103		4	0.72 <i>0.32</i>	6.58 <i>0.18</i>	1.36 <i>0.10</i>	51.20 <i>1.01</i>	34.19 <i>0.50</i>	0.60 <i>0.07</i>	1.25 <i>0.13</i>	0.25 <i>0.14</i>	b.d.	0.05 <i>0.01</i>				96.21
111		2	0.73 <i>0.49</i>	4.33 <i>0.05</i>	1.43 <i>0.15</i>	57.04 <i>0.90</i>	32.22 <i>0.39</i>	0.62 <i>0.06</i>	1.53 <i>0.07</i>	0.27 <i>0.15</i>	0.04 <i>0.06</i>	0.02 <i>0.03</i>				98.26
107	Ilm	3	0.37 <i>0.56</i>	20.06 <i>1.65</i>	0.33 <i>0.02</i>	58.40 <i>3.05</i>	15.35 <i>0.97</i>	0.35 <i>0.02</i>	1.38 <i>0.15</i>	0.25 <i>0.24</i>	b.d.	b.d.				96.49
103		4	0.19 <i>0.08</i>	36.27 <i>1.82</i>	0.23 <i>0.05</i>	27.82 <i>2.79</i>	28.37 <i>1.30</i>	0.64 <i>0.13</i>	2.03 <i>0.11</i>	0.17 <i>0.05</i>	b.d.	b.d.				95.73
111		9	0.14 <i>0.10</i>	26.06 <i>0.64</i>	0.32 <i>0.03</i>	48.20 <i>1.19</i>	20.47 <i>0.48</i>	0.31 <i>0.06</i>	1.38 <i>0.06</i>	0.18 <i>0.06</i>	b.d.	0.02 <i>0.01</i>				97.09
107	Cpx	5	53.08 <i>1.84</i>	0.49 <i>0.12</i>	2.50 <i>1.55</i>		11.87 <i>1.60</i>	0.68 <i>0.14</i>	12.27 <i>1.46</i>	18.29 <i>2.28</i>	0.73 <i>0.45</i>	0.08 <i>0.09</i>				99.92
103		6	51.39 <i>0.59</i>	0.41 <i>0.08</i>	1.67 <i>0.19</i>		12.59 <i>1.02</i>	0.76 <i>0.14</i>	13.35 <i>0.85</i>	17.91 <i>1.48</i>	0.57 <i>0.08</i>	0.02 <i>0.01</i>				98.64
111		10	51.92 <i>1.18</i>	0.58 <i>0.21</i>	2.32 <i>0.56</i>		11.42 <i>1.03</i>	0.68 <i>0.06</i>	13.35 <i>0.73</i>	18.63 <i>0.86</i>	0.67 <i>0.16</i>	0.09 <i>0.10</i>				99.66
107	Pl	4	63.18 <i>0.23</i>	0.15 <i>0.14</i>	23.57 <i>1.26</i>		1.11 <i>1.05</i>	b.d.	0.28 <i>0.13</i>	5.30 <i>0.33</i>	7.88 <i>0.62</i>	0.47 <i>0.12</i>				101.67
103		5	62.34 <i>1.32</i>	0.41 <i>0.07</i>	21.49 <i>0.90</i>		2.92 <i>1.51</i>	b.d.	0.42 <i>0.27</i>	4.90 <i>0.46</i>	7.60 <i>0.34</i>	0.57 <i>0.11</i>				100.64
111		8	62.85 <i>1.39</i>	0.13 <i>0.07</i>	22.93 <i>1.12</i>		1.22 <i>0.59</i>	b.d.	0.13 <i>0.05</i>	5.31 <i>0.51</i>	7.69 <i>0.54</i>	0.43 <i>0.16</i>				100.55
107	Melt	4	78.06 <i>0.32</i>	0.25 <i>0.07</i>	12.29 <i>0.51</i>		1.88 <i>0.49</i>	0.08 <i>0.02</i>	0.28 <i>0.09</i>	1.06 <i>0.13</i>	2.64 <i>0.18</i>	2.67 <i>0.02</i>	0.14 <i>0.05</i>	0.53 <i>0.02</i>	0.12 <i>0.04</i>	100.00
103		6	77.29 <i>0.47</i>	0.27 <i>0.03</i>	11.86 <i>0.41</i>		1.81 <i>0.21</i>	0.06 <i>0.01</i>	0.20 <i>0.03</i>	1.06 <i>0.15</i>	3.87 <i>0.36</i>	2.78 <i>0.15</i>	0.07 <i>0.05</i>	0.57 <i>0.01</i>	0.16 <i>0.02</i>	100.00
111		10	78.59 <i>0.78</i>	0.26 <i>0.03</i>	11.62 <i>0.51</i>		1.43 <i>0.13</i>	0.07 <i>0.01</i>	0.23 <i>0.06</i>	1.12 <i>0.25</i>	3.77 <i>0.37</i>	2.19 <i>0.10</i>	0.08 <i>0.07</i>	0.54 <i>0.03</i>	0.10 <i>0.02</i>	100.00



**Table B.1.2** Continued

*Notes:* Fe concentrations are given as  $\text{FeO}^{\text{tot}}$  (total iron), except for magnetite and Ilmenite, where Fe is given as  $\text{Fe}_2\text{O}_3/\text{FeO}$  contents; totals for melts are normalized to 100 wt%; *b.d.* below detection limit of the electron microprobe;  $\sigma$  standard deviation; for mineral abbreviations and run conditions see Table 1  
<sup>a</sup>number of analyses

Au-capsules were used for the experiments with 40 mg starting glass powder and a defined amount of fluid. For studying the influence of water,  $a\text{H}_2\text{O}$  of the experiments was fixed via a mixture of deionized water and  $\text{CO}_2$  (by using silver-oxalate,  $\text{Ag}_2\text{C}_2\text{O}_4$ ). At one run (defined P, T,  $f\text{H}_2$ ), several experiments can be performed simultaneously. All were fluid-saturated (~5 % total fluid) with different  $\text{H}_2\text{O}-\text{CO}_2$  proportions, verified by bubbles observed in each experiment.

## B.1.5. Experimental methods

### B.1.5.1. Experimental procedure to enlarge melt-pools and crystals

Several static reference experiments (identical run conditions with respect to duration, mean temperature, redox conditions, and water content) were performed to monitor the influence of temperature cycling on phase appearance and composition. For this, static experiments were compared with runs of different length of thermal cycling intervals. Additionally, experiments above and below the temperatures chosen for cycling (i.e., 950°C and 800°C, respectively) were performed in order to consider all potentially crystallizing phases (preliminary results presented by Erdmann et al. 2012). This is crucial as phase relations have to be known and potential transgression of phase stability fields due to varying temperature has to be taken into account. To illustrate this, a simplified phase diagram for high  $a\text{H}_2\text{O}$  is presented in Figure B.1.1 where phase-in boundaries are potentially overstepped.

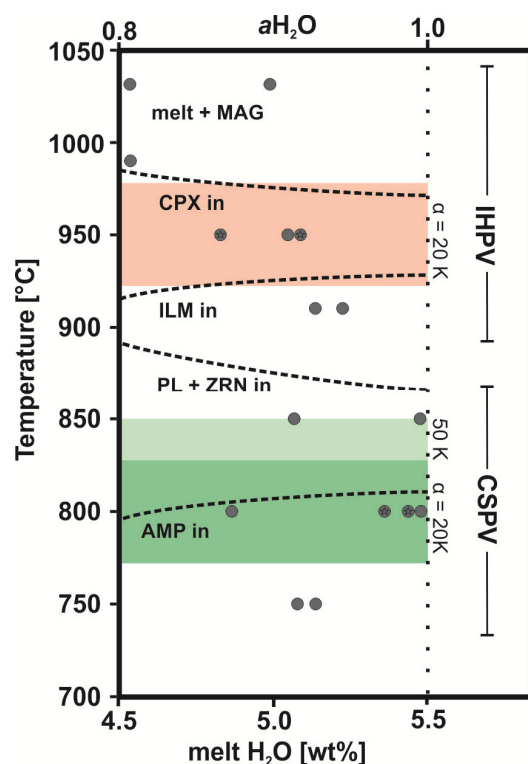


**Figure B.1.1:** Phase stability fields determined for the composition PAR at 200 MPa and high  $a\text{H}_2\text{O}$  as a function of temperature. On the upper x-axes the approximate water activity is given. Redox conditions are not considered here. Each grey dot corresponds to an experimental run (preliminary results presented by Erdmann et al. 2012). Stars indicate cycling experiments. Dashed lines represent the phase in curves of the corresponding minerals; magnetite (labeled MAG) is the liquidus phase at more oxidizing conditions (mineral abbreviations are the same as in Tab. B.1.1). The red field indicates the temperature range affected by cycling in IHPV experiments, the green and light green fields the cycling and peak temperature experiments, respectively, performed in the CSPV (experimental data are given in Tab. B.1.2).

Two cycling experiments at 950°C using an IHPV were initially equilibrated at constant temperature for 40 h in order to generate first crystals at identical conditions as in static runs. Afterwards, the first run was cycled three times for 13 h with 11 h of constant temperature in between (72 h in total). The second run was cycled for 72 h without interruption. The two different approaches (i.e., alternate cycling and static run and solely cycling) were chosen to test of whether equilibration at constant temperature is necessary to generate the same phase composition as in entire static runs. In both cases the experiments were finally equilibrated for 8 h, so that the total run time was always 120 h. Amplitudes ( $\alpha$ ) were 20 K (maximum possible value without overstepping phase boundaries except for amphibole; see simplified phase diagram in Fig. B.1.1) with periods ( $\tau$ ) of 40 min (including heating up and cooling down time with a ramp of 20 K/min; 40 min is the shortest possible time without running the risk of an uncontrolled oscillating of the furnace). The overshoot caused by rapid heating/cooling was 5 K and the temperature was stable ( $\pm 0.5$  K) after  $\sim 3$  min (Fig. B.1.2).

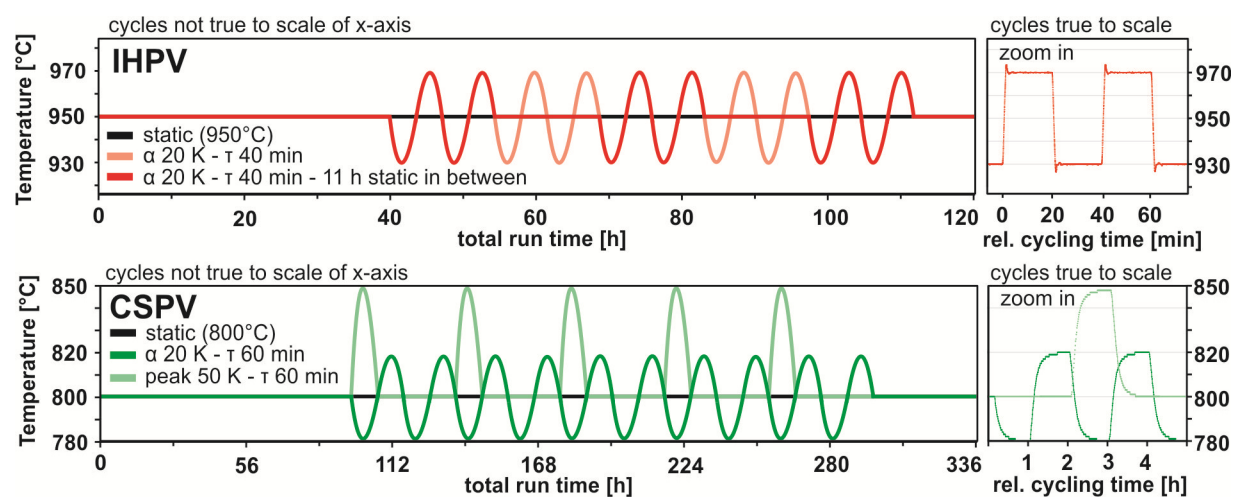


**Figure B.1.2:** Plot of the experimental temperature profiles investigated in this study. Left graphs show the simplified temperature characteristics in IHPV and CSPV experiments, respectively, with different amplitudes ( $\alpha$ ) and periods ( $\tau$ ). Small windows on the right show a detailed plot of the logged temperature during cycling including overshoots and delayed heating and cooling. Colors refer to Figures B.1.1, B.1.3, B.1.4 & B.1.5.

Applying the temperature cycling technique in CSPV's is more challenging in terms of controlling the sample temperature and keeping the pressure constant as the vessel is externally heated. As typical for CSPV's, cooling and heating proceeds more slowly than in IHPV's. Thus, chosen  $\tau$  was longer than in IHPV experiments (120 min instead of 40 min) with the same  $\alpha$  (i.e., 20K). Heating and cooling rates are not constant but fast at the beginning and decelerated close to the target temperature with the result that overshooting was not observed (Fig. B.1.2). The target temperature ( $\pm 1^\circ\text{C}$ ) was reached after 30 min. Total run duration was 336 h/14 days with 192 h/8 days of cycling, 96 h/4 days initial and 48 h/2 days final equilibration. In addition to the temperature cycling runs, a peak temperature series was performed with the idea to keep the temperature constant for most time, omit the kinetically ineffective time at lower temperatures, and quickly dissolve tiny crystals at distinctively higher temperature. For this, temperature was maintained at 800°C for most time with short (1 h) increases up to 850°C. In order to guarantee comparable conditions to temperature cycling experiments, initial (96 h) and final (48 h) equilibration were adopted from cycling experiments. In between, temperature was increased for

1 h up to 850°C, and then held for 5 h at 800°C. This was repeated 32 times. Heating up to 850°C ( $\pm 2^\circ\text{C}$ ) and cooling down to 800 °C ( $\pm 2^\circ\text{C}$ ) proceeded within 24 min (cf. T distribution in Fig. B.1.2).

As the bomb of the CSPV is closed during the experiment, internal pressure is influenced by heating and cooling. However, pressure during the experiment was constant at 200 MPa ( $\pm 5$ ) at 800°C when no temperature cycling was operating. While heating up to 820°C pressure increases to maximal 219 MPa and decreases to 184 MPa at 780°C. Heating up to 850°C causes a pressure increase up to 245 MPa. However, this relatively high pressure prevailed for less than 10 % of total run duration (32 of 336 h) as main temperature was 800°C where pressure was constant at 200 MPa ( $\pm 5$ ). Moreover, pressure change of less than 20 MPa for temperature cycling and even of 45 MPa at the peak temperature series are considered to be negligible (e.g., Feig et al. 2006). This is confirmed by the static comparative test with the same total duration in which pressure was constant and water content at water saturated conditions was the same as in cycling experiments. It is well known that water content is pressure dependent (e.g., Feig et al. 2006). Thus, if the average pressures in the cycling experiments would have been different, the water concentrations in the melt would have been different, which was not observed.

Additionally, static experiments for 650 h/27 days for the different water activities were performed, as this is considered to be required for equilibrium conditions in high-silica systems (74 to 79 wt% SiO<sub>2</sub> in melt; cf. Tab. B.1.2).

#### ***B.1.5.2. Analytical methods***

The run products (glass and minerals) were analyzed with the Cameca SX 100 electron microprobe at Leibniz Universität Hannover, Germany. For the analyses of the crystals, following operating conditions were chosen: 15 kV high voltage, 15 nA beam current, 10 seconds counting time on peak and 10 s on background, focused beam. For the analyses of the remaining melt (water-bearing), which is problematic due to “alkali-loss” effects (e.g., Morgan and London 2005), a special procedure was applied following Koepke et al. (2004). The beam current was set to 4 nA, the counting time varied for the corresponding elements and was 4 s for K, 8 s for Si, Al, Ti and Fe, 10 s for Na and Zr, 12 s for Mg, 16 s for Ca and 30 s for P, Cl and Mn. Na and K were counted first on their spectrometers. Background counting time was always same as the peak time. Whenever possible, a defocused beam with a spot size of 5, 10 or 20  $\mu\text{m}$  was used, and Na-loss was checked by comparing the results of measurements with different beam size on identical glasses of an experimental sample with larger melt pools. Standard glasses with composition similar like the experimental glasses and with known water content (analyses of melt and standard glasses with according water content calculation via by-difference are listed in the electronic supplemental material B.1.ESM) have been used for estimating the water contents in the experimental glasses by the “by-difference” method (Devine et al. 1995).

### **B.1.6. Results and discussion**

#### ***B.1.6.1. Achievement of equilibrium***

Run durations as long as possible are the best way to attain near-equilibrium conditions in experiments, especially in highly polymerized melt compositions. In this study a variation of run

duration at constant P-T conditions,  $fO_2$  and  $aH_2O$  was only performed at one series at 800°C in the CSPV. However, run durations for all other experiments in the IHPV and CSPV are expected to be sufficient since they were conducted in a similar time frame as experiments with rhyolitic starting material in the same IHPV (Almeev et al. 2012) and distinctly longer than experiments on a hydrous tholeiitic basalt (Feig et al. 2010).

The following observations suggest that equilibrium was obtained: (1) Crystals and melt are distributed homogeneously along the capsule; (2) crystals are euhedral and chemically constant within one experimental run (i.e., low standard deviation; Tab. B.1.2); (3) melt measurements are also constant within the analytical error; (4) the compositions of crystals and melt change with the experimental conditions, following expected compositional trends; (5) static experiments were reproduced twice in temperature cycling experiments with the same total run duration and consistent melt and crystal chemistry (see below).

#### ***B.1.6.2. Effect of temperature cycling on phase relation***

**Experiments performed at 950°C in the IHPV.** By comparing the static experiment (i.e., constant temperature for the complete run duration) at 950°C with experiments initially equilibrated at the same temperature but cycled  $\pm 20$  K for different time spans, a significant change in texture can be observed (Fig. B.1.3). While tiny crystals of clinopyroxene and plagioclase residing in the matrix were dissolved, these phases were enlarged significantly in general. This is most effective for clinopyroxene at high  $aH_2O$  (Fig. B.1.3 I) where only one large single crystal is present after cycling. This clinopyroxene is 19 times larger in area (1350  $\mu m^2$ ) than the largest clinopyroxene in the static run # 42 (70  $\mu m^2$ ; Tab. B.1.3). The apparent coarsening of plagioclase due to temperature cycling at 950°C increases with decreasing water activity and shows a maximum effect at  $aH_2O < 0.1$ . In run #66 the average measured area of the 10 largest plagioclase crystals (determined via *ImageJ*; Schneider et al. 2012; <http://imagej.nih.gov/ij/>) is 114  $\mu m^2$  and, thus, 69 times larger as the area of the 10 largest plagioclases of the static run #45 (1.7  $\mu m^2$ ; Tab. B.1.3). The area of pyroxene crystals in low  $aH_2O$  runs reveal a maximum enlargement of 240 % for continuous cycling (#66 compared to #45). However, for *in-situ* analyses this enlargement is crucial as it shifts the crystals in an easily measurable range (from 2.9 to 9.8  $\mu m^2$  in average of the 10 largest crystals). This enlargement also allows to measure orthopyroxene crystals (<0.5 vol%) which were probably also present in the two other experiments but was too small to be identified. Due to dissolution of tiny phases in the matrix and fewer crystals in general, crystal free melt pools in the cycled runs are larger. Different is the behavior of Fe-Ti oxides (magnetite and ilmenite), which are less influenced by temperature cycling than silicate phases. The numbers of tiny crystals of Fe-Ti oxides in the matrix and as inclusions in other phases are reduced but still observable. Coarsening of these phases is insignificant. For this reason, the effect of temperature cycling is less obvious in experiments with high water activity at 950°C, where magnetite is the dominant phase and plagioclase not present. However, the striking enlargement of clinopyroxene in these runs described above show that temperature cycling enlarges at least clinopyroxenes most effectively at high water activity.

**Experiments performed at 800°C in the CSPV.** The aim of temperature cycling applied in experiments performed in CSPV's was to shorten the total run duration and enlarge



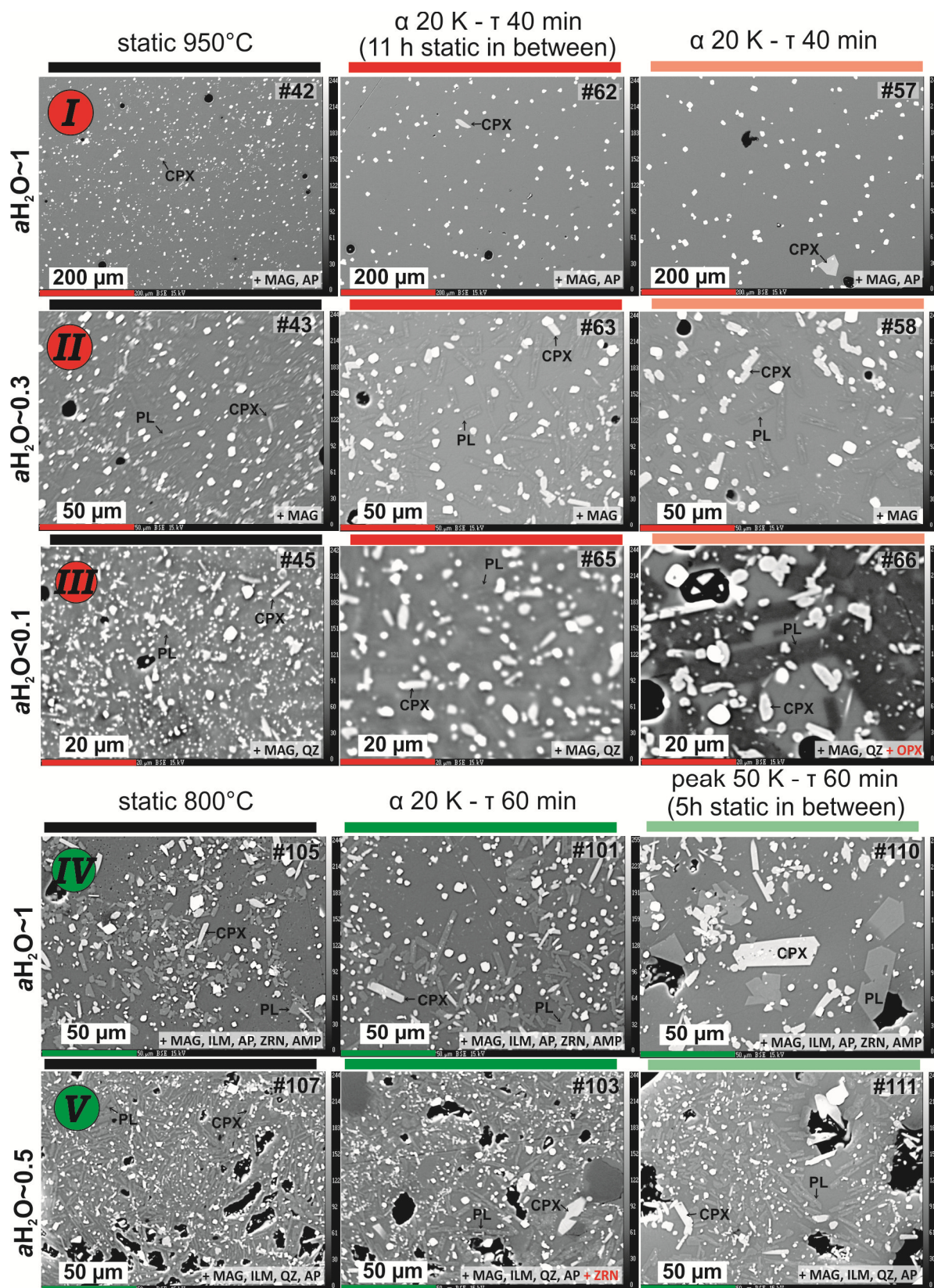


**Figure B.1.3:** Comparison of BSE images (with given run number; see Tab. B.1.1 & B.1.2 for run conditions and compositions) of static and cycled runs for different water activities. Roman numbers refer to experimental conditions (Fig. B.1.1) and phase compositions (Fig. B.1.4 & B.1.5). Colors of the experimental run refer to the corresponding temperature profile in Figure B.1.2. Present phases are given in the lower right (abbreviations are the same as in Tab. B.1.1;  $\alpha$  = amplitude;  $\tau$  = period). The analyzed crystals for Table B.1.3 are highlighted in the apart from that same Figure and can be found in the electronic supplemental material B.1.ESM.

crystals and melt pools simultaneously. Static experiments of 27 days at 800°C and  $a_{\text{H}_2\text{O}} \sim 1$  (#81) exhibit only slightly larger crystals than the static one with a duration of 14 days (#105). Although experiment #81 bears large crystals (mainly clinopyroxene and amphibole), they are all concentrated at the rim close to the capsule wall, obviously influenced by diffused water, indicated by contamination with Ni up to 10 wt%. Experiment #105 does not show any Ni-contamination after 14 days. However, all phases are relatively small (Fig. B.1.3). The corresponding cycling experiment with  $\alpha=20$  K and a duration of 14 days bear clinopyroxenes with a comparable size (with regard to the area of the 10 largest crystals; see Tab. B.1.3). Plagioclases are 3 times larger in area ( $62 \mu\text{m}^2$  compared to  $20 \mu\text{m}^2$ ). Even larger crystals were produced in the peak temperature experiment (T-increase of 50 K every 6 h for 1 h) where plagioclases are 14 times and clinopyroxenes (without Ni contamination) 7 times larger than in the static one (Fig. B.1.3). At reduced water activity the cycling effect is less pronounced but still apparent. The experiment with  $\alpha=20$  K (#103) and especially the one with peak T (#111) show larger crystals than the static reference experiment; however, more obvious are the distinctively larger melt pools, especially in the peak T run #111 (Fig. B.1.3). Cycling run #103 bears, in contrast to static run #107, small amounts of zircon. Similar to the orthopyroxene occurrence in #66 of the IHPV experiment, we assume that zircon was present in the two other experiments (#107 and #111), but was too small to be identified. In all other experiments, phase relations in temperature cycling experiments are the same as in static ones. In summary, an overstepped phase-in boundary during oscillation is uncritical as long as initial and final equilibration was established.

**Table B.1.3** Crystal sizes

Run no.	Temp. [°C]	cycling amplitude	$a_{\text{H}_2\text{O}}$ exp	median area ( $\mu\text{m}^2$ ) of the $n$ largest crystals			
				$n$	Pl	$n$	Cpx
42	950	static	0.98			1	70
62	950	20 K	1.00			1	345
<i>relative enlargement</i>							<b>4.9</b>
57	950	20 K	1.00			1	1348
<i>relative enlargement</i>							<b>19</b>
43	950	static	0.39	10	54	10	7.3
63	950	20 K	0.22	10	60	10	18
<i>relative enlargement</i>					<b>1.1</b>		<b>2.5</b>
58	950	20 K	0.26	10	89	10	36
<i>relative enlargement</i>					<b>1.7</b>		<b>5.0</b>
45	950	static	0.02	10	1.7	10	2.9
65	950	20 K	0.02	10	9.3	10	7.1
<i>relative enlargement</i>					<b>5.6</b>		<b>2.5</b>
66	950	20 K	0.06	10	114	10	9.8
<i>relative enlargement</i>					<b>69</b>		<b>3.4</b>
105	800	static	0.96	10	20	10	22
101	800	20 K	0.86	10	62	10	23
<i>relative enlargement</i>					<b>3.1</b>		<b>1.0</b>
110	800	50 K	1.00	10	281	10	146
<i>relative enlargement</i>					<b>14</b>		<b>6.5</b>
107	800	static	0.62	10	6.7	10	14
103	800	20 K	0.44	10	24	10	40
<i>relative enlargement</i>					<b>3.5</b>		<b>2.8</b>
111	800	50 K	0.50	10	41	10	47
<i>relative enlargement</i>					<b>6.1</b>		<b>3.3</b>

$n$  number of measured crystals

For mineral abbreviations and calculation of  $a_{\text{H}_2\text{O}}$  see Table 1

Single measurements of the 10 largest crystals are present in the deposit material

With regard to phase proportions, a generally good accordance between static and cycling experiments is given. Based on analyzes using *ImageJ* (Schneider et al. 2012; <http://imagej.nih.gov/ij/>), modal proportions are practically identical (Tab. B.1.1). The strongest variations are observed for cycling run #66 with 7 vol% more melt and peak temperature run #110 with 12 vol% less melt than in the corresponding static ones. This is probably caused by considering sample areas with large crystals and meltpools, respectively, for BSE images. Thus, crystals and meltpools are potentially irregularly distributed on the images analyzed and do not represent the sample average.

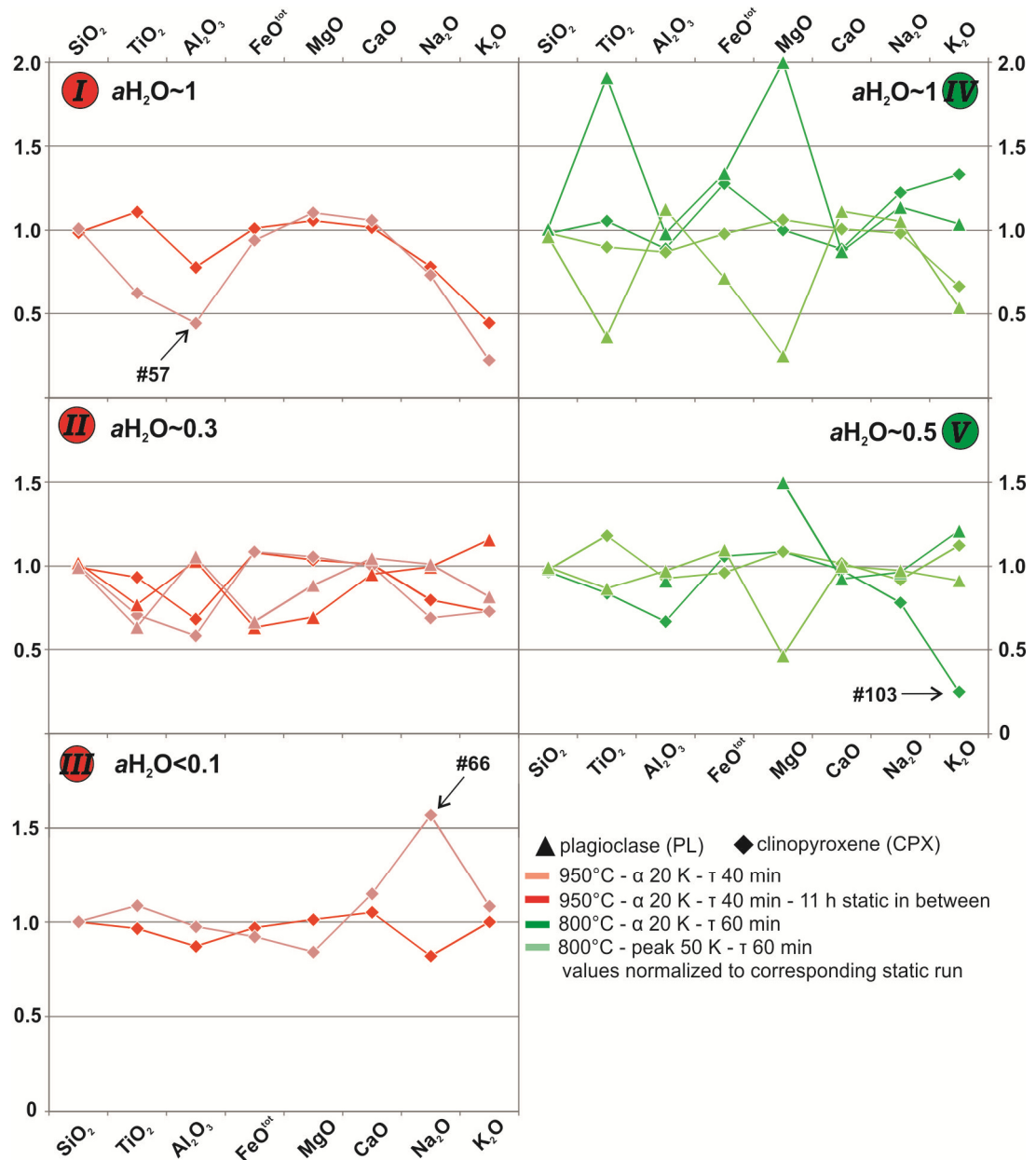


**Figure B.1.4.:** Phase chemistry of clinopyroxene and plagioclase for all measured elements (given as oxides and normalized to the composition of clinopyroxene and plagioclase of the corresponding static run). Roman numbers refer to experimental conditions (Fig. B.1.1) and to BSE images (Fig. B.1.3). Colors of the composition curves refer to the corresponding temperature profile in Figure B.1.2.

### **B.1.6.3. Effect of temperature cycling on phase chemistry**

**Variations of clinopyroxene and plagioclase composition.** Phase chemistry of all major phases is given in Table B.1.2. As stated above, clinopyroxenes and plagioclases are mainly influenced by temperature cycling. Thus, the compositions of these two phases are illustrated in Figure B.1.4 for potential variations of all measured elements (given as oxides and normalized to the composition of clinopyroxene and plagioclase of the corresponding static run). Discrepancies between static and cycling experiments are generally small. This implies that equilibration of the phases occur at the very beginning of an experiment and cycling only minor affects the final composition. In general, no chemical zonation was observed despite enormous growth of the crystals. Variations are accentuated when the content of an oxide is small in the phase (e.g.,  $K_2O$  in clinopyroxene and  $MgO$  in plagioclase). Clinopyroxenes of run #57 show additionally lower values for  $TiO_2$  and  $Al_2O_3$  (Fig. B.1.4 *I*) while they are enriched in  $Na_2O$  in run #66 (Fig. B.1.4 *III*). The static run at  $950^\circ C$  with  $aH_2O < 0.1$  (#45) has many tiny phases making analyses of plagioclase and melt, which are concentrated in the matrix, difficult. Thus, the measurements of these phases (Tab. B.1.2) show probably contaminated values and are omitted in Figure B.1.4 *III* and Figure B.1.5. Variations in phase chemistry of CSPV experiments are also minor and only objectionable for oxides of plagioclase with low contents (i.e.,  $TiO_2$  and  $MgO$ ). Clinopyroxenes of run #103 also show pronounced variations (Fig. B.1.4 *V*). However, the overall good agreement of static and cycling phase chemistry shows that the cycling technique is a valuable tool for increasing the grain sizes of the experimental products without influencing the mineral compositions.

Although Fe-Ti oxides are only marginally enlarged by thermal cycling, they show significant variations in  $TiO_2$  and  $FeO_{total}$  contents in some runs (Tab. B.1.2). The most pronounced discrepancy is observed for cycling run #101 with distinctively higher  $TiO_2$  values in magnetite and ilmenite. A possible explanation is the slightly lower melt water content in this run leading to more reducing conditions compared to the reference experiments. This influences Fe-Ti oxide composition but has little effect on other phases.

**Variations of melt composition.** Melt composition of cycled experiments is normalized to melt composition of the corresponding static runs and illustrated in Figure B.1.5 for all measured elements (given as the corresponding oxide, except Cl). Most distinctive are the variations for  $P_2O_5$  which is mainly due to very low contents in the melt which highlight small variations. Cycling run #62 is additionally slightly enriched in melt  $MgO$  compared to the static run and cycling run #57 (Fig. B.1.5 *I*). Experiments performed at low  $aH_2O$  (i.e.  $< 0.1$ ) without temperature cycling are lacking in measureable meltpools and are, thus, not illustrated in Figure B.1.5. Cycling runs at these conditions (#65 and #66) show moderate variations, probably caused by slightly different melt water contents (Tab. B.1.2). Runs #101 and #110 are enriched in  $TiO_2$  and vary in the Cl content (Fig. B.1.5 *IV*) while #103 and #111 are distinctively enriched in  $Na_2O$  (Fig. B.1.5 *V*), probably caused by small variations in plagioclase crystallization. However, the general variations of the temperature cycling experiments compared to the static ones are marginal and mostly limited to elements with low contents.



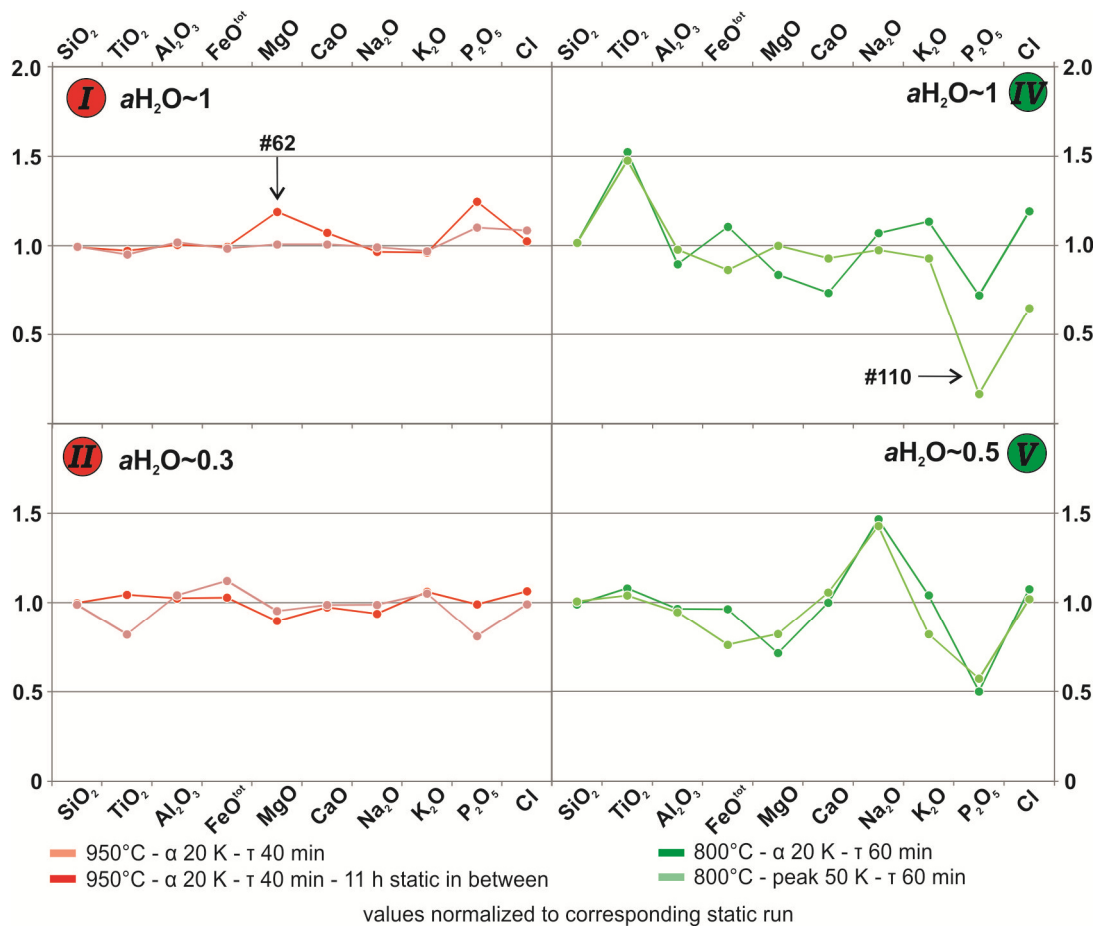


**Figure B.1.5.:** Chemistry of experimental melt for all measured elements/oxides normalized to the composition of the corresponding static run. Roman numbers refer to experimental conditions (Fig. B.1.1) and to BSE images (Fig. B.1.3). Colors of the composition curves refer to the corresponding temperature profile in Figure B.1.2.

### B.1.7. Implications

The aim of this study was to test whether the application of temperature cycling in a dacitic system may help to produce different textures in experiments that allow easier melt analysis with *in-situ* methods. Inspired by the innovative work of Mills et al. (2011), the cycling technique was adopted to the phase equilibria study under pressure and varying water activity, with the goal to obtain larger melt pools and crystals in experiments close to the solidus. As experimental conditions chosen here (i.e., pressure, temperature, redox conditions, water activity) are common for phase relation studies in various magmatic systems, our results have the potential to optimize such experimental approaches and enable experimental petrologists to study their run products for example with *in-situ* trace element techniques as SIMS. We showed that temperature cycling helps to enlarge crystals and melt pools significantly without affecting the phase relations or phase compositions. However, this study only presents first steps for crystal coarsening in a fluid saturated system without considering systematical variations of  $\alpha$  and  $\tau$  in detail, as it was performed by Mills and Glazner (2013) for an alkali basalt at ambient pressure. Since the control of additional parameters like pressure and water-activity which in turn influences the redox conditions is challenging and time consuming, further studies are needed.

Even though experiments are generally designed to simulate natural processes at *equilibrium* conditions (i.e., constant temperature), several processes in nature suggest that oscillating

temperature is common. Potential processes responsible for periodic heating and cooling are: (1) Repeated injection of hot magma (Huppert and Sparks 1988); (2) thermal convection (Martin et al. 1987); (3) variation in water activity. That temperature cycling occurs indeed in nature is inferred for example from K-feldspar megacrysts (Johnson and Glazner 2010; Glazner and Johnson 2013). The experimental confirmation that oscillating temperature causes significant crystal enlargement helps to interpret igneous rock texture, in particular, the generation of phenocrysts. As this is largely governed by the interplay of nucleation and growth rates accompanied with rates of cooling and heating (e.g., Carmichael et al. 1974) the basic conditions are desirable to know. Although we do not consider systematically the effect of  $\tau$  in this study, we assume that it has less impact on growth rates compared to  $\alpha$  indicated by experiment #110 where  $\alpha$  (peak) of 50 K enlarges crystals more compared to  $\alpha$  of 20 K in #101 at same  $\tau$  without static time in between. This is supported by Mills and Glazner (2013) who observed little correlation between  $\tau$  and growth rates in an alkali basalt. Thus, time of temperature change in natural systems seems to be of second order importance, as long as it proceeds in geological short terms (i.e., within days) before a new equilibrium is reached. Then, with increasing temperature, small crystals with a high ratio of surface area to volume are preferentially dissolved relative to large crystals following by reprecipitation onto these large crystals while temperature goes down.

### ***Acknowledgements***

We thank Otto Dietrich and Julian Feige for their careful sample preparation. We gratefully acknowledge the chief scientists of RV Sonne, especially K.M. Haase, for access to the sample 3DS1 used in this study. Thoughtful and thorough reviews by Allen Glazner, Craig Lundstrom, and Editor Charles Lesher greatly improved the manuscript. Funding for this research was provided by grants from the Deutsche Forschungsgemeinschaft (KO 1723/13). This is CRPG contribution number 2407.

# Chapter C

## C.1. Anatexis at the roof of an oceanic magma chamber at IODP Site 1256 (equatorial Pacific): An experimental study

*Martin Erdmann*<sup>1,2</sup>, *Lennart A. Fischer*<sup>1</sup>, *Lydéric France*<sup>2</sup>, *Chao Zhang*<sup>1</sup>, *Marguerite Godard*<sup>3</sup>, and *Jürgen Koepke*<sup>1</sup>

<sup>1</sup>*Institut für Mineralogie, Leibniz Universität Hannover, Callinstr. 3, 30167 Hannover, Germany*

<sup>2</sup>*CRPG, UMR 7358, CNRS, Université de Lorraine, 15 rue Notre Dame des Pauvres, 54501 Vandoeuvre-lès-Nancy, France*

<sup>3</sup>*Géosciences, Université Montpellier 2, Place Eugène Bataillon, 34095 Montpellier, France*

*Contributions to Mineralogy and Petrology, Volume 169(4), pages 1-28, 2015*  
*DOI: 10.1007/s00410-015-1136-5*

### C.1.1. Abstract

Replenished axial melt lenses at fast-spreading mid-oceanic ridges may move upward and intrude into the overlying hydrothermally-altered sheeted dikes, resulting in high-grade contact metamorphism with the potential to trigger anatexis in the roof rocks. Assumed products of this process are anatectic melts of felsic composition and granoblastic, two-pyroxene hornfels, representing the residue after partial melting. Integrated Ocean Drilling Program expeditions 309, 312, and 335 at Site 1256 (eastern equatorial Pacific) sampled such a fossilized oceanic magma chamber. In this study, we simulated magma chamber roof rock anatectic processes by performing partial melting experiments using six different protoliths from the Site 1256 sheeted dike complex, spanning a lithological range from poorly- to strongly-altered basalts to partially- or fully-recrystallized granoblastic hornfels.

Results show that extensively altered starting material lacking primary magmatic minerals cannot reproduce the chemistry of natural felsic rocks recovered in ridge environments, especially elements sensitive to hydrothermal alteration (e.g., K, Cl). Natural geochemical trends are reproduced through partial melting of moderately-altered basalts from the lower sheeted dikes. Two-pyroxene hornfels, the assumed residue, were reproduced only at low melting degrees (<20 vol%). The overall amphibole absence in the experiments confirms the natural observation that amphibole is not produced during peak metamorphism. Comparing experimental products with the natural equivalents reveals that water activity ( $a_{\text{H}_2\text{O}}$ ) was significantly reduced during anatectic processes, mainly based on lower melt aluminum oxide and lower plagioclase anorthite content at lower  $a_{\text{H}_2\text{O}}$ . High silica melt at the expected temperature (1000-1050°C; peak thermal overprint of two-pyroxene hornfels) could only be reproduced in the experimental series performed at  $a_{\text{H}_2\text{O}}=0.1$ .

**Keywords:** *Experimental petrology, Partial melting, Fast-spreading mid-ocean ridge, Oceanic plagiogranite, Granoblastic hornfels, Conductive boundary layer*

### C.1.2. Introduction

Anatectic processes associated with the dynamic behavior of crystal mush zones with an overlying axial melt lens (AML) at fast-spreading mid-ocean ridges have major influences on the composition of the oceanic crust. Based on geophysical studies (e.g., Caress et al. 1992; Crawford et al. 1999; Lamoureux et al. 1999; Dunn et al. 2000) and field observations in ophiolites (e.g., Nicolas et al. 1988, 2000; Gillis and Coogan 2002; Umino et al. 2003; France et al. 2009), the crystal mush zone at fast-spreading mid-ocean ridges has a melt fraction of less than 20% (e.g., Caress et al. 1992; Crawford et al. 1999; Lamoureux et al. 1999; Dunn et al. 2000), and is located between the Moho and the sheeted dikes. At the top of the crystal mush zone, directly beneath or within the sheeted dike root zone, a small (~50 – 100 m thick and ~1000 m wide) melt lens is commonly present (e.g., Detrick et al. 1987). This AML, locally filled with nearly-pure basaltic melt (e.g., Detrick et al. 1987; Dunn et al. 2000), feeds the basalts of the upper crust and is assumed to be the place where the main stage of mid-ocean ridge basalt (MORB) differentiation occurs. The AML roof is a very complex horizon, where magmatic processes interact with metamorphic overprint and hydrothermal influence (Coogan et al. 2003; Nicolas et al. 2008; France et al. 2009, 2013). Below this horizon the AML is filled with a basaltic magma at a temperature of ~1200°C, and above it the seawater-derived hydrothermal cells operate at temperatures <600°C (Alt et al. 2010). The two convective systems are thought to be separated by a thin conductive boundary layer (~100 m thick; e.g., Lister 1974) that has a maximum thermal gradient of approximately 3°C/m (Koepke et al. 2008), by far the most extreme quasi-steady-state thermal boundary on Earth. This boundary layer consists of granoblastic hornfels and former hydrothermally-altered sheeted dikes, which were contact-metamorphosed by the heat of the underlying dynamic AML.

The combination of water influx due to the dehydration of the previously hydrothermally altered dikes and heat supply from an underlying AML (Detrick et al. 1987) may result in anatexis of magma chamber roofs (e.g., Gillis and Coogan 2002; Coogan et al. 2003; France et al. 2009, 2010, 2013, 2014). This is an important process at fast-spreading ridges, since the generated anatectic melts have the potential to skew the composition of fresh MORB (France et al. 2014). Evidence for MORB contamination by assimilation of altered lithologies at crustal levels is widespread at fast-spreading ridges (e.g., Perfit et al. 1983; Michael and Chase 1987; Michael and Cornell 1998; Coogan et al. 2003; Wanless et al. 2010, 2011; France et al. 2014).

Apart from MORB contamination, anatexis at the AML roof is recognized to be an important process that generates felsic melt in the sheeted dike root-zone of oceanic crust (e.g., Gillis and Coogan 2002; Koepke et al. 2004; Brophy 2009; France et al. 2010; Wanless et al. 2010; Grimes et al. 2013), where cross-cutting felsic dikes and veins are often observed (e.g., Wilson et al. 2006; France et al. 2009). The origins of these dikes and veins have been debated for decades (see below) yet are still poorly understood. Beard and Lofgren (1991) pointed out that if dehydration melting of hydrated basaltic rocks is a primary mechanism for the formation of silicic melts, large volumes of anhydrous, pyroxene- and plagioclase-rich restites would be predicted. It is verified that such rocks exist as granoblastic hornfels, sandwiched between the AML and the sheeted dikes, and they are well known both from modern oceanic crust (e.g.,

Wilson et al. 2006; Gillis 2008; Koepke et al. 2008; France et al. 2009, 2014) and from the Oman and Troodos ophiolites (e.g., Gillis and Coogan, 2002; Gillis, 2008; France et al. 2009).

The aim of this study is to experimentally reproduce the complex anatectic processes occurring at the roof of fast-spreading oceanic ridge magma chambers by using six natural analogues recovered from Site 1256 of the Integrated Ocean Drilling Program (IODP) expeditions 309, 312, and 335 as starting materials. These materials span a lithological range from poorly- to strongly-altered dike basalt to partially- or fully-recrystallized granoblastic hornfels. The samples are well suited for characterizing the solidus temperatures for the different starting materials as well as for evaluating the compositional spectrum of the experimental melts and the residual minerals, and for addressing the question of whether water-saturated conditions are required for partial melting. Since the compositions of felsic veins as well as of the granoblastic hornfels from the drilled dike/gabbro transition at Site 1256 are available, a direct comparison of the experimental products with the corresponding natural counterparts is possible. This enables a straightforward approach for unraveling the complex magmatic-metamorphic processes ongoing at the dike/gabbro transitions at fast-spreading mid-oceanic ridges.

### **C.1.3. Background**

#### ***C.1.3.1. Oceanic plagiogranites and granoblastic hornfels***

Oceanic crustal plagiogranites (see Koepke et al. 2007 for a review and definition) are typically found, although not in large volumes, in the upper oceanic crust. They have been described as vein networks and/or discrete intrusive bodies in ophiolites (Gillis and Coogan 2002; France et al. 2009, 2014) and as small felsic veins in the relatively young oceanic crust (e.g., Dick et al. 2000; Blackman et al. 2004; Teagle et al. 2006). The dike/gabbro transition of present day oceanic crust has been sampled at only three locations, all related to crust formed at the East Pacific Rise (EPR; IODP Site 1256, Pito Deep, and Hess Deep). Especially at Site 1256, oceanic plagiogranites have been typically recognized as small felsic veins (Wilson et al. 2006; Koepke et al. 2007), often in association with granoblastic hornfels. As the origin of SiO<sub>2</sub>-enriched rocks is still under controversial debate (extreme fractionation vs. partial melting vs. liquid immiscibility; e.g., Koepke et al. 2007), these rock associations are key to our understanding of felsic melt generation in oceanic crust. Focusing on partial melting, as this study does, the general survey of protoliths, products, and residues can shed light on this complex process.

Rocks from the conducting boundary layer were first described as pyroxene and/or hornblende hornfels (e.g., Gillis and Roberts 1999), which are very-fine-grained to microcrystalline granoblastic rocks corresponding to partially-to-completely re-crystallized, hydrothermally-altered dike rocks. The typical mineral assemblage of the pyroxene hornfels is clinopyroxene, orthopyroxene, magnetite, ilmenite, and plagioclase ( $\pm$ amphibole). The presence of primary amphibole divides these rocks into “dry” and “wet” granoblastic subtypes. A detailed review of granoblastic hornfels evolution and characteristics for a present day oceanic crust is given by Koepke et al. (2008) and Alt et al. (2010).

Granoblastic hornfels were initially observed in ophiolites in intimate association with uppermost gabbros typically located within the dike/gabbro transition zone (Rothery 1983;

Nicolas and Boudier 1991). Other studies from the Troodos and Oman ophiolites focused on processes occurring at the roof of a fossil AML and arrived at the general conclusion that the hornfels are the residues of a partial melting event above the AML, while the felsic veins correspond to the related anatectic melts (Gillis and Roberts 1999; Gillis and Coogan 2002; Gillis 2008; France et al. 2009). Granoblastic hornfels are also common in modern oceanic fast-spreading crust and can be directly linked to magma chamber roof processes, because they are sampled within the top of a frozen AML (Wilson et al. 2006; Gillis 2008; Koepke et al. 2008; Alt et al. 2010). Moreover, because the conductive boundary layer above an AML is mainly composed of granoblastic hornfels (Gillis 2008), these rocks are crucial for understanding the heat flux in the hydrothermally-influenced oceanic crust and the role of this altered crust as potential contaminator of fresh MORB melts.

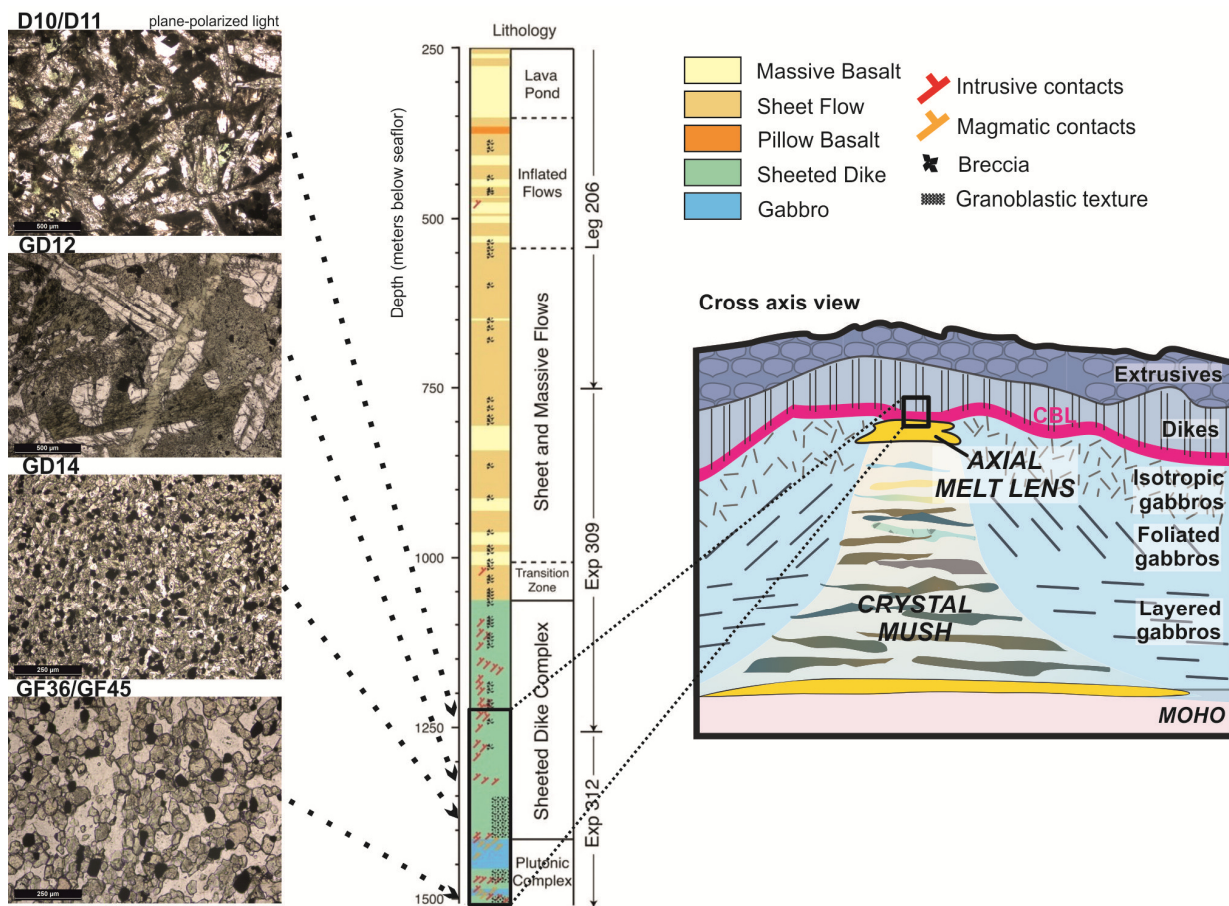


**Figure C.1.1:** Microphotographs of the different starting materials in plane-polarized light. D10 is very similar petrographically to D11 and GF36 to GF45; thus, only one example is shown for each pair. The depth at which each sample was taken is indicated on the IODP Site 1256 lithostratigraphic column (modified after Wilson et al. 2006). The sampled section of the column is shown by the small black rectangle in the schematic cross-axis view of the magmatic system at fast-spreading ridges (modified after France et al. 2014). This model (not to scale, vertical extent ~6 km) highlights the position of the AML (mainly composed of pure melt, yellow color) and the underlying crystal mush (less than 20% melt). At the base of this crystal mush another melt lens is illustrated (yellow) which corresponds to a model from Natland and Dick (2009). The conductive boundary layer (CBL) is highlighted in purple; it consists mainly of granoblastic hornfels.

### C.1.3.2. IODP Site 1256 stratigraphy

IODP Site 1256, located in the eastern Pacific Ocean in ~ 15 Ma old crust, is the only place on Earth where the dike-gabbro transition has been penetrated in a continuous drill section (Fig.

C.1.1; Wilson et al. 2006) and is, thus, perfectly suitable as a source of samples in this study. The gabbro sequence, interpreted as part of the frozen melt lens (Koepke et al. 2011), was reached within seismic layer 2 at 1407 meter below seafloor (mbsf). This shallow level for the gabbros may be related to the high magmatic budget associated with the superfast EPR spreading rate (up to 220 mm/year; Wilson 1996) 19 to 12 Ma ago. The extrusive part of the crust at Site 1256 is composed of a ~100 m thick sequence of lava primarily comprised of a >74 m thick ponded flow, followed by ~700 m of sheet flows and massive lavas, and a relatively thin (~350 m) sequence of sheeted dikes. The lower ~60 m of the sheeted dikes are partially to completely recrystallized to granoblastic hornfels, named "granoblastic dikes" by IODP Expedition 312 scientists (Teagle et al. 2006; Koepke et al. 2008; Alt et al. 2010). One hundred meters below the granoblastic hornfels two intrusive bodies of gabbro (52 m and 24 m thick) are present, separated by 24 m of granoblastic hornfels (Teagle et al. 2006; Koepke et al. 2011). The uppermost gabbros are strongly hydrothermally altered, indicating a deep influence of hydrothermal circulation. These gabbros, interpreted as part of an in-situ frozen AML (Koepke et al. 2011), bear xenoliths of granoblastic hornfels, considered as relics of former dikes, indicating that contamination of a melt lens by overlying roof rocks played a significant role in the evolution of the magmatic system (Teagle et al. 2006; France et al. 2009; Koepke et al. 2011).

#### ***C.1.3.2. Previous experiments testing an anatectic origin of felsic melt in oceanic crust***

Numerous experiments on the dehydration melting of amphibolites and greenstones have been performed in the last decades, in order to investigate the formation of Archean TTG rocks (tonalites, trondhjemites, and granodiorites; Barker 1979; see summarizing chapter on "Dehydration Melting" in Johannes and Holtz 1996). Additionally, some partial melting experiments conducted under hydrous conditions using basaltic compositions as starting material showed that felsic melt production is possible by this process (Holloway and Burnham 1972; Helz 1973; Beard and Lofgren 1991; Kawamoto 1996). However, results of these studies are, for the most part, not directly applicable to the formation of felsic melt at the roof of a mid-ocean ridge AML, as most of the corresponding experiments were performed under elevated pressures ( $\geq 300$  MPa) in order to simulate typical dehydration melting processes related to subduction zones or deep continental basements. Such conditions are not relevant for anatectic processes occurring at the AML roof; these processes are characterized by low lithostatic pressures ( $\leq 100$  MPa) under potentially high water activity ( $a_{\text{H}_2\text{O}}$ ) due to the low water solubility in silicate melts under such shallow pressures. Moreover, these studies used natural starting materials which are different from the lithologies present at the roof of oceanic magma chambers. One study that included experiments at low pressure (100 MPa) was performed by Beard and Lofgren (1991) who systematically investigated the effects of pressure and water on different metamorphosed protoliths. For simulating anatectic processes operating in the deep oceanic crust (e.g., Koepke et al. 2005a,b), partial melting experiments were performed using oceanic gabbro as starting material (Koepke et al. 2004; Wolff et al. 2013; Koepke et al. 2014). However, these studies used fresh, rather primitive cumulate gabbro as starting material, and did not address the special compositional nature of the AML roof rocks which consist of a rock spectrum ranging from hydrated, altered basalts to dry granoblastic hornfels.

The first experimental study using hydrothermally-altered basalt from the lower sheeted dikes as starting material was performed by France et al. (2010). The starting material for that study, however, was sampled in the Oman ophiolite, which may not be the best proxy for fast spreading ridges, because typical basalts from Oman are relatively enriched in SiO<sub>2</sub>, Al<sub>2</sub>O<sub>3</sub>, and K<sub>2</sub>O and depleted in TiO<sub>2</sub> for a given MgO content as consequence of formation in a fore arc of a subduction zone (e.g. MacLeod et al. 2013). The starting material used in France et al. (2010) was thus relatively enriched in SiO<sub>2</sub>, Al<sub>2</sub>O<sub>3</sub>, and K<sub>2</sub>O (54.1, 16.2, and 0.2 wt%, respectively, on an anhydrous basis); this rarely corresponds to the more primitive MORBs at Site 1256. Moreover, their starting material was fully altered (greenschist facies condition) and lacked any primary magmatic mineral, which is uncommon at Site 1256, where the roof rocks are basalts bearing either primary phases or partially- to fully-recrystallized granoblastic hornfels. Thus, a direct application of France et al. (2010) experimental results to Hole 1256D should be performed with caution.

## **C.1.4 Experimental and analytical techniques**

### ***C.1.4.1. Starting material***

Six different samples from IODP Site 1256 were used as starting material for hydrous partial melting experiments, representative of the different basaltic lithologies of the drilled section. For petrographic details, modal amounts, and texture type classification indicating the grade of contact-metamorphic overprint according to Koepke et al. (2008) see electronic supplemental material C.1.ESM). The rocks were sampled at the lower part of the sheeted dike complex, close to the AML. Two of the samples are basalts showing different grades of typical hydrothermal alteration (D10: 27 % alteration, D11: 11 %), containing low-grade hydrous alteration phases (e.g. actinolite, chlorite, secondary oxides) and preserved primary magmatic phases (plagioclase, clinopyroxene, oxides). Sample GD12 is a basalt with an initial granoblastic overprint (type 5 according to the classification of Koepke et al. 2008); GD12 is the sample with the highest grade of secondary low-grade alteration (43%). Three samples show a strong imprint of contact-metamorphism expressed by granoblastic, hornfelsic textures composed of newly-formed plagioclase, clinopyroxene, orthopyroxene, and oxides. Sample GD14 shows a "hydrous", amphibole-rich paragenesis equilibrated in the amphibolite facies, while GF36 and GF45 are "dry" two-pyroxene hornfels with amphibole only present as a secondary alteration phase in very small amounts (electronic supplemental material C.1.ESM). Two of the six samples are significantly enriched in amphibole: GD12 has 36% actinolitic amphibole as a result of hydrothermal alteration, while GD14 has 20% hornblende amphibole regarded as part of the prograde contact-metamorphism leading to the granoblastic overprint (see also microphotographs in Fig. C.1.1).

Major and trace element data of the starting materials were determined by inductively coupled plasma optical emission spectroscopy (ICP-OES) and ICP-mass spectrometry (MS), respectively, at "ACTLABS" (Activation Laboratories Ltd., Ancaster, Ontario, Canada). While the major element compositions of the starting materials vary only slightly (e.g., SiO<sub>2</sub> 48.6-51.5 wt%; Al<sub>2</sub>O<sub>3</sub> 12.1-15.0 wt%; see Table C.1.1), the trace element pattern of the whole rocks varies significantly from slightly enriched to more depleted compositions in comparison to typical N-MORB (see electronic supplemental material C.1.ESM). The starting materials with anhydrous



granoblastic textures (two-pyroxene hornfels GF36 and GF45) are strongly depleted in light rare earth elements (LREEs) displaying marked positive Sr and Eu anomalies, and negative Zr and Hf anomalies as is typical of residues from a former partial melting event (France et al. 2014).

**Table C.1.1** Starting compositions of this study and other related studies; compositions of tonalites from IODP Hole 1256D

Sample	SiO <sub>2</sub>	TiO <sub>2</sub>	Al <sub>2</sub> O <sub>3</sub>	FeO	MnO	MgO	CaO	Na <sub>2</sub> O	K <sub>2</sub> O	P <sub>2</sub> O <sub>5</sub>	Cl	Total	C (ppm)	S (ppm)	Mg#	LOI
Basalts and hornfels from the IODP 1256D drilling used as starting material in this study																
D10	52.27	1.73	12.24	13.51	0.29	7.21	9.80	2.66	0.11	0.14	0.06	100.00	767	733	51.2	2.52
D11	52.22	1.08	13.62	13.18	0.20	9.15	8.71	1.64	0.07	0.08	0.03	100.00		652	56.8	3.31
GD12	49.90	1.34	15.10	10.00	0.19	8.35	12.34	2.43	0.09	0.17	0.10	100.00	388	144	62.4	1.50
GD14	49.34	1.77	13.34	14.96	0.23	6.65	10.53	2.89	0.09	0.13	0.05	100.00	367	69	46.6	0.80
GF36	49.53	1.39	13.73	13.17	0.18	7.66	11.53	2.67	0.09	0.00	0.06	100.00		181	53.1	0.79
GF45	50.54	1.07	13.81	14.12	0.21	8.71	8.95	2.49	0.06	0.01	0.03	100.00	220	7	53.8	-0.52
Basalt used as starting material in the experimental study of France et al. (2010, 2014)																
08OL30	54.14	1.50	16.16	9.95	0.07	5.36	7.72	4.77	0.20	0.12		100.00			49.0	4.74
Basaltic rocks used as starting material in the experimental study of Beard and Lofgren (1991)																
478	52.99	1.76	15.44	11.91	0.22	5.34	9.30	2.58	0.16	0.29		100.00				0.49
466	49.87	1.19	17.90	12.59	0.26	4.78	10.99	1.98	0.15	0.30		100.00				0.21
Tonalites from the dike/gabbro transition of the IODP Hole1256D drill core																
212-1-P6	71.58	0.72	10.98	6.09	0.04	1.93	4.68	3.62	0.09	0.19	0.06	100.00			38.5	1.01
212-1-P7	71.57	0.84	11.17	6.19	0.03	1.10	4.86	3.97	0.10	0.17		100.00			24.0	2.34
214-1-P14	63.58	1.48	11.05	12.28	0.08	2.09	4.46	4.18	0.10	0.61	0.09	100.00			42.6	0.92
235-1-P1	71.17	1.00	11.08	6.36	0.04	1.11	3.78	4.97	0.12	0.32	0.07	100.00			26.4	0.98

All values in weight % (except C and S). For a better comparability all rock compositions are recalculated to a total of 100 wt%. Details of the different starting materials of this study in terms of IODP description, texture, and mineral modes can be found in Table A1 in the electronic supplementary. France et al. (2010, 2014) used an altered basalt from the Oman ophiolite. For the comparison with the experimental study of Beard and Lofgren (1991) two of their starting compositions are chosen (greenschist 478 and hornblende hornfels 466).  $Mg\# = Mg/(Mg + Fe_{total}) * 100$ ; *LOI* loss on ignition.

Tonalite analyses used for comparison with the experimental melts are from this study except 212-1P-7 which is from Teagle et al. (2006; Table T37). Original IODP descriptions of the used tonalites: 212-1-P6: 312-1256D-212R-1, 25-28cm; 212-1-P7: 312-1256D-212R-1, 29-32cm; 214-1-P14: 312-1256D-214R-1, 68-70cm; 235-1-P1: 335-1256D-235R-1, 23-26cm (expedition - hole - core - section - cm top, bottom)

#### **C.1.4.2. Felsic rocks from IODP Site 1256**

A characteristic feature of the dike/gabbro transition drilled at IODP Site 1256 is the intrusion of felsic, evolved plutonic rocks both in the gabbros and in the granoblastic hornfels. These are small, irregular patches, veins, and dikelets consisting of quartz-bearing gabbro, diorite, and tonalite with a fine- to medium-grained granular texture. Here, for the comparison with the experimental anatectic melts, we focus only on those mm to cm thick felsic, highly evolved dikelets intruding mostly granoblastic hornfels, which are interpreted as frozen melts generated by partial melting of the altered basalts from the lowermost sheeted dikes (Wilson et al. 2006; Koepke et al. 2008; France et al. 2009, 2010, 2014; Teagle et al. 2012). These rocks are characterized as fine-grained tonalites containing a granular plagioclase/quartz framework with

minor amounts of magmatic amphibole (now pervasively altered to secondary amphibole), granular Fe-Ti oxide, sometimes in association with anhedral to subhedral clinopyroxene.

**Table C.1.2** Experimental conditions

Protolith	Run#	P [MPa]	T [°C]	Duration [h] <sup>1)</sup>	H <sub>2</sub> O melt <sup>2)</sup>	aH <sub>2</sub> O <sup>3)</sup>	log fO <sub>2</sub> <sup>4)</sup>	ΔQFM <sup>5)</sup>	Phase assemblage
D10	#1	200	1030	68	4.5	1.00	-9.45	+0.9	melt, Ol, Cpx
	#6	200	1000	68	5.0	1.00	-9.47	+1.3	melt, Ol, Cpx, Mt
	#23	100	1030	72	3.7	1.00	-8.82	+1.6	melt, Ol, Cpx, Pl
	#17	100	1000	146	3.6	1.00	-9.18	+1.6	melt, Ol, Cpx, Mt, Pl
	#42	100	1000	138	0.8	0.09	-11.25	-0.4	melt, Ol, Cpx, Opx, Mt, Ilm, Pl
	#11	100	970	160	3.9	1.00	-9.90	+1.4	melt, Ol, Cpx, Mt, Ilm, Pl
	#29	100	940	120	4.7	1.00	-9.94	+1.8	melt, Cpx, Opx, Mt, Ilm, Pl
	#35/39	100	910	162	4.0	1.00	-10.87	+1.4	melt, Cpx, Mt, Ilm, Pl, Ap, Py
D11	#24	100	1030	72	4.4	1.00	-8.64	+1.7	melt, Ol, Cpx, Pl
	#18	100	1000	146	3.8	1.00	-10.36	+0.5	melt, Cpx, Opx, Mt, Pl
	#43	100	1000	138	2.0	0.44	-11.08	-0.3	melt, Cpx, Opx, Mt, Ilm, Pl
	#12	100	970	160	3.3	0.86	-10.03	+1.3	melt, Cpx, Opx, Mt, Ilm, Pl
	#30	100	940	120	3.3	0.89	-10.05	+1.7	melt, Cpx, Opx, Mt, Ilm, Pl
	#36/40	100	910	162	3.9	1.00	-10.85	+1.4	melt, Cpx, Opx, Mt, Ilm, Pl
GD12	#2	200	1030	68	4.7	1.00	-9.45	+0.9	melt, Ol, Cpx
	#7	200	1000	68	5.1	1.00	-9.47	+1.3	melt, Ol, Cpx, Mt
	#25	100	1030	72	3.5	1.00	-8.66	+1.7	melt, Ol, Cpx, Mt, Pl
	#19	100	1000	146	3.7	1.00	-10.36	+0.5	melt, Ol, Cpx, Mt, Pl
	#44	100	1000	138	2.0	0.46	-11.03	-0.2	melt, Ol, Cpx, Opx, Ilm, Pl
	#13	100	970	160	3.5	1.00	-9.91	+1.4	melt, Ol, Cpx, Mt, Ilm, Pl
	#31	100	940	120	5.0	1.00	-9.95	+1.8	melt, Cpx, Opx, Mt, Ilm, Pl, Amph, Zirc
GD14	#3	200	1030	68	4.5	1.00	-9.39	+0.9	melt, Ol, Cpx, Mt
	#26	100	1030	72	3.4	1.00	-8.66	+1.7	melt, Ol, Cpx, Mt
	#20	100	1000	146	3.1	0.82	-9.57	+1.3	melt, Ol, Cpx, Mt, Pl
	#45	100	1000	138	1.9	0.42	-10.15	+0.7	melt, Ol, Cpx, Opx, Mt, Pl
	#14	100	970	160	5.0	1.00	-9.91	+1.4	melt, Ol, Cpx, Mt, Ilm, Pl
	#32	100	940	120	3.7	1.00	-9.95	+1.8	melt, Cpx, Opx, Mt, Ilm, Pl
GF36	#4	200	1030	68	4.7	1.00	-9.39	+0.9	melt, Ol, Cpx, Mt
	#9	200	1000	68	4.9	1.00	-9.47	+1.3	melt, Ol, Cpx, Mt
	#27	100	1030	72	3.7	1.00	-8.52	+1.9	melt, Ol, Cpx, Mt, Pl
	#21	100	1000	146	3.6	1.00	-9.40	+1.4	melt, Ol, Cpx, Mt, Pl
	#15	100	970	160	3.4	0.92	-9.99	+1.3	melt, Ol, Cpx, Opx, Mt, Ilm, Pl
GF45	#5	200	1030	68	4.6	0.98	-9.40	+0.9	melt, Ol, Mt
	#10	200	1000	68	5.0	1.00	-9.47	+1.3	melt, Ol, Mt
	#28	100	1030	72	3.3	1.00	-8.52	+1.9	melt, Ol, Cpx, Pl
	#22	100	1000	146	3.6	1.00	-9.40	+1.4	melt, Ol, Cpx, Mt, Pl
	#16	100	970	160	3.5	0.95	-9.95	+1.3	melt, Cpx, Opx, Mt, Ilm, Pl

*Cpx* clinopyroxene, *Opx* orthopyroxene, *Ol* olivine, *Pl* plagioclase, *Mt* magnetite, *Ilm* ilmenite, *Ap* apatite, *Py* pyrite, *Amph* amphibole, *Zirc* zircon; <sup>1)</sup> time between reaching desired T and rapid quench; <sup>2)</sup> determination via by-difference (see text); <sup>3)</sup> calculated from the measured composition of the fluid phase after Burnham (1979); <sup>4)</sup> calculated following the procedure of Scaillet et al. (1995); <sup>5)</sup> ΔQFM indicates log fO<sub>2</sub> (experiment) - log fO<sub>2</sub> (QFM buffer) as estimated by Schwab and Küstner (1981)

Accessory minerals are always present and include apatite and zircon. The tonalites are pervasively altered which is expressed by a high amount of secondary minerals (chlorite, secondary amphibole, titanite, albite). Unfortunately, the dike/gabbro transition at Site 1256 penetrated by Expedition 312 and 335 is strongly hampered by a very low recovery, so that only a few pieces in the drilled cores exist showing tonalitic veins or dikelets. In addition, only a few

of these dikelets are big enough and show clear boundaries to the host rock, so that they could be cut by saw for producing a homogeneous piece of rock which could be analyzed accordingly with bulk techniques. Therefore, only four analyses of intrusive tonalites are available and presented in Table 1 (three new analysis presented in this study, and one of Teagle et al. 2006, Table T27). The bulk rock analyses reveal coherent results with SiO<sub>2</sub> contents varying between 64 and 72 wt%, and with MgO contents between 1.1 and 2.1 wt% (Tab. C.1.1). High amounts of P<sub>2</sub>O<sub>5</sub> (0.19 to 0.61 wt%) demonstrate the evolved character of the tonalites.

#### **C.1.4.3. Experiments**

For the experiments, the natural rocks were crushed and sieved. France et al. (2010) investigated the influence of starting material grain size on the composition of the experimental phases, and showed that the experimental products up to a grain size of 250 µm exhibit identical phase compositions. Thus, a starting material grain size of 125 to 200 µm was used here in order to obtain larger melt pools in low-temperature experiments, under virtually equilibrium conditions. Additionally, for low-temperature experiments close to the solidus we used "micro-rocks" as starting material (mm-sized fragments of the whole rocks; see Wolff et al. 2013) in order to obtain melt pools large enough for analysis. To ensure comparability among starting compositions, deionized water was added to the majority of the experiments in order to guarantee water-saturated conditions. Since all runs were performed at temperatures ≤1030°C, Au capsules were used which afforded the advantage of avoiding Fe loss to the capsule material.

To simulate conditions prevailing directly above the AML, an H<sub>2</sub>-controlled internally-heated pressure vessel (IHPV) at the Institut für Mineralogie in Hannover, Germany was used. Temperature varied from 910°C to 1030°C in steps of 30°. The vessel was pressurized with argon gas to 100 MPa. This corresponds to a lithostatic pressure found at ~2-3 km depth in oceanic crust. Even though this is slightly deeper than the environment where the samples used were obtained at the EPR, this pressure enables a direct comparison to other experimental studies (e.g., Beard and Lofgren 1991; France et al. 2010). Moreover, at lower pressure it is difficult to ensure stable conditions in the vessel, especially with regard to a defined oxygen fugacity ( $fO_2$ ). The  $fO_2$  corresponds to QFM +1 (QFM corresponds to the  $fO_2$  of the quartz-fayalite-magnetite oxygen buffer) and was set with a defined  $P_{H_2}$ , depending on the experimental temperature, controlled by a Shaw membrane (e.g., Scaillet et al. 1992). While the  $fO_2$  for primitive, dry MORB melts is suggested to be slightly below (e.g. Bézou and Humler 2005) or slightly above QFM (Cottrell and Kelly 2011), the supposed hydrothermal influence in nature and the accompanying mostly water-saturated conditions in our experiments justify this higher  $fO_2$ . A lower  $fO_2$  was simulated in one experimental series at T=1000°C where CO<sub>2</sub> was added to the fluid phase in order to lower the  $a_{H_2O}$  and, thus, the  $fO_2$  (e.g., Scaillet et al. 1995). These experiments aim to answer the question of whether extensive hydrothermal influence and, thus, water-saturated conditions are required to produce anatectic melts at the AML roof. Additionally, two experimental series were performed at higher pressure (i.e. 200 MPa) at T=1000 and 1030°C to test the pressure influence on phase stabilities (corresponding to ~ 6 km crustal depth). The pressure was monitored with a strain gauge manometer with an uncertainty of ±5 MPa. The temperature range over the sample was ± 10°C. Experimental run products (six

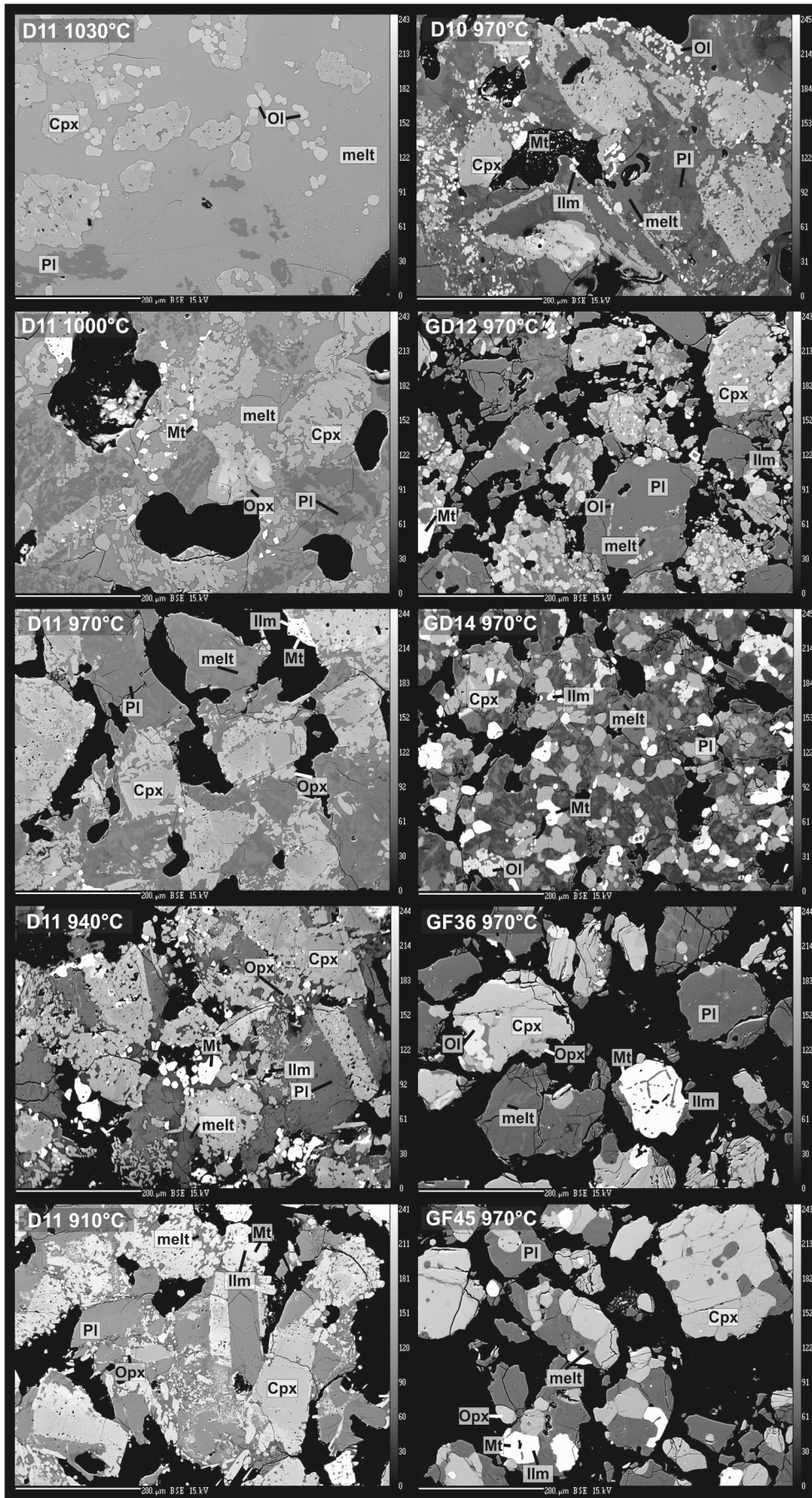


**Figure C.1.2:** Backscattered electron images of selected experimental results under water-saturated conditions. On the left, the complete temperature range (i.e. 910°C to 1030°C) of starting material D11 is shown. On the right, all different starting materials are compared for T=970°C. The scale (200 μm) is the same for each image. *Cpx* clinopyroxene, *Opx* orthopyroxene, *Pl* plagioclase, *Mt* magnetite, *Ilm* ilmenite, *Ol* olivine



capsules with the six different starting materials were run at the same time) were isobarically quenched, using a rapid quench unit. All experimental conditions are listed in Table C.1.2 and the detailed setup of the rapid-quench IHPV that was used is described in Berndt et al. (2002).

#### ***C.1.4.4. Electron-probe micro analyzer (EPMA)***

Experimental products (glass and minerals) were analyzed with the Cameca SX 100 electron microprobe in Hannover. For minerals, we used 15 kV high voltage, 15 nA beam current, 10 seconds counting time on peak and 10 seconds on background, and a focused beam. For analysis of water-bearing glasses, which is problematic due to “alkali-loss” effects (e.g., Morgan and London 2005), a special procedure was applied following Koepke et al. (2004). The beam current was set to 4 nA and the counting time varied for the different elements; 4 s for K, 8 s for Si, Al, Ti, and Fe, 10 s for Na and Zr, 12 s for Mg, 16 s for Ca, and 30 s for Ba, P, S, Cl, and Mn. Alkalis were measured first. Background counting time was always the same as peak counting time. Whenever possible, a defocused beam with a spot size of 5, 10, or 20  $\mu\text{m}$  was used, and Na loss was checked by comparing the results of measurements with different beam sizes on identical glasses of an experimental sample with larger melt pools. Standard glasses with compositions similar to the experimental glasses and with known water contents have been used for estimating water contents in experimental glasses by applying the “by-difference” method (e.g., Devine et al. 1995). Even though the uncertainties are relatively high ( $\pm 0.5\text{-}0.7$  wt% according to Parat et al. 2008), the application of the “by-difference” method controls the problem of small melt pools precluding water determination with a direct method such as infrared spectroscopy. With known melt composition and water content the  $a_{\text{H}_2\text{O}}$  was calculated following the thermodynamic model of Burnham (1979) for a given water solubility in a melt subjected to known pressure (major effect) and temperature (minor effect).

### **C.1.5. Results**

#### ***C.1.5.1. Attainment of equilibrium***

Attainment of global equilibrium in partial-melting experiments is strongly dependent on the grain size (see review of Johannes and Koepke 2001). The use of fine-grained starting material (i.e.  $\leq 10$   $\mu\text{m}$ ) enhances the chance of achieving overall equilibrium. However, in-situ analyses of newly-formed experimental phases are virtually impossible due to tiny crystals and melt pools (e.g., Koepke et al. 2003). Consequently, here we use a relatively large grain size of 125-200  $\mu\text{m}$ . As expected, in some experiments cores of unaffected starting material are still present after the experiment (e.g. clinopyroxene at D11 and  $T \leq 970^\circ\text{C}$ , Fig. C.1.2). However, longer run durations (i.e. several weeks) did not guarantee that residual mineral cores in the starting material would dissolve (e.g., Wolf and Wyllie 1994; Johannes and Koepke 2001). The partial melting experiments of Johannes and Koepke (2001) used a starting material with a grain size of  $\sim 10$   $\mu\text{m}$ ; even after 36 days, unreacted cores of the starting material were observed. Thus, the possibility of disequilibrium melting and the subsequent effect on interpretation of results should be considered. Wolff et al. (2013) addressed the potentially unsystematic effects caused by unreacted starting material cores which do not take part in the general melting reaction on both phase relations and phase compositions. Because the effect is strongest at low temperatures, this should be considered when comparing low-temperature runs with those performed at higher temperature. However, the achievement of at least local equilibrium in our experiments is

supported by several observations: (1) Compositions of newly-formed mineral phases, both as isolated crystals and as rim growth, are homogeneous within a sample, i.e., no zonation in newly-formed phases; (2) newly-formed crystals at higher temperature (e.g., olivine at  $\geq 1000^\circ\text{C}$ ) are commonly euhedral; at lower temperatures plagioclase forms sponge-like grains that are homogenous in composition and widely infiltrated by melts (e.g., D10 at  $970^\circ\text{C}$  in Fig. C.1.2); (3) all phase compositions vary systematically with temperature, and compositional trends are consistent with trends expected from the literature; and (4) melt compositions vary systematically with temperature and are homogeneous within each experiment.

Experiments close to the solidus using altered dikes as starting materials (D10 and D11) were duplicated with mm-sized pieces of the starting material in order to obtain melt pools large enough for de-focused EPMA measurements. It is obvious that the conditions of these experiments are far away from global equilibrium conditions. However, when comparing phase compositions (melt and minerals) of these experiments with those performed with a fine-grained powder under the same conditions, it can be stated that they are identical within analytical error. Such an experimental procedure has previously been shown to be suitable (Wolff et al. 2013).

### ***C.1.5.2. Phase relations***

Phase relations of the experiments are illustrated in Figure C.1.3a and highlighted with backscattered electron (BSE) images for starting material D11 at different temperatures and for all starting compositions at  $970^\circ\text{C}$  in Figure C.1.2 (see also experimental conditions in Table C.1.2). Each experiment was analyzed with ImageJ image processing and analysis software (Schneider et al. 2012) which determined solid phase and melt proportions using BSE image grey scales. In most experiments, the residual assemblage is composed of clinopyroxene + plagioclase (except for GD14 at  $T=1030^\circ\text{C}$ ) + titanomagnetite (except for D10, D11, and GF45 at  $T=1030^\circ\text{C}$ ). Ilmenite is stable in all runs at  $T \leq 970^\circ\text{C}$ . Olivine occurs only at higher temperatures (variable from  $940^\circ\text{C}$  to  $1000^\circ\text{C}$ ) and replaces orthopyroxene. Orthopyroxene and olivine only coexist in the GF36 composition at  $T=970^\circ\text{C}$ . The reaction from orthopyroxene to olivine with increasing temperature is crucial because this relation can be used for constraining the temperature of granoblastic hornfels formation, since the natural rocks are in general orthopyroxene-bearing and practically free of olivine. Olivine is present in most of our experiments at  $T \geq 970^\circ\text{C}$  except for in sample D11 (only present at  $T=1030^\circ\text{C}$ ) and for GF45 (only present at  $T \geq 1000^\circ\text{C}$ ), implying that the formation temperatures of the natural granoblastic lithologies were generally below  $1000^\circ\text{C}$ .

Although most experiments were water saturated, amphibole is absent in all experimental products. This is in contrast to Beard and Lofgren (1991) who produced strongly peraluminous water-saturated melts that coexisted with an amphibole-rich residual assemblage. Such a scenario is also observed in granoblastic rocks from the Troodos ophiolite where amphiboles occur as interstitial crystals and are interpreted to be magmatic (Gillis and Coogan 2002). However, magmatic amphiboles are not observed in granoblastic rocks from Site 1256. Moreover, the results of our study show that for the boundary conditions applied here, amphibole is not a required phase for the residue, implying that the absence of amphibole in natural granoblastic hornfels does not necessarily indicate that these rocks were formed under low  $a_{\text{H}_2\text{O}}$ . Phase relations and reactions for the starting materials that were used are formulated in

Table C.1.3 in order to emphasize the temperature at which the anhydrous granoblastic mineral assemblage could be reproduced.

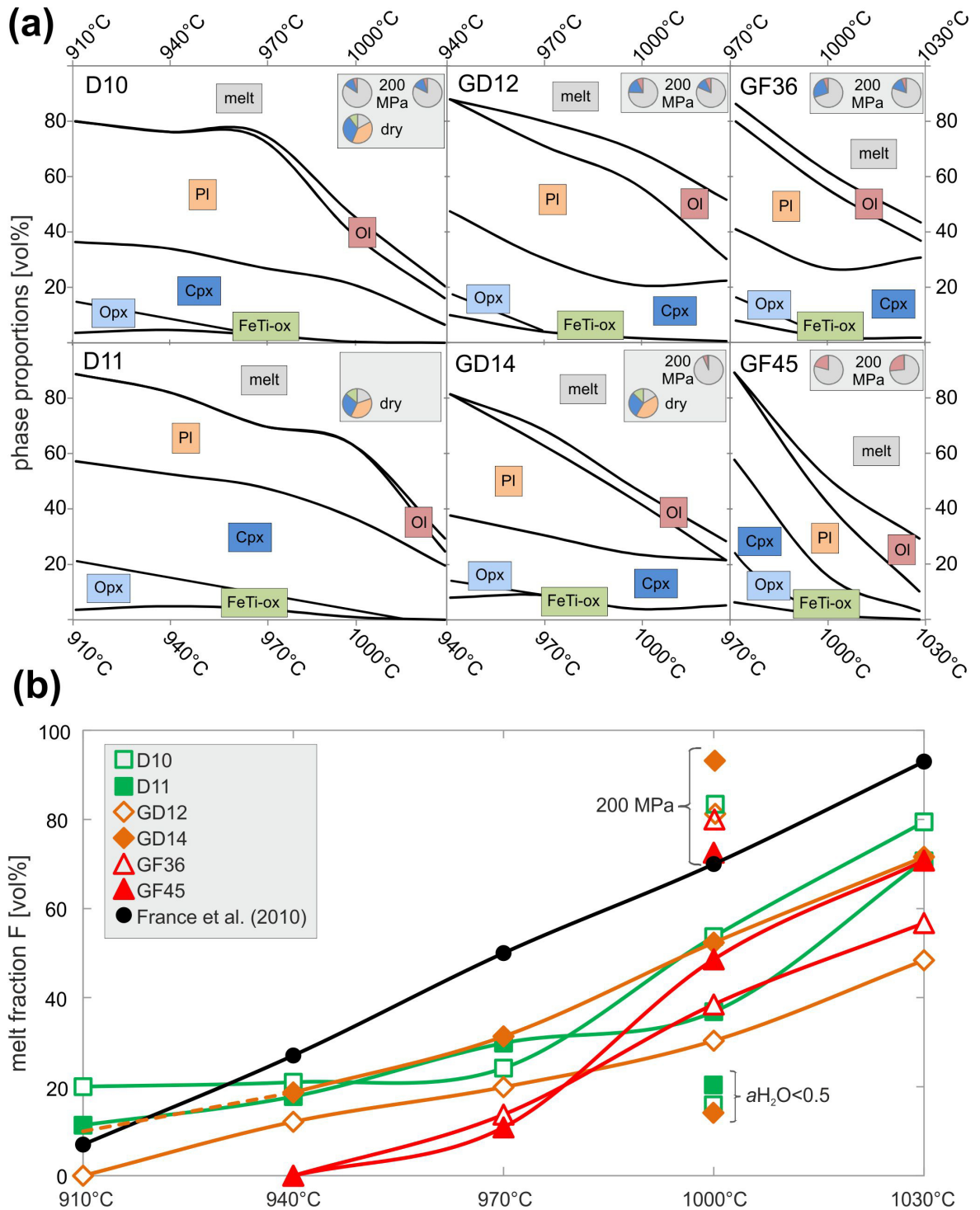


**Figure C.1.3:** **a** Phase proportions over the experimental temperature range for the different starting materials estimated by ImageJ (Schneider et al. 2012). Mineral abbreviations are the same as in Fig. C.1.2; magnetite and ilmenite are reported as FeTi-ox. In the box at the upper right of each graph the composition of experiments performed at 200 MPa and low  $a_{H_2O}$ , respectively, at the corresponding temperature are inserted as pie charts. Colors refer to the proportions of the corresponding phases indicated in the diagrams. **b** Comparison of the melt fraction (F) evolution with increasing temperature for the different starting materials. Experiments at 200MPa and low  $a_{H_2O}$ , respectively, performed at T=1000°C are highlighted. Due to a bad sample recovery phase proportions of GD12 at low  $a_{H_2O}$  could not be determined. Black data points refer to France et al.'s (2010) experiments.

**Table C.1.3** Phase relations and reactions for the different starting materials

Protolith	Temperature	Phase assemblage protolith	Phase assemblage experiment
D10	≤940°C	Cpx ( <i>I,mag</i> ) + Pl ( <i>I,mag</i> ) + Mt ( <i>I</i> ) + Chl + H <sub>2</sub> O alteration phases	Cpx ( <i>II</i> ) + Opx + Pl ( <i>II</i> ) + Mt ( <i>II</i> ) + Ilm + hydrous felsic melt
D11	≤1000°C	+ accessories + H <sub>2</sub> O	
GD12	940°C	Cpx ( <i>I,mag</i> ) + Pl ( <i>I,mag</i> ) + Mt ( <i>I</i> ) + Ilm ( <i>I</i> ) + Amph + Chl + accessories + H <sub>2</sub> O	Cpx ( <i>II</i> ) + Opx ( <i>II</i> ) + Pl ( <i>II</i> ) + Mt ( <i>II</i> ) + Ilm ( <i>II</i> ) + hydrous felsic melt
GD14		Cpx ( <i>I,gr</i> ) + Opx ( <i>I,gr</i> ) + Pl ( <i>I,gr</i> ) + Mt ( <i>I</i> ) + Ilm ( <i>I</i> ) + Amph + accessories + H <sub>2</sub> O	
GF36	970°C	Cpx ( <i>I,gr</i> ) + Opx ( <i>I,gr</i> ) + Pl ( <i>I,gr</i> )	Cpx ( <i>II</i> ) + Opx ( <i>II</i> ) + Pl ( <i>II</i> ) + Mt ( <i>II</i> ) + Ilm ( <i>II</i> ) + hydrous felsic melt
GF45		+ Mt ( <i>I</i> ) + Ilm ( <i>I</i> ) + H <sub>2</sub> O	

*Cpx* clinopyroxene, *Opx* orthopyroxene, *Pl* plagioclase, *Mt* magnetite, *Ilm* ilmenite, *Amph* amphibole, *Chl* chlorite; *mag* primary magmatic formation, *gr* formation by granoblastic overprint

Additionally, for one experimental series at T=1000°C and 100 MPa, beside water, a second fluid phase (CO<sub>2</sub>) was added in order to test the effect of lower  $a_{H_2O}$  (<0.5) on phase relations and composition. As expected, a reduced  $a_{H_2O}$  shifted the solidus temperature to significantly higher values. The phase relations and modal fractions of these experiments (~20 vol% melt, ~40 vol% plagioclase, ~30 vol% pyroxenes, ~10 vol% Fe-Ti oxides; Fig. C.1.3a) are very similar to the corresponding runs performed under water saturation at T=940°C. Hence, runs with “dry” granoblastic hornfels as starting material (GF36, GF45) are below the solidus under a reduced  $a_{H_2O}$ . Crystallization of Fe-Ti oxides proceeds at significantly higher temperatures in water-undersaturated experiments compared to the corresponding experiments at water saturation, which is probably due to the more reduced redox conditions at lower  $a_{H_2O}$  (e.g., Berndt et al. 2005) which destabilizes Fe-Ti oxides.

In addition to the 100 MPa experiments, two runs (T=1000°C and 1030°C) were performed at 200 MPa and water-saturated conditions in order to study the influence of pressure on phase assemblages. Pressure is expected to influence phase relations because fluid and water solubilities are strongly dependent on pressure (e.g., Holtz et al. 1992, 2001; Berndt et al. 2002). Previous crystallization experiments have shown that the main pressure effect is the shift of plagioclase saturation to lower temperatures (e.g., Feig et al. 2006). Accordingly, plagioclase crystallization was suppressed in runs performed at 200 MPa, while remaining stable in all comparable experiments at 100 MPa (Fig. C.1.3a). The 200 MPa pressure (equivalent to ~6 km depth) represents an unrealistic depth for the AML roof at the fast-spreading EPR, but may be suitable for slower spreading-rates (e.g. 5-7 km depth at the Mid-Atlantic Ridge; Wilson et al. 2006; McCaig and Harris 2012). Thus, experiments at higher pressure provide important preliminary data on the phases occurring in this geological setting, where coupled magmatic–hydrothermal interactions have already been recognized (McCaig and Harris 2012).



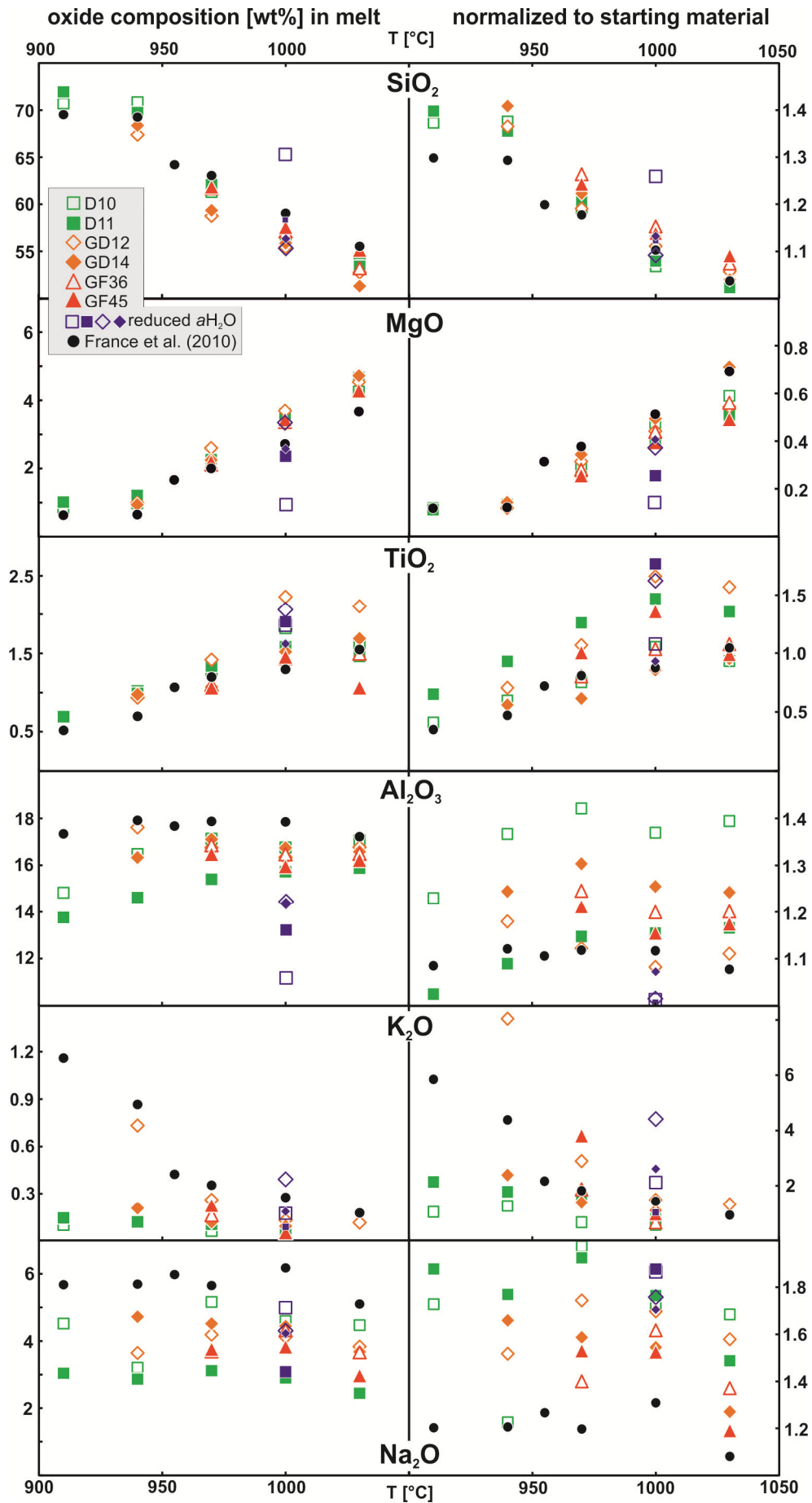


**Figure C.1.4:** (see previous page) Compositional evolution of experimental melts of different starting materials in wt% as a function of temperature (*left column*). The compositional evolution of the starting material was normalized in order to remove the influence of varying starting material composition (*right column*). Experiments performed at low aH<sub>2</sub>O are highlighted with blue data points. Black data points refer to France et al.'s (2010) experiments.

### **C.1.5.3. Composition of the anatectic melts**

The degree of partial melting (melt fraction  $F$ ; see Figure C.1.3b) is, as expected, strongly temperature dependent but also varies significantly with the starting material. The first melts of D10 and D11, analyzable by EPMA, occur at  $T=910^{\circ}\text{C}$  ( $F \approx 10\text{-}20$  vol%). First melts of GD12 and GD14 occur at  $T=940^{\circ}\text{C}$  ( $F \approx 10\text{-}20$  vol%), and of GF36 and GF45 at  $T=970^{\circ}\text{C}$  ( $F \approx 10$  vol%). This trend is in agreement with the increasingly refractory character of the starting material, varying from altered sheeted dikes (D10, D11) to partially re-crystallized (GD12, GD14) to fully re-crystallized granoblastic hornfels (GF36, GF45). The first melts of D10 and D11 are high in SiO<sub>2</sub> contents at 70.7 and 72.0 wt%, respectively. The first GD12 and GD14 melts = 67.4 and 68.4 wt% SiO<sub>2</sub>, respectively, while GF36 and GF45 are less evolved (61.7 and 61.9 wt% SiO<sub>2</sub>, respectively; Fig. C.1.4, left column). Melt compositional evolution with increasing melt fraction and temperature is consistent for all starting materials and follows the expected trend (i.e. towards the bulk rock composition; Fig. C.1.4 and Tab. C.1.4).

In order to better track the effect of the different protoliths on the extent of enrichment or depletion with regard to the different elements at different melting degrees (or temperatures), all melt compositions were normalized to the starting material composition (Fig. C.1.4, right column). These plots show that the degree of enrichment or depletion of a specific element in the melt is distinctly different depending on the protolith. A strong discrepancy between the different protoliths, even within the same lithological subtype (D10 compared to D11 and GD12 compared to GD14), is distinctive for Al<sub>2</sub>O<sub>3</sub> and the alkalis, which are mainly controlled by plagioclase crystallization (present in all experiments at 100 MPa except for GD14 at  $T=1030^{\circ}\text{C}$ ). With respect to Al<sub>2</sub>O<sub>3</sub>, starting material D11 is characterized by an increase with increasing temperature, while GD12, GF36, and GF45 decrease. D10 and GD14 increase initially up to  $T=970^{\circ}\text{C}$  followed by a slight decrease at higher temperature. Al<sub>2</sub>O<sub>3</sub> in D11 is  $\sim 2.0$  wt% lower at  $T \leq 970^{\circ}\text{C}$  than are all other compositions, resulting in a weak enrichment when normalized to the starting material, while D10 is strongly enriched (Fig. C.1.4). K<sub>2</sub>O is generally low in all experiments due to low concentrations in the protolith. However, the behavior for varying degrees of melting is significantly different. Although the K<sub>2</sub>O content is relatively constant for the anatectic melts of the altered basalts D10 and D11, anatectic melts of GD12 and one “dry” granoblastic hornfels (GF45) are strongly enriched with initial melting; this is clearly shown when normalized to the starting material (Fig. C.1.4). In contrast, Na<sub>2</sub>O is only subtly lowered with increasing temperature within individual samples even though the variation between the different protoliths is significant (Fig. C.1.4). Moreover, the normalized starting material diagram for Na<sub>2</sub>O reveals the challenge of achieving global equilibrium in partial melting experiments. The normalized value of sample D10 at  $T=940^{\circ}\text{C}$  is far from the trend, suggesting that in this experiment the number of relict phases is particularly high. However, as this is the only obvious outlier, it can be assumed that, although present, relict phases in other experiments have less influence over the chemical composition of the melt.

**Table C.1.4** Composition of the experimental melt obtained from the different starting materials

Protolith	P [Mpa]	T [°C]	SiO <sub>2</sub>	TiO <sub>2</sub>	Al <sub>2</sub> O <sub>3</sub>	FeO	MnO	MgO	CaO	Na <sub>2</sub> O	K <sub>2</sub> O	P <sub>2</sub> O <sub>5</sub>	Cl	Total	n	Mg#		
D10	200	1030	melt	53.86	2.13	13.20	13.18	0.31	5.10	9.09	2.79	0.10	0.18	0.08	100.00	13	44.0	
		±	0.47	0.07	0.29	0.50	0.02	0.17	0.28	0.13	0.01	0.01	0.00				2.0	
		1000	melt	53.31	2.14	13.12	13.62	0.32	4.97	9.31	2.86	0.09	0.18	0.07	100.00	10	42.4	
		±	0.47	0.07	0.35	0.48	0.02	0.13	0.25	0.18	0.01	0.01	0.00				1.5	
		1030	melt	53.72	1.61	17.06	9.71	0.18	4.26	8.79	4.47	b.d.	0.12	0.07	100.00	5	47.3	
		±	0.39	0.09	0.43	0.51	0.02	0.13	0.29	0.12			0.02	0.01				1.6
	100	1000	melt	55.77	1.82	16.75	9.46	0.20	3.44	7.62	4.60	0.06	0.18	0.10	100.00	5	43.3	
		±	0.31	0.10	0.22	0.15	0.02	0.12	0.16	0.09	0.01	0.01	0.01				0.7	
		1000	melt	65.71	1.88	11.30	9.92	0.14	1.02	3.33	4.98	0.23	0.99	0.49	100.00	9	17.8	
		dry	±	0.69	0.30	0.34	0.48	0.03	0.05	0.21	0.48	0.04	0.14	0.09				0.6
		970	melt	61.25	1.28	17.11	7.17	0.17	2.11	5.23	5.16	0.07	0.29	0.16	100.00	10	37.8	
		±	0.59	0.08	0.29	0.43	0.01	0.10	0.18	0.25	0.02	0.02	0.01				1.4	
940	940	melt	70.93	1.02	16.49	3.42	0.12	0.98	3.00	3.21	0.13	0.34	0.35	100.00	5	39.9		
	±	0.59	0.12	0.39	0.60	0.03	0.29	0.24	0.44	0.02	0.03	0.06				3.0		
	910	melt	70.71	0.70	14.83	4.18	0.09	0.85	3.68	4.52	0.11	0.13	0.20	100.00	12	29.3		
	±	0.37	0.06	0.40	0.29	0.01	0.09	0.19	0.36	0.02	0.02	0.01				1.2		
	1030	melt	53.42	1.46	15.88	11.75	0.23	4.67	10.00	2.44	b.d.	0.12	0.03	100.00	5	43.8		
	±	0.34	0.10	0.40	0.59	0.01	0.27	0.35	0.06			0.00	0.00				2.1	
D11	1000	1000	melt	56.31	1.58	15.70	10.99	0.22	3.61	8.36	2.90	0.07	0.21	0.04	100.00	5	39.6	
		±	0.44	0.05	0.45	0.39	0.01	0.07	0.16	0.24	0.01	0.02	0.00				0.8	
		1000	melt	58.90	1.93	13.32	12.04	0.21	2.39	7.50	3.08	0.11	0.41	0.10	100.00	3	28.8	
		dry	±	0.41	0.03	0.30	0.26	0.01	0.11	0.14	0.14	0.02	0.05	0.00				0.9
		970	melt	62.09	1.34	15.40	8.57	0.17	2.26	6.54	3.12	0.11	0.33	0.07	100.00	5	34.8	
		±	0.32	0.03	0.34	0.32	0.00	0.09	0.11	0.34	0.02	0.03	0.00				1.1	
	940	940	melt	69.76	0.99	14.62	4.66	0.11	1.21	5.21	2.87	0.13	0.32	0.11	100.00	8	35.7	
		±	0.74	0.04	0.41	0.43	0.02	0.35	0.39	0.17	0.03	0.03	0.01				2.5	
		910	melt	71.95	0.69	13.76	4.51	0.11	1.02	4.53	3.04	0.15	0.16	0.09	100.00	18	31.2	
		±	1.05	0.04	0.43	0.36	0.03	0.39	0.59	0.49	0.03	0.02	0.03				2.8	
		1030	melt	50.70	1.64	17.21	9.29	0.20	6.28	11.64	2.67	0.09	0.16	0.12	100.00	13	58.3	
		±	0.42	0.07	0.31	0.49	0.02	0.12	0.19	0.18	0.01	0.02	0.00				1.8	
GD12	200	1000	melt	50.27	1.71	18.12	9.65	0.21	5.49	11.14	3.01	0.11	0.15	0.13	100.00	10	54.0	
		±	0.43	0.07	0.33	0.39	0.02	0.11	0.23	0.18	0.02	0.02	0.00				1.5	
		1030	melt	52.75	2.10	16.77	9.78	0.21	4.54	9.51	3.83	0.12	0.22	0.16	100.00	5	50.0	
		±	0.53	0.08	0.25	0.48	0.02	0.27	0.16	0.07	0.03	0.02	0.01				2.1	
		1000	melt	55.43	2.23	16.34	9.26	0.21	3.70	7.98	4.12	0.14	0.35	0.24	100.00	5	46.9	
		±	0.52	0.04	0.16	0.28	0.01	0.13	0.24	0.16	0.02	0.02	0.00				1.3	
	100	1000	melt	54.91	2.16	14.41	10.96	0.25	3.29	7.43	4.33	0.43	0.99	0.83	100.00	3	38.8	
		dry	±	0.09	0.05	0.25	0.10	0.02	0.03	0.14	0.09	0.05	0.03	0.00				0.5
		970	melt	58.76	1.42	16.75	8.08	0.18	2.60	6.71	4.19	0.27	0.62	0.42	100.00	5	39.9	
		±	0.58	0.14	0.75	0.61	0.02	0.05	0.42	0.32	0.01	0.07	0.05				1.7	
		940	melt	67.39	0.94	17.61	3.05	0.11	0.99	4.24	3.64	0.74	0.38	0.91	100.00	8	43.2	
		±	1.63	0.16	0.93	0.75	0.04	0.54	1.00	1.01	0.10	0.06	0.16				3.8	
GD14	200	1030	melt	50.59	1.92	13.93	13.74	0.24	5.93	10.72	2.76	b.d.	0.14	0.04	100.00	13	46.3	
		±	0.39	0.09	0.23	0.49	0.02	0.14	0.19	0.18		0.02	0.00				1.5	
		1030	melt	51.31	1.69	16.58	11.66	0.25	4.72	9.90	3.68	b.d.	0.18	0.04	100.00	5	44.8	
		±	0.25	0.09	0.22	0.30	0.02	0.09	0.11	0.18			0.03	0.00				0.8
		1000	melt	55.87	1.52	16.74	9.79	0.22	3.29	7.72	4.44	0.10	0.25	0.06	100.00	5	40.4	
		±	0.27	0.08	0.16	0.50	0.02	0.09	0.15	0.20	0.03	0.03	0.00				1.1	
	100	1000	melt	56.57	1.64	14.27	12.07	0.24	2.70	6.57	4.47	0.24	0.92	0.29	100.00	3	30.7	
		dry	±	0.40	0.06	0.11	0.12	0.03	0.13	0.24	0.05	0.02	0.03	0.01				0.7
		970	melt	59.36	1.07	17.11	8.58	0.21	2.25	6.12	4.52	0.13	0.53	0.13	100.00	10	33.9	
		±	0.53	0.04	0.30	0.49	0.01	0.44	0.12	0.27	0.02	0.02	0.00				3.1	
		940	melt	68.37	0.98	16.33	4.17	0.13	0.94	3.60	4.72	0.22	0.31	0.22	100.00	5	32.9	
		±	0.38	0.03	0.06	0.54	0.01	0.17	0.09	0.51	0.03	0.03	0.01				2.5	
GF36	200	1030	melt	51.06	1.72	14.95	11.92	0.16	6.15	10.96	3.00	b.d.	0.00	0.08	100.00	13	51.0	
		±	0.71	0.09	0.34	0.56	0.02	0.16	0.27	0.14		0.00	0.01				1.9	
		1000	melt	50.63	1.67	16.34	11.98	0.16	5.18	10.46	3.50	b.d.	b.d.	0.08	100.00	10	46.5	
		±	0.29	0.09	0.18	0.24	0.02	0.10	0.15	0.12			0.00	0.00				0.8
		1030	melt	53.19	1.50	16.49	11.16	0.17	4.30	9.48	3.66	b.d.	b.d.	0.06	100.00	5	43.4	
		±	0.40	0.05	0.10	0.41	0.02	0.16	0.21	0.42			0.00	0.00				1.7
	100	1000	melt	57.05	1.44	16.46	9.46	0.17	3.37	7.54	4.32	0.06	0.05	0.08	100.00	5	41.8	
		±	0.41	0.09	0.32	0.37	0.01	0.08	0.17	0.30	0.01	0.01	0.00				1.0	
		970	melt	61.69	1.10	16.85	7.82	0.15	2.12	5.95	3.68	0.17	0.21	0.24	100.00	6	35.1	
		±	0.41	0.06	0.64	0.50	0.01	0.08	0.32	0.42	0.01	0.01	0.01				1.5	
		1030	melt	53.92	1.30	15.34	12.20	0.22	5.72	8.55	2.71	b.d.	b.d.	0.03	100.00	13	47.5	
		±	0.39	0.06	0.26	0.40	0.02	0.12	0.17	0.16			0.01	0.00				1.5
GF45	200	1000	melt	54.36	1.37	16.12	11.32	0.22	4.49	9.09	3.01	b.d.	b.d.	0.03	100.00	10	43.7	
		±	0.34	0.05	0.27	0.26	0.02	0.11	0.20	0.15			0.00	0.00				1.1
		1030	melt	55.13	1.06	16.22	10.78	0.21	4.28	9.31	2.97	b.d.	b.d.	0.04	100.00	5	43.2	
		±	0.47	0.06	0.24	0.62	0.01	0.14	0.14	0.16			0.00	0.00				1.8
		1000	melt	57.50	1.46	15.94	9.98	0.19	3.44	7.55	3.82	0.06	b.d.	0.05	100.00	5	40.9	
		±	0.23	0.06	0.25	0.44	0.02	0.16	0.20	0.08	0.02		0.00	0.00				1.4
	970	970	melt	61.86	1.06	16.47	7.98	0.13	2.19	5.83	3.76	0.23	0.27	0.21	100.00	5	35.3	
		±	0.19	0.05	0.23	0.23	0.02	0.11	0.15	0.17	0.01	0.03	0.01				1.0	

n number of analyses; Mg# = Mg/(Mg + Fe<sub>total</sub>)\*100

TiO<sub>2</sub> and FeO in the melt are strongly affected by a decrease in magnetite and ilmenite crystallization with increasing temperature. TiO<sub>2</sub> exhibits relatively constant increases up to T=1000°C where the highest content can be observed, followed by a slight decrease at higher temperature (Fig. C.1.4). This peak is due to the absence of ilmenite at T ≥ 1000°C. P<sub>2</sub>O<sub>5</sub> contents in the melt (see Fig. C.1.7c in the Discussion) are generally below 0.4 wt% except for GD12 and

GD14 at  $T=970^{\circ}\text{C}$  where an increase of up to 0.62 wt% is observed. Cl content in the melt (see Fig. C.1.7d), which can be used as a tracer for sea water contamination due to hydrothermal circulation, is strongly dependent upon the Cl contents of the starting material (1000 ppm for GD12, 300-600 ppm for all others, Tab. C.1.1) and is accordingly highest in the first melt using the GD12 starting material, reaching 0.91 wt% in the run performed at  $T=940^{\circ}\text{C}$  (for a detailed description and illustration of Cl and  $\text{P}_2\text{O}_5$  see section C.1.6.3).

Experiments at  $T=1000^{\circ}\text{C}$  with water-undersaturated samples (i.e.  $\sim 0.8$  wt%  $\text{H}_2\text{O}$ ,  $a_{\text{H}_2\text{O}} \sim 0.1$  for D10;  $\sim 2.0$  wt%  $\text{H}_2\text{O}$ ,  $a_{\text{H}_2\text{O}} \sim 0.45$  for D11, GD12, and GD14) at 100 MPa correspond in terms of melt fraction and mineral proportions to those performed at  $T=940^{\circ}\text{C}$  at water saturation (Fig. C.1.3). Thus, GF36 and GF45 are below the solidus. D10 contains 65.7 wt%  $\text{SiO}_2$  at  $a_{\text{H}_2\text{O}} \sim 0.1$ , while  $\text{SiO}_2$  is minor enriched at  $a_{\text{H}_2\text{O}} \sim 0.45$  (54.9 to 58.9 wt%, Fig. C.1.4). Consequently, the lowest MgO value (1.0 wt%) is observed in D10.  $\text{Al}_2\text{O}_3$  is distinctively lower at reduced  $a_{\text{H}_2\text{O}}$  resulting in contents from 11.3 to 14.4 wt%, in each case close to the starting material composition (Fig. C.1.4). As already observed for water saturated condition, GD12 experimental melts show the strongest increase in  $\text{K}_2\text{O}$ . The FeO content at water-undersaturated conditions is notably higher, resulting in a potentially higher degree of Fe-oxide crystallization (e.g., magnetite) at lower temperature, while  $\text{TiO}_2$  is only slightly affected by reduced  $a_{\text{H}_2\text{O}}$  and, thus, more reducing conditions (Fig. C.1.4).  $\text{P}_2\text{O}_5$  (0.4 to 1.0 wt%) and Cl (0.1 to 0.8 wt%) are higher in all water-undersaturated experiments than in water-saturated experiments (see Fig. C.1.7).

200 MPa experiments (at  $T=1000$  and  $1030^{\circ}\text{C}$ ) display a high melt fraction (from 70 to 94 vol%) triggered by the higher water content (4.5 to 5.1 wt%) in the melt at higher pressure (Berndt et al. 2002). This results in a melt composition similar to that of the starting material.  $\text{SiO}_2$  contents do not exceed 54.4 wt% and the  $\text{Al}_2\text{O}_3$  content is too low to crystallize plagioclase (Table C.1.4).

#### ***C.1.5.4. Compositions of newly-formed mineral phases***

The average mineral compositions of the starting materials and the corresponding experiments are presented in Table C.1.4. In most experiments, at low temperature and correspondingly low melt fraction, the assemblages and the compositions of the newly-formed minerals correspond to those of the natural granoblastic hornfels from the IODP Site 1256 or the Oman ophiolite dike/gabbro transition (e.g., Koepke et al. 2008; Alt et al. 2010; France et al. 2010; Zhang et al. 2014). At higher temperature and higher melt fraction, orthopyroxene is often replaced by minor amounts of olivine, which is not present in natural granoblastic hornfels. Because olivine is absent in all starting materials it is always newly formed. It is stable at  $T \geq 970^{\circ}\text{C}$ , except for starting material GF45 ( $\geq 1000^{\circ}\text{C}$ ) and D11 (only at  $1030^{\circ}\text{C}$ ) and mostly forms euhedral crystals (see BSE images in Fig. C.1.2). Olivine compositions changes with increasing temperature from  $\text{Fo}_{61.2}$  (GD14 at  $970^{\circ}\text{C}$ ) to  $\text{Fo}_{76.8}$  (GD12 at  $1030^{\circ}\text{C}$ ). All other olivine-bearing experiments fall within this range.

Newly formed clinopyroxenes are present in all experiments at 100 MPa both at the rim of residual protolith clinopyroxenes and as isolated euhedral crystals (see BSE images in Fig. C.1.2) Compositions are always homogeneous within individual experimental runs. The application of the Al-in-clinopyroxene thermometer of France et al. (2010), which was calibrated in a comparable system, reveals good agreement with the experimental temperature. While  $\text{TiO}_2$

is in a narrow range within all experiments using one starting material (Fig. C.1.5),  $\text{Al}_2\text{O}_3$  and Mg# ( $\text{Mg}\# = \text{Mg}/(\text{Mg}+\text{Fe}_{\text{total}})*100$ ) continuously increase with temperature from  $\text{Al}_2\text{O}_3 = 1.35$  wt% and  $\text{Mg}\# = 65$  (D10 at 910°C) to  $\text{Al}_2\text{O}_3 = 3.19$  wt% and  $\text{Mg}\# = 87$  (D10 at 1030°C). Clinopyroxene compositions of all other experiments fall within this range. Orthopyroxene typically grows at the rim of clinopyroxene relics and only rarely forms euhedral crystals. Mg# (62.3 to 70.0),  $\text{Al}_2\text{O}_3$  (0.90 to 1.45 wt%),  $\text{TiO}_2$  (0.25 to 0.34 wt%), and CaO (1.71 to 2.21 wt%) increase systematically with temperature, best demonstrated by sample D11, where orthopyroxene is stable over the widest temperature range (i.e. from 910°C to 1000°C).

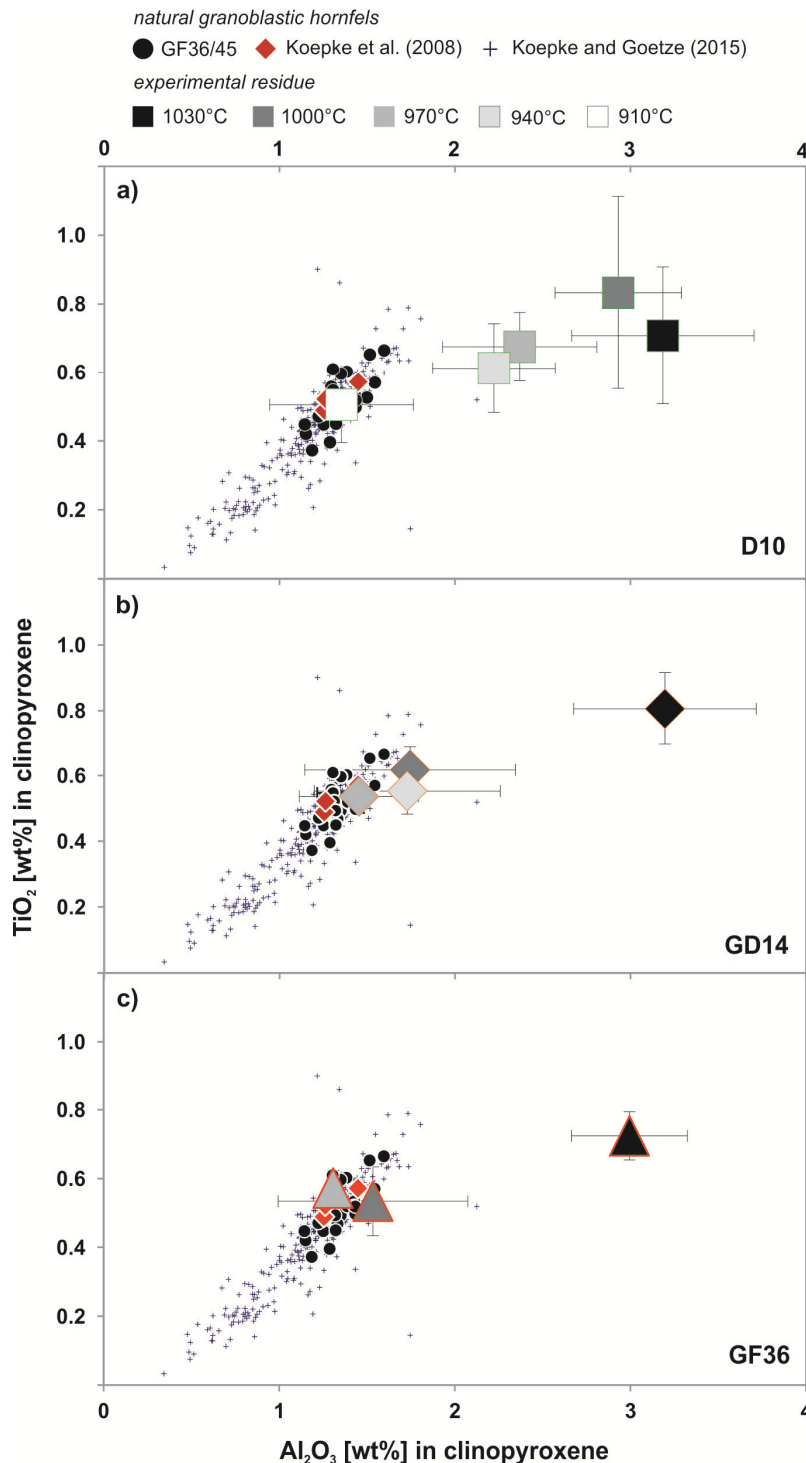
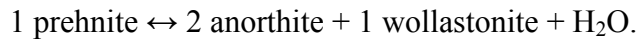


**Figure C.1.5:** Clinopyroxene compositions as a function of  $\text{TiO}_2$  and  $\text{Al}_2\text{O}_3$ . Shown are the average residual clinopyroxene compositions from experiments with starting materials D10 (a), GD14 (b), and GF36 (c) with a comparison to the clinopyroxene composition of natural “dry” (i.e. amphibole-free) granoblastic hornfels from IODP Site 1256. For this comparison, clinopyroxene compositions of “dry” granoblastic hornfels from this study (GF36 and GF45; black dots) are shown, as well as those measured by Koepke et al. (2008) and Koepke and Goetze (2015). Error bars represent the standard deviation of the single measurements.

Plagioclase is present in all 100 MPa experiments (except for GD14 at T=1030°C). It occurs either as euhedral crystals or as rim overgrowths around relic cores. The Anorthite (An) content (in mol%) varies systematically with temperature with an average increase of <2 %/10°C for D11 and up to ~5 %/10°C for GF36 and GF45. An contents vary up to 20 mol% between the different protolith compositions at the same temperature (Fig. C.1.6). The FeO<sub>total</sub> content of plagioclase increases with temperature coinciding with the increase of FeO<sub>t</sub> in the melt, up to 1.39 wt% (D10 at 1000°C). In D10 and D11 metastable An was observed. As previously proposed by France et al. (2010) this phase may form during the breakdown of prehnite, which is present as an alteration phase in the starting material, following the reaction:



Titanomagnetite is present in all experimental runs up to T=1000°C and, additionally, in GD12, GD14, and GF36 at T=1030°C. TiO<sub>2</sub> content varies between 9.09 wt% (GF36) and 16.52 wt% (D10). Ilmenite is only present in experiments up to T=970°C; its Al<sub>2</sub>O<sub>3</sub> content is generally relatively low (≤0.5 wt%, except for D11 at T=910°C), while MgO uniformly increases with temperature (from 2.79 to 4.99 wt%).

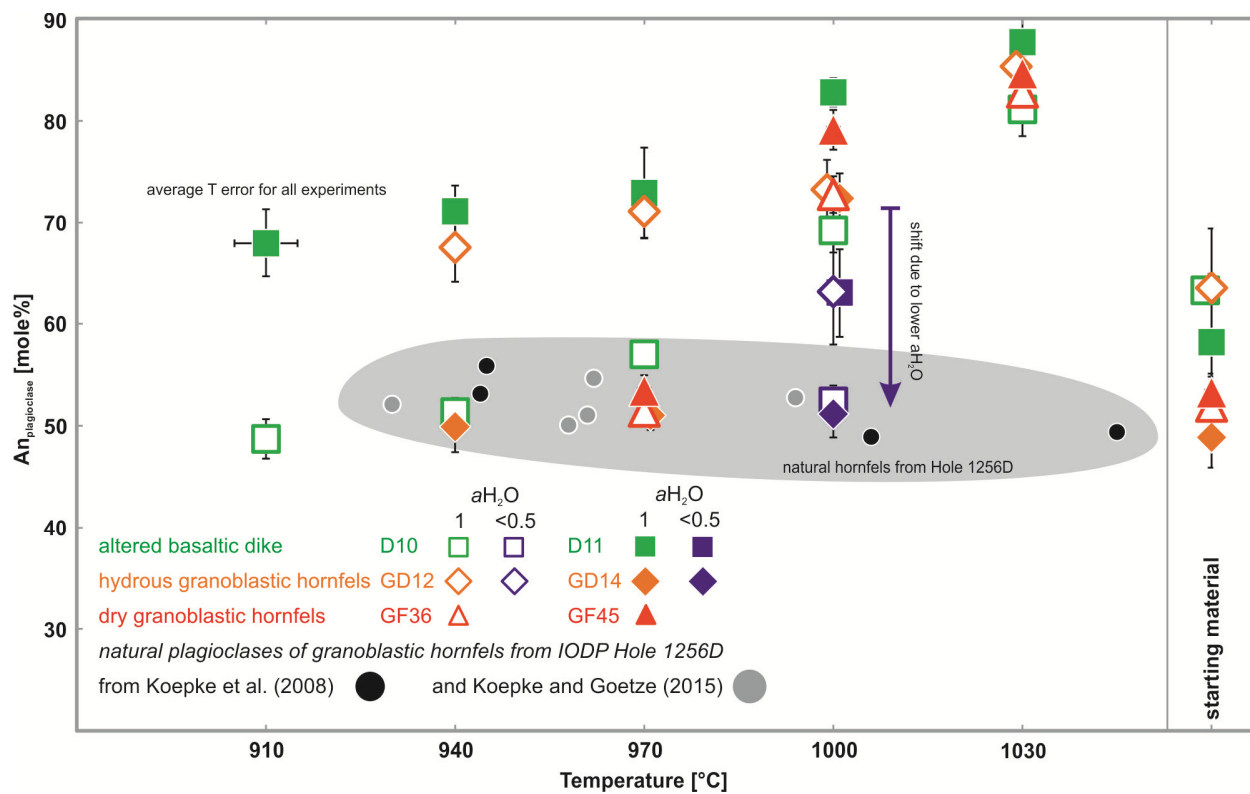


**Figure C.1.6.:** An content of plagioclase as a function of temperature. Shown are the average plagioclase composition of the different starting materials and the average composition of newly-formed plagioclases from the experiments. Blue data points highlight experimental plagioclases formed under reduced  $a_{\text{H}_2\text{O}}$  ( $a_{\text{H}_2\text{O}}=0.1$  for D10,  $a_{\text{H}_2\text{O}}\sim 0.5$  for the others). Note that the plagioclases of the starting material from D10, D11, and GD12 correspond to the primary magmatic plagioclase while those from GD14, GF36, and GF45 are of the metamorphic granoblastic assemblage. The grey field corresponds to natural plagioclases of granoblastic hornfels from IODP Site 1256. The temperatures were obtained by Koepke et al. (2008) and Koepke and Goetze (2015) by applying the two-pyroxene geothermometer in the corresponding natural rocks.

Elevated pressure (i.e. 200 MPa) has only a minor effect on the composition of the crystallized phases when compared to experiments at the same temperature at 100 MPa. Lower  $a_{\text{H}_2\text{O}}$  (<0.5) influences the chemistry of crystallized phases; this is mainly due to the change to more reducing conditions. Olivine equilibrates at higher FeO contents (from +6 to +16 wt%), and, thus, to lower Mg# (down to 24 units lower). FeO in clinopyroxene and, in particular, orthopyroxene is also enriched (up to 11 wt% higher) compared to all other experiments at  $a_{\text{H}_2\text{O}} = 1$ , while plagioclase compositions transform to more evolved compositions that correspond to experiments performed at lower temperatures under water-saturated conditions. The  $\text{Fe}^{2+}/\Sigma\text{Fe}$ -ratio calculated for oxides is lower at water-saturated conditions (e.g., for D10:  $\text{Fe}^{2+}/\Sigma\text{Fe} = 0.8\text{-}0.9$  at  $a_{\text{H}_2\text{O}} \sim 0.1$ , and  $\text{Fe}^{2+}/\Sigma\text{Fe} = 0.5$  at  $a_{\text{H}_2\text{O}} = 1$ ).

## C.1.6. Discussion

### C.1.6.1. Influence of the starting material composition on anatectic products

One of the main objectives of the present study was to evaluate the influence of the starting material composition (modal and chemical) on the modal and chemical composition of experimental results. Our results will be compared hereafter to France et al. (2010), who examined partial melting effects of a fully altered dike from the Oman ophiolite, and to selected experiments of Beard and Lofgren (1991), who studied the anatexis of greenschist and hornblende hornfels at 100 MPa. As a whole, anatectic melts produced in the present study display lower  $\text{SiO}_2$  concentrations than melts produced at similar temperatures by Beard and Lofgren (1991) (Fig. C.1.7). This is probably related to the more primitive and less altered character of our starting material. However, this discrepancy with our experimental melts is limited to higher temperature (or high partial melting degree). It is less pronounced for Beard and Lofgren's (1991) first dry anatectic melts at lower temperature (i.e.  $\leq 970^\circ\text{C}$ ), whereas their low temperature wet partial melts remain at relatively low  $\text{SiO}_2$ . This is due to a distinctively higher melt fraction with added water (+10 to 15 vol% at  $T=950^\circ\text{C}$ ). However, in experiments with low melt fraction at temperatures close to the solidus ( $\sim 900^\circ\text{C}$ ) all anatectic melts (wet and dry) of Beard and Lofgren (1991), France et al. (2010), and altered basalts from this study (D10, D11) exhibit  $\text{SiO}_2$  contents in a similar range ( $\sim 70$  to 75 wt%).

The alteration of protoliths mainly influences the melt composition for minor elements that are particularly sensitive to hydrothermal alteration (e.g., K, Cl). As an example, the observed enrichment in  $\text{K}_2\text{O}$  is highly sensitive to the  $\text{K}_2\text{O}$  content of the starting material. Anatectic melts are generally  $\text{K}_2\text{O}$ -poor in our results (starting material  $\text{K}_2\text{O} \sim 0.1$  wt%), and strongly enriched in France et al. (2010) and Beard and Lofgren (1991); i.e., starting material  $\text{K}_2\text{O}=0.20$  and 0.16 wt%, respectively.  $\text{K}_2\text{O}$  can be enriched in the starting material due to alteration by seawater circulation, which is in agreement with the fully altered character of the France et al. (2010) starting material and the amphibole rich/pyroxene poor starting materials of Beard and Lofgren (1991).

Although  $\text{K}_2\text{O}$  in protolith GD12 (0.09 wt%) is similar to that in the other starting materials used it is significantly enriched in the first melts. That is not the case for the five other samples used in this study (Fig. C.1.7b) which also include potentially different melt fractions. Despite low  $\text{K}_2\text{O}$  in the protolith, GD12 generally shows the strongest alteration imprint. This is expressed by

the substitution of clinopyroxene for secondary amphibole. GD12 also shows the highest Cl concentration in the protolith (0.10 wt%), potentially caused by rock/seawater interaction during hydrothermal alteration with the consequence that Cl contents of the anatectic melts leads to the most pronounced enrichment trend (Fig. C.1.7d). The same effect is obvious for phosphorous, where the protolith with the highest  $P_2O_5$  (GD12) shows the strongest enrichment in the experimental

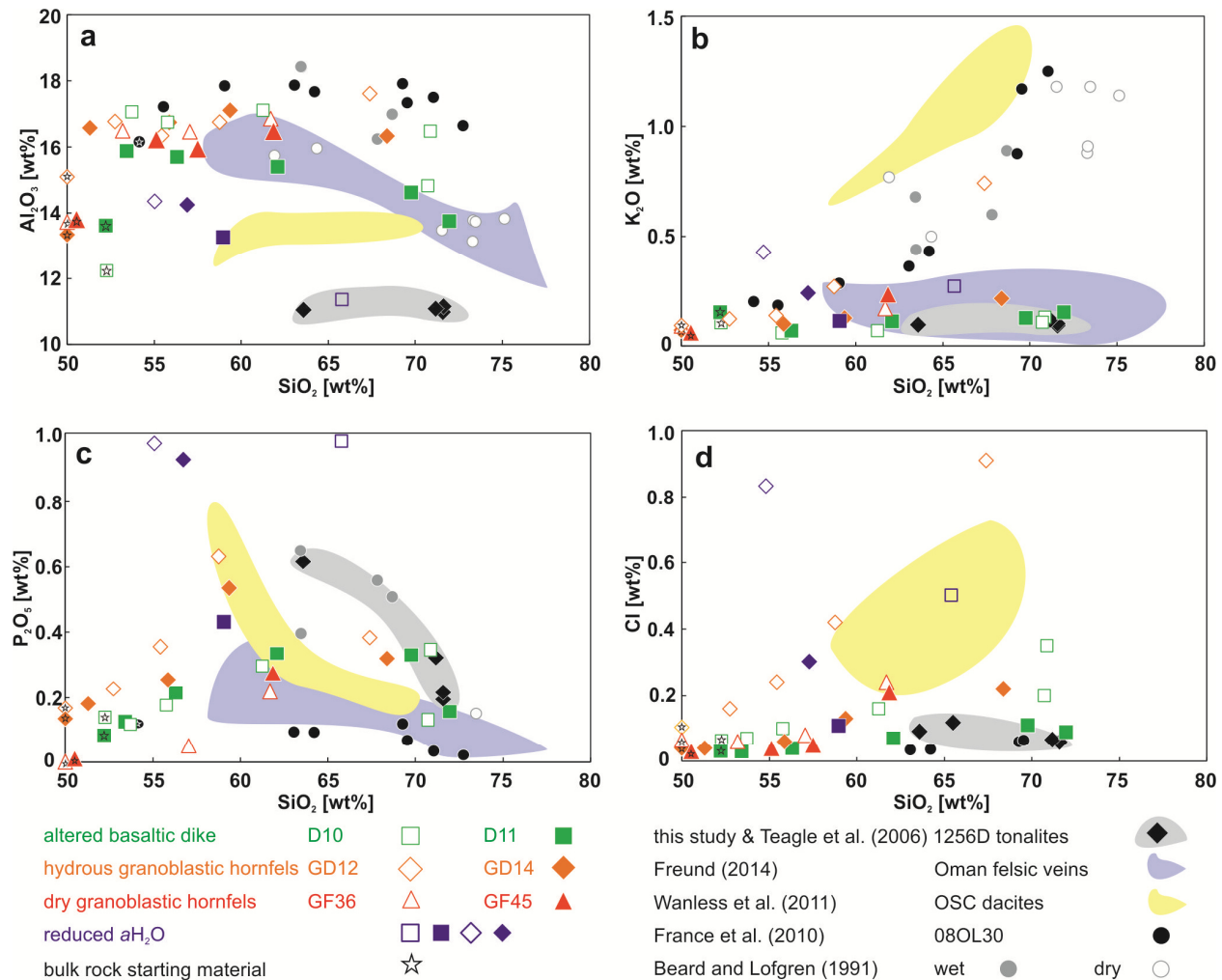


**Figure C.1.7:** Harker diagrams (oxide versus  $SiO_2$ ). Comparison of experimental melts from this study with experimental studies from Beard and Lofgren (1991) and France et al. (2010). Also shown are natural tonalite rock data from IODP Site 1256 (this study; Teagle et al. 2006), data from Oman ophiolite felsic veins (Freund 2014), and dredged lavas (andesitic to dacitic; labeled as OSC dacites) from the 9°N overlapping spreading center (OSC) at the EPR (Wanless et al. 2011). The bulk rock composition of the starting materials is marked with stars; experiments performed at reduced  $aH_2O$  are highlighted with blue data points.

melts (Fig. C.1.7c). However, the concentration of Cl and  $P_2O_5$  in protolith GD12 is only little higher when compared to the average of Cl and  $P_2O_5$  in the D10, D11, and GD14 protoliths (Cl: 0.10 to 0.05;  $P_2O_5$ : 0.17 to 0.12; see Table C.1.1). Moreover, despite the distinctive altered character of France et al.'s (2010) starting material, that material is low in  $P_2O_5$  (0.12 wt%; Cl not given) and their experimental melts show only moderate enrichment trends for both Cl and  $P_2O_5$ . Thus, the degree to which the protoliths have been altered seems to have a minor influence on the concentration of phosphorus in anatectic melts, but rather the effective concentration of



phosphorus in the starting material phase assemblages. Consequently,  $P_2O_5$  concentration in the melt is dominated by the amount of apatite and the degree of apatite melting. Although Cl is slightly enriched in GD12, an additional influence of the alteration degree on strong Cl enrichment is likely to be the major source for elevated Cl contents in seafloor alteration.

The MORB normalized diagram (Gale et al. 2013) of all oxides for experiments with a melt fraction  $\leq 20$  vol% highlights the different influence of our starting materials and those of Beard and Lofgren (1991) and France et al. (2010) on the generated melts (Fig. C.1.8). Anatectic melts from other experimental studies generally exhibit lower MORB normalized values and are distinctly enriched in  $K_2O$ . Moreover, a different evolution in MORB normalized values is apparent for France et al.'s (2010) anatectic melts which exhibit a step from low  $TiO_2$  to enriched  $Al_2O_3$ , followed by low values for FeO, MgO, and CaO and strong enrichment in  $Na_2O$  and  $K_2O$  finalized by pronounced low  $P_2O_5$  values. This deviation from the anatectic melts of this study highlights again the difference between the Oman ophiolite protolith used by France et al. (2010) and the IODP Site 1256 protoliths used in this study.

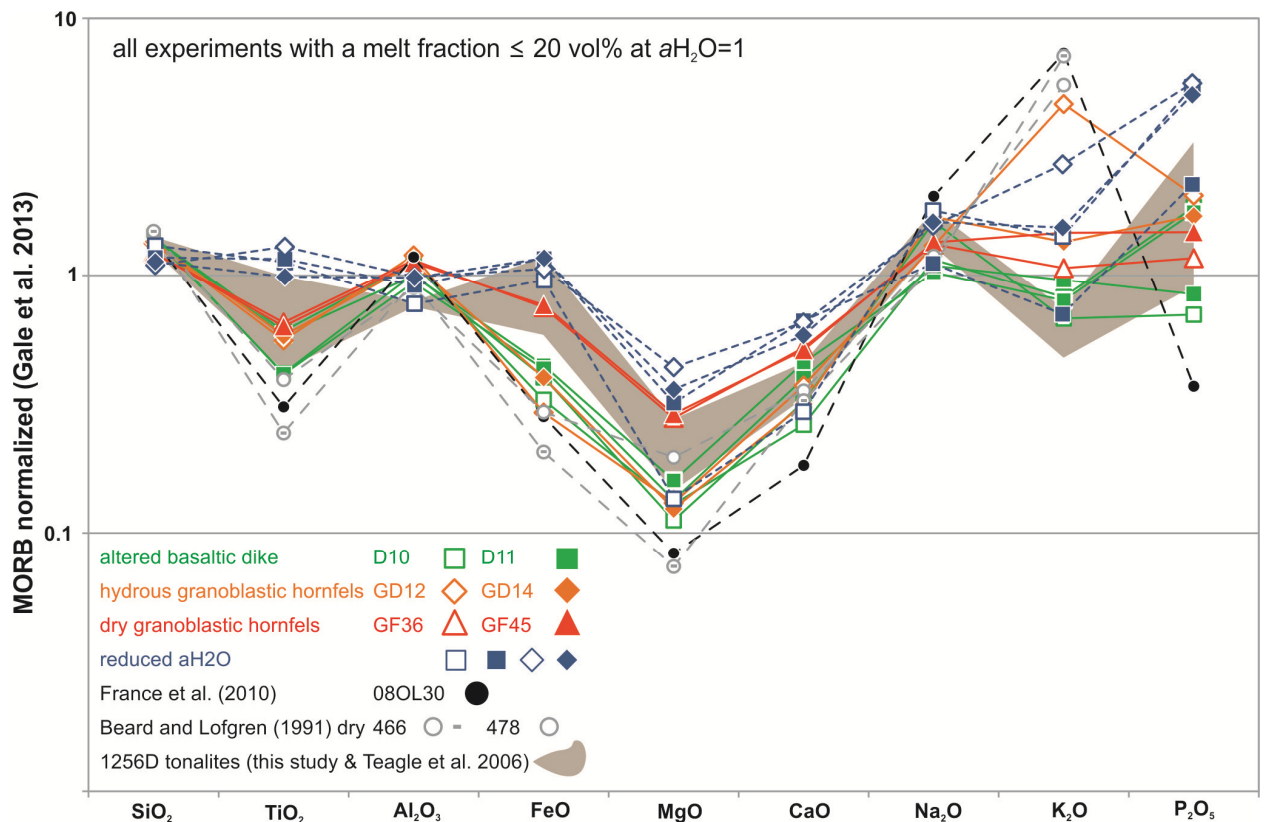


**Figure C.1.8.:** Major element-MORB normalized diagram (using MORB data of Gale et al. 2013) for experimental melts and natural tonalites from IODP Site 1256 (grey field). Shown are all experiments from this study and from Beard and Lofgren (1991) and France et al. (2010) with a melt fraction  $\leq 20$  vol% in comparison to 1256D tonalites. Experiments performed at reduced  $a_{H_2O}$  are highlighted with blue data points.

The large span in crystallized plagioclase composition is also reflected in the difference in the starting materials (Fig. C.1.6). In experiments at a given temperature, the spread in An values is  $\sim 20$  mol% ( $T \leq 940^\circ C$ ), caused by varying Ca/Na ratios of the different starting materials ( $D11 > D10$ ;  $GD12 > GD14$ ). This spread decreases with increased temperature, revealing a deviation of only 6 mol% at  $1030^\circ C$  at generally high An values ( $> 80$  mol%).

### ***C.1.6.2. Temperature evolution through the sheeted dike complex root zone***

Equilibrium temperatures of the peak metamorphic overprint recorded by two-pyroxene thermometry (Brey and Koehler 1990; Andersen et al. 1993) of pyroxene hornfels, sampled at the AML roof either in modern oceanic crust or in ophiolites, give an estimation of temperatures of the anatexis processes in the dike/gabbro transition (e.g. Gillis and Coogan 2002; Gillis 2008; Koepke et al. 2008; Alt et al. 2010; Koepke and Goetze 2015). Temperature calculations of granulite facies rocks from Hess Deep, for example, result in an average temperature of 900 to 950°C (Gillis 2008), perfectly matching the temperatures of our experiments for relatively small melt fractions, which produce highly-evolved partial melts under water-saturated conditions. Similar values were estimated for hornfels from the Troodos and Oman ophiolite dike/gabbro transitions (e.g., T=850-1050°C; Gillis and Coogan 2002; Gillis 2008). Amphibole-plagioclase thermometry generally yields lower temperatures for the studied sample suites (400-700°C), reflecting the record of hydrothermal alteration at relatively high temperatures (amphibolite facies) mainly after the contact metamorphic overprint (Gillis and Coogan 2002; Gillis 2008; Alt et al. 2010).

For two-pyroxene hornfels of the dike/gabbro transition penetrated at Site 1256, several studies deal with the temperature evolution of this particular zone (Koepke et al. 2008, 2011; France et al. 2009; Alt et al. 2010; Zhang et al. 2014). While Alt et al. (2010) applied the two-pyroxene thermometer of Brey and Koehler (1990) and report equilibrium temperatures of 800°C-924°C, the QUILF two-pyroxene thermometer of Andersen et al. (1993) applied by Koepke et al. (2008, 2011) and France et al. (2009) determined distinctly higher temperatures for the peak metamorphic overprint (935°C-1045°C), where the metamorphic grade is highest (presence of two-pyroxene hornfels). In those granulite facies hornfels from the Site 1256 dike/gabbro transition, which underwent hydrothermal alteration after the metamorphic imprint, amphiboles are ubiquitous, enabling the application of amphibole thermometers (i.e., plagioclase-amphibole by Holland and Blundy 1994, and Ti-in-amphibole by Ernst and Liu 1998). As noted above, results reveal distinctly lower equilibrium temperatures for this event. Koepke et al. (2008) obtained temperatures of 708°C-854°C and 650°C-747°C by using the plagioclase-amphibole thermometer and the Ti-in-amphibole thermometer, respectively. Even though Alt et al. (2010) calculated temperatures with the Ti-in-amphibole thermometry of up to 913°C for individual samples, the majority of estimated temperatures are significantly lower, consistent with the hypothesis that hornfels cooling proceeded under hydrous conditions due to seawater-derived hydrothermal circulation.

### ***C.1.6.3. Comparison of the experimental melts with felsic rocks from IODP Site 1256***

The great advantage of using IODP Site 1256 samples as starting material is that experimental melts and residues can be directly compared to their natural equivalents. The compositions of mm-to-cm-thick felsic veins, consisting of tonalites cutting granulite facies hornfels in the drill core from Site 1256, are used for comparison. These are regarded as products of in-situ partial melting of AMC roof basalts (Koepke et al. 2008; Alt et al. 2010; Zhang et al. 2014). In Figure C.1.7 we also included the compositions of small felsic veins cutting hornfels sampled from the dike/gabbro transitions of the southern Oman Semail ophiolite blocks (Freund 2014); these are also regarded as anatexis melts generated in the roof rocks of AMLs (France et al. 2009, 2014).

It is important to note that plagiogranites in the Oman ophiolite, in general, are very heterogeneous in composition and size and are believed to have been formed by different processes (i.e., fractional differentiation of wet, subduction-zone related basalt or melting of sediments from the subducted slab (Rollinson 2009; Haase et al. 2015)). We also plotted extrusive andesitic and dacitic lavas from the 9° N overlapping spreading center (OSC) at the EPR (Wanless et al. 2011) for an additional comparison. Wanless et al. 2011 interpreted these rocks as a product of extreme fractional crystallization of a MOR basalt parent combined with partial melting and assimilation of amphibole-bearing altered oceanic crust. Thus, they are only in parts comparable to our experimental melts and the proposed model of anatexis. Although discussed to a lesser extent in the following, they are illustrated in Figure C.1.7 in order to present a larger spectrum of evolved rocks from fast-spreading oceanic crust.

The relatively wide compositional range of the Oman felsic veins (i.e.  $\text{SiO}_2 \sim 58 - 77$  wt%) covers the complete range of  $\text{SiO}_2$  contents of the experimental results at  $T \leq 970^\circ\text{C}$  (Fig. C.1.7). While most major and minor elements of the experimental melts with relatively low melt fraction ( $\leq 20$  vol%) fit quite well with 1256D tonalites, there is a large discrepancy with respect to  $\text{Al}_2\text{O}_3$  (Fig. C.1.7). While the Oman plagiogranites show  $\text{Al}_2\text{O}_3$  contents similar to those of the experimental melts (Fig. C.1.7), the tonalites from 1256D sampled to date are significantly lower in  $\text{Al}_2\text{O}_3$ .  $\text{Al}_2\text{O}_3$  in the melt is mainly influenced by plagioclase crystallization which is, in turn, controlled mainly by the prevailing  $a\text{H}_2\text{O}$  (e.g., Gaetani et al. 1993; Feig et al. 2006; Koepke et al. 2009). Most of the experiments of this study were performed under water-saturated conditions with  $a\text{H}_2\text{O}$  close to 1 (i.e. total  $\text{H}_2\text{O}$  in the melt  $\sim 3.5$  wt%) leading to high  $\text{Al}_2\text{O}_3$  contents in the melt (Fig. C.1.7a), indicating that 1256D tonalitic melt generation proceeded under vast plagioclase crystallization as a function of reduced  $a\text{H}_2\text{O}$  (see discussion below).

$\text{K}_2\text{O}$  is very low in 1256D tonalites and Oman felsic veins ( $\leq 0.12$  wt%, and  $\leq 0.36$  wt%, respectively) and, thus, accords with the experimental melt trends except for GD12, which is the sample showing strong hydrothermal alteration. The strong enrichment of GD12 and also those of Beard and Lofgren's (1991) and France et al.'s (2010) experiments is similar to the high  $\text{K}_2\text{O}$ -values presented by Wanless et al. (2011; Fig. C.1.7b) and in accord to their interpretation of partial melting and assimilation of altered oceanic crust. While  $\text{P}_2\text{O}_5$  is generally low (0.11 to 0.38 wt%) for most experimental melts, it is significantly higher in the less-evolved 1256D tonalite 214-1-P14 (0.61 wt%) and in Wanless et al. (2011) samples. Those high values are only observed at reduced  $a\text{H}_2\text{O}$  in water saturated samples GD12 and GD14, which show a peak in  $\text{P}_2\text{O}_5$  at intermediate temperature/composition. At higher  $\text{SiO}_2$  contents 1256D tonalites have the same  $\text{P}_2\text{O}_5$  range as experimental melts (at  $a\text{H}_2\text{O}=1$ ) and even mirror the step towards lower  $\text{P}_2\text{O}_5$  between  $T=940^\circ\text{C}$  and  $910^\circ\text{C}$  shown by altered basaltic dikes (Fig. C.1.7c). This is most likely caused by stable apatite in the residue, which in turn would dramatically decrease the content of rare earth elements, Y, and Sr of the first melts because they are compatible in apatite and apatite is, thus, a trap for Y and Sr (Prowatke and Klemme 2006). This would be one explanation for the lower-than-expected trace element enrichments of anatectic melts in comparison to those predicted for melts generated by large extents of fractional crystallization (Brophy 2009; France et al. 2014). Oman plagiogranites are generally low in  $\text{P}_2\text{O}_5$  ( $\leq 0.36$  wt%) and are in the range of experimental anatectic melts.

Chlorine concentrations are generally low, even in the very first experimental melts ( $\leq 0.35$  wt%). This is in agreement with 1256D tonalites which are also low in Cl (max. 0.12 wt%) and which are well reproduced by the compositional trend of melts from D11 starting material. Only the melts generated with starting material GD12, which is the sample with the most pronounced secondary alteration, is again out of the range compared to the melts produced by the other protoliths and contains 0.91 wt% Cl. Wanless et al.'s (2011) andesitic and dacitic lavas are enriched in Cl (up to 0.71 wt%) and reflect the trend to Cl-enriched experimental melts found in GD12. Wanless et al. (2011) concluded that this enrichment is, in part, due to a combination of partial melting and assimilation of a previously hydrothermalized protolith at the roof of the AML. The results of our study show that such Cl enrichment in anatectic melts is possible, provided that the protoliths are strongly altered, as is the case for sample GD12.

#### ***C.1.6.4. Comparison of the experimental residue with granoblastic hornfels from IODP Site 1256***

As discussed above, in most of our experiments performed at lower temperatures, the residual minerals coexisting with felsic melts are plagioclase, clino- and orthopyroxene, and Fe-Ti oxides; exactly the same minerals compose the granoblastic hornfels at the roof of AMLs. In the following, the experimental residual phases are compared with mineral data from natural granoblastic hornfels recovered from Hole 1256D (Koepke et al. 2008; Koepke and Goetze 2015).

With respect to the  $\text{TiO}_2$  versus  $\text{Al}_2\text{O}_3$  trend (Fig. C.1.5), the high-temperature experiments (i.e.  $1000^\circ\text{C}$  and  $1030^\circ\text{C}$ ) show clinopyroxene enrichment in both  $\text{TiO}_2$  and  $\text{Al}_2\text{O}_3$  in comparison to the starting material. With decreasing temperature,  $\text{TiO}_2$  and  $\text{Al}_2\text{O}_3$  decrease. For the hydrated basalts as protolith, clinopyroxene compositions at  $T=910^\circ\text{C}$  (see example for starting material D10, Fig. C.1.5a) match those of natural “dry” granoblastic hornfels from 1256D, but those from higher temperature deviate significantly. When using the more refractory “hydrous” and “dry” granoblastic hornfels as starting material (GD14, GF36, and GF45), clinopyroxenes at all temperatures fit quite well with the clinopyroxene compositions of the natural rocks, except for the highest temperature condition (see examples for starting materials GD14 and GF36, Fig. C.1.5b and c). Thus,  $\text{TiO}_2$  and  $\text{Al}_2\text{O}_3$  in the experimental clinopyroxenes are controlled by both starting material and temperature, if the starting material for the natural processes at the dike/gabbro transitions was already refractory due to previous dehydration processes (corresponding to our GD and GF samples). Our results imply that a partial melting event proceeded at  $T < 1030^\circ\text{C}$ , which is also consistent with the composition of the coexisting melt which is too low in  $\text{SiO}_2$  at  $T > 1000^\circ\text{C}$  compared to 1256D tonalites.

The plagioclase compositions in granoblastic hornfels from Site 1256 vary only slightly, between 49 and 56 mol% An. The corresponding equilibrium temperatures for the granoblastic hornfels were estimated by the two-pyroxene geothermometer (Koepke et al. 2008; Koepke and Goetze 2015) and are shown in Figure C.1.6. The experimental plagioclases produced with D11 and GD12 starting materials are generally too high in An when compared to the natural hornfels from Hole 1256D (Fig. C.1.6), which is a consequence of the high Ca/Na ratios in these rocks (see above). Plagioclases from the other starting materials at  $T \leq 970^\circ\text{C}$  are within the compositional range of the plagioclases from the natural hornfels. However, all these evaluations

are based on experiments performed under water saturation. In the following, we argue that this was probably not the case during the anatectic processes at the roof of the Site 1256 AML.

#### **C.1.6.5. The role of water activity**

There are several arguments that partial melting processes at the roof of the AML, producing felsic melts and granoblastic hornfels, proceed under reduced  $a_{\text{H}_2\text{O}}$  rather than at water-saturated conditions.

- When comparing the  $\text{Al}_2\text{O}_3$  contents of the experimental melts generated under water-saturated conditions with 1256D tonalites, it is obvious that the experimental melts contain significantly higher  $\text{Al}_2\text{O}_3$ , provided that sampled 1256D tonalites are representative of the partial melt composition (Fig. C.1.7a). Most of our experiments were performed under water saturation; it is well-known that water suppresses plagioclase stability (e.g., Gaetani et al. 1993; Feig et al. 2006; Koepke et al. 2009), resulting in melts which are strongly enriched in  $\text{Al}_2\text{O}_3$  compared to corresponding experiments with reduced  $a_{\text{H}_2\text{O}}$ . However, this enrichment in  $\text{Al}_2\text{O}_3$  relative to starting compositions is not present in experiments performed at  $1000^\circ\text{C}$  and  $a_{\text{H}_2\text{O}} \approx 0.5$  (D11, GD12, GD14) and at  $a_{\text{H}_2\text{O}} \approx 0.1$  (D10) (Fig. C.1.9a). Moreover, the trend of 1256D tonalites is perfectly matched by the strongly water-undersaturated D10 sample ( $a_{\text{H}_2\text{O}} \sim 0.1$ ). Figure C.1.9a shows that either a very low  $a_{\text{H}_2\text{O}}$  is required during the anatectic processes (i.e.  $a_{\text{H}_2\text{O}} \leq 0.1$ ) at  $T \sim 1000^\circ\text{C}$  or a moderately-reduced  $a_{\text{H}_2\text{O}}$  (e.g.,  $a_{\text{H}_2\text{O}} \sim 0.5$ ) is required at  $T < 1000^\circ\text{C}$ . Also in the MORB-normalized diagram (Fig. C.1.8) 1256D tonalites are best reproduced by water undersaturated experiments D10 and D11. It is important to add a note of caution here, since our database on tonalites from the drilled core at Site 1256 comprises only three samples, a number which is too low to guarantee full representativeness. However, these rocks form a coherent group in terms of petrographic features and geochemical compositions. Thus, we believe that the conclusion drawn here is justified.
- The two-pyroxene geothermometer of Andersen et al. (1993) applied to the granoblastic hornfels (data from Koepke et al. 2008; Koepke and Goetze 2015) indicated equilibrium temperatures from  $930$  to  $1045^\circ\text{C}$  and is, thus, in accord with scenarios discussed above for very low or moderately-reduced  $a_{\text{H}_2\text{O}}$ . Irrespective of the high  $\text{Al}_2\text{O}_3$  contents, water-saturated melts over this temperature range exhibit a relatively high melt fraction (up to 50 vol%, see Fig. C.1.3b) resulting in  $\text{SiO}_2$  contents of less than 62 wt%, which are lower than the Site 1256 felsic veins (Fig. C.1.9b). Only by reducing the  $a_{\text{H}_2\text{O}}$  can higher  $\text{SiO}_2$  contents at temperatures corresponding to those calculated for the hornfels be reached.
- At  $T = 1000^\circ\text{C}$ , which is in the range of natural granoblastic hornfels formation temperatures, experimental An contents match the plagioclase composition from the natural hornfels at water-undersaturated conditions (Fig. C.1.6). The best fit at that temperature results from a run with  $a_{\text{H}_2\text{O}} \sim 0.1$ .
- At the equilibrium temperatures estimated for natural granoblastic hornfels (average  $\sim 970^\circ\text{C}$ ; Koepke et al. 2008; Koepke and Goetze 2015) in most of our water-saturated experiments, olivine becomes a stable residual phase, crystallizing at the expense of orthopyroxene (Fig. C.1.3a), which is not in accord with the natural phase assemblage

where olivine is rare. Despite minor amounts of olivine coexisting with orthopyroxene, our experiments show that reduced  $a_{\text{H}_2\text{O}}$  leading to lower melt fractions has the same effect as lower temperatures, thus shifting the ‘olivine-in’ curve to higher temperatures, which is in accord with the natural record.

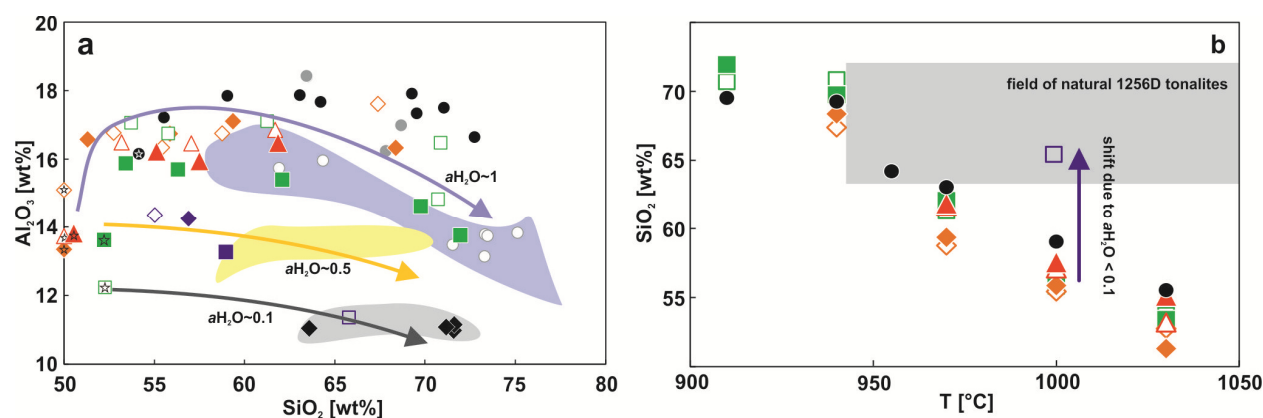


**Figure C.1.9.:** **a**  $\text{Al}_2\text{O}_3$  versus  $\text{SiO}_2$  as shown in Figure C.1.7a focusing on experiments performed at reduced  $a_{\text{H}_2\text{O}}$ . Trends for the different  $a_{\text{H}_2\text{O}}$ s are highlighted with arrows. **b**  $\text{SiO}_2$  (wt%) of the experimental melts as a function of temperature as shown in Figure C.1.4a including the range of natural 1256D tonalite rock data obtained by this study and the temperature calculations of Koepke et al. (2008). The shift due to reduced  $a_{\text{H}_2\text{O}}$  is highlighted. For signs and symbols see Figure C.1.7.

These observations raise the question of how anatexis processes can occur under strongly water-undersaturated conditions if distinct hydrothermal influence at the dike/gabbro transition is assumed. This is especially true at low degrees of melting, where a small amount of water in the protolith can lead to high  $a_{\text{H}_2\text{O}}$  in the melt. Hence, for low  $a_{\text{H}_2\text{O}}$  virtually no water can be present close to the melt lens and water-bearing alteration phases of potential protoliths must lose their water at the initial stage of partial melting. Additionally, pressure fluctuations should be minor because decreasing pressure, caused by an ongoing upward movement of the AML, in turn increases the  $a_{\text{H}_2\text{O}}$ . A possible model (Fig. C.1.10b) allows the hydrothermal flux to penetrate most of the oceanic crust until deep in the sheeted dike complex. However, at a certain distance from the AML (~50 to 100m according to Zhang et al. 2014) prevailing conditions hamper water migration deeper into the conducting boundary where anatexis starts. In addition, due to the metamorphic imprint triggered from below by the heat of an advancing melt lens, alteration phases containing  $\text{H}_2\text{O}$  or  $\text{OH}^-$  groups produced by an earlier hydrothermal alteration lose their water, causing the protolith to become "dry". Hence, for partial-melting processes, only minor amounts of water are available due to previously-altered protoliths. In our model most of the water released due to the breakdown of alteration phases migrates up at the prevailing supercritical conditions because it is an ‘open cooking pot’ rather than a closed system with a lid. Thus, an  $a_{\text{H}_2\text{O}}$  below 0.5 can be reached.

#### **C.1.6.6. The absence of amphibole-rich rocks as possible protoliths for felsic melt generation**

Amphibole-rich protoliths are often used to explain the generation of felsic melts at mid-ocean ridges (e.g., Haase et al. 2005; Brophy 2008; Rollinson 2009; Wanless et al. 2010). However, one surprising aspect of this study is that amphibole was never produced as a residual phase in our experiments, although most experiments were performed under water-saturated conditions.

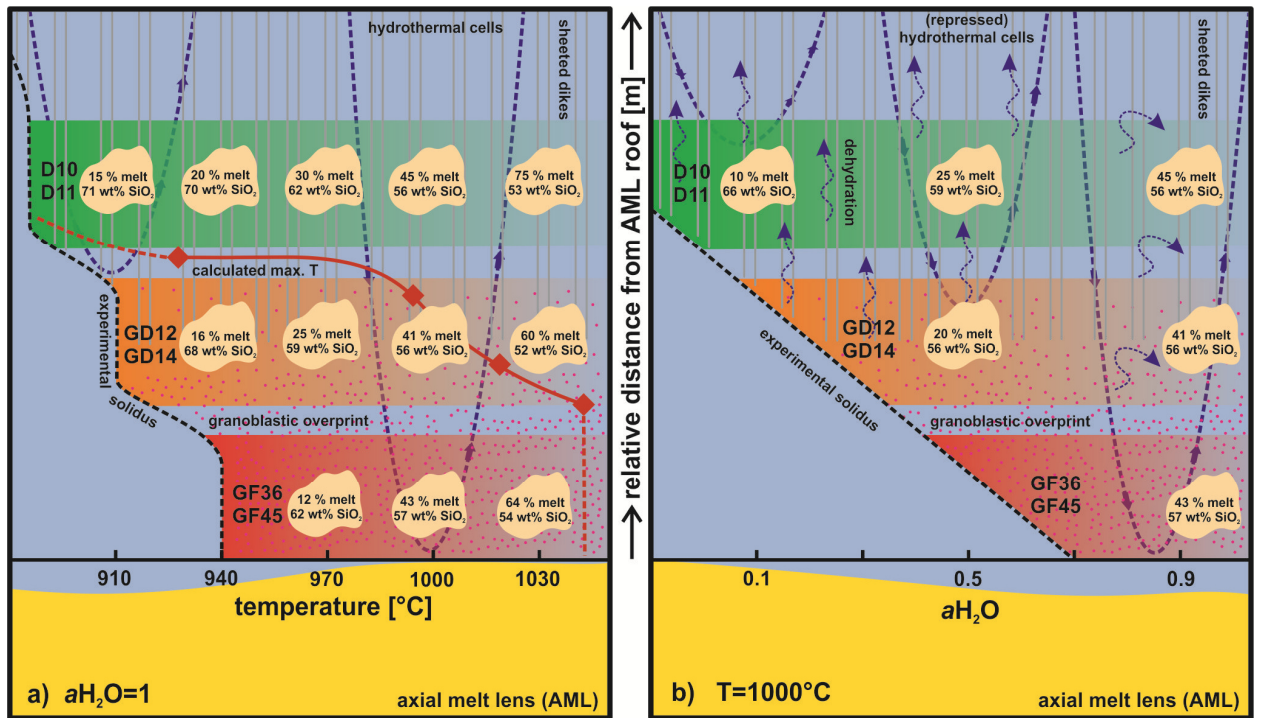


**Figure C.1.10:** Schematic model of the proposed stratigraphy at the oceanic magma chamber roof under **a** water-saturated conditions and varying temperature or **b** constant temperature ( $1000^\circ C$ ) and different  $aH_2O$ . Shown are the generated felsic melts with melt volume (in vol%) and  $SiO_2$  content for the different starting materials (with the average for each lithology) at the relative depth where they were sampled as a function of temperature (**a**) and  $aH_2O$  (**b**). The granoblastic overprint is highlighted with purple dots. Blue dashed lines represent the hydrothermal cells (**a** and **b**) and potential dehydration at reduced  $aH_2O$  (**b** only). The red curve in (**a**) is based on calculated 2-pyroxene maximum temperatures from Koepke et al. (2008) which are adapted for the depth from which the GD samples were taken. This curve highlights the result that that D samples can only be affected by anatexis when the AML and, thus, the temperature curve migrates upwards.

The reason for the absence of amphibole is probably the very low pressure at which the experiments were performed, since it is well-known that too-low pressure destabilizes amphibole (e.g., Rutherford and Devine 2003). The absence of amphibole is in agreement with the natural drilling record from IODP Site 1256, where amphibole exists in those two-pyroxene hornfelses from the lowermost horizon of the sheeted dikes only as a secondary phase generated by a stage of hydrothermal overprint after the peak metamorphism (e.g. Zhang et al. 2014; Koepke and Goetze 2015). Amphibole as part of the prograde metamorphic paragenesis occurs only at a higher crustal level where the heat supply of the underlying AML is minor, away from the zone where the main anatexis processes are ongoing. Koepke et al. (2008) and Alt et al. (2010) present equilibration temperatures varying from  $650^\circ C$  to  $854^\circ C$  and from  $464^\circ C$  to  $913^\circ C$ , respectively, for amphiboles in hornfelses, and similar amphibole-bearing hornfelses with equilibrium temperatures between  $850$  and  $900^\circ C$  were reported from Pito Deep (EPR) and the Troodos ophiolite (Gillis 2008). These temperatures are in the range of the solidus of altered basalts (France et al. 2010; this study). Thus, such rocks may be regarded as residues remaining after a partial melting process, provided the  $aH_2O$  was very high; this possibility can be excluded for the anatexis conditions at Site 1256. It seems that the critical point is whether water liberated during the partial melting reaction can escape the zone of reaction or not; such escape, in turn, is depending on the velocity of the uprising heat source (heat emanating from the AML after



replenishment), and the efficiency of establishing a fluid pathway system in the caprocks overlying the reaction zone.

### C.1.7. Conclusion

We experimentally simulated anatectic processes occurring at the roof of an oceanic magma chamber at fast-spreading ridges with special focus on IODP drilling Site 1256, representing 15 Ma old crust generated at the EPR. To accomplish this, we partially melted different lithologies drilled at Hole 1256D and compared the experimental results (melts and residues) with the natural counterparts from the same location (felsic rocks and 2-pyroxene hornfels). Our results lead to the following conclusions:

- The experimental melt composition is strongly influenced by the degree of alteration/recrystallization of the starting material. The first melts in the comparative experimental studies of Beard and Lofgren (1991) and France et al. (2010) using strongly-altered starting material show, for example, strong enrichments in  $K_2O$  caused by pervasive hydrothermal circulation in the protolith. Those high values ( $K_2O \gg 0.3$  wt%) are in contrast to natural tonalites from Hole 1256D. Except for the strongly-altered starting material GD12, all other starting materials lead to low  $K_2O$  concentration in the partial melts, following the trend to direct  $SiO_2$  enrichment which reproduces the natural trend.
- The expected residue (i.e. 2-pyroxene hornfels) is reproduced in the residual experimental mineral composition (modal and chemical) at low melting degrees (<20 vol%).
- Equilibrium temperatures of granoblastic hornfels, estimated by several studies (e.g. Koepke et al. 2008; Koepke und Goetze 2015), imply high temperatures of 930°C to 1045°C for anatectic processes, leading to high melt fraction under water-saturated conditions (up to 50 vol%), resulting in  $SiO_2$  contents which are, in general, too low in comparison to the natural counterparts. Moreover, the use of granoblastic two-pyroxene hornfels as starting material leads to low melt fraction (e.g., ~10 vol% at  $T=970^\circ C$ ). However, the corresponding melts are too low in  $SiO_2$  when compared with the natural tonalites, implying that these rocks are unlikely to be protoliths (Fig. C.1.9).
- Because experimental melts are generally higher in  $Al_2O_3$  than are 1256D tonalites, the assumption of partial melting under water saturation has to be scrutinized. Experiments performed at water-undersaturated conditions exhibit a good correlation to natural counterparts with the best fit at  $a_{H_2O}=0.1$ . Moreover, only at reduced  $a_{H_2O}$  can a low melting degree and thus high  $SiO_2$  content in anatectic melts be realized in the temperature range obtained for the peak metamorphic event (930°C to 1045°C), when using the most likely protolith (i.e. moderately-altered basaltic dike). Low  $a_{H_2O}$  is also indicated by the An content of plagioclase in the natural hornfels, which is best mirrored in the experimental residues at reduced  $a_{H_2O}$ .
- The lack of amphibole in our experimental residue supports the observations in two-pyroxene hornfels from IODP Site 1256 where amphibole only occurs as a secondary phase, generated by a late stage hydrothermal overprint (e.g. Zhang et al. 2014; Koepke and Goetze 2015). Thus, amphibole-rich protoliths for anatexis at the dike/gabbro



transition from present day fast-spreading ridges, which are often used for chemical modeling of felsic rock suites in the oceanic crust, are probably less important.

### ***Acknowledgements***

We thank Otto Dietrich and Julian Feige for their careful sample preparation. The manuscript has been substantially improved after thorough reviews by M. Perfit and two anonymous reviewers. This research used samples and/or data provided by the International Ocean Drilling Program (IODP). IODP is sponsored by the U.S. National Science Foundation (NSF) and participating countries under management of the Consortium for Ocean Leadership (COL). Funding for this research was provided by grants from the Deutsche Forschungsgemeinschaft (KO 1723/13).



## C.2. Trace element evidence for anatexis at oceanic magma chamber roofs and the role of partial melts for contamination of fresh MORB

Lennart A. Fischer<sup>1</sup>, **Martin Erdmann**<sup>1,2</sup>, Lydéric France<sup>2</sup>, Paul E. Wolff<sup>1</sup>, Etienne Deloule<sup>2</sup>, Chao Zhang<sup>1</sup>, Marguerite Godard<sup>3</sup>, and Jürgen Koepke<sup>1</sup>

<sup>1</sup>*Institut für Mineralogie, Leibniz Universität Hannover, Callinstr. 3, 30167 Hannover, Germany*

<sup>2</sup>*CRPG, UMR 7358, CNRS, Université de Lorraine, 15 rue Notre Dame des Pauvres, 54501 Vandoeuvre-lès-Nancy, France*

<sup>3</sup>*Géosciences, Université Montpellier 2, Place Eugène Bataillon, 34095 Montpellier, France*

*Lithos, Volume 260, pages 1-8, 2016*

*DOI: 10.1016/j.lithos.2016.05.001*

### C.2.1. Abstract

At oceanic spreading centers, interactions between magma and hydrothermal convecting systems trigger major physical, thermal, and chemical exchanges. The two-pyroxene hornfels recovered from the base of the sheeted dike sequence at Integrated Ocean Drilling Program (IODP) Site 1256 (equatorial Eastern Pacific) is interpreted as a conducting boundary layer between the underlying axial melt lens and the hydrothermally cooled sheeted dikes. They are cut by numerous small, felsic veins, which were recently interpreted as a product of hydrous partial melting of sheeted dikes. Here, we present trace element compositions of products (melts and residues) of hydrous partial melting experiments using basalts and hornfels from IODP Site 1256 as starting material. The experimental products generated between 910°C and 970°C match the natural lithologies from Site 1256 in terms of major and trace element compositions. The composition of the anatectic melt corresponds to the composition of the felsic veins, while the residual minerals match the compositions of the two-pyroxene hornfels, evidencing that hydrous partial melting is an important magmatic process in the gabbro/dike transition of fast-spreading mid-oceanic ridges. Our results complement previous experimental studies on anatectic processes occurring at the roof of the magma chambers from fast-spreading mid-ocean ridges. Moreover, calculations of mixing and assimilation fractional crystallization using the experimental partial melts as contaminant/assimilant showed that anatectic melts can only be a minor contributor to the contamination process.

**Keywords:** *Partial melting, Fast-spreading Mid-ocean ridge, Oceanic plagiogranite, Granoblastic hornfels, MORB contamination, Conductive boundary layer*

### C.2.2. Introduction

Present-day oceanic crust as well as ophiolites show a small, but ubiquitous amount of felsic evolved lithologies within the overall basaltic crust. In the plutonic part of the oceanic crust, these felsic lithologies mainly form late intrusions of diorites, quartz diorites, tonalites and trondjemites (often grouped as oceanic plagiogranites; e.g., Coleman and Peterman 1975; Aldiss 1981; Koepke et al. 2007; Rollinson 2009). They typically bear albite-rich plagioclase, quartz, and amphibole and have SiO<sub>2</sub> contents >60 wt%. Three endmember-models for their

formation in the oceanic crust are debated. (1) Hydrous partial melting of mafic rocks (e.g., Flagler and Spray 1991; Koepke et al. 2004; Brophy 2009; France et al. 2010; Brophy and Pu 2012; France et al. 2014); (2) extreme fractional crystallization of mid-ocean ridge basalt (MORB; e.g., Niu et al. 2002; Berndt et al. 2005; Rollinson 2009); or (3) liquid immiscibility (e.g., Dixon and Rutherford 1979; Natland et al. 1991). For some of these felsic lithologies, models of formation including both, fractional crystallization and partial melting of hydrated mafic rocks are proposed (Rollinson 2009; Wanless et al. 2010). A general model for the formation of felsic melts at the sheeted dike / gabbro transition is proposed for fast-spreading ridges (e.g., Gillis and Coogan 2002; Koepke et al. 2008; France et al. 2009; France et al. 2010). This model suggests an upward moving steady-state axial melt lens (AML; e.g., Carbotte et al. 2013) located at the top of the mush zone forming the axial magma chamber (e.g., Detrick et al. 1987) triggering granulite-facies contact metamorphism in the overlying hydrothermally altered sheeted dikes. This prograde metamorphic stage may result in partial melting reactions. The related anatectic process at the gabbro/dike transition zone was first experimentally tested by France et al. (2010, 2014), who simulated anatectic processes at the top of the AML in the Oman ophiolite, by using a hydrothermally altered andesitic basalt from the ophiolite as starting material.

#### ***C.2.2.1. Felsic veins intruding granoblastic hornfels at IODP Site 1256***

The IODP multi-leg mission “Superfast Crust” at Site 1256 penetrated, for the first time, an intact section of oceanic crust from the pillow basalts, through the sheeted dikes into the uppermost gabbros, providing the first detailed insight into the conductive boundary layer consisting of granoblastic hornfels, sandwiched between the AML and the sheeted dike sequence. Thus, IODP Site 1256 represents the best place to-date to study anatectic processes and felsic melt generation at the roof of an AML at fast-spreading ridges. The drilled oceanic crust was formed at the equatorial East Pacific Rise (EPR) about 15 Myr ago during a period of superfast spreading (for details of the drilling see Wilson et al. 2006 and Teagle et al. 2012). Hornfelses from IODP Site 1256 correspond to former basalts from the sheeted dike sequence which were close to the gabbro/dike contact metamorphosed in the pyroxene hornfels facies showing a very fine-grained, granoblastic texture consisting of clino- and orthopyroxene, plagioclase and Fe-Ti oxides in the highest metamorphic grade (Koepke et al. 2008; France et al. 2009; Alt et al. 2010; Teagle et al. 2012; Zhang et al. 2014; Koepke and Goetze 2015). Major element compositions of the hornfelses still correspond to basalts, but their normalized trace element patterns display strong depletions in rare earth elements (REE), positive Rb and Sr anomalies, and negative Nb and Zr anomalies (e.g., France et al. 2014; Erdmann et al. 2015). This conductive boundary layer represents one of the steepest (quasi) steady-state thermal gradients in a crustal system on Earth (e.g., Nicolas et al. 2008; Koepke et al. 2008). Below this 60 to 90 m thick (Koepke et al. 2008; Teagle et al. 2012) conductive boundary layer, the AML is located, filled with a basaltic magma at a temperature of ~1200°C. Above, seawater-derived hydrothermal cells are operating at temperatures of max. 400°C to 600°C (Alt et al. 2010). Equilibrium temperatures for the peak metamorphic event, estimated with the two-pyroxene hornfelses, vary between 850°C and 1050°C (Koepke et al. 2008; France et al. 2009; Alt et al. 2010; Zhang et al. 2014; Koepke and Goetze 2015), thus high enough to trigger partial melting when considering the solidus temperatures of wet MORB (~850°C; e.g., Beard and Lofgren

1991; France et al. 2010). A characteristic feature of these granoblastic hornfels is that they contain intrusions of felsic, evolved plutonic rocks (Fig. C.2.1). These have a fine to medium grained granular texture and occur as small, irregular patches, 0.1-0.2 cm wide veins, and <1.5 cm wide dikelets (Wilson et al. 2006; Teagle et al. 2012; Erdmann et al. 2015). The mineral assemblages of the felsic rocks include a large proportion of anhedral to subhedral feldspar and quartz, lesser amphibole and Fe-Ti oxides, and accessory apatite and zircon. The contact to the background granoblastic dikes is sutured without any chilled margin, implying intrusion into the host while this was still very hot. Studies on such hornfels/tonalite associations in the gabbro/dike transition of Site 1256 and ophiolites demonstrate that these felsic intrusions can be regarded as products of hydrous partial melting of the sheeted dikes and that the granoblastic hornfels can be regarded as the residue of this process (Gillis and Coogan 2002; France et al. 2010, 2014; Erdmann et al. 2015). For the Oman ophiolite, this model was recently confirmed by the marked complementarity between the trace element patterns of the granoblastic dikes and the tonalitic intrusions (France et al. 2014). The ubiquitous occurrence of primary magmatic amphibole in these felsic veins and patches from Site 1256D suggests high water activities during their formation. The presence of high amounts of quartz, as well as accessory apatite and zircon in many of these rocks, indicates also that these felsic intrusions crystallized from highly evolved melts.

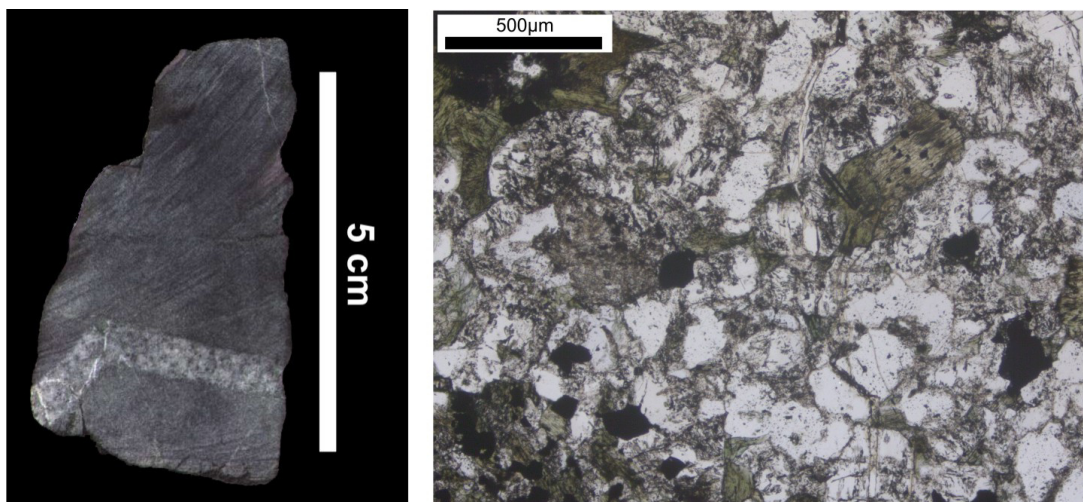


**Figure C.2.1.:** *left* Core image from IODP sample 312-1256D-212R-1, 25–28 cm showing a tonalitic vein intruding granoblastic hornfels from (Expedition 309/312 Scientists 2006). *right* Microscope image of the tonalitic vein from the sample shown on the *left*. Visible is quartz (colorless clear), plagioclase (colorless cloudy), amphibole (greenish) and Fe-Ti oxides (opaque phase).

#### **C.2.2.2. Previous study**

Recently, Erdmann et al. (2015) presented a combination of geochemical investigation of tonalitic veins cutting hornfels from the dike/gabbro transition at IODP Site 1256 and a related experimental partial melting study. They showed that the tonalitic veins correspond to partial melting products of altered sheeted dikes, and that the pyroxene hornfels, which host the felsic intrusions, can be regarded as the residuum after a partial melting event. Erdmann et al. (2015) used six different natural starting materials from the sheeted dike sequence drilled at IODP Site 1256 in order to simulate metamorphic and magmatic processes at the transition between AML and sheeted dikes of fast-spreading ridges. Their basaltic protoliths are representatives of the lower part of the sheeted dike complex and are characterized by different grades of metamorphic

overprint. The detailed experimental procedure is described in Erdmann et al. (2015), and experimental conditions are presented in the electronic supplemental material C.2.ESM.1.

**Table C2.1** Major element whole rock compositions of natural rocks from IODP Hole 1256 D and compositions of experimental melts from (Erdmann et al. 2015)

Comments	Sample	Type	Rock/mineral	Method	SiO <sub>2</sub>	TiO <sub>2</sub>	Al <sub>2</sub> O <sub>3</sub>	FeO	MnO
					wt%	wt%	wt%	wt%	wt%
starting material	312-1256D-173R-1, 0-10 cm	nat.	basalt	ICP-OES	52.22	1.08	13.62	13.18	0.20
felsic vein	312-1256D-212R-1, 25–28 cm	nat.	tonalite	ICP-AES	71.58	0.72	10.98	6.09	0.04
felsic vein	312-1256D-214R-1, 68–70 cm	nat.	tonalite	ICP-AES	63.58	1.48	11.05	12.28	0.08
felsic vein	335-1256D-235R-1, 23–26 cm	nat.	tonalite	ICP-AES	71.17	1.00	11.08	6.36	0.04
exp. partial melts	910°C, 100MPa, 162h*	exp.	glass	EPMA	71.76	0.70	13.89	4.48	0.11
				<i>S.D.</i>	<i>1.38</i>	<i>0.05</i>	<i>0.55</i>	<i>0.42</i>	<i>0.05</i>
exp. partial melts	940°C, 100MPa, 120h	exp.	glass	EPMA	69.76	0.99	14.62	4.66	0.11
				<i>S.D.</i>	<i>0.74</i>	<i>0.04</i>	<i>0.41</i>	<i>0.43</i>	<i>0.02</i>
exp. partial melts	970°C, 100MPa, 160h	exp.	glass	EPMA	62.09	1.34	15.40	8.57	0.17
				<i>S.D.</i>	<i>0.32</i>	<i>0.03</i>	<i>0.34</i>	<i>0.32</i>	<i>0.00</i>
exp. partial melts	1000°C, 100MPa, 146h	exp.	glass	EPMA	56.31	1.58	15.70	10.99	0.22
				<i>S.D.</i>	<i>0.44</i>	<i>0.05</i>	<i>0.45</i>	<i>0.39</i>	<i>0.01</i>
exp. partial melts	1030°C, 100MPa, 72h	exp.	glass	EPMA	53.42	1.46	15.88	11.75	0.23
				<i>S.D.</i>	<i>0.34</i>	<i>0.10</i>	<i>0.40</i>	<i>0.59</i>	<i>0.01</i>

Comments	Sample	MgO	CaO	Na <sub>2</sub> O	K <sub>2</sub> O	P <sub>2</sub> O <sub>5</sub>	Cl**	Total
		wt%	wt%	wt%	wt%	wt%	ppm	wt%
starting material	312-1256D-173R-1, 0-10 cm	9.15	8.71	1.64	0.07	0.08	300.00	100.00
felsic vein	312-1256D-212R-1, 25–28 cm	1.93	4.68	3.62	0.09	0.19	600.00	100.00
felsic vein	312-1256D-214R-1, 68–70 cm	2.09	4.46	4.18	0.10	0.61	900.00	100.00
felsic vein	335-1256D-235R-1, 23–26 cm	1.11	3.78	4.97	0.12	0.32	700.00	100.00
exp. partial melts	910°C, 100MPa, 162h*	1.03	4.64	3.01	0.15	0.16	1128.00	100.00
		<i>0.56</i>	<i>0.83</i>	<i>0.40</i>	<i>0.03</i>	<i>0.03</i>	<i>194.00</i>	
exp. partial melts	940°C, 100MPa, 120h	1.21	5.21	2.87	0.13	0.32	1091.00	100.00
		<i>0.35</i>	<i>0.39</i>	<i>0.17</i>	<i>0.03</i>	<i>0.03</i>	<i>64.00</i>	
exp. partial melts	970°C, 100MPa, 160h	2.26	6.54	3.12	0.11	0.33	675.00	100.00
		<i>0.09</i>	<i>0.11</i>	<i>0.34</i>	<i>0.02</i>	<i>0.03</i>	<i>39.00</i>	
exp. partial melts	1000°C, 100MPa, 146h	3.61	8.36	2.90	0.07	0.21	429.00	100.00
		<i>0.07</i>	<i>0.16</i>	<i>0.24</i>	<i>0.01</i>	<i>0.02</i>	<i>35.00</i>	
exp. partial melts	1030°C, 100MPa, 72h	4.67	10.00	2.44	b.d.	0.12	329.00	100.00
		<i>0.27</i>	<i>0.35</i>	<i>0.06</i>		<i>0.00</i>	<i>37.00</i>	

\*only powder experiments

\*\*Cl values in Erdmann et al. 2015 are rounded values in wt%

*S.D.*: Standard Deviation

b.d.: below detection limit

This study focuses on sample D11 (IODP description: 312-173-R-1, 0-10 cm) presented by Erdmann et al. (2015), who identified this sample as the probable protolith based on major

elements, targeting on the trace element compositions of the experimental melts. Sample D11 was drilled within the sheeted dike complex approximately 150 meters above the dike/gabbro contact. The sample still preserves its original basaltic texture and does not show any sign of granoblastic overprint. D11 is a moderately altered (alteration degree 11 % according to Erdmann et al. 2015), fine grained basalt with an intergranular texture, containing plagioclase (An = 50 - 57 mol%), clinopyroxene (Mg# = 55 - 60), and minor chlorite, quartz and small amounts of amphibole as secondary phases, and sulfides and Fe-Ti-oxides as accessory minerals. All experiments with protolith D11 were performed under water saturation in order to guarantee comparable conditions and consistent redox conditions (i.e., oxygen fugacity = QFM +1; with QFM = quartz-fayalite-magnetite oxygen buffer), at temperatures ranging between 910°C and 1030°C. The applied pressure was 100 MPa. The major element evolution trends of the experimental partial melts are in general consistent with the natural tonalitic veins from IODP Site 1256 (Tab. C.2.1). In all experiments, newly formed crystals coexist with a melt. Orthopyroxene crystallizes only at lower temperatures at the expense of olivine, which is only stable in the 1030°C run product (Erdmann et al. 2015). The upper magnetite stability is 1000°C and the upper ilmenite stability is 970°C. Plagioclase and clinopyroxene are present in all experimental products. Thus, for runs at temperatures  $\leq 970^\circ\text{C}$  the residual paragenesis is in full agreement with the mineral assemblage of typical pyroxene hornfels from IODP Site 1256: clinopyroxene - orthopyroxene - plagioclase - magnetite - ilmenite (Fig. C.2.2). The results for sample D11 suggest a model that the tonalitic veins represent melts produced by hydrous partial melting of altered sheeted dikes at temperatures below 970°C (Erdmann et al. 2015).

Our study complements the results of Erdmann et al. (2015) by presenting trace element compositions analyzed by SIMS of the experimental melts in the same set of experiments of Erdmann et al. (2015) performed with the starting material D11. Trace elements are in many respects far more sensitive than major elements in constraining magma evolution, and magma chamber processes (e.g., Klein 2003; O'Neill and Jenner 2012; Lissenberg et al. 2013; France et al. 2014). Since such felsic melts are generated at the roof of the AML from mid-oceanic ridges, they can also be regarded as a potential contaminator for primary MORB (e.g., Coogan et al. 2003; Wanless et al. 2010; France et al. 2010, 2013, 2014). Thus, another aim of this study is to test the potential of MORB contamination caused by such melts.

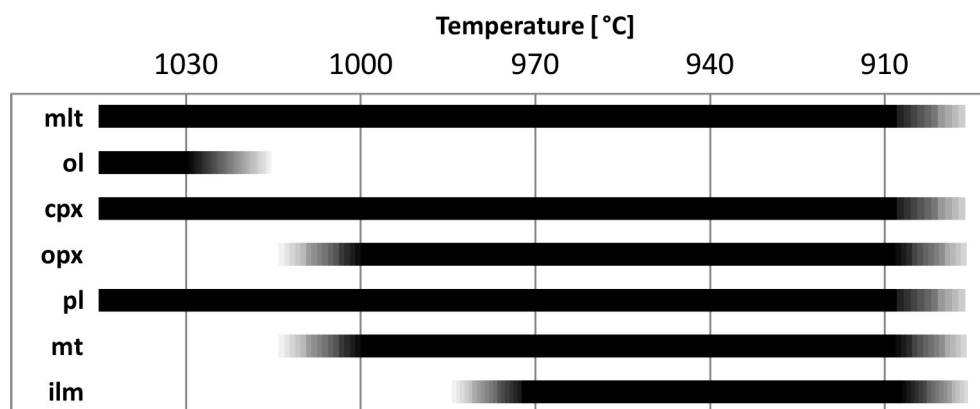


**Figure C.2.2:** Phases present in experimental products as a function of temperature. The color fading indicates the extrapolation of the upper or lower temperature limit of the phase stabilities between two run temperatures. Abbreviations: mlt (melt) ol (olivine), cpx (clinopyroxene), opx (orthopyroxene), pl (plagioclase), mt (magnetite), ilm (ilmenite).

For the experimental run at 910°C, Erdmann et al. (2015) show major element results as a combination of powder and microrock experiments. To ensure the comparability between the different experimental temperatures, especially in terms of equilibrium, we only take those major element compositions revealed from powder experiments. Major elements from Erdmann et al. (2015) are presented in Table C.2.1.

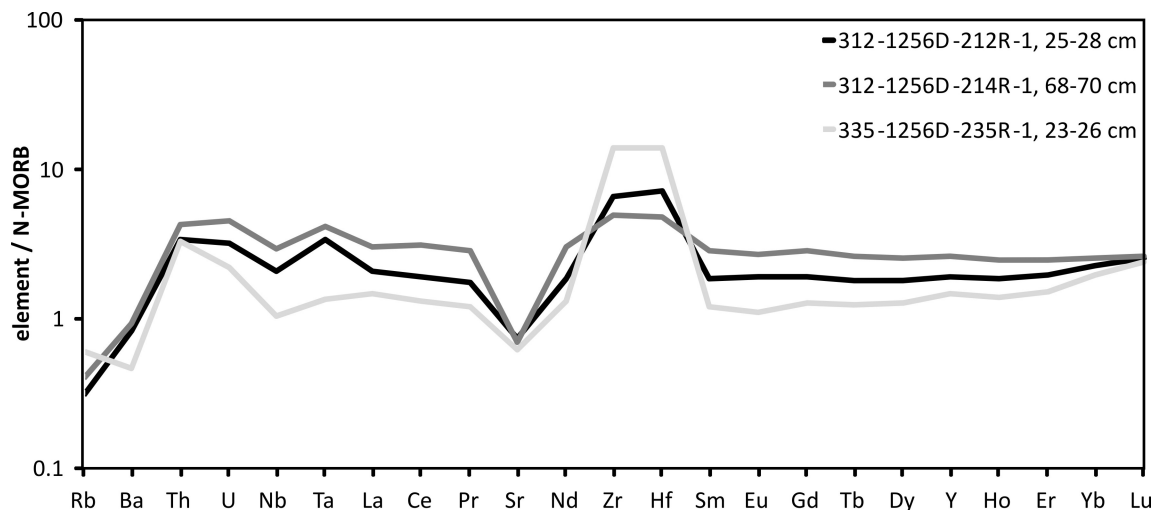


**Figure C.2.3:** N-MORB normalized (Gale et al. 2013) trace element patterns in three representative samples of tonalitic veins from IODP Site 1256 (C.2.ESM.2).

### C.2.2.3. Trace element characteristics of felsic veins

From all felsic rocks of the Hole 1256D drill core, we focus here only on those felsic veins and dikelets characterized as tonalites based on the mineral mode. Those tonalites are fine-grained rocks with mainly granular plagioclase and quartz and minor previously magmatic and now altered secondary amphibole, Fe-Ti oxides and/or clinopyroxene. A detailed petrography and the major element compositions of these rocks are presented in Erdmann et al. (2015). Their SiO<sub>2</sub> contents vary between 63 and 71 wt% with MgO contents varying between 1.1 and 2.1 wt%. High amounts of P<sub>2</sub>O<sub>5</sub> (0.19 to 0.60 wt%) demonstrate their evolved character. Here we present the results of the trace element analyses (Fig. C.2.3; Tab. C.2.2 and C.2.ESM.2). N-MORB normalized trace element patterns of the tonalites are roughly flat with pronounced negative anomalies of Ba, Rb and Sr (Fig. C.2.3). The positive anomalies of Zr and Hf are strong and gradually enhanced with decreasing total trace element content.

### C.2.3. Analytical technique

We used the same polished and carbon coated sections of the experimental runs for trace elements analysis that were used and reported by Erdmann et al. (2015) for major and minor element analysis by electron probe micro-analyzer (EPMA). Trace elements were analyzed with a “Cameca IMS-1270” secondary ion mass spectrometer (SIMS) at the Centre de Recherches Pétrographiques et Géo-chimiques in Nancy, France. An O- primary beam with an intensity of 5-30 nA was used at an acceleration voltage of 13 kV. The secondary beam was accelerated with 10 kV, and we analyzed with a mass resolving power of 5500 and 8000, respectively. The energy offset was set to -40 and 0 V, respectively, with a 40 eV energy window. The beam size was between 20 and 30 μm with a slightly oval shape. For seeking the point of interest on the sample a reflected light microscope was used and points were checked after measurement by



backscattered electron (BSE) images with an EPMA. One analysis consists of 6 cycles, each starting from mass  $^{28}\text{Si}$  going up to  $^{30}\text{Si}$ ,  $^{47}\text{Ti}$ ,  $^{85}\text{Rb}$ ,  $^{88}\text{Sr}$ ,  $^{89}\text{Y}$ ,  $^{90}\text{Zr}$ ,  $^{93}\text{Nb}$ ,  $^{138}\text{Ba}$ ,  $^{139}\text{La}$ ,  $^{140}\text{Ce}$ ,  $^{142}\text{Ce}$ ,  $^{146}\text{Nd}$ ,  $^{147}\text{Sm}$ ,  $^{151}\text{Eu}$ ,  $^{152}\text{Sm}$ ,  $^{153}\text{Eu}$  and then  $^{181}\text{Ta}$  with mass 27.7 and 29.5 as background. For data processing  $^{30}\text{Si}$  was used as reference mass, and the BHVO-2-G standard (Wilson 1997; Ila and Frey 2000; Gao et al. 2002; Raczek et al. 2003; Strnad et al. 2005) was used for calibration. To provide high-quality data, standard measurements were performed between every analytical session. Data were corrected for oxide interferences following Fahey et al. (1987) and the sensitivity factor was calculated for each analyses to account for its time dependence.  $^{30}\text{Si}$  was used as an internal reference, and the useful yield of the measured elements relative to Si determined with BHVO-2-G, measured with the same analytical condition.

**Table C.2.2** Trace element compositions of experimental melts and natural samples.

Comments	Sample	Type	Rock/mineral	Method	Ba	Rb	Nb	Ta	La
					ppm	ppm	ppm	ppm	ppm
starting material	312-1256D-173R-1, 0-10 cm	nat.	basalt	ICP-MS	15.00	2.00	2.00	0.20	2.70
felsic vein	312-1256D-212R-1, 25-28 cm	nat.	tonalite	ICP-MS	16.30	0.58	7.46	0.81	8.62
felsic vein	312-1256D-214R-1, 68-70 cm	nat.	tonalite	ICP-MS	18.18	0.73	10.72	1.00	12.82
felsic vein	335-1256D-235R-1, 23-26 cm	nat.	tonalite	ICP-MS	9.06	1.10	3.76	0.33	6.15
exp. partial melts	910°C, 100MPa, 162h*	exp.	glass	SIMS	36.08	2.83	16.37	2.00	9.76
				<i>S.D.</i>	<i>3.77</i>	<i>0.38</i>	<i>2.36</i>	<i>0.14</i>	<i>1.63</i>
exp. partial melts	940°C, 100MPa, 120h	exp.	glass	SIMS	19.80	1.70	15.20	1.20	6.80
				<i>S.D.</i>	<i>2.60</i>	<i>0.20</i>	<i>1.60</i>	<i>0.30</i>	<i>0.70</i>
exp. partial melts	970°C, 100MPa, 160h	exp.	glass	SIMS	20.70	6.20	9.80	2.70	6.40
				<i>S.D.</i>	<i>4.70</i>	<i>0.50</i>	<i>2.60</i>	<i>0.40</i>	<i>1.20</i>
exp. partial melts	1000°C, 100MPa, 146h	exp.	glass	SIMS	15.30	5.20	4.00	1.40	5.20
				<i>S.D.</i>	<i>1.40</i>	<i>1.40</i>	<i>1.40</i>	<i>0.20</i>	<i>0.60</i>
exp. partial melts	1030°C, 100MPa, 72h	exp.	glass	SIMS	15.80	3.80	5.80	0.30	8.70
				<i>S.D.</i>	<i>1.60</i>	<i>0.40</i>	<i>0.20</i>	<i>0.00</i>	<i>1.80</i>

Comments	Sample	Ce	Sr	Nd	Zr	Sm	Eu	Y
		ppm	ppm	ppm	ppm	ppm	ppm	ppm
starting material	312-1256D-173R-1, 0-10 cm	7.40	62.00	6.00	51.00	2.20	0.86	21.00
felsic vein	312-1256D-212R-1, 25-28 cm	23.47	93.89	19.73	675.30	6.37	2.39	63.67
felsic vein	312-1256D-214R-1, 68-70 cm	38.05	89.50	32.13	500.90	9.83	3.44	85.70
felsic vein	335-1256D-235R-1, 23-26 cm	16.14	78.31	13.75	1424.00	4.19	1.40	49.01
exp. partial melts	910°C, 100MPa, 162h*	26.35	98.00	23.48	354.55	8.08	1.88	49.62
		<i>0.73</i>	<i>20.88</i>	<i>1.30</i>	<i>44.32</i>	<i>0.25</i>	<i>0.02</i>	<i>1.85</i>
exp. partial melts	940°C, 100MPa, 120h	21.00	63.70	20.30	248.10	6.40	1.50	47.50
		<i>2.10</i>	<i>9.90</i>	<i>1.80</i>	<i>29.60</i>	<i>0.50</i>	<i>0.10</i>	<i>2.90</i>
exp. partial melts	970°C, 100MPa, 160h	18.80	68.30	16.90	210.50	6.00	2.80	61.20
		<i>2.90</i>	<i>17.40</i>	<i>3.20</i>	<i>42.20</i>	<i>1.00</i>	<i>0.20</i>	<i>4.70</i>
exp. partial melts	1000°C, 100MPa, 146h	13.00	62.50	8.20	121.60	4.70	2.90	36.50
		<i>1.30</i>	<i>9.60</i>	<i>1.40</i>	<i>19.50</i>	<i>0.50</i>	<i>0.50</i>	<i>4.80</i>
exp. partial melts	1030°C, 100MPa, 72h	20.70	103.50	12.60	100.50	4.70	1.70	33.30
		<i>3.60</i>	<i>11.10</i>	<i>1.30</i>	<i>3.20</i>	<i>0.60</i>	<i>0.20</i>	<i>2.90</i>

*S.D.*: Standard deviation

## C.2.4. Results and discussion

### C.2.4.1. Comparison: Natural felsic veins from IODP Site 1256 versus experimental melts

N-MORB normalized trace element patterns of the natural tonalitic veins from Site 1256 are in good agreement with the experimental melts generated at low temperatures (910°C - 970°C; Fig C.2.4). Characteristic features of both experimental melts and natural tonalites are marked negative Sr anomalies and enrichment in Zr in comparison to N-MORBs. Experimental melts are more enriched in Rb and Ba than the natural lithologies; this is probably caused by secondary hydrothermal alteration of the natural tonalitic veins, which is visible in each of the investigated rocks. In turn, Zr is relatively immobile during hydrothermal alteration and shows a higher enrichment in the natural tonalites compared to the experimental felsic melts. There is also a slight discrepancy with respect to Nb and Ta, which are more enriched in the experimental melts than the natural tonalites from Site 1256. These elements are mainly controlled by magnetite and ilmenite as residual phases, and both minerals are stable in the experiments at lower temperatures. Their stability is strongly dependent on the prevailing oxygen fugacity (e.g.; Toplis and Carroll 1995), as well as on the FeO and TiO<sub>2</sub> contents of the starting material, which may explain the differences. Similar trace element characteristics like those recorded here for the IODP Site 1256 drilling are observed in the felsic veins and dikelets within the dike/gabbro transition of the Oman ophiolite (France et al. 2014).

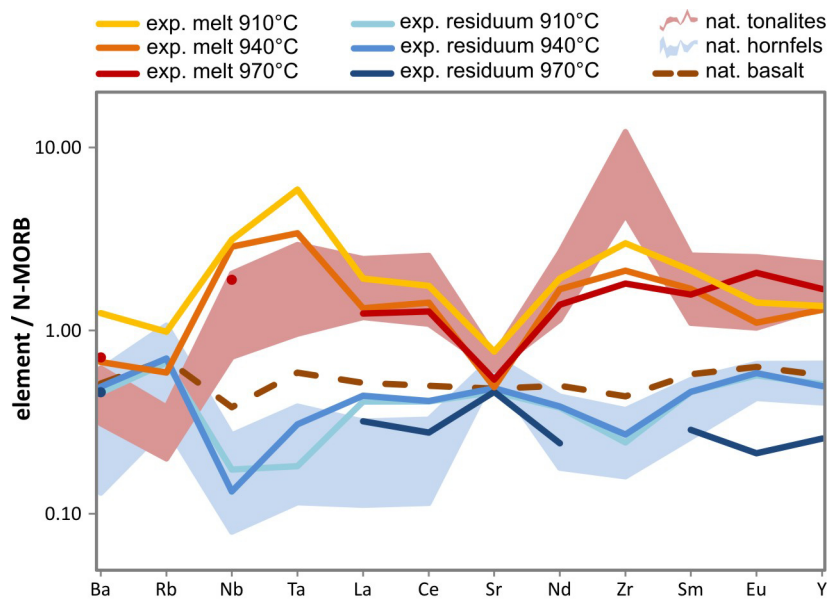


**Figure C.2.4:** N-MORB normalized (Gale et al. 2013) patterns for selected trace elements in both felsic (this study) and residual phases (nat. hornfels compositions correspond to granoblastic dikes from (France et al. 2014)). Experimental partial melts and the calculated residue of the experimental products are shown as lines. The natural trace element distribution in the tonalitic veins (red) and the hornfels (blue) are shown as shaded areas. The basaltic starting material is marked as brown dashed line in the diagram. X-axis intersects at 0.5 on Y-axis.

### C.2.4.2. Comparison: Granoblastic hornfels versus experimental residues

While major element results of Erdmann et al. (2015) and trace element results from this study show that the tonalitic intrusions from IODP Site 1256 could be regarded as frozen partial melts produced by anatexis of sheeted dikes, the question is raised of whether a similarly good match

could be achieved when considering the trace elements of the associated residues. For the natural two-pyroxene hornfels from IODP Site 1256 it was already shown by France et al. (2014) that these hornfels can be regarded as natural residuum.

Erdmann et al. (2015) showed that the experimental residue of the lower temperature runs, composed of plagioclase, clinopyroxene, orthopyroxene, magnetite and ilmenite (Fig. C.2.2), matches exactly the mineral assemblage of typical pyroxene hornfels from IODP Site 1256 (Teagle et al. 2012). Interestingly, both the experimental and the natural rocks do not show the presence of magmatic amphibole, which is surprising since most of their experiments were performed at high water activities. Several experimental studies (e.g., Koepke et al. 2004; France et al. 2010) have shown that amphibole is stable during the partial melting of mafic rocks at conditions and compositions similar to Erdmann et al. (2015). However, also in the drilled rocks from IODP Site 1256 magmatic amphibole is not observed and only documented as secondary phase (e.g., Koepke and Goetze 2015).

Figure C.2.4 shows that the calculated (mass balance with bulk composition and anatectic melt) trace element concentrations for the experimental residue correspond to those compositions measured in granoblastic two-pyroxene hornfels (France et al. 2014). N-MORB normalized patterns for both the experimental residue and the natural granoblastic hornfels from Site 1256 show a good correspondence with positive anomalies for Rb and Sr and negative anomalies for Nb and Zr.

#### ***C.2.4.3. Implications for the contamination of MOR basalts from fast-spreading ridges***

In contrast to MORBs from slow-spreading ridges, where contamination is only sparsely reported (van der Zwan et al. 2015), MORBs from fast-spreading ridges can generally be regarded as “contaminated”, according to geochemical studies using chlorine as a proxy for contamination (e.g., Michael and Chase, 1987; Michael and Cornell, 1998). Besides interaction with seawater, two end-member models may explain the mechanism of contamination: Model (1) - leucocratic melts derived by partial melting of previously hydrothermally altered roof-rocks may be either mixed with fresh MORBs (Model 1a; e.g., France et al. 2014), or mixed while the crystallization proceeds (assimilation fractional crystallization, AFC, Model 1b), and Model (2) - parts of the AML roof rocks that are hydrothermally altered and enriched in Cl, may be incorporated within the AML by stoping and assimilation enhancing crystallization (AFC; e.g., Coogan et al. 2003; Wilson et al. 2006; France et al. 2009).

The new data presented here allow us to identify the origin of MORB contamination, and to quantify its degree. Hereafter we model the various end-members (Model 1a, Model 1b, Model 2) and compare the results with a database composed of fresh EPR MORBs from literature for which Cl and Nb analysis are available (see C.2.ESM.3-5 and related references). Cl content of uncontaminated MORB has been proposed to be comprised between 2 and 25 ppm (Michael and Cornell 1998 and Le Roux et al. 2006), while concentrations observed in natural EPR MORB from our database are up to 1282 ppm, calling for a contamination contribution.

In order to account for major element MORB composition variability, we use different fresh MORB starting compositions in our models (e.g., Fig. C.2.5). Felsic melt contaminant for Models 1a and 1b is obtained from the experimental results presented herein; we considered that

partial melts generated between 910°C and 970°C are strongly relevant as at these temperatures experimental melts and residues correspond to the natural compositions (tonalitic veins and granoblastic hornfelses from Site 1256, respectively; Erdmann et al. 2015). The hydrothermally altered basalt that is assimilated in Model 2 is represented by a hydrothermally altered basaltic rock from the EPR; we used the composition of sample GD12 from Erdmann et al. (2015), which is a hydrothermally altered dike from the magma chamber roof at IODP Site 1256, and has an initial granoblastic overprint.

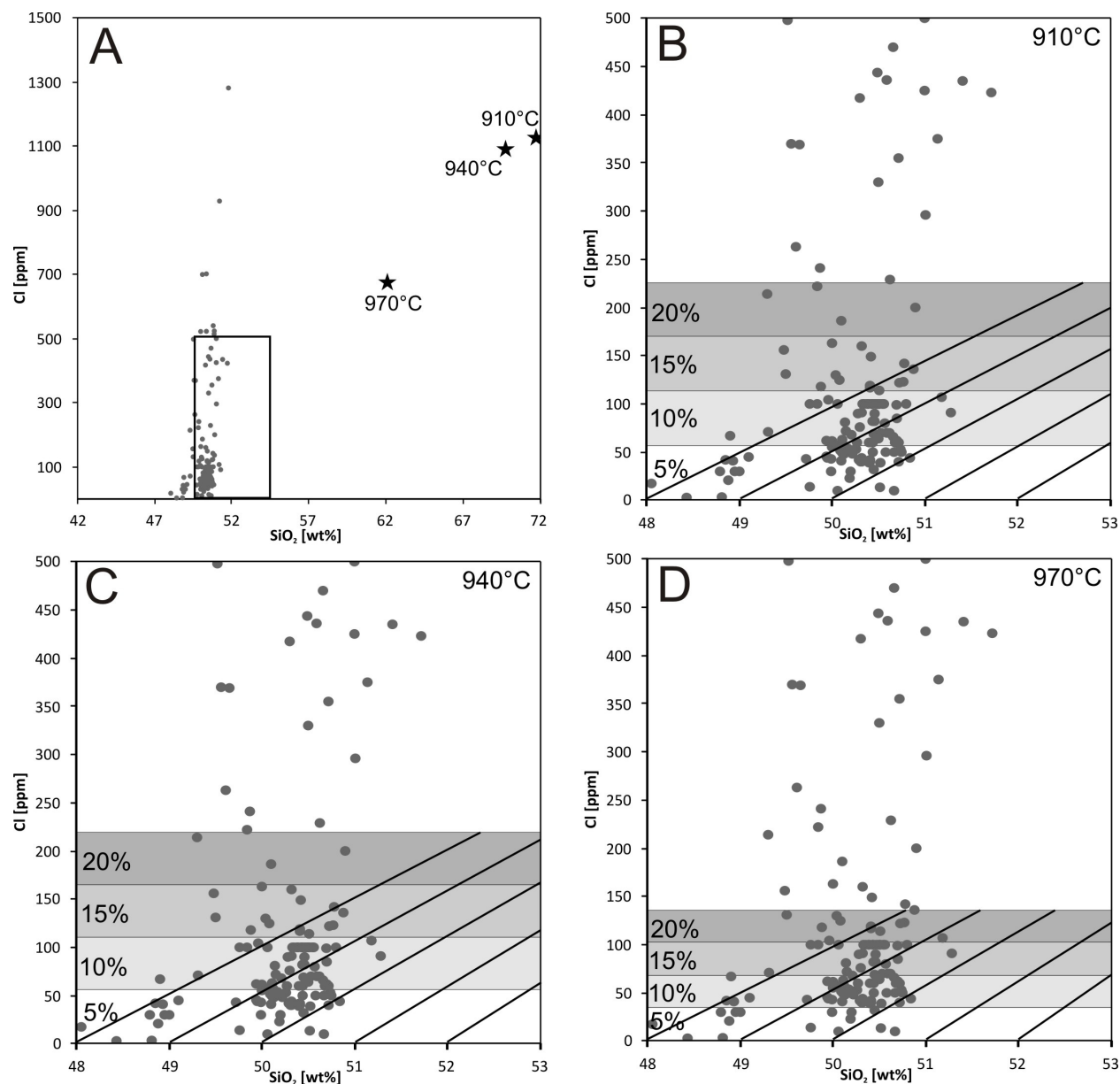


**Figure C.2.5:** MORBs from EPR (see C.2.ESM.3-5 and references therein) in a Cl vs. SiO<sub>2</sub> diagram. **A** Compositions of experimental partial melts are shown as black stars and grey points correspond to natural EPR MORB compositions. Box indicates the close up of **B-D**. **B-D**: Black lines show the calculated evolution trends of MORB contamination by mixing of fresh MORB with different proportions of anatectic melt based on three different experimental partial melt compositions (B: 910°C; C: 940°C; D: 970°C). Individual lines correspond to mixing trends with respect to different initial SiO<sub>2</sub> concentration of the uncontaminated MORB. For example: the addition of 5% anatectic melt generated at 910°C to a MORB with initially 50 wt% SiO<sub>2</sub> leads to an increase in SiO<sub>2</sub> of the mix composition to ~ 51 wt%. Grey fields mark the amount of mixed anatectic melt in the fresh MORB (5, 10, 15 and 20 wt% from light to dark shade).

For simple mixing (Model 1a) we have calculated the compositional change of a fresh, uncontaminated MORB by adding different proportions of an anatectic melt component (up to 20 wt%). Cl concentration of the fresh, uncontaminated MORB was set to 2 ppm according to Michael and Cornell (1998). Results show that mixing with anatectic melts drives the new compositions, in addition to enrichment in Cl, towards more evolved ones (increased SiO<sub>2</sub>; Fig. C.2.5). This strongly limits the potential contribution of simple mixing with felsic melts to a possible MORB contamination, since they can only reproduce the intermediate Cl values, whereas significantly higher Cl contents are observed in EPR MORBs.

In Model 1b, we test the chemical modification that a primitive MORB experiences when assimilation of anatectic felsic melts occurs along with crystallization. The AFC model developed by DePaolo (1981) is used. Results show that similar Cl contents as those observed in contaminated MORB can be obtained with this Model 1b process. However, further calculations using "MELTS" (Ghiorso and Sack 1995) and "Petrolog" (Danyushevsky and Plechov 2011) suggest that such an assimilation suppresses plagioclase crystallization, leading to even more pronounced SiO<sub>2</sub> enrichment compared to mixing. Therefore, anatectic melts cannot be further regarded as a possible contaminant.

In Model 2, the AML bulk composition is modified by the addition of a basaltic rock together with an alteration component (e.g., chlorine) related to the hydrothermal circulation stage (e.g., Coogan et al. 2003). The potential MORB contamination by pure assimilation of rocks from the hydrothermally altered magma chamber roof is also tested using the AFC model of DePaolo (1981). The ratio of mass assimilated to mass crystallized (Ma/Mc) has a strong influence on the Cl content produced by AFC (Fig. C.2.6). We have therefore used minimum (0.1), intermediate (0.25) and maximum values (0.5) according to Michael and Schilling (1989), to bracket the possible compositional range obtained by AFC, and obtain similar results to the ones obtained by those authors.

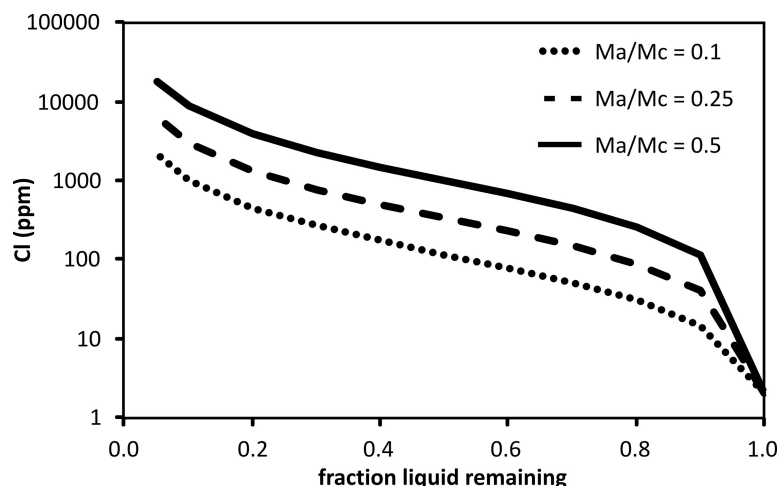


**Figure C.2.6:** Enrichment of Cl during assimilation fractional crystallization (AFC) with hydrothermal altered MORB as assimilant. Ratios of mass assimilated to mass crystallized ( $r$ ) were set to 0.1 (points), 0.25 (dashed line) and 0.5 (solid line) according to Michael and Schilling (1989), bracketing minimum and maximum of possible compositions.

Models 1a, 1b, and 2 are also compared using trace element compositions (Fig. C.2.7). During MORB crystallization process Cl and Nb are two incompatible elements with similar mineral/melt partition coefficients ( $\sim 0.01$ ; Sun et al. 2007). Thus, pure fractionation cannot modify Cl/Nb ratio (Fig. C.2.7). In contrast, assimilation of hydrothermally altered roof rocks, or the corresponding anatectic melts have the potential to modify this ratio (e.g., van der Zwan et al.

2015). Because Cl is more enriched than Nb in the potential contaminants, mixing of uncontaminated MORB with anatectic melts as well as AFC simulations, although differently pronounced, result in elevated Cl/Nb ratios (Fig. C.2.7). The La/Sm ratio is a proxy for mantle source enrichment and shows only minor effects of contamination. It slightly decreases with mixing felsic melts with MORB, because Sm is more enriched in the felsic component relative to La. Model 2 triggers a decrease in La/Sm ratio as an effect of different partition coefficients (McKenzie and O'Nions 1991). Although natural and calculated La/Sm values show the same trend (Fig. C.2.7) the calculated values are slightly elevated. However, Rubin and Sinton (2007) showed that the La/Sm ratio for fast-spreading ridges is  $\sim 1$ , which is significantly lower than the used N-MORB values from Gale et al. (2013) and in turn would shift our calculation towards the natural La/Sm ratios.

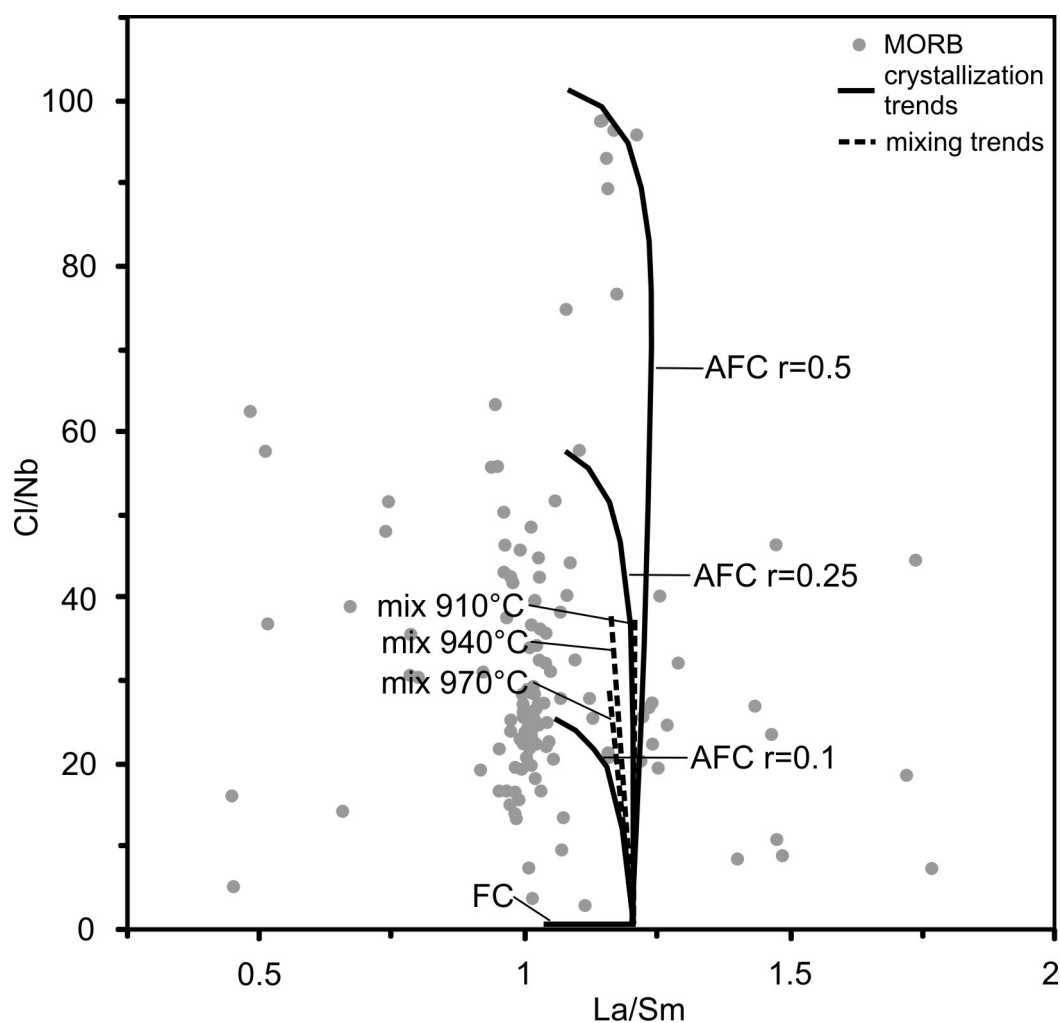


**Figure C.2.6:** Trends for Cl/Nb and La/Sm during assimilation fractional crystallization (AFC; model 2), fractional crystallization (FC) with hydrothermally altered MORB and mixing (mix) with anatectic melts (model 1a) compared to EPR MORB (see C.2.ESM.3-5 and references therein). Cl/Nb ratio is an indicator for assimilation/contamination. La/Sm ratio is a proxy for mantle source enrichment. Dashed lines represent up to 20 wt.% mixing of an anatectic melt component (compositions from 910 °C, 940 °C and 970 °C experiments) with N-MORB (composition from Gale et al. 2013).

One key result of our models is that simple mixing of fresh MORB with anatectic melt (Model 1a) has only a subtle effect on the Cl/Nb ratio, and therefore cannot reproduce the elevated values observed in EPR MORB (Fig. C.2.5 & C.2.7). Also this process (Model 1a) drives  $\text{SiO}_2$

compositions of the mixing product out of the basaltic field, and thus cannot account for the contamination process (Fig. C.2.5). We thus conclude that mixing with anatectic melts at the roof of an AML could only be regarded as a minor contributor to contamination of MORB, whereas stopping and assimilation of altered dikes at the roof of an AML, in association with crystallization, should be considered as the main process for the formation of high-Cl MORB (Michael and Schilling 1989). Based on field, geophysical and geochemical observations from ophiolites and recent oceanic crust, Coogan et al. (2003) and Coogan (2003) came to a similar conclusion that MORB from medium to fast-spreading ridges are contaminated via assimilation of hydrothermal altered oceanic crust.

### **C.2.5. Conclusion**

This study complements results of Erdmann et al. (2015) supporting a model in which anatexis is a major process in forming small felsic intrusions in hornfels of the sheeted dike rooting zone of fast-spreading oceanic crust. Trace element compositions of partial melts generated in experiments at temperatures between 910°C and 970°C correspond to those of natural felsic veins intruding hornfels in the dike/gabbro transition at Site 1256 in the equatorial Pacific. Our results also show that the products of these anatectic processes have in general the potential to contaminate fresh MORB by mixing, but should only be regarded as a minor contributor to the contamination process. This is dominated by AFC with altered dikes as assimilant. The anatectic melts as main assimilant during AFC can be precluded, because SiO<sub>2</sub> enrichment drives compositions out of the basaltic field.

### ***Acknowledgements***

This research used samples and/or data provided by the International Ocean Discovery Program (IODP) expeditions 312, and 335. Funding for this research was provided by grants from the Deutsche Forschungsgemeinschaft (KO 1723/13). We would like to thank Julian Feige and Otto Dietrich for the sample preparation, Tim Müller for the EPMA assistance and André Stechern for the IHPV support. The manuscript has been substantially improved after thorough reviews by H. Rollinson and an anonymous reviewer. This is CRPG contribution no. 2427.





## C.3. Trace elements in anatectic products at the roof of mid-ocean ridge magma chambers: an experimental study

Martin Erdmann<sup>1,2</sup>, Lydéric France<sup>2</sup>, Lennart A. Fischer<sup>1</sup>, Etienne Deloué<sup>2</sup>, and Jürgen Koepke<sup>1</sup>

<sup>1</sup>*Institut für Mineralogie, Leibniz Universität Hannover, Callinstr. 3, 30167 Hannover, Germany*

<sup>2</sup>*CRPG, UMR 7358, CNRS, Université de Lorraine, 15 rue Notre Dame des Pauvres, 54501 Vandoeuvre-lès-Nancy, France*

*Chemical Geology, 2017, submitted version*

*DOI: 10.1016/j.chemgeo.2017.03.004*

### C.3.1. Abstract

At fast-spreading mid-ocean ridges (MORs), the horizon between the axial melt lens (AML) and the overlying sheeted dikes is characterized by extensive anatectic processes. The heat flux of the AML in combination with hydrothermal fluids from above causes high-grade contact metamorphism, which may result in anatexis of the roof rocks above the AML. The products of this process are silica-rich anatectic melts that have the potential to contaminate MOR basalts and residual hornfels. Here, we experimentally simulate the complex igneous and metamorphic processes occurring at the AML roof and provide trace element partition coefficients, which are useful to quantify those processes. We present trace element patterns from experimental anatectic felsic melts and the related residue produced by hydrous partial melting of various types of AML roof rocks. The starting materials used are sheeted dikes and hornfelses from Hole 1256D drilled by the Integrated Ocean Drilling Program. Results are compared with directly-related natural lithologies (i.e., felsic veins and granoblastic hornfels) from the same site, and show that experimental melts produced at low water activity ( $a_{\text{H}_2\text{O}} < 0.5$ ) can be highly enriched in trace elements despite relatively low  $\text{SiO}_2$  contents (58.9 to 65.7 wt%). A low  $a_{\text{H}_2\text{O}}$  is required to reproduce the low  $\text{Al}_2\text{O}_3$  contents observed in natural silica-rich rocks. However, low  $a_{\text{H}_2\text{O}}$  puts into question the importance of residual amphibole for anatectic processes. Residual amphibole is often used as an important phase for explaining trace element characteristics in relevant felsic rocks formed at MORs when modeling anatexis. Because amphibole is lacking in any experimental residue, which is in agreement with natural hornfelses from the dike/gabbro transition at Site 1256, we assume that partial melting within the AML roof rocks proceeds without the participation of amphibole as residual phase. We present a comprehensive set of bulk and mineral/melt trace element partition coefficients obtained from our amphibole-free experimental results for different potential protoliths over a large range of temperature and at different  $a_{\text{H}_2\text{O}}$ s.

### Keywords

*Partial melting, Trace elements, Partition coefficients, Oceanic plagiogranites, Granoblastic hornfels, Fast spreading mid-ocean ridge*

### C.3.2. Introduction

The lower parts of magma chambers at fast-spreading mid-ocean ridges (MORs) are composed of a large zone of crystal mush with less than 20 % of melt, topped by a relatively small axial melt lens (AML) at the transition between crystal mush and sheeted dikes, assumed to be filled locally with nearly pure basaltic melt, the source for MOR basalt (MORB; e.g., Vera et al. 1990; Dunn et al. 2000). Seismic, structural, and geochemical studies from fast-spreading ridges imply that the AML is a transient phenomenon that moves up and down and is likely related to the magmatic activity beneath the spreading segments (Pedersen et al. 1986; Coogan et al. 2003; Wilson et al. 2006; Gillis 2008; Koepke et al. 2008; France et al. 2009, 2010, 2013, 2014; Zhang et al. 2014). Due to the heat flux of an upward-moving AML in combination with hydrothermal fluids released by dehydration of previously-altered sheeted dikes in the AML roof, complex processes, such as metamorphic overprint (producing hornfels) and hydrous anatexis (producing felsic rocks), occur at this horizon. Hornfels is concentrated at the sheeted dike root zone, forming a conducting boundary layer separating the AML, which is filled with a basaltic magma at ~1200°C, from the seawater hydrothermal cells operating at temperatures of max. 400-500°C (e.g., Lister 1974; Gillis 2008); felsic anatectic rocks crosscut the different lithologies of the dike/gabbro transition (e.g., Wilson et al. 2006; France et al. 2009; Teagle et al. 2012). Moreover, these anatectic melts have the potential to contaminate fresh MORB (Coogan et al. 2003; France et al. 2010, 2013, 2014; Fischer et al. 2016), which is temporarily stored in the AML and then transported to the seafloor. The main objective of the present study is to experimentally simulate the complex igneous and metamorphic processes occurring at the roof of AMLs, and to provide partition coefficients for geochemical modeling of those magmatic processes. MORB contamination at crustal levels has indeed been considered in several studies (e.g., Coogan et al. 2003; Haase et al. 2005; Le Roux et al. 2006; France et al. 2010, 2013, 2014; Van der Zwan et al. 2015; Fischer et al. 2016). With new, appropriate trace element partition coefficients as presented in this paper, models and interpretations of such studies could be significantly improved.

At Site 1256 of the International Ocean Discovery Program (IODP), located in the eastern Pacific Ocean in ~15-Ma-old crust, the complete upper crust down to the top of the gabbro sequence, interpreted as a frozen AML, was penetrated for the first time (Fig. C.3.1; Wilson et al. 2006). The core drilled at this site, therefore, provides a perfect sample suite to study the interactions between hydrothermal and magmatic processes at AML margins. In the lower ~60 m of the sheeted dike root zone, above the uppermost gabbros, granoblastic hornfels dominate, representing former hydrothermally-altered sheeted dike basalts with a contact metamorphic overprint (Wilson et al. 2006; Koepke et al. 2008; France et al. 2009, 2010). The gabbros of the former AML are separated by two additional sequences of hornfels. Hornfels xenoliths within the gabbros indicate that assimilation in the melt lens of the overlying roof rocks is an important process (Teagle et al. 2006; France et al. 2009; Koepke et al. 2011). Gabbros and granoblastic hornfels of the core drilled at Site 1256 are intruded by cm-thick felsic rocks in the form of irregular patches, veins, and dikelets consisting of quartz-bearing gabbro, diorite, and tonalite with a fine- to medium-grained granular texture. These rocks bear granular plagioclase, quartz,

magmatic amphibole (altered to secondary amphibole), Fe-Ti oxides, and clinopyroxenes (see Erdmann et al. 2015 for a detailed petrographic description). They are interpreted as frozen melts generated by hydrous partial melting of altered basalt from the sheeted dike root zone (Wilson et al. 2006; Koepke et al. 2008; France et al. 2009, 2010, 2014; Teagle et al. 2012; Erdmann et al. 2015; Fischer et al. 2016). Despite a very low recovery rate of felsic rocks during IODP expeditions 312 and 335, trace element characteristics of these leucocratic veins are characteristic and show pronounced negative anomalies of Ba, Rb, and Sr and positive anomalies of Zr and Hf relative to normal (N-)MORB (Fischer et al. 2016).

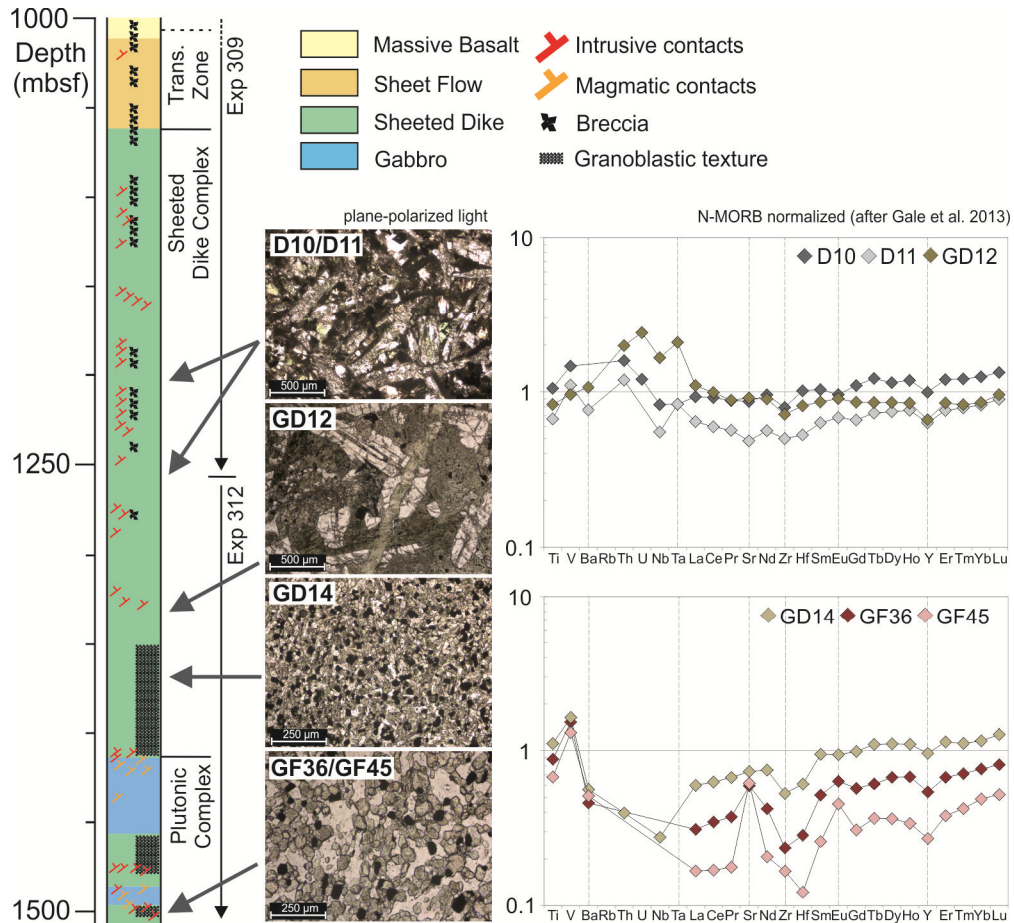


**Figure C.3.1:** Lower part of IODP Site 1256 lithostratigraphic column (modified after Wilson et al. 2006) and the position at which each protolith used for the experiments of this study was sampled. Typical microphotographs in plane-polarized light of the protoliths are given. D10/D11 and GF36/GF45 are petrographically very similar and, thus, only one representative example is shown for each pair. N-MORB normalized (after Gale et al. 2013) trace element patterns are shown for each starting material. Protolith D11 is from Fischer et al. (2016). Modified after Erdmann et al. (2015).

In this experimental study we pursue two goals. First, we aim to reproduce the typical trace element patterns of natural leucocratic veins by testing different sheeted dike rocks drilled at IODP Site 1256 as possible protoliths for felsic melt generation. Thus, instead of using only one starting material, as has often been done in comparable experimental studies, we aim here to present the whole compositional band width of trace elements in felsic melts produced in such an environment. The lithologies used for partial melting experiments vary from poorly- to strongly-altered basalt, to partially- or fully-recrystallized hornfels (Fig. C.3.1). With the results generated

herein we are able to identify which dike material (strongly or weakly altered, and strongly or weakly recrystallized) is affected by hydrous partial melting and, thus, which material should be considered as the protolith of the anatectic felsic rocks that are observed at AML margins. We used the same experiments performed by Erdmann et al. (2015), who investigated the major element characteristics of melts and residual minerals, but in this study we focus exclusively on trace elements analyzed by secondary ion mass spectrometer (SIMS). The second and main objective is to provide trace element bulk partition coefficients between experimental residue and the corresponding melt, as well as partition coefficients for clinopyroxene/melt and plagioclase/melt. These new data are well-suited for modeling the contamination of MORB by assimilation of anatectic melts, with special focus on the metamorphic and alteration state of the sheeted dike protolith.

Numerous experimental studies have been published dealing with dehydration melting of amphibolites and greenstones (see summary in Johannes and Holtz 1996). However, results of these studies are not directly applicable to anatectic processes occurring at the sheeted dike root zone because they mainly focus on processes in the deep continental crust with elevated pressures, often with garnet stable in the residuum. Other studies have included experiments at lower pressure (i.e., 100-200 MPa), but used fresh materials, either rather primitive cumulate gabbro as starting material (Koepke et al. 2004, 2014) or greenstones and amphibolites (Beard and Lofgren 1991), different from the hydrated, altered basalts and dry hornfels of an AML roof. France et al. (2010, 2014) used, for the first time, a strongly hydrothermally-altered basalt from the lower sheeted dikes as starting material. However, the protolith was sampled in the Oman ophiolite whose geodynamic setting and, hence, significance for MOR processes is controversial because protolith composition is untypical for MORB (e.g., MacLeod et al. 2013).

Results of the present study complement two previously-published experimental studies dealing with the same natural protoliths: (1) The comprehensive study of Erdmann et al. (2015) aimed to determine the origin of felsic and granoblastic rocks from IODP Hole 1256D by comparing their modal and major element compositions to experimentally-produced anatectic melts and associated residues. The main approach of this study was to explore the effect of varying protolith modal composition, alteration grade, and recrystallization degree on the experimental products. In order to complement Erdmann et al.'s (2015) study, we have used the same experimental products in the present study, focusing exclusively on trace elements. (2) The study of Fischer et al. (2016) used major and trace element compositions of run products from experiments with one protolith from Erdmann et al. (2015; # D11) to quantify fresh MORB contamination induced by anatectic processes at the roof of AMLs.

### **C.3.3. Methods**

#### ***C.3.3.1. Experimental setup***

The experimental procedure is described in detail by Erdmann et al. (2015) who presented a related study using the same starting material. Here, we give a brief summary of the applied procedure. The natural protoliths were crushed and sieved to a grain size of 125-200  $\mu\text{m}$ . For the

experiments at 910°C close to the solidus, we used, in addition to the powder, mm-sized fragments of the starting material (“microrocks”) in order to obtain larger melt pools, even though equilibrium conditions are thus hampered for these experiments. All experiments were performed in Au capsules and most were water saturated (by adding deionized water). One experimental series was performed under reduced water activity ( $a_{\text{H}_2\text{O}}$ ) by adding  $\text{CO}_2$  to the fluid phase. All experiments were performed in an  $\text{H}_2$ -controlled internally-heated pressure vessel (IHPV) at the Institut für Mineralogie in Hannover at temperatures from 910 to 1030°C and a pressure of 100 MPa. The oxygen fugacity ( $f_{\text{O}_2}$ ) was set with a defined  $P_{\text{H}_2}$  (depending on the experimental temperature, measured by a Shaw membrane) and corresponds to QFM+1 at water-saturated conditions (QFM corresponds to  $f_{\text{O}_2}$  of the quartz-fayalite-magnetite oxygen buffer). Duration of experiments varied from 68 h at 1030°C to 162 h at 910°C and all experimental run products were isobarically quenched (Berndt et al. 2002).

### **C.3.3.2. Analytical methods**

In order to preserve the maximum of sample material, either Au capsules containing experimental run products were carefully sawn apart at the axis and mounted in a ring, or large pieces of the sample material were selected and fixed on a rounded thin section (both 1 inch in diameter). After polishing, high-resolution backscattered electron (BSE) image scans were produced from all experiments with an electron probe micro-analyzer (EPMA). Thus, the exact position of unzoned crystals and crystal-free melt pools within the capsule or sample piece could be determined for SIMS measurements. Analytical techniques to determine major element composition via EPMA, melt-water content (with the “by-difference” method; e.g., Devine et al. 1995), and the calculation of phase proportions (by *ImageJ*; Schneider et al. 2012; <http://imagej.nih.gov/ij/>) of the run products are described in detail by Erdmann et al. (2015).

Trace elements of melt and crystals were analyzed with a Cameca IMS-1270 SIMS at the Centre de Recherches Pétrographiques et Géochimiques in Nancy, France. A 5-30 nA 13 kV  $\text{O}^-$  primary beam was focused on the sample surface, providing spots between 20 and 30  $\mu\text{m}$  in diameter with a slightly oval shape. The secondary ions were accelerated with 10 kV, and analyzed with a mass resolving power of 5500 (analytical session 1, AS1) and 8000 (analytical session 2, AS2). The energy offset was set to -40 V (AS 1) and 0 V (AS 2) with a 40 eV energy window. A reflected light microscope was used to seek the point of interest on the sample by comparison with the high-resolution BSE image scans, and analyzed points were checked after measurement using BSE images of an EPMA. Each analysis (in AS 1 and AS 2) consisted of six cycles, starting from mass  $^{28}\text{Si}$  and increasing to  $^{30}\text{Si}$ ,  $^{47}\text{Ti}$ ,  $^{51}\text{V}$  (3 s each),  $^{85}\text{Rb}$ ,  $^{88}\text{Sr}$ ,  $^{89}\text{Y}$ ,  $^{90}\text{Zr}$ ,  $^{93}\text{Nb}$ ,  $^{138}\text{Ba}$  (6 s each),  $^{139}\text{La}$ ,  $^{140}\text{Ce}$ ,  $^{142}\text{Ce}$ ,  $^{146}\text{Nd}$ ,  $^{147}\text{Sm}$ ,  $^{151}\text{Eu}$ ,  $^{152}\text{Sm}$ ,  $^{153}\text{Eu}$ ,  $^{156}\text{Gd}$ ,  $^{158}\text{Gd}$ ,  $^{161}\text{Dy}$ ,  $^{162}\text{Dy}$ ,  $^{167}\text{Er}$ ,  $^{174}\text{Yb}$ ,  $^{175}\text{Lu}$ ,  $^{176}\text{Lu}$ ,  $^{178}\text{Hf}$ ,  $^{180}\text{Hf}$ , and finally  $^{181}\text{Ta}$  (9 s each) with mass 27.7 and 29.5 as background for electron multiplier and Faraday cup, respectively.  $^{137}\text{Ba}^{16}\text{O}$  (interfering oxide of  $^{153}\text{Eu}$ ) was additionally measured in order to quantify the oxide/element ratio of interfering elements and to compare the results to published values (e.g., Fahey 1998; Hellebrand et al. 2002). However, it is worth mentioning that these authors used a different SIMS (CAMECA ims-4f and -3f) and a direct comparison should be performed with caution. Nevertheless, isotopes affected by interfering oxides were corrected following the general principle of Fahey

(1998). Due to the lower mass resolving power in AS1, the deconvolution in this session was performed for more isotopes ( $^{142}\text{Ce}$ ,  $^{151}\text{Eu}$ ,  $^{152}\text{Sm}$ ,  $^{153}\text{Eu}$ ,  $^{156}\text{Gd}$ ,  $^{158}\text{Gd}$ ,  $^{161}\text{Dy}$ ,  $^{162}\text{Dy}$ ,  $^{167}\text{Er}$ ,  $^{174}\text{Yb}$ ,  $^{176}\text{Lu}$ ,  $^{178}\text{Hf}$ ,  $^{180}\text{Hf}$ ) than in AS2 (for  $^{142}\text{Ce}$ ,  $^{161}\text{Dy}$ ,  $^{162}\text{Dy}$ ,  $^{167}\text{Er}$ ,  $^{174}\text{Yb}$ ,  $^{176}\text{Lu}$ ,  $^{178}\text{Hf}$ ,  $^{180}\text{Hf}$ ).

For further data processing  $^{30}\text{Si}$  was used as reference mass and the Basalt, Hawaiian Volcano Observatory (BHVO)-2-G standard (Wilson 1997; Ila and Frey 2000; Gao et al. 2002; Raczek et al. 2003; Strnad et al. 2005;) was used for calibration. To provide high-quality data, standard measurements were performed at the beginning and the end of the analytical sessions as well as after each sample exchange. Thus, it was possible to determine an individual sensitivity factor (necessary for the exact calculation of the element concentration in ppm; e.g., Fahey 1998) for each single measurement of the unknowns. This individual sensitivity factor arise from a simple linear equation which produces time-dependent values. Data accuracy was checked by analyzing the Basalt, Columbia River (BCR)-2-G standard (Wilson 1997) and the rhyolitic standard of the National Bureau of Standards (NBS)-614 (Gladney et al. 1987) as unknowns. Due to an inaccurate calibration of the  $^{156}\text{Gd}$ ,  $^{158}\text{Gd}$ , and  $^{181}\text{Ta}$  mass peak centers in a few measurements, those data were deleted for the corresponding sample. When this was the case, GdO was not used for the oxide correction of Yb and Lu (up to 30 % overestimation for the corresponding isotopes is possible).

The composition of the starting materials (major and trace elements) was determined by “ACTLABS” (Activation Laboratories Ltd, Ancaster, ON, Canada) via inductively-coupled plasma (ICP) optical emission spectroscopy and ICP-mass spectrometry.

### **C.3.4. Results**

#### ***C.3.4.1. Trace element characteristics of the starting material from IODP Site 1256***

Thanks to the continuous drill section of IODP Site 1256 down to the dike-gabbro transition, we have access to samples from various lithologies of a fast-spreading oceanic crust. For this study we used starting material sampled from the sheeted dike sequence during expeditions 309, 312, and 335 (Fig. C.3.1). We used six different starting materials: two altered basalts from a higher crustal level (D10 and D11); two basalts with granoblastic overprint above the dikes/gabbro (GD12 and GD14); and two high-grade metamorphic granoblastic hornfelses (GF 36 and GF45). For petrographic details of the starting materials that were used, including the original IODP sample names, see Erdmann et al. (2015). Protoliths D10, D11 (previously investigated by Fischer et al. 2016), and GD12 were drilled at depths of 1204 meters below sea-floor (mbsf), 1260 mbsf, and 1334 mbsf, respectively, and exhibit  $\text{SiO}_2$  contents from 48.6-51.5 wt% and  $\text{Al}_2\text{O}_3$  contents from 12.1-15.0 wt%. They are moderately (D10: 27 % alteration, D11: 11 %) to strongly (GD12: 43 %) hydrothermally altered (for details see Erdmann et al. 2015). However, the different grades of alteration are, in contrast to some major elements (e.g., higher  $\text{Al}_2\text{O}_3$  and CaO, lower FeO for GD12), not mirrored by the trace element patterns of the different starting materials. D10 shows N-MORB-like trace element content. D11 is, compared to N-MORB, slightly depleted in most trace elements while the strongly-altered GD12 protolith shows only a marginal depletion in the heavy rare earth elements (HREE). Interestingly, GD14 shows, despite

**Table C.3.1** Trace element compositions (in ppm) of experimental melts with the average (AVG) of  $n$  analyses and the standard deviation ( $SD$ ). Also given is the melt fraction ( $F$ ) and the bulk rock composition of the starting materials

Protolith	Sample	Temperature	Phase	F		Ti	V	Ba	Rb	Th	U	Nb	Ta	La
D-10	starting material		bulk rock			9676	410.00			0.40	0.10	3.00	0.20	3.90
	#23	1030°C	melt	0.79	AVG (n=2)	12645	330.91	3.57	3.22			4.86	0.62	6.64
					SD	657	62.59	1.20	0.09			0.56	0.17	0.03
	#17	1000°C	melt	0.54	AVG (n=3)	14381	387.72	7.82	5.86			3.75		5.16
					SD	835	25.85	0.88	1.19			0.49		0.08
	#11	970°C	melt	0.24	AVG (n=4)	7268	128.29	7.57	4.73			7.41		6.28
					SD	296	7.78	1.70	0.40			0.35		0.26
			cpx	0.25	AVG (n=2)	4012	535.85	0.41	5.85			0.09	1.24	0.50
					SD	146	22.55		0.85					0.08
			pl	0.47	AVG (n=2)	5992	181.70	9.06	4.35			1.24	0.99	2.85
					SD	493	32.50	2.93	0.40			0.92	0.21	0.95
	#29	940°C	melt	0.24	AVG (n=5)	5344	133.50	13.17	3.42			20.44		10.80
					SD	338	35.44	3.12	0.50			3.48		1.87
	#39	910°C	melt	0.20	AVG (n=6)	4359	103.84	19.88	3.63			12.16	1.38	8.26
				SD	181	56.90	6.08	0.15			1.84	0.29	0.90	
#42	1000°C	melt	0.17	AVG (n=2)	7665	72.04	14.67	3.53			17.14		11.90	
	$\alpha\text{H}_2\text{O} < 0.5$			SD	1589	2.17	0.90	0.94			0.27		0.46	
D-11	starting material		bulk rock			6136	309.00	15.00		0.30		2.00	0.20	2.70
	#24	1030°C	melt	0.66	AVG (n=9)	11517	416.40	15.83	3.83			5.81	0.29	8.72
					SD	516	36.64	1.61	0.38			0.20	0.03	1.83
			cpx	0.20	AVG (n=3)	3891	340.05	2.21	5.70			1.05	1.12	0.82
					SD	874	15.55	1.39	0.31			0.62	0.14	0.37
			pl	0.05	AVG (n=2)	5699	244.20	6.79	6.21			2.78	1.34	2.23
					SD	1497	77.56	0.94	3.69			0.63	0.51	0.50
	#18	1000°C	melt	0.38	AVG (n=6)	9522	232.76	15.30	5.23			3.97	1.35	5.23
					SD	728	15.17	1.40	1.37			1.39	0.24	0.64
			cpx	0.36	AVG (n=3)	3485	323.01	2.54	3.49			0.56	0.62	0.89
					SD	504	185.77	1.16	1.31			0.33	0.16	0.26
			pl	0.26	AVG (n=2)	5992	181.70	9.06	4.35			1.24	0.99	2.85
					SD	493	32.50	2.93	0.40			0.92	0.21	0.95
	#12	970°C	melt	0.22	AVG (n=3)	6935	159.91	20.71	6.18			9.84		6.40
					SD	528	9.68	2.78	0.63			1.22		0.62
			cpx	0.44	AVG (n=3)	2242	367.85	0.64	3.67			0.26	0.67	0.23
					SD	132	50.79		0.29			0.12	0.05	0.14
	#30	940°C	melt	0.09	AVG (n=8)	5270	141.50	19.82	1.69			15.20	1.16	6.81
					SD	787	22.10	2.63	0.22			1.60	0.29	0.70
#36	910°C	melt	0.07	AVG (n=4)	2185	60.97	36.08	2.83			16.37	2.00	9.76	
				SD	108	9.30	3.77	0.38			2.36	0.14	1.63	
#40	910°C	melt	0.12	AVG (n=2)	3665	32.84	36.70	3.81			23.15		10.60	
				SD	212	6.32	0.68	0.17			0.54		0.22	
#43	1000°C	melt	0.20	AVG (n=11)	10334	285.32	36.60	5.97			13.89		12.28	
	$\alpha\text{H}_2\text{O} < 0.5$			SD	974	52.98	5.07	0.91			1.78		1.57	
GD-12	starting material		bulk rock			7611	269.00	21.00		0.50	0.20	6.00	0.50	4.60
	#25	1030°C	melt	0.71	AVG (n=9)	11524	331.06	33.64				11.43		8.47
					SD	668	25.91	2.00				0.70		0.52
	#19	1000°C	melt	0.37	AVG (n=1)	8944	179.15	21.99	1.29			13.78	1.03	5.98
					SD									
#13	970°C	melt	0.30	AVG (n=2)		88.81	34.65	1.57			19.32	0.65	9.17	
				SD		7.44	7.62	0.32			0.78	0.38	0.55	
GD-14	starting material		bulk rock			10207	459.00	11.00		0.10		1.00		2.50
	#26	1030°C	melt	0.72	AVG (n=4)	7674	243.94	8.29				3.28		2.40
					SD	384	9.02	0.20				0.33		0.40
	#20	1000°C	melt	0.52	AVG (n=5)	8388	174.73	12.98	2.23			6.78		4.08
					SD	373	4.13	0.48	0.08			0.13		0.54
	#14	970°C	melt	0.31	AVG (n=4)	4989	85.86	16.49	1.55			10.77	0.70	5.20
					SD	1072	35.70	1.24	0.15			1.09	0.22	0.37
	#32	940°C	melt	0.19	AVG (n=4)	4488	110.54	23.32	2.90			15.50		7.82
				SD	895	27.14	0.88	0.66			1.16		0.86	
#45	1000°C	melt	0.16	AVG (n=2)	8457	258.27	28.36	2.73			8.17		9.32	
	$\alpha\text{H}_2\text{O} < 0.5$			SD			1.57	0.36			1.18		0.89	
GF-36	starting material		bulk rock			8083	429.00	9.00						1.30
	#27	1030°C	melt	0.57	AVG (n=4)	11750	524.25	10.96						1.74
					SD	606	21.44	0.21						0.12
#21	1000°C	melt	0.38	AVG (n=4)	7762	253.04	9.94						1.72	
				SD	277	6.32	0.39						0.15	
GF-45	starting material		bulk rock			6195	367.00	10.00						0.70
	#28	1030°C	melt	0.71	AVG (n=4)	6712	351.53	6.41						0.82
					SD	947	47.75	0.84						0.11

**Table C.3.1** *continued*

Sample	Phase	Ce	Pr	Sr	Nd	Zr	Hf	Sm	Eu	Gd	Tb	Dy	Ho	Y	Er	Tm	Yb	Lu
start.	bulk	11.40	1.74	111.00	10.20	81.00	2.50	3.60	1.21	5.00	1.00	6.30	1.40	33.00	4.10	0.63	4.10	0.64
#23	melt	16.44		46.34	10.80	80.81	3.78	3.86	1.39					34.12	3.30		3.34	
		<i>0.27</i>		<i>0.54</i>	<i>0.66</i>	<i>13.12</i>	<i>0.18</i>	<i>0.16</i>	<i>0.14</i>					<i>3.42</i>	<i>0.12</i>		<i>0.21</i>	
#17	melt	16.19		54.47	15.12	153.36		5.00						52.92			4.12	0.69
		<i>0.44</i>		<i>7.44</i>	<i>0.51</i>	<i>8.06</i>		<i>0.37</i>						<i>4.04</i>			<i>0.25</i>	<i>0.13</i>
#11	melt	20.50		33.93	18.05	199.03	4.94	6.22						60.27	6.73		6.01	1.17
		<i>1.27</i>		<i>4.11</i>	<i>1.30</i>	<i>11.63</i>	<i>0.76</i>	<i>0.51</i>						<i>3.95</i>	<i>0.51</i>		<i>0.51</i>	<i>0.04</i>
	cpx	2.16		7.01	4.31	16.84	2.17	2.41	1.51	20.32				30.19	3.04		2.29	0.42
					<i>0.56</i>		<i>0.52</i>	<i>0.20</i>	<i>0.17</i>	<i>0.89</i>					<i>0.25</i>		<i>0.43</i>	<i>0.07</i>
	pl	8.41		49.26	6.77	80.08	2.49	2.67	1.74	1.34				26.39	1.54		2.10	0.13
		<i>1.94</i>		<i>15.11</i>	<i>0.90</i>	<i>8.50</i>	<i>0.12</i>	<i>0.99</i>	<i>0.61</i>	<i>0.97</i>				<i>0.21</i>	<i>0.49</i>		<i>0.43</i>	<i>0.00</i>
#29	melt	41.06		23.42	34.30	336.97		12.12	2.02					77.10				
		<i>11.71</i>		<i>3.91</i>	<i>6.48</i>	<i>55.29</i>		<i>2.73</i>	<i>0.43</i>					<i>16.43</i>				
#39	melt	28.86		40.17	28.20	343.76	7.39	10.74	1.94					70.95	8.57			
		<i>6.29</i>		<i>11.01</i>	<i>4.74</i>	<i>92.63</i>	<i>1.36</i>	<i>1.68</i>	<i>0.23</i>					<i>12.19</i>	<i>1.63</i>			
#42	melt	35.59		31.86	40.83	399.84		14.82	2.31	17.43				114.11			11.51	1.50
		<i>0.90</i>		<i>10.59</i>	<i>1.11</i>	<i>16.13</i>		<i>0.45</i>	<i>0.04</i>	<i>2.91</i>				<i>0.64</i>			<i>1.07</i>	<i>0.16</i>
start.	bulk	7.40	1.12	62.00	6.00	51.00	1.30	2.20	0.86	3.00	0.60	4.10	0.90	21.00	2.60	0.41	2.70	0.43
#24	melt	20.75		103.46	12.63	100.48	1.51	4.74	1.75	10.57				33.32	3.86		3.88	0.52
		<i>3.58</i>		<i>11.09</i>	<i>1.27</i>	<i>3.17</i>	<i>0.41</i>	<i>0.62</i>	<i>0.22</i>	<i>1.09</i>				<i>2.92</i>			<i>1.12</i>	<i>0.16</i>
	cpx	2.71		20.88	3.45	27.52	1.60	1.50	1.35	4.63				21.19	2.29		1.95	0.39
		<i>1.17</i>		<i>10.63</i>	<i>1.03</i>	<i>13.06</i>	<i>0.84</i>	<i>0.18</i>	<i>0.36</i>	<i>1.57</i>				<i>3.05</i>	<i>0.34</i>		<i>0.19</i>	<i>0.04</i>
	pl	6.30		74.25	5.84	67.19	2.35	1.64	1.72	5.87				22.86	2.39		2.50	0.44
		<i>1.45</i>		<i>17.50</i>	<i>1.51</i>	<i>16.24</i>	<i>0.91</i>	<i>0.32</i>	<i>0.38</i>	<i>1.53</i>				<i>6.02</i>	<i>0.66</i>		<i>0.77</i>	<i>0.11</i>
#18	melt	12.99		62.47	8.17	121.58	5.64	4.72						36.54	3.91		4.61	
		<i>1.29</i>		<i>9.58</i>	<i>1.43</i>	<i>19.51</i>	<i>1.01</i>	<i>0.53</i>						<i>4.77</i>	<i>0.78</i>		<i>0.66</i>	
	cpx	2.35		12.11	2.24	20.16	2.14	1.47	0.87	0.66				12.86	1.55		1.84	0.10
		<i>0.65</i>		<i>3.51</i>	<i>0.57</i>	<i>9.32</i>	<i>0.28</i>	<i>0.30</i>	<i>0.27</i>	<i>0.18</i>				<i>4.96</i>	<i>0.36</i>		<i>0.20</i>	<i>0.01</i>
	pl	8.41		49.26	6.77	80.08	2.49	2.67	1.74	1.34				26.39	1.54		2.10	0.13
		<i>1.94</i>		<i>15.11</i>	<i>0.90</i>	<i>8.50</i>	<i>0.12</i>	<i>0.99</i>	<i>0.61</i>	<i>0.97</i>				<i>0.21</i>	<i>0.49</i>		<i>0.43</i>	<i>0.00</i>
#12	melt	18.82		68.34	16.86	210.45	3.06	5.98						61.18	6.65		5.57	0.92
		<i>1.94</i>		<i>7.28</i>	<i>1.86</i>	<i>25.59</i>	<i>0.39</i>	<i>0.66</i>						<i>4.71</i>	<i>0.66</i>		<i>0.38</i>	<i>0.04</i>
	cpx	1.06		5.40	2.02	8.13	0.73	1.11	0.87	17.27				16.07	1.81		1.36	0.18
		<i>0.40</i>		<i>1.30</i>	<i>0.50</i>	<i>2.74</i>	<i>0.12</i>	<i>0.41</i>	<i>0.23</i>	<i>3.32</i>				<i>2.24</i>	<i>0.23</i>		<i>0.31</i>	<i>0.02</i>
#30	melt	21.02		63.72	20.30	248.10	4.59	6.38	1.50					47.49	9.17		4.27	0.25
		<i>2.11</i>		<i>9.88</i>	<i>1.82</i>	<i>29.57</i>	<i>0.54</i>	<i>0.51</i>	<i>0.09</i>					<i>2.85</i>	<i>0.75</i>		<i>0.29</i>	<i>0.02</i>
#36	melt	26.35		98.00	23.48	354.55	4.41	8.08	1.88	6.67				49.62	9.59		5.68	0.88
		<i>0.73</i>		<i>20.88</i>	<i>1.30</i>	<i>44.32</i>	<i>0.71</i>	<i>0.25</i>	<i>0.02</i>	<i>1.47</i>				<i>1.85</i>	<i>3.63</i>		<i>1.36</i>	<i>0.21</i>
#40	melt	26.31		96.31	28.06	421.75	6.23	8.64	2.72	9.73				69.89	10.71		9.28	1.48
		<i>1.72</i>		<i>0.53</i>	<i>0.27</i>	<i>28.05</i>	<i>0.61</i>	<i>1.30</i>	<i>0.32</i>	<i>1.82</i>				<i>1.07</i>	<i>1.44</i>		<i>1.38</i>	<i>0.25</i>
#43	melt	42.56		113.14	27.39	276.64		10.26	3.05	13.47				72.33	18.15		11.58	1.58
		<i>10.84</i>		<i>31.90</i>	<i>3.78</i>	<i>33.31</i>		<i>1.14</i>	<i>0.69</i>	<i>4.11</i>				<i>6.09</i>	<i>6.65</i>		<i>4.16</i>	<i>0.64</i>
start.	bulk	12.30	1.75	117.00	9.60	73.00	2.00	3.00	1.14	3.90	0.70	4.70	1.00	22.00	2.90	0.43	2.80	0.46
#25	melt	21.92		149.65	16.06	138.76	3.81	4.23						39.68	4.19		3.62	0.67
		<i>1.15</i>		<i>5.56</i>	<i>1.11</i>	<i>6.01</i>	<i>0.58</i>	<i>0.49</i>						<i>2.21</i>	<i>0.54</i>		<i>0.35</i>	<i>0.08</i>
#19	melt	14.66		123.05	13.19	155.92	4.00	3.42	1.21					33.38	2.86			
#13	melt	25.31		154.37	21.19	268.26	5.01	6.23	1.81	5.68				43.43	5.48		3.09	0.59
		<i>0.21</i>		<i>44.93</i>	<i>0.08</i>	<i>31.56</i>	<i>1.55</i>	<i>0.16</i>	<i>0.05</i>	<i>1.39</i>				<i>3.47</i>	<i>0.08</i>		<i>0.95</i>	<i>0.33</i>
start.	bulk	7.80	1.33	94.00	8.00	54.00	1.50	3.30	1.19	4.50	0.90	6.10	1.30	32.00	3.90	0.58	3.80	0.61
#26	melt	7.56		98.04	7.82	52.95	2.96	0.86	2.54					30.88	3.31		3.42	0.39
		<i>0.69</i>		<i>0.85</i>	<i>0.51</i>	<i>1.21</i>		<i>0.17</i>	<i>0.41</i>	<i>0.66</i>				<i>1.13</i>	<i>0.46</i>		<i>0.62</i>	<i>0.04</i>
#20	melt	12.40		111.09	13.51	112.90	5.54	4.90	1.91					48.08	5.38			
		<i>0.72</i>		<i>3.48</i>	<i>0.58</i>	<i>2.75</i>	<i>0.34</i>	<i>0.21</i>	<i>0.07</i>					<i>1.11</i>	<i>0.15</i>			
#14	melt	15.59		108.41	17.03	152.96	2.27	6.14	2.08	7.79				48.35	6.87		6.01	1.18
		<i>1.57</i>		<i>8.56</i>	<i>1.38</i>	<i>10.82</i>	<i>0.39</i>	<i>0.53</i>	<i>0.10</i>	<i>1.18</i>				<i>3.69</i>	<i>0.51</i>		<i>0.76</i>	<i>0.25</i>
#32	melt	35.47		90.43	23.11	203.26	3.33	8.79	2.21					63.16	9.63		4.52	
		<i>11.30</i>		<i>45.33</i>	<i>2.20</i>	<i>15.36</i>	<i>1.12</i>	<i>1.34</i>	<i>0.43</i>					<i>14.02</i>	<i>1.74</i>		<i>0.62</i>	
#45	melt	23.98		265.44	19.29	110.93		6.28	3.45	8.42				10.73			6.32	0.97
		<i>4.56</i>		<i>0.28</i>	<i>2.30</i>	<i>14.66</i>		<i>0.80</i>	<i>0.09</i>	<i>0.43</i>				<i>1.85</i>			<i>0.87</i>	<i>0.04</i>
start.	bulk	4.30	0.74	76.00	4.50	24.00	0.70	1.80	0.80	2.60	0.50	3.70	0.80	18.00	2.30	0.37	2.50	0.39
#27	melt	4.94		130.08	4.91	35.97	1.89	2.16	2.12					24.25	2.65		2.71	0.33
		<i>0.18</i>		<i>3.77</i>	<i>0.86</i>	<i>1.83</i>	<i>0.34</i>	<i>0.28</i>	<i>0.19</i>					<i>1.02</i>	<i>0.25</i>		<i>0.11</i>	<i>0.04</i>
#21	melt	4.61		85.19	4.32	36.13	1.99	1.62	1.03	6.49				18.74	1.83			
		<i>0.50</i>		<i>3.33</i>	<i>0.28</i>	<i>1.26</i>	<i>0.15</i>	<i>0.12</i>	<i>0.06</i>	<i>0.77</i>				<i>0.78</i>	<i>0.18</i>			
start.	bulk	2.10	0.35	79.00	2.20	17.00	0.30	0.90	0.57	1.40	0.30	2.00	0.40	9.00	1.30	0.22	1.60	0.25
#28	melt	2.19		99.08	2.28	18.65	0.98	0.99	1.29	3.24				13.95	1.80		1.72	0.25
		<i>0.41</i>		<i>15.99</i>	<i>0.23</i>	<i>3.33</i>	<i>0.44</i>	<i>0.17</i>	<i>0.28</i>									



a distinct granoblastic texture, N-MORB-like trace element content for the medium REE (MREE) and the HREE (similar to D10), only a slight depletion for light REE and Sr, and a pronounced depletion for the high-field-strength elements (HFSE). Protoliths GF36 and GF45 are extensively affected by contact metamorphism and correspond to typical hornfels. This is expressed on the one hand by the obvious granoblastic, hornfelsic texture (see microphotographs in Fig. C.3.1), and, on the other hand, by moderate to strong depletion of the incompatible elements (large ion lithophile elements, LILE, and HFSE). Because granoblastic rocks are generally regarded as the residue of anatectic processes (e.g., Koepke et al. 2008; Alt et al. 2010; France et al. 2010), this depletion is obvious. All protoliths show a slight negative Y anomaly compared to neighboring REE.

#### **C.3.4.2. Trace element contents of experimental products**

Experimental anatectic melt compositions for all six starting materials vary from 51.3 to 72.0 wt% SiO<sub>2</sub> when temperature decreases from 1030°C to 910°C. As shown in Tab. 1, melt fraction decreases simultaneously from 79 to 7 vol% (Tab. C.3.1; determined by *ImageJ*; Schneider et al. 2012; <http://imagej.nih.gov/ij/>) and causes a variation in MgO from 6.3 to 0.9 wt%, in FeO from 11.8 to 3.1, in Al<sub>2</sub>O<sub>3</sub> from 17.1 to 11.3, in TiO<sub>2</sub> from 2.2 to 0.7, and in K<sub>2</sub>O from 0.1 to 0.7. Most experiments are water saturated (*a*H<sub>2</sub>O=1) with water contents from 3.1 to 5.0 wt% (determined with the “by-difference” method; e.g., Devine et al. 1995). One experimental series at 1000°C was performed at water-undersaturated conditions (fluid saturation was ensured by adding CO<sub>2</sub> to the fluid phase), with *a*H<sub>2</sub>O < 0.5 and melt-water contents from 0.8 to 2.0 wt%. The experimental conditions, phase relations, and major element compositions of the phases are described in detail by Erdmann et al. (2015).

The trace element concentrations of all measured experimental anatectic melts are listed in Table C.3.1, and the corresponding MORB-normalized trace element patterns are shown in Figure C.3.2. Depending on the anatectic melt fraction, trace elements could be determined for temperatures from 1030°C down to 910°C for D10 and D11, to 940°C for GD14, to 970°C for GD12, and to 1000°C for GF36. Trace elements for experiments with reduced *a*H<sub>2</sub>O at 1000°C are shown for D10, D11, and GD14. For clarity, REE patterns of D10 and D11 are shown in additional diagrams (Fig. C.3.2). REE patterns of GD 12, GD14, GF36, and GF45 are presented in the electronic supplemental material C.3.ESM).

Moreover, in Figure C.3.2 the calculated composition of the related residue is shown for selected experiments with low partial melting degree and high SiO<sub>2</sub> content. The bulk composition of this mineral assemblage (*c*<sub>residue</sub>) was calculated by using the whole rock composition of the natural protolith (*c*<sub>protolith</sub>) and the experimental melt composition (*c*<sub>melt</sub>) including its known fraction *F*. Hence, the simple mass balance

$$c_{\text{residue}} = [c_{\text{protolith}} - F \cdot c_{\text{melt}}] / [1 - F]$$

can be applied, provided that phases of unreacted starting material in the experimental run product are absent. However, the partial melting reaction in experiments is often inefficient, resulting in relicts of primary magmatic phases of the natural protolith (Johannes and Koepke

2001). This is also the case in some of our experiments, especially at lower temperatures ( $T \leq 970^\circ\text{C}$ ) where a few small cores of unaffected plagioclase and clinopyroxene starting material grains are observed (generally below 1 vol%). Thus, the possibility of disequilibrium melting should be considered when interpreting the results; this may also be an important process in nature (e.g., Naslund 1986; Sawyer 1991). However, due to the low amount of unreacted cores, we consider the procedure of bulk residue calculation to be valid.

With the exception of Sr, which generally behaves compatibly, the concentrations of all trace elements of water-saturated experiments displayed in Figure C.3.2 increase with decreasing temperature and, thus, decreasing degree of partial melting. The N-MORB-normalized trace element patterns (after Gale et al. 2013) exhibit, in general, a negative Eu anomaly, especially for D10 and, to a lesser extent, for D11. Due to a lower concentration in the starting material, the overall melt trace element content is lower in D11 than in D10 when comparing experiments performed under the same conditions.

Experiments performed at reduced  $a\text{H}_2\text{O}$ , despite the relatively high experimental temperature ( $T=1000^\circ\text{C}$ ), show the strongest enrichment of D10 and D11 in all REE and also in most other trace elements. This is remarkable because the melt fraction is, at  $\sim 20\%$ , relatively large, comparable to experiments performed at 940 and  $970^\circ\text{C}$  under water-saturated conditions and distinctly higher than in water-saturated experiments performed at  $910^\circ\text{C}$ .

The exceptional behavior of low  $a\text{H}_2\text{O}$  experiments becomes apparent when the residual composition is calculated. While the D10 experimental residue is in a similar range to low-temperature water-saturated experiments, it is extremely depleted compared to MORB in the D11 series, caused by the relatively high melt fraction in comparison to high  $a\text{H}_2\text{O}$  experiments at 940 and  $910^\circ\text{C}$ . The residue of these two high  $a\text{H}_2\text{O}$  experiments is in a similar range as the D10 residues. While Zr in low  $a\text{H}_2\text{O}$  experiments is less enriched in the partial melts and shows no positive anomaly compared to neighboring elements, it exhibits strong negative anomalies in the experimental residues.

### **C.3.5. Discussion**

#### ***C.3.5.1. Attainment of equilibrium***

Due to the relatively large grain size of the starting material (powder with 125-200  $\mu\text{m}$  for all experiments + mm-sized pieces for experiments at  $910^\circ\text{C}$ ), which is required to generate phases large enough for trace element in-situ analyses, few unreacted clinopyroxene and plagioclase protolith cores (generally below 1 vol% in the runs with powder) were observed, especially at lower temperatures (i.e.  $\leq 970^\circ\text{C}$ ). Thus, a general global equilibrium cannot be assumed in our experiments; rather, disequilibrium partial melting has to be considered when interpreting the experimental results. However, disequilibrium melting may also be an important process in nature (e.g., Naslund, 1986; Sawyer, 1991). Particularly when comparing low-temperature runs with those performed at high temperature, changes in phase relationship (i.e., modes, mineral and melt compositions) cannot simply be interpreted as reflecting changes due to changing temperature but also reflect a change in bulk composition of the system. However, based on the

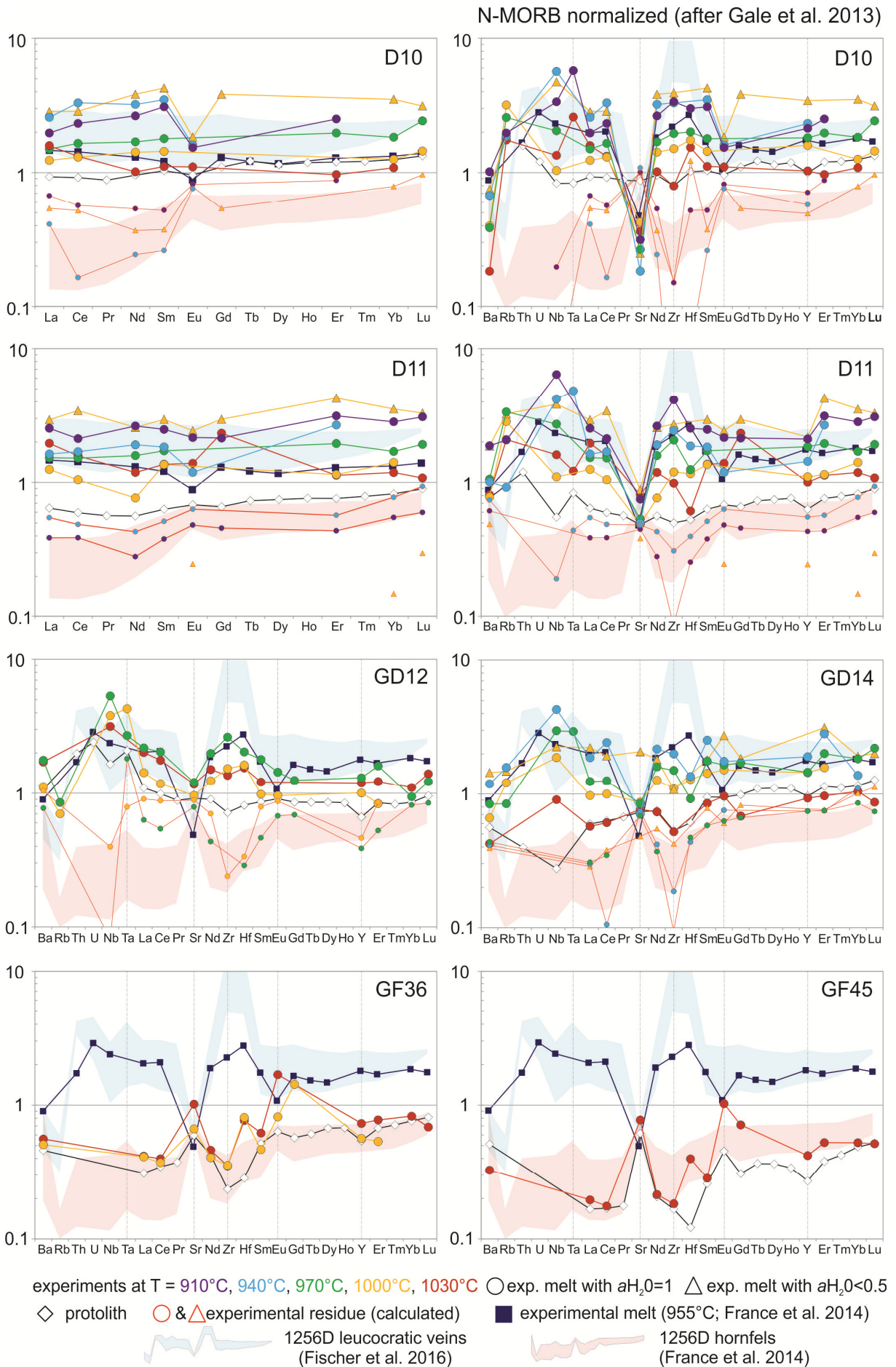


**Figure C.3.2:** (*see previous page*) N-MORB normalized REE and trace element contents of experiments obtained using the different starting materials and natural lithologies. Next to the measured experimental melts produced at varying temperatures, trace element patterns of selected calculated experimental residues and of the natural protoliths are shown. Moreover, the ranges of natural leucocratic veins drilled at IODP Hole 1256D (Fischer et al. 2016) and natural hornfels from 1256D (France et al. 2014) are added for comparison. Normalization values are from Gale et al. (2013). D11 experiment data are partly published in Fischer et al. (2016). GD12, GD14, GF36, and GF45 REE patterns are presented in C.3.ESM.

low amount of unreacted starting material, this change is marginal and has minor influence on the overall results of this study, especially because unreacted areas are generally composed of plagioclase and clinopyroxene. Trace-element-rich accessory minerals (e.g., apatite, zircon) that would be easy to identify on BSE images are not detected. The accordance of partition coefficients determined in this study in comparison to those presented in the literature (e.g., France et al. 2014 who did not observe unreacted starting material; see below) support the reliability of the partial melting experiments of this study and show that small unreacted cores in the experimental residue have minor impact on the partitioning. Evidence for local equilibrium is summarized by Erdmann et al. (2015).

Nevertheless, without global equilibrium, calculation of the melt fraction and proportion of residual phases by mass balance is unfavorable because the composition of the unreacted cores has to be considered. Instead we analyzed the BSE images with *ImageJ* (Schneider et al. 2012; <http://imagej.nih.gov/ij/>) where the small relicts could be easily identified.

#### **C.3.5.2. Comparison of experimental products to natural lithologies**

Due to the large suite of different lithologies drilled at Hole 1256D of IODP Site 1256, a direct comparison of the experimental melts and residues to their natural equivalents is possible. Concerning the felsic melts, a small number of mm-to-cm-thick leucocratic intrusives (fine-grained tonalities) is available for comparison to the experimental anatectic melts (for a detailed petrographic description see Erdmann et al. 2015; for the trace element concentrations see Fischer et al. 2016). These tonalitic veins are regarded as products of in-situ partial melting of AML roof rocks (Koepke et al. 2008; Alt et al. 2010; Zhang et al. 2014). Additionally, trace element compositions of granoblastic hornfels from Site 1256 are available (France et al. 2014) for comparison to the experimental residue of this study. The corresponding diagrams are presented in Figure C.3.2.

While generally similar to trace element patterns of natural leucocratic veins, the experimental D10 and D11 anatectic melts are only enriched in Zr and Hf to a minor extent. Anatectic silica-rich experimental melts from protolith D10 are at least in a similar Zr-Hf range as 1256D leucocratic veins while anatectic melts from D11 and the other protoliths are distinctly lower. Interestingly, the other HFSE (Nb, Ta) and REE of the anatectic silica-rich experimental melts are strongly enriched, in contrast to Zr and Hf, and in some samples are even higher than the natural leucocratic veins. Despite their intergranular to granoblastic textures and, thus, an (initial) metamorphic overprint of the protoliths, experimental melts of GD12 and GD14 are relatively enriched in trace elements in a comparable range to 1256D leucocratic veins. Only the HREE of GD12 melts are slightly less enriched. Due to the refractory character of the GF36 and GF45 starting materials (high grade metamorphic two-pyroxene hornfels), melts measurable with

SIMS could only be produced in the high-temperature range. Their trace element patterns (Figure C.3.2) are highly depleted in trace elements, and their patterns differ from those of the natural tonalites, excluding any model results that suggest felsic melts could be produced by remelting of two-pyroxene hornfels.

The residual mineral assemblage of anatectic silica-rich experiments from protoliths D10, D11, GD12, and GD14 are displayed in Figure C.3.2 in comparison to granoblastic hornfels, recovered from IODP Site 1256 (France et al. 2014), that are generally regarded as the residues of a partial melting event above the AML (Gillis and Roberts 1999; Gillis and Coogan 2002; Gillis 2008; France et al. 2009). Except for a few outliers, the residual assemblage of the low-temperature runs under water-saturated conditions and the experiments performed under reduced  $a_{\text{H}_2\text{O}}$  show a depletion in N-MORB comparable to that seen in natural hornfels from 1256D. This confirms the hypothesis that the trace element enrichment / melt fraction ratio is realistic (see procedure for calculation of the residue in C.4.2) and the chosen D10 and D11 protoliths (moderately altered basalts) are appropriate to simulate partial melting processes at the top of an AML (Erdmann et al. 2015; Fischer et al. 2016). Even initially metamorphic overprinted rocks such as GD12 and GD14 can contribute to the process of felsic melt generation with a granoblastic residual assemblage. However, some elements (e.g., Sr) contradict the general trend and the residue of low  $a_{\text{H}_2\text{O}}$  experiment D11 is completely out of the range. This is mainly caused by varying trace element contents of the protoliths, which is discussed in the following.

#### ***C.3.5.3. Influence of the protolith on trace element enrichment of anatectic melt***

For this study we simulated anatexis with six different protoliths from IODP Site 1256 (Fig. C.3.1). The SIMS results show that the trace element contents of the experimental melts are strongly influenced by the trace element composition of the starting material (Fig. C.3.2). In Figure C.3.2 we additionally included the trace element melt composition of a partial melting experiment from France et al. (2014) who used a fully-altered dike from the Oman ophiolite as protolith. However, the fully-altered character of their protolith, which lacked any primary magmatic mineral (which is typical for the Oman), is uncommon at IODP Site 1256, where basalts are relatively fresh (Teagle et al. 2006, 2012). Additionally, as a consequence of formation in a subduction-related environment (e.g., MacLeod et al. 2013), the starting material used in France et al. (2010, 2014) was relatively enriched in  $\text{SiO}_2$  (54.1 wt%),  $\text{Al}_2\text{O}_3$  (16.2 wt%), and  $\text{K}_2\text{O}$  (0.2 wt%). Moreover, due to analytical issues, they only could measure trace elements down to a melt fraction of 40 vol% (at  $T = 955^\circ\text{C}$ ) which is distinctly higher than in our low temperature experiments ( $< 20$  vol% at  $T \leq 940^\circ\text{C}$ ). Nevertheless, their data are useful for a direct comparison with our results and provide a valuable insight into the anatectic influence on felsic melt generation with regard to trace elements. The trace element pattern of France et al.'s (2014)  $955^\circ\text{C}$  experiment is comparable to those of the anatectic melts of GD12 starting material and generally is in a similar range as our experiments performed at  $970^\circ\text{C}$  and  $1000^\circ\text{C}$ , except in comparison to the strongly-depleted experimental products of protoliths GF36 and GF45.

Because a direct comparison of experiments performed at similar temperatures but with diverse protoliths is difficult, and in order to quantify enrichments / depletions in trace elements, we

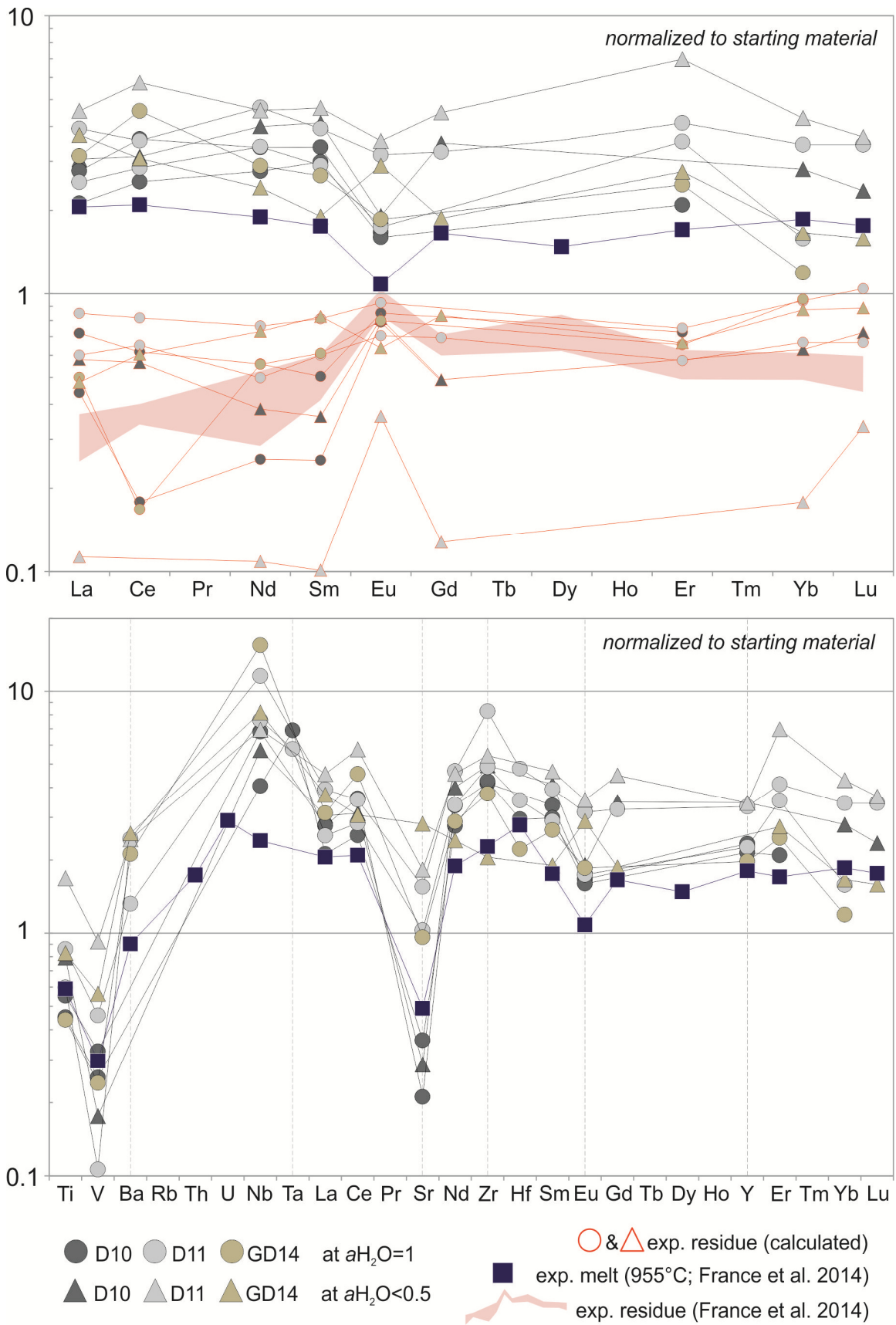


**Figure C.3.3:** a REE and trace element compositions of selected experimental products and calculated residues (only for REE) normalized to the corresponding starting composition. Also shown is the starting material from the normalized experiment by France et al. (2014) performed at 955°C and water-saturated conditions as well as the corresponding range of their calculated residual. Data from experiment D11 are partly from Fischer et al. (2016).



present selected experimental results normalized to the composition of the starting material (Fig. C.3.3). In order to avoid creating diagrams that are overly complex, we only show the D10, D11, and GD14 silica-rich experiments at temperatures of 910 and 940°C and  $a_{\text{H}_2\text{O}} = 1$  and at 1000°C and  $a_{\text{H}_2\text{O}} < 0.5$  in Figure C.3.3; these conditions match best the natural tonalites. The experiment with the lowest melt fraction of France et al. (2014), generated at 955°C, is shown for comparison. Moreover, the corresponding experimental residues of the presented experiments are given and compared to the residual range of France et al. (2014).

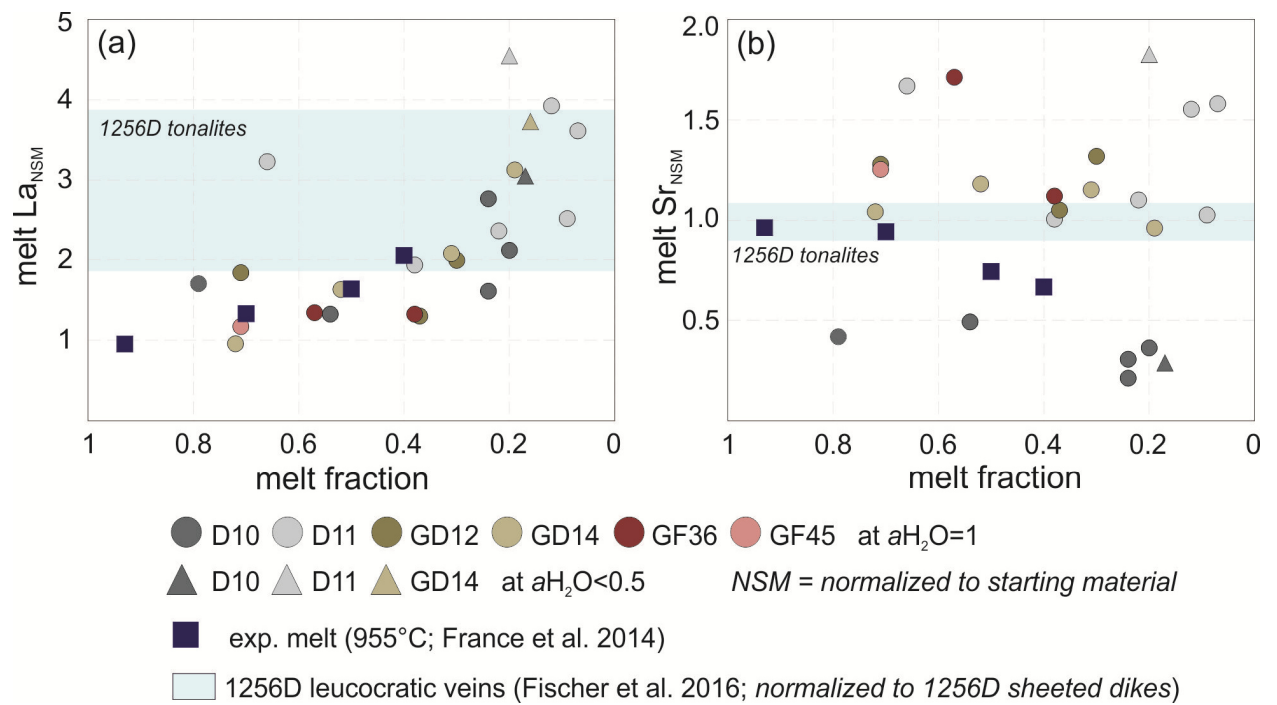


**Figure C.3.4:** Melt (a) La and (b) Sr composition normalized to the starting material versus melt fraction. For comparison, experimental results of France et al. (2014) are indicated as well as the range of 1256D tonalites (Fischer et al. 2016) normalized to 1256D sheeted dikes (expected protolith). D11 experiment data are partly from Fischer et al. (2016).

As already indicated in Figure C.3.2, the exceptional behavior of the water-undersaturated D10 and D11 experiments (1000°C) is shown to be even more pronounced in Figures C.3.3 and C.3.4a. Caused by normalization to the slightly depleted starting material, the low- $a_{\text{H}_2\text{O}}$  D11 run exhibits the strongest enrichment in all REE and most other trace elements. The anatectic melt of the water-saturated D11 experiment performed at 910°C is in a similar range, followed by the low- $a_{\text{H}_2\text{O}}$  D10 run and the water-saturated D11 experiment performed at 940°C. However, the difference from the low- $a_{\text{H}_2\text{O}}$  D11 experiment becomes apparent with regard to the experimental residue (for clarity only shown for REE). While the 910°C/high- $a_{\text{H}_2\text{O}}$  D11 experimental run is only moderately depleted, the water-undersaturated D11 run exhibits an extremely depleted REE pattern. This is mainly caused by the slightly higher melt fraction at low  $a_{\text{H}_2\text{O}}$  (Fig. C.3.4) which is, next to the composition of the protolith, the main influencing variable when calculating the residue. The higher melt fraction of France et al.'s (2014) experiment is also responsible for the relatively strong depletion of the corresponding residue despite a minor enrichment of their anatectic melt. The depletion of their residue is in a similar range as or even stronger than most of the calculated residues of this study except for the

aforementioned water-undersaturated D11 residue (Fig. C.3.3). Figure C.3.4a highlights the continuous increase of REE (exemplarily shown for La) with decreasing melt fraction in all experimental melts (independently of the protolith), and shows a good accordance to 1256D tonalites for melt fractions between 0.1 and 0.3 vol%.

By presenting the experimental results normalized to the starting composition, the fractionation of trace elements between melt and residue can be visualized. One major difference between the anatectic melts of the varying protoliths is the behavior of Sr in D10 in contrast to D11 and GD14 (Fig. C.3.3 and C.3.4b). Sr is depleted in the experimental D10 residue that can be explained by the incorporation of Sr into plagioclase and the slightly higher amount of Sr in the D10 protolith (N-MORB-like, see Fig. C.3.1) compared to the D11 and GD14 protoliths. In the experimental anatectic melts of these starting materials, the Sr content is equal to the starting material (at  $T = 940^{\circ}\text{C}$ ) and, thus, in accordance with 1256D tonalites (Fig. C.3.4b) or slightly enriched (at  $T = 910^{\circ}\text{C}$  and at low  $a_{\text{H}_2\text{O}}$ ). The water-undersaturated GD14 experiment contradicts the observations from the other experiments with low melt fraction. It shows enrichment in Sr, a slight negative anomaly for Zr, and a positive anomaly for Eu (Fig. C.3.3). The GD14 protolith is characterized by a relatively high amount of amphibole (20 vol% compared to  $<1$  vol% in D10 and D11 according to Erdmann et al. 2015), which influences the melting behavior at reduced  $a_{\text{H}_2\text{O}}$  and lowers the  $\text{SiO}_2$  content of the experimental anatectic melt. Thus, the GD14 protolith is less comparable to anatectic silica-rich melts experimentally generated from amphibole-poor protoliths (i.e., D10 and D11).

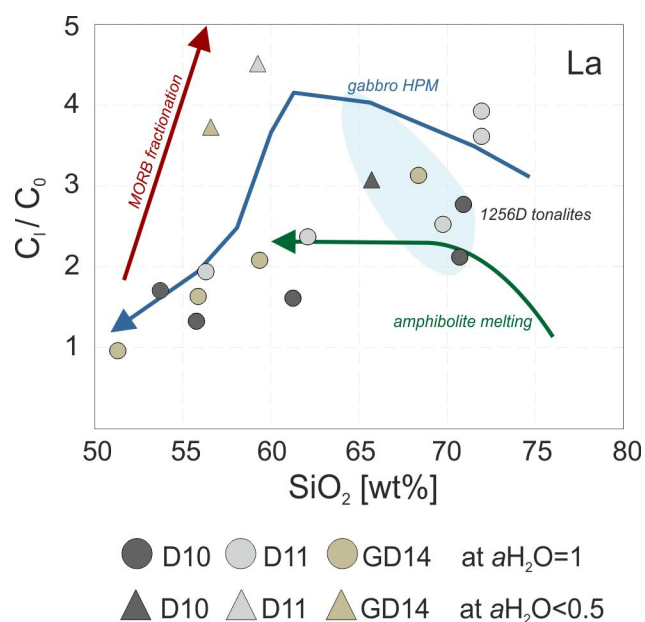


**Figure C.3.5:** La melt concentrations ( $C_i$ ) normalized to the protolith concentrations ( $C_0$ ) versus melt  $\text{SiO}_2$  for selected protoliths (D10, D11, and GD14). Also shown are different processes modeled by Brophy (2008, 2009): (1) equilibrium amphibolite melting (green), (2) hydrous partial melting (HPM) of a cumulative oceanic gabbro (blue), and (3) fractional crystallization of MORB under moderately oxidizing conditions (QFM; red). The field of 1256D tonalites (Fischer et al. 2016) normalized to 1256D sheeted dikes (expected protolith) is indicated in light blue. D11 experiment data are partly from Fischer et al. (2016).

By modeling the partitioning behavior of amphibolite melting (Brophy 2008) and of cumulate gabbro (Brophy 2009), a negative correlation between REE abundances and increasing  $\text{SiO}_2$  was observed for liquids with more than  $\sim 62$  wt%  $\text{SiO}_2$  (Fig. C.3.5). Following the calculations of Brophy (2008), only fractional crystallization leads to steadily increasing REE abundances. Here, we show that continuous REE enrichment in melts with high  $\text{SiO}_2$  contents (up to 72.0 wt%) can also be caused by partial melting of amphibole-free protoliths under water-saturated



conditions. However, the strong REE enrichment of the low- $a_{\text{H}_2\text{O}}$  D11 and GD14 experiments ( $\text{SiO}_2$  only 58.9 and 56.8 wt%, respectively), caused by low global partition coefficients ( $Kd_{\text{residue/melt}}^{\text{REE}} \ll 1$ , see below), is congruent with Brophy's (2008) findings, even though the protoliths are amphibole free (Fig. C.3.5).

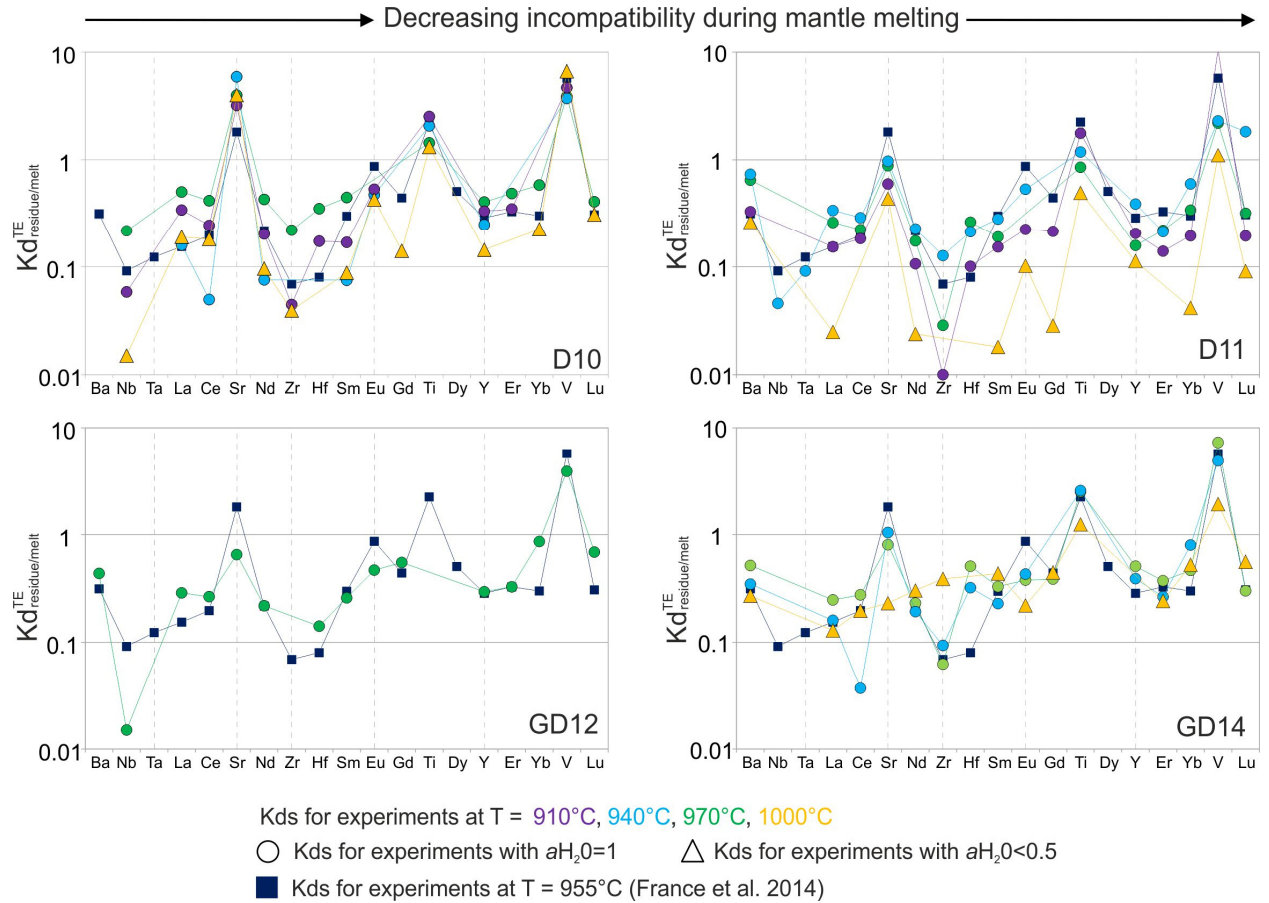


**Figure C.3.6:** Calculated global apparent partition coefficients ( $Kd_{\text{residue/melt}}^{\text{TE}}$ ) for experimental residues and melts obtained from the different protoliths (see text for details). For comparison, the partition coefficients determined by France et al. (2014) are also shown. Data from the D11 experiment are partly from Fischer et al. (2016). Elements are ordered according to decreasing incompatibility during mantle melting (Sun and McDonough 1989).

#### C.3.5.4. Partitioning of trace elements between melt and residue

France et al. (2014) provided the first global apparent partition coefficients quantifying the element partitioning between melt and residue during hydrous partial melting of hydrothermally-altered basalts. Because anatectic melts are an important component for MORB contamination, it is fundamental to provide detailed coefficients in order to track MORB contamination. However, coefficients provided by France et al. (2014) are, on the one hand, related to experiments performed with a fully-altered basalt from the Oman ophiolite (potentially influenced by a subduction zone) and, on the other hand, restricted to one temperature (955°C) with a relatively high melt fraction (40 vol%) under water-saturated conditions. Here, we present for the first time a systematic study performed with different protoliths drilled at a fast-spreading oceanic crust. The anatectic melts were generated at varying temperature down to a melt fraction of 10 vol%

and, in addition, at both high and low  $a\text{H}_2\text{O}$ . The trace element (TE) partitioning between the residual assemblage and the anatectic melt  $Kd_{\text{residue/melt}}^{\text{TE}}$  was calculated following the equation

$$Kd_{\text{residue/melt}}^{\text{TE}} = c_{\text{residue}}/c_{\text{melt}}$$

where  $c_{\text{residue}}$  and  $c_{\text{melt}}$  are the compositions of the residue and the melt, respectively. All calculated  $Kd_{\text{residue/melt}}^{\text{TE}}$  values are listed in Table C.3.2.  $Kd_{\text{residue/melt}}^{\text{TE}}$  for water-saturated experiments from 910 to 970°C and experiments at low  $a\text{H}_2\text{O}$  at 1000°C are plotted in Figure C.3.6 in comparison to  $Kd_{\text{residue/melt}}^{\text{TE}}$  values published by France et al. (2014). Elements have been ordered according to their decreasing incompatibility during mantle melting (Sun and McDonough 1989) in order to highlight the differences in element behaviors ( $Kd_{\text{residue/melt}}^{\text{TE}}$ ) between the generation of primitive basalt caused by mantle melting and silica-rich melts produced by anatexis. As expected, LILE, HFSE, and HREE behave incompatibly and are strongly enriched in the melt (Fig. C.3.6).  $Kd_{\text{residue/melt}}^{\text{TE}}$ -positive anomalies relative to neighboring elements are obtained for Ba, Sr, Ti, V, and, to a lesser extent, Eu. Negative Zr anomalies, probably resulting from the incompatible behavior of Zr in plagioclase, are observed in all experimental melts. The presence of magnetite in all experiments presented in Figure C.3.6 is responsible for the compatible behavior of V and Ti.

Experiments performed at low  $a\text{H}_2\text{O}$  exhibit a distinctive character. While the low  $a\text{H}_2\text{O}$  D10 experiment follows the general trend of  $Kd_{\text{residue/melt}}^{\text{TE}}$ -positive and -negative anomalies in a similar range as the water-saturated experiment with the lowest melt fraction, the water-undersaturated D11 run shows pronounced  $Kd_{\text{residue/melt}}^{\text{TE}}$ -negative anomalies reflecting the very low trace element contents of the calculated residue. Even though the general  $Kd_{\text{residue/melt}}^{\text{TE}}$  trend is comparable to that seen in water-saturated experiments, the low  $a\text{H}_2\text{O}$  D11 experiment shows overall an incompatible behavior (except for V with  $Kd_{\text{residue/melt}}^{\text{V}} = 1.1$ ) with  $Kd_{\text{residue/melt}}^{\text{TE}}$  values approximately one order of magnitude lower than those of D10. The low  $a\text{H}_2\text{O}$  GD14 experiment shows deviating  $Kd_{\text{residue/melt}}^{\text{TE}}$  values for Sr, Zr, and Eu. As stated above, we attribute this to the presence of amphibole in the GD14 protolith that influences the melting behavior at reduced  $a\text{H}_2\text{O}$ .

When comparing  $Kd_{\text{residue/melt}}^{\text{TE}}$  values of this study with those presented by France et al. (2014), a general accordance can be observed (Fig. C.3.6). Despite the fully altered character of their protolith, the partitioning behavior during partial melting is comparable. The residual mineral assemblage of France et al.'s (2014) 955°C experiment is comparable to the assemblage presented in this study, even though they only reproduce the mineral assemblage of natural hornfels at lower temperature (at 955°C small amounts of olivine are still present, and orthopyroxene is not stable yet).

Brophy (2008) stated that for most igneous minerals the partitioning behavior of REE increase significantly with increasing  $\text{SiO}_2$  content of the melt. This can lead to a change of REE

partitioning from incompatible ( $Kd_{residue/melt}^{REE} < 1$ ) at low melt SiO<sub>2</sub> content to compatible ( $Kd_{residue/melt}^{REE} > 1$ ) at higher SiO<sub>2</sub> content in the melt in some minerals, especially hornblende and augite. This is crucial to know for interpreting the generation of felsic rocks by modeling partial melting and fractional crystallization processes. If a change in  $Kd_{residue/melt}^{REE}$  from incompatible to compatible with increasing melt SiO<sub>2</sub> is the normal case, generating felsic melts with SiO<sub>2</sub> contents > 62 wt% and relatively high REE content by partial melting could be excluded, because, following Brophy (2008), REE would be incorporated into the residue. When considering the global residue,  $Kd_{residue/melt}^{REE}$  is always below 1, even at high melt SiO<sub>2</sub> (72.0 wt%), and  $Kd_{residue/melt}^{REE}$  values are generally higher in those experiments with lower melt SiO<sub>2</sub>. Thus, at least in an amphibole-free residue, as is the case in our experiments, we can conclude that continuous REE enrichment at high SiO<sub>2</sub> contents is possible by partial melting (cf. Fig. C.3.5).

**Table C.3.2** Calculated partition coefficients (KD) for residue/melt, clinopyroxene (cpx) /melt, and plagioclase (pl) /melt

Protolith	Sample	Temperature	KD	Ba	Nb	Ta	La	Ce	Sr	Nd	Zr	Hf
D-10	#23	1030°C	residue/melt						7.645	0.736	1.011	
	#17	1000°C	residue/melt		0.566		0.468	0.357	3.256	0.293		
	#11	970°C	residue/melt		0.217		0.502	0.416	3.989	0.428	0.220	0.350
			cpx/melt		0.013		0.079	0.105	0.207	0.239	0.085	0.440
			pl/melt		0.167		0.455	0.410	1.452	0.375	0.402	0.504
	#29	940°C	residue/melt				0.159	0.050	5.919	0.076		
	#39	910°C	residue/melt		0.058		0.340	0.244	3.204	0.202	0.045	0.173
	#42	1000°C dry	residue/melt		0.015		0.190	0.181	3.993	0.096	0.039	
D-11	#24	1030°C	residue/melt	0.846		0.076						0.596
			cpx/melt	0.139	0.181		0.094	0.131	0.202	0.273	0.274	1.062
			pl/melt	0.429	0.478		0.255	0.304	0.718	0.462	0.669	1.560
	#18	1000°C	residue/melt	0.968	0.199		0.220	0.306	0.988	0.571	0.064	
			cpx/melt	0.166	0.140	0.460	0.170	0.181	0.194	0.273	0.166	0.380
			pl/melt	0.592	0.311	0.733	0.546	0.647	0.788	0.828	0.659	0.442
	#12	970°C	residue/melt	0.646			0.259	0.222	0.881	0.174	0.029	0.262
			cpx/melt	0.031	0.026	0.251	0.036	0.056	0.079	0.120	0.039	0.237
	#30	940°C	residue/melt	0.733	0.046	0.091	0.337	0.288	0.970	0.226	0.127	0.212
	#36	910°C	residue/melt	0.372	0.056	0.032	0.222	0.227	0.605	0.199	0.079	0.242
#40	910°C	residue/melt	0.328			0.153	0.183	0.595	0.107	0.010	0.101	
#43	1000°C dry	residue/melt	0.262			0.025		0.435	0.024			
GD-12	#25	1030°C	residue/melt						0.248			
	#19	1000°C	residue/melt	0.929	0.104	0.184	0.635	0.745	0.922	0.568	0.156	0.206
	#13	970°C	residue/melt	0.437	0.015		0.288	0.266	0.654	0.219		0.141
GD-14	#26	1030°C	residue/melt	2.170			1.156	1.113	0.853	1.083	1.071	
	#20	1000°C	residue/melt	0.682			0.194	0.227	0.680	0.150		
	#14	970°C	residue/melt	0.518			0.248	0.276	0.807	0.231	0.062	0.510
	#32	940°C	residue/melt	0.348			0.160	0.037	1.049	0.193	0.093	0.322
	#45	1000°C dry	residue/melt	0.271			0.129	0.197	0.231	0.303	0.389	
GF-36	#27	1030°C	residue/melt	0.585			2.007	2.346	0.355	2.467	2.166	0.521
	#21	1000°C	residue/melt	0.847			1.729	2.113	1.167	2.371	1.798	0.603
GF-45	#28	1030°C	residue/melt	2.935			0.494	0.866	0.301	0.872	0.695	

**Table C.3.2** *continued*

Protolith	Sample	Temperature	KD	Sm	Eu	Gd	Ti	Y	Er	Yb	V	Lu
D-10	#23	1030°C	residue/melt	0.675	0.386			0.844	2.149	2.088	2.138	
	#17	1000°C	residue/melt	0.390			0.289	0.182		0.990	1.125	0.829
	#11	970°C	residue/melt	0.445			1.436	0.405	0.486	0.582	3.889	0.407
			cpx/melt	0.387			0.552	0.501	0.452	0.382	4.177	0.362
			pl/melt	0.429			0.824	0.438	0.228	0.349	1.416	0.112
	#29	940°C	residue/melt	0.075	0.473		2.066	0.247			3.725	
	#39	910°C	residue/melt	0.169	0.532		2.525	0.331	0.348		4.686	
#42	1000°C dry	residue/melt	0.088	0.426	0.141	1.316	0.144		0.224	6.653	0.308	
D-11	#24	1030°C	residue/melt						0.039	0.104	0.241	0.500
			cpx/melt	0.315	0.773	0.438	0.338	0.636	0.594	0.503	0.817	0.748
			pl/melt	0.347	0.982	0.556	0.495	0.686	0.619	0.642	0.586	0.841
	#18	1000°C	residue/melt	0.138			0.426	0.314	0.459	0.332	1.528	
			cpx/melt	0.312			0.366	0.352	0.396	0.398	1.388	
			pl/melt	0.565			0.629	0.722	0.393	0.455	0.781	
	#12	970°C	residue/melt	0.190			0.852	0.158	0.219	0.339	2.195	0.317
			cpx/melt	0.185			0.323	0.263	0.273	0.243	2.300	0.196
	#30	940°C	residue/melt	0.280	0.532		1.181	0.387	0.213	0.596	2.301	1.825
	#36	910°C	residue/melt	0.217	0.417	0.409	2.944	0.380	0.216	0.436	5.374	0.447
	#40	910°C	residue/melt	0.153	0.223	0.214	1.766	0.205	0.140	0.194	10.557	0.194
	#43	1000°C dry	residue/melt	0.018	0.102	0.028	0.492	0.113		0.042	1.104	0.091
GD-12	#25	1030°C	residue/melt							0.219	0.354	
	#19	1000°C	residue/melt	0.804	0.907		0.763	0.459	1.022		1.796	
	#13	970°C	residue/melt	0.259	0.469	0.552		0.295	0.328	0.865	3.899	0.690
GD-14	#26	1030°C	residue/melt	1.409	2.358	3.757	2.179	1.130	1.640	1.391	4.149	3.085
	#20	1000°C	residue/melt	0.319	0.214		1.452	0.303	0.427		4.389	
	#14	970°C	residue/melt	0.329	0.380	0.388	2.516	0.510	0.373	0.467	7.298	0.301
	#32	940°C	residue/melt	0.229	0.431		2.573	0.391	0.265	0.802	4.892	
	#45	1000°C dry	residue/melt	0.435	0.220	0.446	1.246		0.242	0.526	1.925	0.560
GF-36	#27	1030°C	residue/melt	2.234			0.274	1.743	2.094	1.932	0.577	2.977
	#21	1000°C	residue/melt	2.665	1.248	0.505	1.067	2.141	2.817		2.122	
GF-45	#28	1030°C	residue/melt	0.687			0.735			0.761	1.152	1.036

Thus, the models of Brophy (2008) must be observed critically with respect to the question of whether amphibole is present in the residue or not.

With regard to  $Kd_{cpx/melt}^{TE}$  and  $Kd_{pl/melt}^{TE}$ , REE and other trace elements show no significant variation with decreasing temperature, which also corresponds to increasing SiO<sub>2</sub> content (Fig. C.3.7). Unfortunately, due to small crystals in low temperature experiments, trace element measurements of minerals were, only possible at temperatures  $\geq 970^\circ\text{C}$  and, thus, at SiO<sub>2</sub> contents  $\leq 62$  wt%. The change from incompatible to compatible behavior is expected to proceed at higher SiO<sub>2</sub> values (Brophy 2008). However, the clinopyroxene / melt trace element partitioning shows an increasing incompatibility with decreasing temperature, and  $Kd_{cpx/melt}^{TE}$  increases continuously with decreasing incompatibility during mantle melting (Sun and McDonough 1989; Fig. C.3.7). A significant  $Kd_{cpx/melt}^{TE}$  positive anomaly is only observed for V at  $T \leq 1000^\circ\text{C}$ ; V is a compatible element. Trace element partitioning between plagioclase

and melt is less pronounced for temperatures  $\geq 1000^\circ\text{C}$  with most  $Kd_{pl/melt}^{TE}$  values slightly below 1 (Fig. C.3.7).  $Kd_{pl/melt}^{TE}$  positive anomalies, as expected for partitioning between plagioclase and melt, are observed for Sr, Ba, and V at  $970^\circ\text{C}$ . In general, partition coefficients are congruent with published  $Kd_{pl/melt}^{TE}$  values for partitioning in natural silica-rich rocks (e.g., Severs et al. 2009).

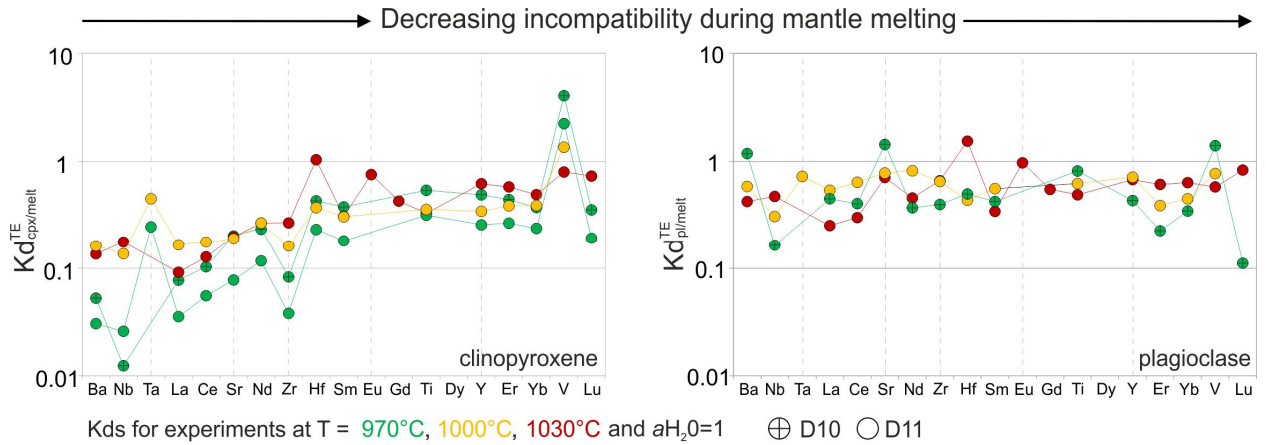


**Figure C.3.7:** Clinopyroxene (cpx)-melt ( $Kd_{cpx/melt}^{TE}$ ) and plagioclase (pl)-melt ( $Kd_{pl/melt}^{TE}$ ) partition coefficients for experiments D10 and D11 performed at temperatures  $\geq 970^\circ\text{C}$ . Elements are ordered according to their decreasing incompatibility during mantle melting (Sun and McDonough 1989).

### C.3.5.5. Implications for modeling anatectic processes, and for tracing MORB contamination

An important outcome of this study is to provide trace element patterns from experimental anatectic felsic melts produced by using various types of dike basalts as starting material under different experimental conditions. These patterns are useful for a direct comparison to natural felsic rocks generated in the MOR environment in order to retrace their origin. We show that the concentration of individual trace elements in experimentally-produced anatectic melts may vary considerably, mainly as a function of the amount of melt fraction, which in turn is controlled by  $a\text{H}_2\text{O}$  and temperature, but also of protolith composition, alteration degree, and recrystallization degree. In order to trace MORB contamination, the large set of experimental results is useful for calculations of mixing and assimilation fractional crystallization processes with the anatectic melts as contaminant (e.g., Fischer et al. 2016).

The heterogeneity of the experimental results is expressed by a large span in  $Kd_{residue/melt}^{TE}$  values for most elements and partition coefficients vary particularly for  $Kd_{residue/melt}^{Ba,Nd,Zr,Sm,Gd}$ . Crystal / melt partition coefficients for some elements can be higher or lower than 1 with the consequence that these elements have the potential to behave either compatibly or incompatibly, depending on the modal amount of individual crystals and melt (Hf, V for clinopyroxene, Ba, Sr, Hf, V for plagioclase). This surprisingly strong variation in element partitioning shown by our experiments brings into question the use of classical partial melting modeling in such a complex environment. Such modeling assumes equilibrium partial melting, crystal/melt equilibrium partition coefficients from the literature, calculated bulk partition coefficients, and a

preconditioned protolith composition. Instead, it seems more appropriate to use the specific characteristics of the trace element patterns obtained in this study, for a direct comparison with felsic rocks formed at oceanic spreading centers.

Another complication in modeling partial melting within such an environment is that related studies often require distinct amounts of residual amphibole for explaining trace element characteristics in relevant felsic rocks formed at fast- or intermediate-spreading MORs (e.g., Haase et al. 2005; Brophy 2008; Wanless et al. 2010; Freund et al. 2013). For their modeling, they involve high-temperature amphibole in the corresponding melting reactions, using amphibole/melt equilibrium partition coefficients obtained experimentally in the magmatic regime. As protolith, these authors assume high temperature amphibolites, but such rocks do not exist at the dike/gabbro transition at IODP Site 1256, where amphibole-bearing rocks are mostly in greenschist facies due to secondary hydrothermal alteration. Moreover, the experimental products of Erdmann et al. (2015) lack any residual amphibole. Thus, it seems more reasonable to assume partial melting within the AML roof rocks at fast-spreading ridges without the participation of amphibole as residual phase, and our experimental results may be used as a suitable alternative in future studies.

### C.3.6. Conclusion

With this study we provide a comprehensive set of bulk and mineral/melt trace element partition coefficients for different potential protoliths of anatectic processes in the roof of AMLs from MORs.  $Kd_{residue/melt}^{TE}$ ,  $Kd_{cpx/melt}^{TE}$ , and  $Kd_{pl/melt}^{TE}$  values are given for a large range of temperature and for different  $aH_2O$ . These data will be useful for future studies that aim to decipher the different processes of felsic melt generation and to track MORB contamination by assimilation of AML roof rocks.

We highlight the importance of trace elements in order to distinguish between different processes of felsic melt generation (i.e., partial melting or fractional crystallization) on the one hand, and potential conditions of felsic melt generation at MORs by anatexis on the other, in particular considering the prevailing  $aH_2O$ . Results of the accompanying Erdmann et al. (2015) study showed that experiments at low  $aH_2O$  are the only way to reproduce the low  $Al_2O_3$  values observed in natural anatectic veins from the dike/gabbro transition at IODP Site 1256. However, relatively low  $SiO_2$  values in the experimental melts cast doubt on the question of whether those anatectic melts can be highly enriched in REE and other trace elements. With this study, we can confirm that anatexis at low  $aH_2O$  is an important process in felsic melt generation. Anatectic experimental melts with melt-water contents  $< 0.5$  wt% produced from protoliths D10 and D11 exhibit not only low  $Al_2O_3$  contents (11.3 to 13.3 wt%) but are also the most enriched in trace elements despite relatively low  $SiO_2$  contents (58.9 to 65.7 wt%). It has to be noted that the experimental residue of the low  $aH_2O$  run D11 is out of the range of natural hornfels; this result was caused by a depleted protolith in combination with a relatively high melt fraction. However, the experimental residue of low  $aH_2O$  run D10 is in accord with the natural equivalent. Experimental anatectic melts at lower temperatures (i.e.  $\leq 940^\circ C$ ) but water-saturated conditions are similarly enriched in trace elements as experiments performed at low  $aH_2O$ . However, these

conditions are unlikely to be due to high  $\text{Al}_2\text{O}_3$  values (up to 16.5 wt%) that are not observed in leucocratic veins from IODP Site 1256.

### ***Acknowledgements***

We thank Otto Dietrich and Julian Feige for their careful sample preparation. This research used samples and/or data provided by the International Ocean Drilling Program (IODP). IODP is sponsored by the U.S. National Science Foundation (NSF) and participating countries under management of the Consortium for Ocean Leadership (COL). Funding for this research was provided by grants from the Deutsche Forschungsgemeinschaft (KO 1723/13).





# Chapter D

## D.1. Constraints on the magmatic evolution of the oceanic crust from plagiogranite intrusion in the Oman ophiolite

Karsten M. Haase<sup>1</sup>, Sarah Freund<sup>1</sup>, Christoph Beier<sup>1</sup>, Jürgen Koepke<sup>2</sup>, Martin Erdmann<sup>2</sup>, Folkmar Hauff<sup>3</sup>

<sup>1</sup>GeoZentrum Nordbayern, Friedrich-Alexander Universität Erlangen-Nürnberg, Schlossgarten 5, 91054 Erlangen

<sup>2</sup>Institut für Mineralogie, Leibniz Universität Hannover, Callinstr. 3, 30167 Hannover, Germany

<sup>3</sup>GEOMAR Helmholtz Centre for Ocean Research Kiel, Wischhofstr. 1-3, 24148 Kiel, Germany

**Contributions to Mineralogy and Petrology, Volume 171(5), pages 1-16, 2016**

**DOI: 10.1007/s00410-016-1261-9**

### D.1.1. Abstract

We present major and trace element as well as Sr, Nd, and Hf isotope data on a suite of 87 plutonic rock samples from 27 felsic crustal intrusions in seven blocks of the Oman ophiolite. The rock compositions of the sample suite including associated more mafic rocks range from 48 to 79 wt% SiO<sub>2</sub>, i.e. from gabbros to tonalites. The samples are grouped into a Ti-rich and relatively light rare earth element (LREE)-enriched P1 group [(Ce/Yb)<sub>N</sub> > 0.7] resembling the early V1 lavas, and a Ti-poor and LREE-depleted P2 group [(Ce/Yb)<sub>N</sub> < 0.7] resembling the late-stage V2 lavas. Based on the geochemical differences and in agreement with previous structural and petrographic models, we define phase 1 (P1) and phase 2 (P2) plutonic rocks. Felsic magmas in both groups formed by extensive fractional crystallization of olivine, clinopyroxene, plagioclase, apatite, and Ti-magnetite from mafic melts. The incompatible element compositions of P1 rocks overlap with those from mid-ocean ridges but have higher Ba/Nb and Th/Nb trending towards the P2 rock compositions and indicating an influence of a subducting slab. The P2 rocks formed from a more depleted mantle source but show a more pronounced slab signature. These rocks also occur in the southern blocks (with the exception of the Tayin block) of the Oman ophiolite implying that the entire ophiolite formed above a subducting slab. Initial Nd and Hf isotope compositions suggest an Indian-MORB-type mantle source for the Oman ophiolite magmas. Isotope compositions and high Th/Nb in some P2 rocks indicate mixing of a melt from subducted sediment into this mantle.

**Keywords:** *Mid-ocean ridge, Fractional crystallization, Subduction*

### D.1.2. Introduction

About two thirds of the Earth's surface are covered by oceanic crust that is formed at a rate of about 3 km<sup>2</sup>/yr at spreading centres and generally, this crust consists of rocks with mafic composition. Periodic intrusion of magma from the mantle into the crust leads to the formation of deep ultramafic to mafic cumulate rocks and gabbroic intrusions below a sheeted dyke complex that forms by magma transport to the uppermost volcanic layer of the oceanic crust

(Coleman 1977; Coogan 2007; Delaney et al. 1998; Wright et al. 2012). This layered structure of the crust, and especially the sheeted dyke complex, reflect the spreading process. At fast-spreading ridges the Moho forms within 2 km of the rift axis and the axial low-velocity zone extends to a width of 10 km implying fast accretion of the crust (Detrick et al. 1987; Phipps Morgan et al. 1994). At slow-spreading ridges the oceanic crust is believed to form within about 200,000 years and within about 3 km of the rift axis (Meurer and Gee 2002) and a similar time span has been determined by zircon age dating for the vertical crystallization of the plutonic part of the crust (Grimes et al. 2008; Lissenberg et al. 2009; Rioux et al. 2012b). The deep plutonic crust apparently forms by multiple intrusions of sills several kilometres below the axial melt lens (Marjanovic et al. 2014; Wanless and Shaw 2012). However, the composition and structure of the oceanic crust can only be studied in three dimensions in ophiolites, although these portions of oceanic crust obducted on continents rarely represent true mid-oceanic spreading but often show geochemical signatures indicating a supra-subduction formation (Dilek and Furnes 2011; Pearce 2003). Felsic intrusives are common both in the oceanic crust and in ophiolites. These rocks are generally called oceanic plagiogranites, which represent a group of SiO<sub>2</sub>-enriched rocks varying from diorite to trondhjemite (Coleman and Peterman 1975). Plagiogranite intrusions occur in the oceanic crust and the uppermost mantle but are most abundant at the boundary between the sheeted dykes and gabbros, i.e. at depths of 1.5 to 2.5 km (Amri et al. 1996; Freund et al. 2014; Pallister 1981). Thus, they could reflect either extreme products of fractional crystallization in shallow melt lenses or they may form by re-melting of hydrothermally altered mafic crustal rocks (e.g. Amri et al. 1996; Brophy 2008). The reasons for the formation of felsic melts of variable compositions and volumes in the predominantly mafic oceanic crust are still poorly understood but these processes are important for the chemical differentiation of the Earth (Rollinson 2008). Additionally, plagiogranitic rocks yield important insights into the evolution of the oceanic crust by magma intrusion (Grimes et al. 2011; Rioux et al. 2013). The Semail ophiolite in northern Oman and United Arab Emirates (UAE) is the largest, best-preserved and best-exposed ophiolite complex on Earth and contains abundant plagiogranite intrusions (Lippard et al. 1986). It is therefore ideally suited to study the evolution of the deeper oceanic crust by magma intrusion and the origin of felsic magmas.

Here we petrologically and geochemically investigate the formation of the shallow-level plagiogranite intrusions in order to define the tectono-magmatic evolution of the Oman ophiolite crust. Systematic sampling of the felsic and associated mafic intrusive rocks in different crustal transects, settings and structural levels can decipher relations and differences of felsic and mafic intrusions and lavas within the Oman ophiolite. We confirm that the plutonic rocks of the Oman ophiolite formed from the same two magma series known from the early V1 and later V2 lava successions. Because the sheeted dyke complex apparently consists of V1 rocks (MacLeod et al. 2013; Umino et al. 2003), the geochemical difference of the late-stage plutonic (P2) samples implies that a considerable portion of the deeper crust was generated off-axis.

### **D.1.3. Geological background**

#### ***D.1.3.1. Geological overview***

The Oman ophiolite (Fig. D.1.1) extends almost 600 km along the Gulf of Oman and covers >20,000 km<sup>2</sup> of the Arabian Peninsula. It comprises twelve blocks extending over several tens of

kilometres that are separated by faults. The northernmost blocks (Khor Fakkan, Aswad and the northern tip of Fizh) are situated within the United Arab Emirates, the central and southern blocks lie on continental crust belonging to the Sultanate Oman (Lippard et al. 1986). Each block comprises a complete section from the mantle (harzburgites, dunites), lower crustal intrusive rocks (wehrlites, pyroxenites, gabbros), and a sheeted dyke complex, in several blocks overlain by lava units with intercalated pelagic sediments (Nicolas et al. 2000a).

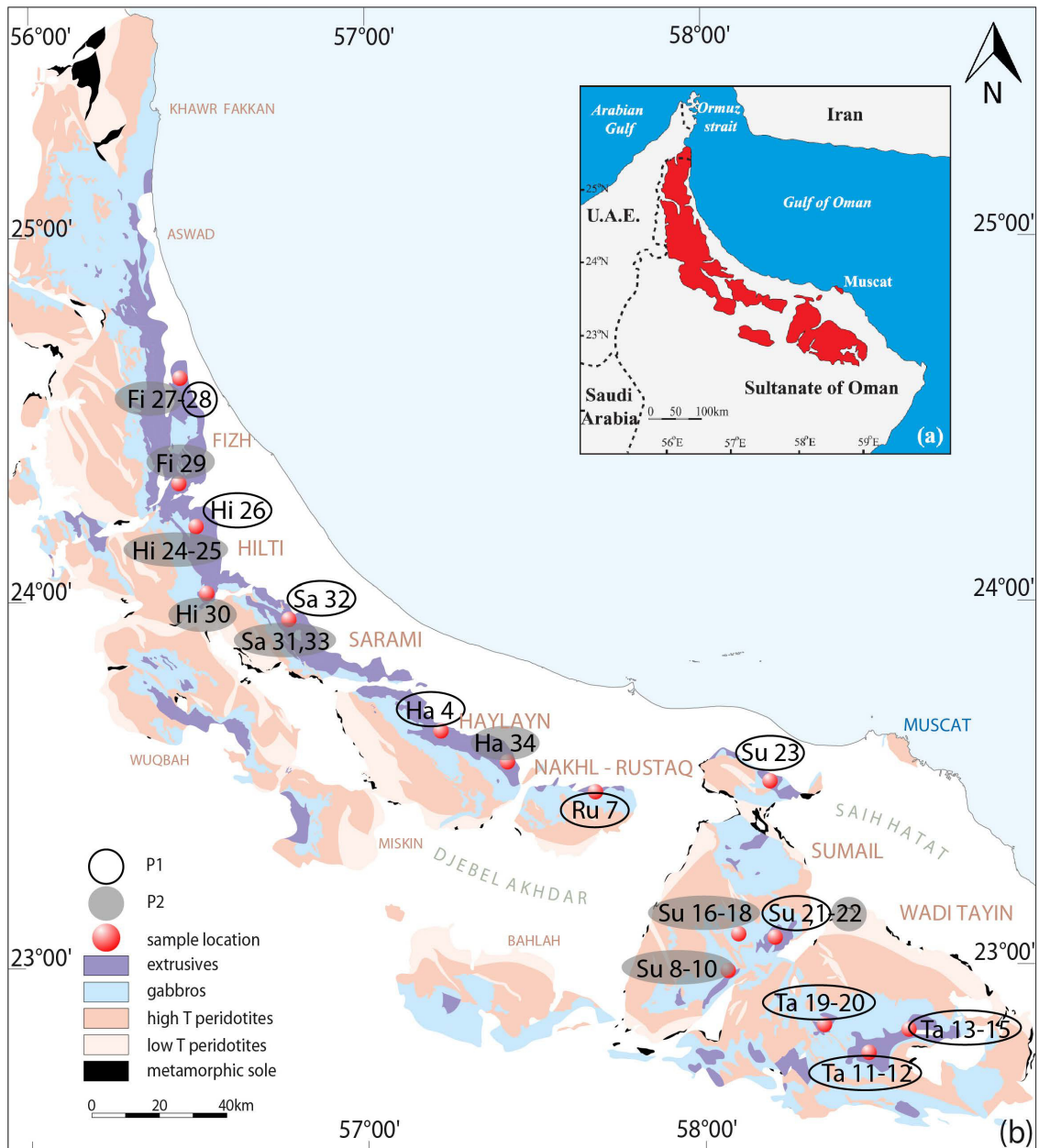


**Figure D.1.1:** Maps of the Semail ophiolite modified after Nicolas et al. (2000a). The ophiolite consist of 12 blocks, each massif comprises a complete section from the mantle, lower crust, sheeted dyke complex up to the lava units. The northernmost blocks (Khor Fakkan, Aswad and the northern tip of Fizh) lie within the United Arab Emirates, the others (most of the Fizh, Hilti, Sarami, Haylayn, Nakhl-Rustaq, Sumail, Tayin, Wuqbah, Miskin and Bahlah massif) belong to the sultanate Oman. **(a)** Geographical overview of the Semail ophiolite. **(b)** Simplified geological map of the Semail ophiolite with sample locations: red dots mark the plagiogranite sample locations, gray circle = P2 group, empty black circle = P1 group.

The geodynamic environment during formation of the Oman ophiolite oceanic crust is debated. Some authors emphasize the fast-spreading character and suggest formation at a mid-ocean-ridge setting (e.g. Coleman 1981; Nicolas et al. 1988) whereas others find geochemical evidence for a supra-subduction zone setting (e.g. Alabaster et al. 1982; Pearce et al. 1981). Geochemical variations may suggest geographically variable tectonic settings, e.g. a north-south gradient within the Oman ophiolite between the MOR-related southern blocks and the subduction-related northern parts (Hanghoj et al. 2010).

Plagiogranites in the Semail Ophiolite are abundant in the upper oceanic crust, most commonly at the base of the sheeted dyke complex as dykes and lenses between 0.5 m up to 1 km length but also within the peridotites of the upper mantle and in the lower gabbro section (Amri et al. 1996; Lippard et al. 1986; Rollinson 2009). Age-dating of these rocks and the surrounding gabbros suggests that the mafic and felsic magmatism was contemporaneous (Rioux et al. 2013; Tilton et al. 1981). However, the formation of plagiogranite magmas has been explained by either partial melting of pre-existing mafic rocks (Amri et al. 1996; Tsuchiya et al. 2013) or by extensive fractional crystallization of a mafic melt (Rollinson 2009; Stakes and Taylor 2003). In contrast, the mantle-hosted plagiogranites formed by partial melting of sediments either early during subduction or late during the obduction process (Briqueu et al. 1991; Cox et al. 1999; Haase et al. 2015; Peters and Kamber 1994; Rioux et al. 2013; Rollinson 2015).

#### ***D.1.3.2. Geochemical overview***

The Oman ophiolite lavas are commonly divided into three consecutive stages; (1) the V1 (or Geotimes) lavas with MORB-like chemistry, (2) the V2 (or Lasail, Alley, clinopyroxene-rich) lavas with a tholeiitic to boninitic composition and subduction signature, and the incompatible element-enriched V3 lavas (e.g. Alabaster et al. 1982; Einaudi et al. 2003; Ernewein et al. 1988; Ishikawa et al. 2002). The V1 lavas are most abundant whereas the V2 and V3 lavas appear to be most common in the northern blocks of the ophiolite. The V2 lavas postdate the V1 lavas but both lava types erupted within a relatively short time interval without significant sediment layers between the two stages (Ernewein et al. 1988). In contrast, the alkaline to transitional tholeiites of the V3 (Salahi) lavas erupted considerably later and probably represent an off-axis magmatic stage (Alabaster et al. 1982; Lippard et al. 1986). The rocks of the sheeted dyke complex have a V1 composition and different magmatic stages with comparable compositions to V1 and V2 lavas are also observed within the plutonic section of the ophiolite (Adachi and Miyashita 2003; Rollinson 2009). Detailed mapping in combination with petrologic and geochemical studies of the cumulate rocks in the deeper crust also revealed early MORB-like magmas during the spreading stage, whereas voluminous post-spreading intrusions formed from a more depleted but water-rich mantle source (Amri et al. 2007; Benoit et al. 1999; Juteau et al. 1988; Python and Ceuleneer 2003; Yamasaki et al. 2006). In agreement with these results, Goodenough et al. (2014) divided the plutonic rocks of the northern Oman ophiolite into a phase 1 and a phase 2 rock series based on mineralogical and textural differences. Additionally, Rollinson (2009) suggested two plagiogranite types with different composition and magma genesis in the crust of the Oman ophiolite; (1) plagiogranites with nearly flat rare earth element (REE) patterns that formed early by partial melting of gabbros, and (2) plagiogranites with a distinct depletion in

light REE compared to the middle and heavy REE that formed late by fractional crystallization from melts from slab-fluid induced melting of depleted mantle.

#### ***D.1.3.3. Ophiolite crust formation age and age of obduction***

The age of the oceanic crust of the Oman ophiolite was determined by the U-Pb isotope analysis of zircons in gabbroic to plagiogranitic intrusions. Tilton et al. (1981) dated zircons from plagiogranites in the upper gabbros of the Oman ophiolite and found U-Pb ages of 93.5 to 97.9 Ma whereas Warren et al. (2005) determined ages of  $95.5 \pm 0.3$  Ma to  $94.3 \pm 0.3$  Ma for rock samples from the same localities. Goodenough et al. (2010) found a range of ages between  $96.4 \pm 0.3$  Ma and  $95.2 \pm 0.3$  Ma in rocks from the northern part of the ophiolite in the United Arab Emirates and suggested an older ( $> 96.4$  Ma) and a younger crustal section. Rioux et al. (Rioux et al. 2012a; 2013) determined zircon U-Pb ages of  $96.44 \pm 0.06$  to  $95.48 \pm 0.06$  Ma for spreading-stage gabbros and plagiogranites of the Oman ophiolite and  $95.41 \pm 0.06$  to  $95.08 \pm 0.06$  Ma for the late-stage gabbros and plagiogranites. After the magmatic formation the oceanic crust underwent thrusting followed by transport of up to 400-500 km in a southwestern direction over the Tethyan Hawasina basin before being emplaced onto the Arabian Plate at about 79 Ma (e.g. Boudier et al. 1988; Coleman 1981; Cowan et al. 2014; Warren et al. 2003).

### **D.1.4. Sampling and analytical methods**

#### ***D.1.4.1. Field observations and sampling***

During field work in 2011 we sampled about thirty felsic intrusions in the Fizh, Hilti, Sarami, Haylayn, Rustaq, Sumail and Wadi Tayin blocks of the Oman ophiolite and recovered about 90 samples (Fig. D.1.1). For simplicity, we will combine the samples under the umbrella term “plagiogranites” in the following because they are mostly tonalites but we also sampled diorites, gabbros, and granodiorites that were associated in the same intrusion (Fig. D.1.2). The samples generally contain plagioclase, quartz, and mostly amphibole as primary major phases (Table 1). Large, isolated plagiogranite bodies occur within the sheeted dyke complex in the northern and central blocks of the Oman ophiolite (Fig. D.1.1, Fizh, Hilti, Sarami, Haylayn and Nakhil-Rustaq blocks). The intrusive bodies are mostly cutting the upper sequences of the crust and are again intruded by aphyric dykes. We also sampled plagiogranites from the southern blocks (Sumail and Wadi Tayin massif) that occur as large bodies or as dykes intruding the gabbros or the sheeted dyke-gabbro transition zone. During our sampling we discriminated (1) the host rocks of the intrusions, i.e. the sheeted dyke complex and the sheeted dyke-root-zone (SDRZ) and (2) the size of the intrusions, i.e. small-scale dykes or sills (cm- to 10 m) and large isolated bodies (10 m- to hundreds of m in diameter).

#### ***D.1.4.2. Analytical methods***

Fresh cores of samples were cut with a rock saw, washed in deionized H<sub>2</sub>O, crushed and pulverized in an agate mill. The loss on ignition (LOI) was determined by weighing the rock powder before and after drying; (1) 12 hours at 105 °C in a cabinet dryer and (2) 12 hours at 1030°C in a muffle furnace. The major element concentrations (SiO<sub>2</sub>, TiO<sub>2</sub>, Al<sub>2</sub>O<sub>3</sub>, Fe<sub>2</sub>O<sub>3</sub><sup>T</sup>, MnO, MgO, CaO, Na<sub>2</sub>O, K<sub>2</sub>O, P<sub>2</sub>O<sub>5</sub>) of whole rocks were measured by X-ray fluorescence (Spectro XEPOS plus) at the GeoZentrum Nordbayern in Erlangen. Averages and recommended values of rock standards GA and BE-N are given in supplementary Table 1.

The major element concentrations of minerals were measured on a JEOL JXA 8200 Superprobe electron microprobe at the GeoZentrum Nordbayern, Erlangen. The oxides SiO<sub>2</sub>, TiO<sub>2</sub>, Al<sub>2</sub>O<sub>3</sub>, FeO<sup>T</sup>, MnO, MgO, CaO, Na<sub>2</sub>O, K<sub>2</sub>O, Cr<sub>2</sub>O<sub>3</sub> (and Cl) were measured. The EMP was operated at an accelerating voltage of 15 kV, a beam current of 15 nA and a focused beam diameter (<< 1 μm) for the mineral analyses (except for feldspar where the beam diameter was set to 3 μm). Counting times were set to 20 s and 10 s for peaks and backgrounds for all elements.

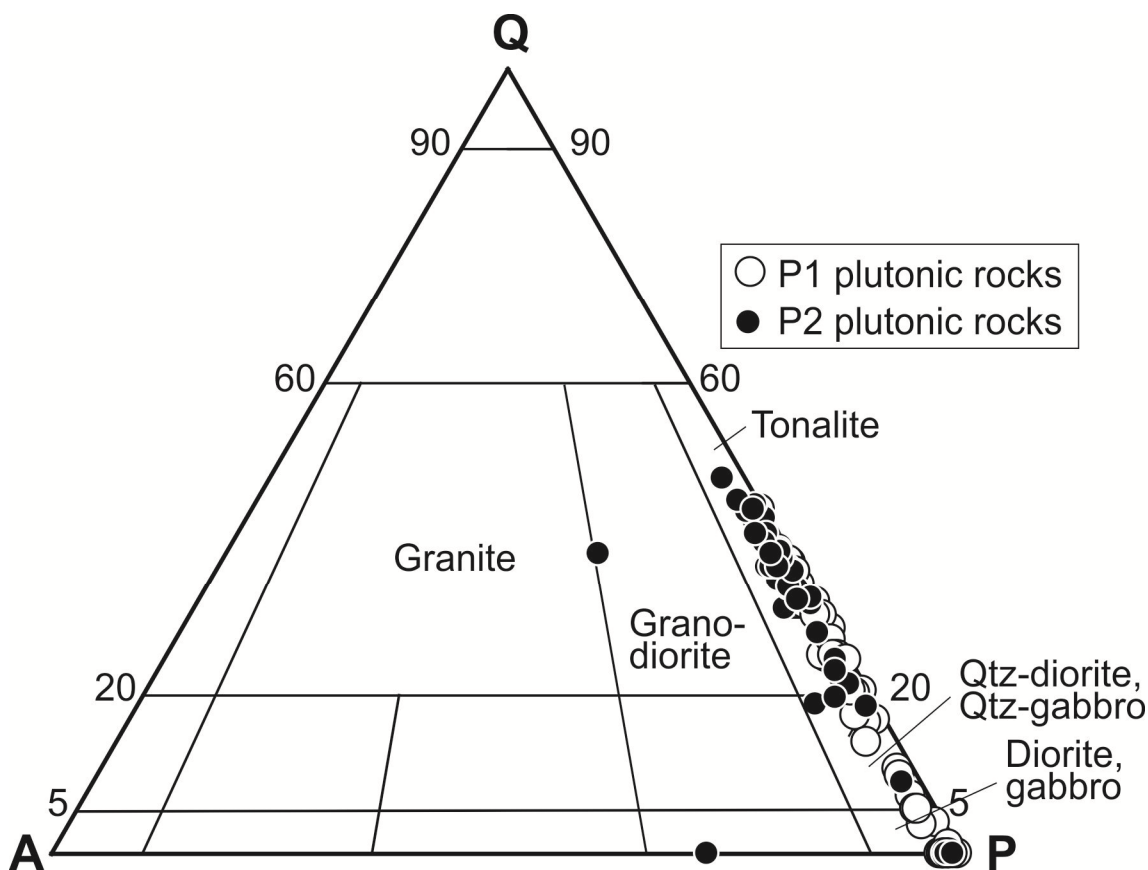


**Figure D.1.2:** Classification of the plutonic rock from this study using CIPW norms (Le Bas and Streckeisen 1991).

Trace elements were analysed using a Merchantek 266 LUV (266nm) laser coupled with an Agilent 7500i inductively coupled plasma-mass spectrometer (LA-ICP-MS) at the GeoZentrum Nordbayern following the procedure described in Schulz et al. (2006). Each glass disc (produced from sample powder for the XRF) was measured four times and the used values are averages. The external calibration was conducted by using NIST 610 (given values from Pearce et al. (1997)). Average values of repeated analyses of international rock standards GH and JA-2 are given in supplementary Table 1. Repeated analyses (n=4) of granitic rock standard GH give a standard deviation for precision  $1\sigma < 5.5\%$  for all elements (except Rb  $< 8\%$ ), and an accuracy  $< 10\%$  for all elements (except Rb, Zr, Ba, Tb, Ho, Th  $< 15\%$ , Sr, Dy, Er, Yb, Lu, Hf  $< 19\%$ , Nb  $< 24\%$ ) and reproducibility of  $< 6\%$  for all elements (except for Eu  $< 14\%$ ). Repeated analyses (n=16) of basaltic rock standard NIST 612 give a standard deviation for precision  $1\sigma < 4\%$  for all elements, accuracy  $< 5\%$  for all elements (except Y, Gd, Er, Tm  $< 10\%$ , Nb, Ta  $< 14.5\%$ ) and reproducibility of  $< 5\%$  for all elements (except Ta  $< 11\%$ ) respectively. Blanks for all trace elements are below 0.030 ppm. Due to more available values and therefore better discrimination

between the crustal plagiogranites we use XRF measurements of Zr concentrations in the following text.

Radiogenic isotope data were generated at GEOMAR Helmholtz Centre for Ocean Research Kiel. Sr-Nd were measured on a TRITON TIMS and Hf on a Nu Plasma II MC-ICPMS both operating in static mode. Sample data is reported in Table 1 relative to  $^{87}\text{Sr}/^{86}\text{Sr} = 0.710250$  ( $2\sigma = 0.000006$ ) for NBS987 ( $n = 8$ ),  $^{143}\text{Nd}/^{144}\text{Nd} = 0.511850$  ( $2\sigma = 0.000007$ ) for the La Jolla standard ( $n = 8$ ) and  $^{176}\text{Hf}/^{177}\text{Hf} = 0.282170$  ( $2\sigma = 0.000004$ ) for the inhouse SPEX monitor ( $n = 16$ ), which corresponds to  $^{176}\text{Hf}/^{177}\text{Hf} = 0.282163$  for JMC-475 (Blichert-Toft et al. 1997).  $\epsilon$  values were calculated using the following CHUR (Chondritic Uniform Reservoir) parameters: present-day reference values are  $^{143}\text{Nd}/^{144}\text{Nd}_{\text{CHUR}} = 0.512630$  and  $^{147}\text{Sm}/^{144}\text{Nd}_{\text{CHUR}} = 0.196$ ,  $^{176}\text{Hf}/^{177}\text{Hf}_{\text{CHUR}} = 0.282785$  and  $^{176}\text{Lu}/^{177}\text{Hf}_{\text{CHUR}} = 0.0336$  (Bouvier et al. 2008),  $^{87}\text{Sr}/^{86}\text{Sr}_{\text{CHUR}} = 0.7045$  and  $^{87}\text{Rb}/^{86}\text{Sr}_{\text{CHUR}} = 0.0827$  following Tsuchiya et al (2013) and  $\lambda_{\text{Sm}} = 6.54 \times 10^{-12} \text{ yr}^{-1}$ ,  $\lambda_{\text{Lu}} = 1.867 \times 10^{-11} \text{ yr}^{-1}$  and  $\lambda_{\text{Rb}} = 1.42 \times 10^{-11} \text{ yr}^{-1}$ . The measured isotope ratios from plagiogranites and mafic wall rocks were age-corrected to 96 Ma (assumed ophiolite age).

## D.1.5. Results

### D.1.5.1. Petrology of the samples

The felsic rocks of the crustal plagiogranite intrusions typically consist of 40 to 60% of euhedral plagioclase laths that are frequently strongly sericitized, and 30 to 50% of quartz. Plagioclase and quartz often occur in granophyric intergrowths (Coleman and Donato 1979). Green amphibole abundance ranges between 5 and 20% in the tonalites and increases in the more mafic rocks. Amphibole is euhedral to anhedral and compositions range from calcium amphiboles (mainly magnesiohornblendes) to actinolite. Biotite is rare in the crustal plagiogranites and both, amphibole and biotite are often replaced by chlorite. Accessory phases are magnetite, ilmenite, sphene, apatite, zircon, and rarely clinopyroxene in variable contents. Most rocks show signs of hydrothermal alteration expressed by minor amounts of actinolite, chlorite, epidote-clinozoisite, prehnite, carbonates and by variable amounts of plagioclase alteration.

### D.1.5.2. Geochemistry and isotope composition

The plutonic rocks ( $n=87$ ) range from (normatively calculated) gabbro, diorite, quartz diorite, granodiorite to tonalite or trondhjemite compositions (Fig. D.1.2). The  $\text{SiO}_2$  contents of the samples from the plagiogranite intrusions range from 48 to 79 wt.% at MgO contents ranging from 10 to 0.1 wt.%. The rocks from larger intrusions frequently show a significant range in compositions. For example, the samples from the 400 m large intrusion SU8 (Sumail block) range between 51.4 and 72.5 wt.%  $\text{SiO}_2$  and those from the RU7 intrusion (Rustaq block) from 49.6 to 70.5 wt.%  $\text{SiO}_2$ . The rocks from plagiogranite intrusions from all blocks show comparable trends in  $\text{CaO}$ ,  $\text{Fe}_2\text{O}_3^{\text{T}}$ ,  $\text{Al}_2\text{O}_3$  and  $\text{MnO}$  for a given MgO. Most rocks contain less than 0.5 wt.%  $\text{K}_2\text{O}$ . Samples from smaller intrusions and dykes are generally more homogeneous and felsic. We observe large variations of  $\text{TiO}_2$  contents between 2 and 10 wt.% MgO in the intrusive rocks and such a variation resembles that known from volcanic rocks and sheeted dykes in the Oman ophiolite (Fig. D.1.3b). Similar variations are observed in  $\text{P}_2\text{O}_5$  for rocks more primitive than 2 wt.% MgO where some samples have higher contents of  $\text{P}_2\text{O}_5$  than other samples for a given MgO content (Fig. D.1.3). The two plutonic groups overlap with the V1 and



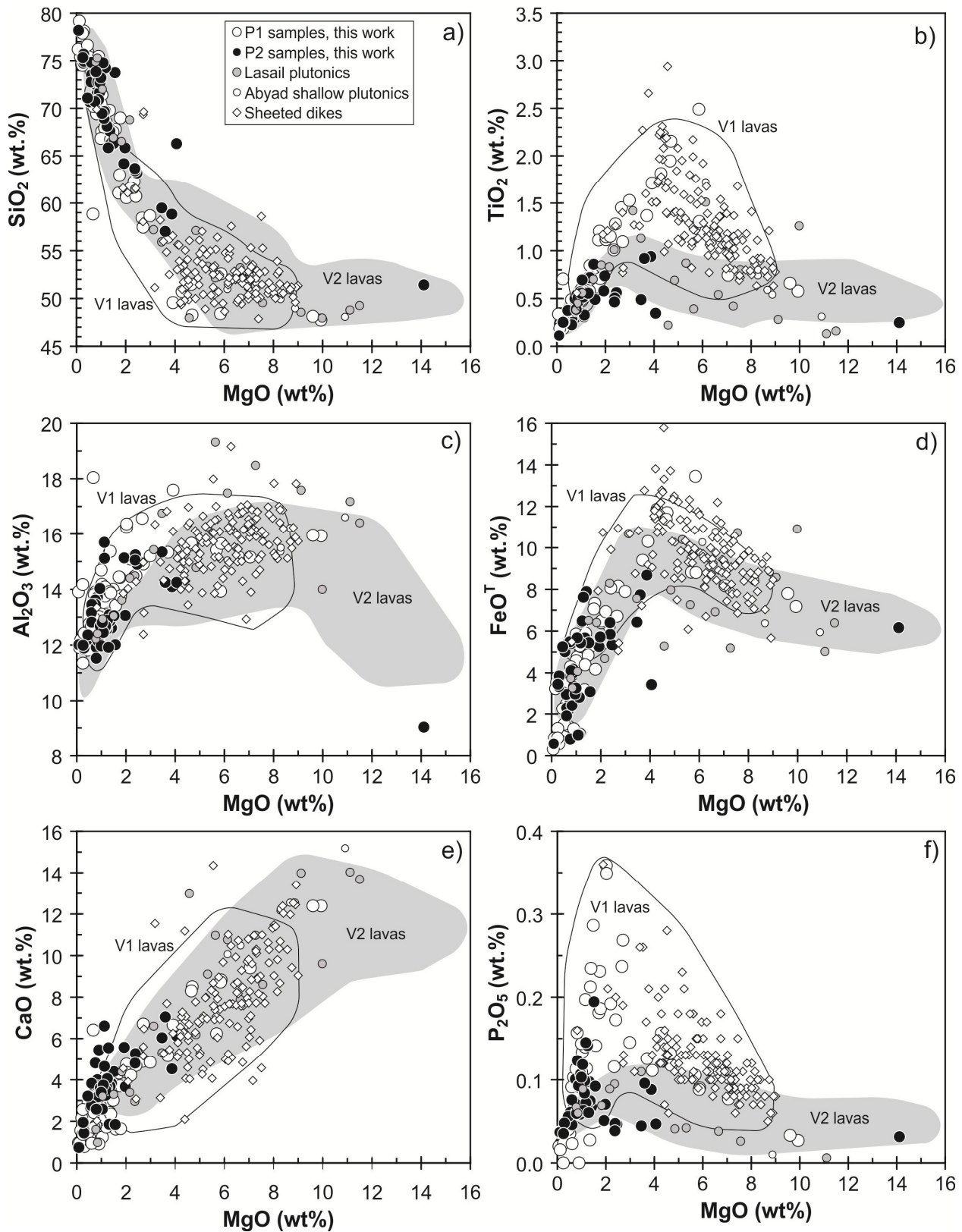


**Figure D.1.3:** Major element variations of plutonic groups P1 and P2 and wall-rocks (this study) compared to V1 and V2 lavas as well as sheeted dyke rocks (Alabaster et al. 1982; Godard et al. 2003; Kusano et al. 2012; MacLeod et al. 2013; Umino et al. 2003), plutonic rocks from the Lasail complex (Fizh block) (Tsuchiya et al. 2013) and from the Abyad complex (Nakhl-Rustaq block) (MacLeod and Yaouancq 2000).



V2 lavas (Godard et al. 2003) but extend to higher SiO<sub>2</sub> contents (Fig. D.1.3). Rocks with less than 2 wt.% MgO all lie on one positive trend of TiO<sub>2</sub> versus MgO but we find significant variations in these rocks in terms of some incompatible elements like Zr or Ce (Fig. D.1.4). Based on the TiO<sub>2</sub>, Zr and Ce variation with MgO we can define a group of rocks from intrusions with higher contents of these incompatible elements for a given MgO than in samples from the other group of intrusions. This compositional systematics closely resembles the chemically distinct volcanic V1 and V2 groups (Figs. D.1.3 and D.1.4). Consequently, we distinguish two groups of the plutonic rocks P1 and P2 where the former generally have higher Ti, Zr, and Ce contents at a given MgO than the latter. In terms of P<sub>2</sub>O<sub>5</sub>, TiO<sub>2</sub>, Zr and Ce the P1 group overlaps with the V1 lava trend and the P2 group overlaps with the V2 lava trend.

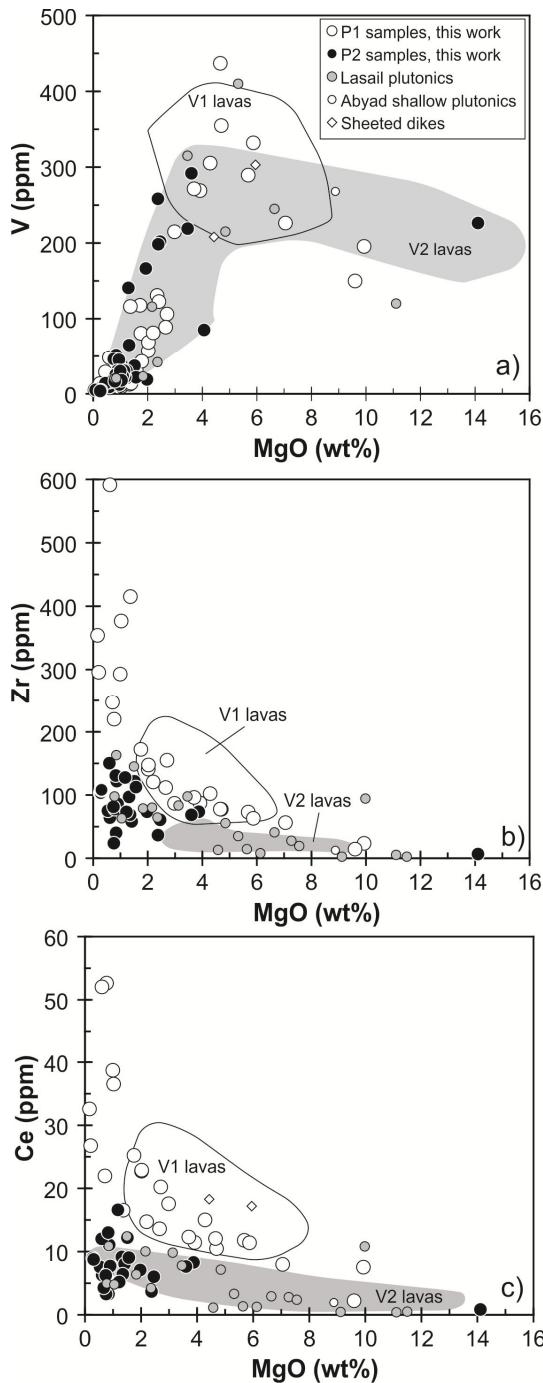


**Figure D.1.4:** Compatible element V (a) and incompatible element concentrations of (b) Zr, and (c) Ce plotted versus MgO showing the distinct compositions of the volcanic and plutonic rock groups. Data sources for V1 and V2 lavas as in Fig. D.1.3.

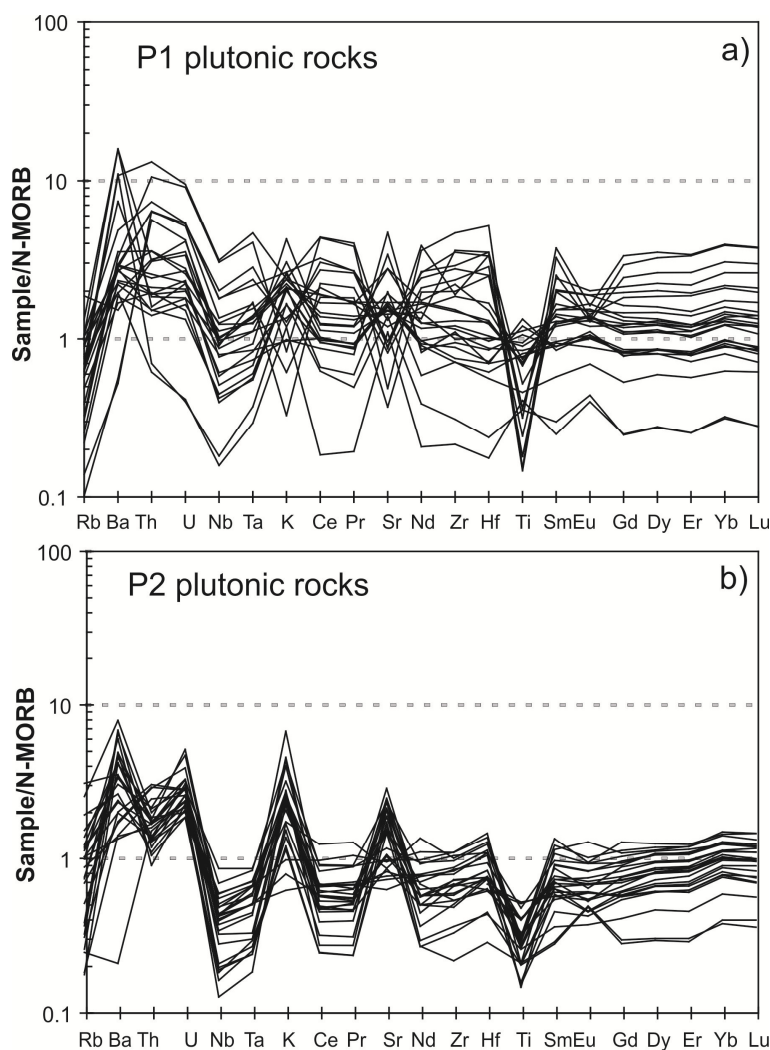


**Figure D.1.5:** Multi element diagrams, comparing the relative element enrichment/depletion and element anomalies of the plagiogranite groups and lavas (P1 & V1 and P2 & V2) versus MORB. Lava glass data are taken from Godard et al. (2003). **(a)** P1 group compared to the V1 lavas: the plagiogranites are more enriched in incompatible elements but overlap with the lavas. P1 and V1 have both pronounced negative Nb and Sr anomalies. **(b)** P2 group compared to the V2 lavas: the plagiogranites are distinct more enriched and do nearly not overlap with the lavas. P2 and V2 have pronounced negative Th, Nb and Ta, and positive Sr anomalies.

The plutonic rocks of both groups show increasing V contents at high MgO but decreasing V between about 4 and 0 wt% MgO (Fig. D.1.4a). The Zr and Ce concentrations of the P1 group rocks are higher at any given MgO content than those of the P2 rocks but both groups show increasing trends with decreasing MgO (Figs. D.1.4b and c). Compared to normal MORB all crustal plagiogranites ( $n=41$ ) show a slight depletion in Rb but are enriched in Ba, U, and K (Fig. D.1.5). Between the groups of the plagiogranites there are differences such as positive and negative Sr and Th anomalies, enrichment or depletion in high field strength elements (HFSE) and rare earth elements (REE) compared to MORB (Fig. D.1.5). With increasing incompatible element compositions the rocks of the P1 group develop negative Sr, Eu and Ti anomalies compared to the neighbouring elements in contrast to the samples from the P2 group, which have distinctly positive Sr anomalies. The P2 group displays enrichments in Ba, Th and U but distinct depletions in Nb and Ta relative to Ce (Fig. D.1.5b). Additionally the REE and HFSE patterns of the P2 group are flat compared to the slightly increasing light REE of the P1 group (Fig. D.1.5).

The P2 group has negative Th anomalies whereas the P1 group displays a slight enrichment and a larger variability of Th compared to neighbouring elements Ba and U. The P1 group exhibits significantly higher  $(\text{Ce}/\text{Yb})_N$  ratios ( $> 0.7$ ), lower  $\text{Sm}/\text{Nd}$  ( $< 0.35$ ) compared to the P2 group (Fig. D.1.6a and b). The  $\text{Eu}/\text{Eu}^*$  ratio of the rocks with more than 3 to 4 wt% MgO are constant but decrease at MgO contents lower than 3 wt.% (Fig. 6c). The  $\epsilon_{\text{Nd}}(96\text{Ma})$  are constant over a large range of MgO contents and those of the plutonic rocks are similar to the  $\epsilon_{\text{Nd}}(96\text{Ma})$  of the lavas (Fig. D.1.6d). The P1 group overlaps in incompatible element ratios (e.g.  $\text{Zr}/\text{Hf}$  vs.  $(\text{Ce}/\text{Yb})_N$ ) with the V1 lavas and the P2 group with the V2 lavas (Fig. D.1.7a, b). The P1 and V1 samples have higher  $(\text{Ce}/\text{Yb})_N$ ,  $(\text{Sm}/\text{Yb})_N$ ,  $\text{Zr}/\text{Hf}$ , and  $\text{Zr}/\text{Yb}$  than the V2/P2 rocks that fall into the lowermost end of the East Pacific MORB field (Fig. D.1.7).

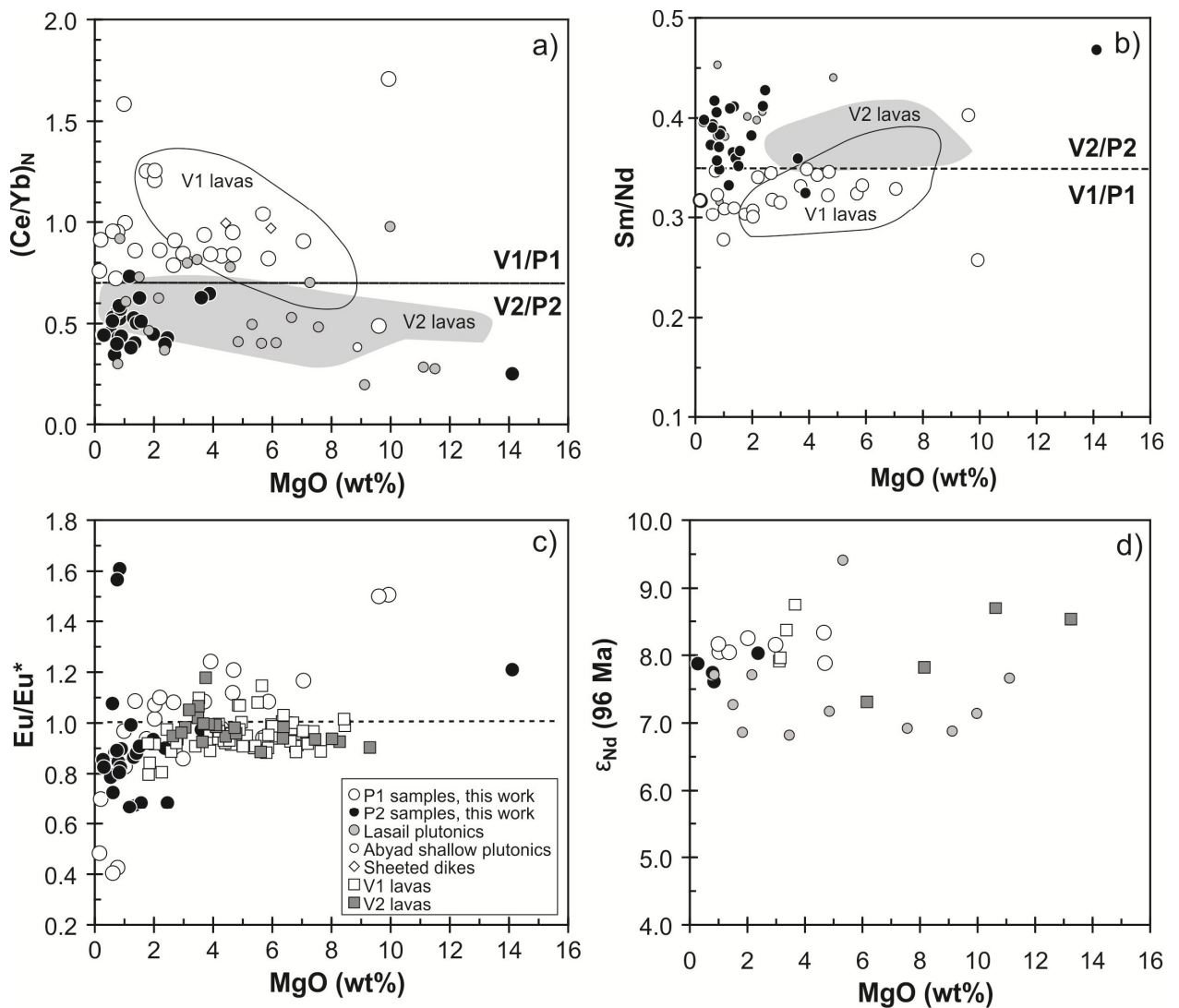


**Figure D.1.6:** Variations of element ratios of a)  $(\text{Ce}/\text{Yb})_N$ , b)  $\text{Sm}/\text{Nd}$ , c)  $\text{Eu}/\text{Eu}^*$ , and d)  $\epsilon_{\text{Nd}}(96\text{Ma})$  versus MgO contents. Data sources as in Figure D.1.3.

The P1 group has age-corrected  $\epsilon_{\text{Hf}}(96\text{Ma}) = 17.1$  to  $24.2$ , whereas the P2 group has  $\epsilon_{\text{Hf}}(96\text{Ma}) = 15.7$  to  $19.7$  (Fig. D.1.8) and the P1 and P2 group samples overlap in age-corrected  $\epsilon_{\text{Nd}}$  values (Figs. D.1.6d and D.1.8). Thus, there is no clear distinction of the P1 and P2 but the P1 rocks tend to higher  $\epsilon_{\text{Hf}}(96\text{Ma})$  than the P2 samples. The P1 group generally has lower  $^{87}\text{Sr}/^{86}\text{Sr}(96\text{Ma})$  ranging from  $0.7035$  to  $0.7060$  compared to P2  $^{87}\text{Sr}/^{86}\text{Sr}(96\text{Ma})$   $0.7044$  to  $0.7060$ . Our Oman

ophiolite plutonic rock samples have high Hf and Nd isotope values (Fig. D.1.8b) resembling Indian MORB and rocks from the Cretaceous Dehshir ophiolite in Iran (Moghadam et al. 2012). The Oman ophiolite samples show a negative trend between  $\epsilon\text{Nd}_{(96\text{Ma})}$  and Th/Nb ratios with some V2/P2 samples having the highest Th/Nb and lowest  $\epsilon\text{Nd}_{(96\text{Ma})}$  (Fig. D.1.8c).

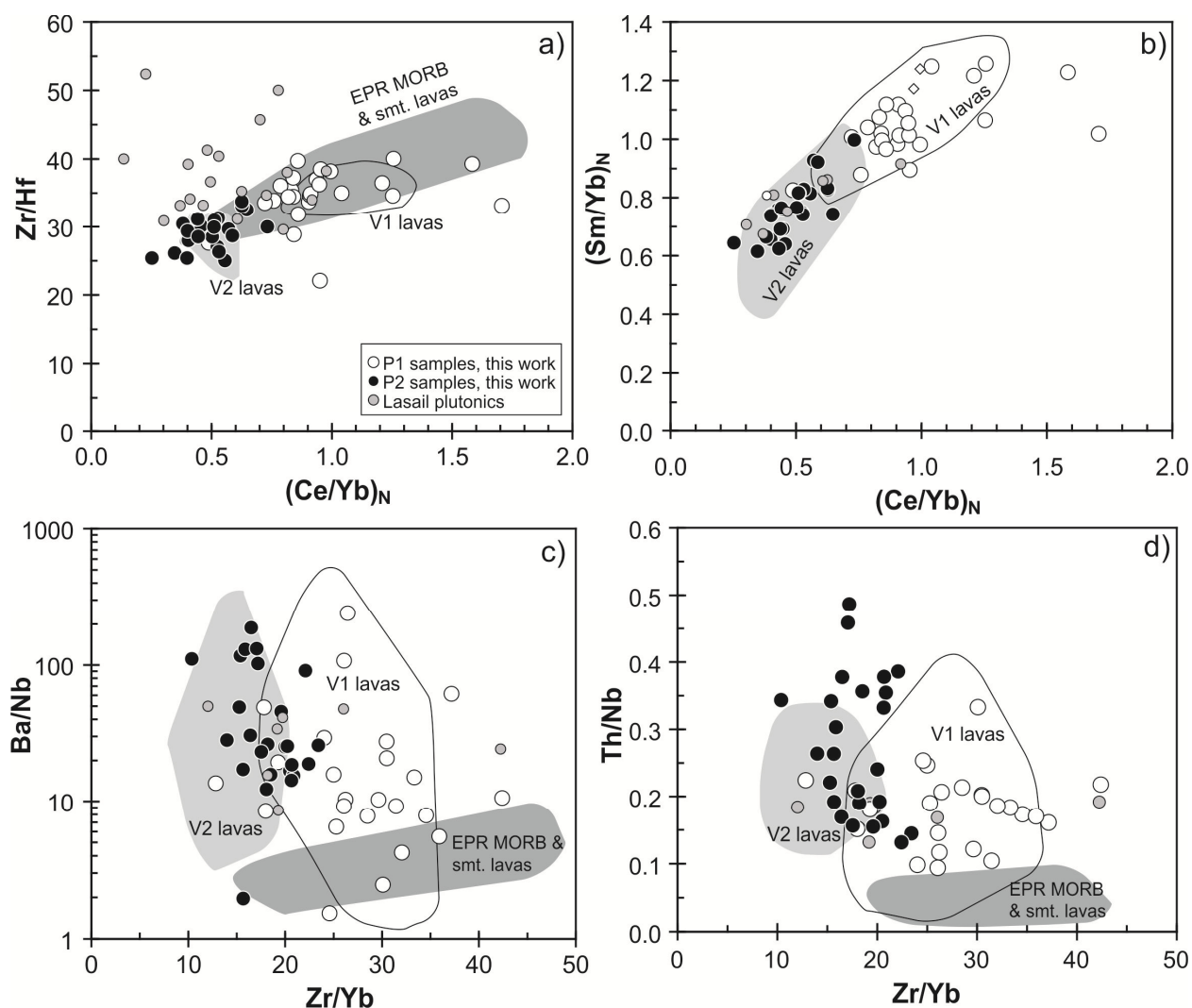


**Figure D.1.7:** Incompatible element ratios (a) Zr/Hf versus  $(\text{Ce}/\text{Yb})_N$ , (b)  $(\text{Sm}/\text{Yb})_N$  versus  $(\text{Ce}/\text{Yb})_N$ , (c) Ba/Nb versus Zr/Yb, and (d) Th/Nb versus Zr/Yb for the Oman ophiolite crust felsic intrusions. Data for EPR MORB and seamount lavas from Niu and Batiza (1997), Haase (2002) and data for Oman ophiolite rocks as in Figure D.1.3.

## D.1.6. Discussion

### D.1.6.1. Hydrothermal alteration of the plutonic rocks

Ophiolitic rocks are often significantly altered in mineralogical and geochemical composition as a result of reaction with seawater-derived hydrothermal fluids (e.g. Gillis and Robinson 1988; Gregory and Taylor 1981; Stakes and Taylor 2003). The occurrence of minerals such as chlorite, albite, secondary quartz, epidote - clinozoisite, and actinolite in the Oman ophiolite plagiogranites are most likely the result of a pervasive greenschist to lower amphibolite facies metamorphism of the oceanic rocks. Any hydrothermal alteration of the crust is accompanied by a high water and carbonate content in the rocks that is expressed by a high loss on ignition (LOI). However, most of our studied samples have LOI below 2 wt.% in the range of fresh rocks. Some

authors suggested hydrous conditions during fractional crystallization (e.g. V2 lavas, wehrlites), during partial melting of altered crustal rocks, and during fluid-induced mantle melting of the P2 magmas (Ernewein et al. 1988; Goodenough et al. 2014). Most recently, MacLeod et al. (2013) suggested water contents of 0.2 to 1 wt% in the primary magmas to explain the variable crystal fractionation processes in the lavas of the Oman ophiolite. Consequently, higher water contents in some of the plagiogranitic rocks may also be due to the varying magmatic processes. Generally higher LOI are observed in the P2 group compared to the P1 group with low LOI that is in agreement with higher initial water contents of the P2 magmas. Positive correlations of fluid-mobile elements like Rb and CaO with LOI could suggest enrichment during seawater alteration although significant enrichment processes by hydrothermal fluxes are observed only in the uppermost 1 kilometre of the oceanic crust (e.g. Bach et al. 2003). However, a deep penetration of hydrothermal fluids into the plutonic rocks of the Oman Ophiolite was shown previously and resulted in increased Sr and decreased O isotope ratios (Bosch et al. 2004; Kawahata et al. 2001; Stakes and Taylor 2003). The observed high  $^{87}\text{Sr}/^{86}\text{Sr}$  isotope ratios for a given  $\epsilon\text{Nd}_{(96\text{Ma})}$  compared to MORB (Fig. D.1.8a) suggest seawater alteration of the plutonic rocks. Consistent positive anomalies of Ba, U, K, and Sr in P2 rock patterns (Fig. D.1.5) are unlikely to be due to alteration but rather indicate differences in magma compositions of the P1 and P2 groups. We propose that hydrothermal alteration after the intrusion has only a minor effect on the rock composition, hence most major and trace elements reflect magmatic processes. In agreement with the model of MacLeod et al (2013) we assume that the higher LOI of the P2 sample group reflects magmas with 1 to 2 wt.%  $\text{H}_2\text{O}$  whereas the P1 group rocks were relatively dry and thus have lower LOI. However, the  $\text{H}_2\text{O}$  contents of the mafic P2 magmas were not sufficient to stabilize amphibole and thus magmatic amphibole may only occur in the highly evolved rocks.

#### ***D.1.6.2. The geochemical relationship between the plutonic and volcanic rocks***

The shallow level plutonic rocks have similar major element compositions to the lavas (Fig. D.1.3) suggesting that the gabbros, diorites and tonalites generally represent melt compositions rather than cumulates. Only a few plutonic rocks have  $\text{Al}_2\text{O}_3$  contents that are significantly higher than the lava trend and these samples frequently also show  $\text{Eu}/\text{Eu}^* > 1$  indicating plagioclase accumulation. The evolution of the lava succession in the uppermost crust of the Oman ophiolite is reasonably well understood and it has been shown in several profiles that the MORB-like V1 (or Geotimes) lavas are overlain by the V2 (or Lasail and Alley) lavas with a clear subduction signature (Alabaster et al. 1982; Godard et al. 2003). The V1 lavas have been interpreted as extrusives at a spreading axis whereas the younger, overlying V2 lavas are believed to have formed off-axis (Alabaster et al. 1982; Ernewein et al. 1988). In agreement with this model, the rocks from the sheeted dyke complex geochemically resemble the V1 stage rocks (Fig. D.1.3) whereas numerous younger dykes have variable compositions of V2 to boninitic affinity (Adachi and Miyashita 2003; MacLeod et al. 2013; Yamasaki et al. 2006). Thus, most of the crust probably formed at a spreading axis (Ernewein et al. 1988). The geochemical differences in terms of  $\text{TiO}_2$ , Zr and  $(\text{Ce}/\text{Yb})_{\text{N}}$  between the V1 and the V2 lavas are also observed in our new data from the shallow level intrusives in the whole Oman ophiolite (Figs. D.1.3, D.1.4, and D.1.5). Our results confirm the findings of V1-type and V2-type plutonic rocks in the Abyad and Lasail complexes, respectively (MacLeod et al. 2013; Tsuchiya et al. 2013),

and indicate that these distinct (P1 and P2) magma types exist in large portions of the Oman ophiolite (Fig. D.1.1). In agreement with previous studies we conclude that the oceanic crust of the Oman ophiolite was formed during two magmatic phases (Adachi and Miyashita 2003; Goodenough et al. 2010; Python and Ceuleneer 2003; Yamasaki et al. 2006). Concerning the distribution of magmatic phase 1 and 2, we found a similar regional pattern as Goodenough et al. (2014), with P2 plagiogranites more pronounced in the North (Fig. D.1.1) and absent in the most southern block of the ophiolite (Wadi Tayin block).

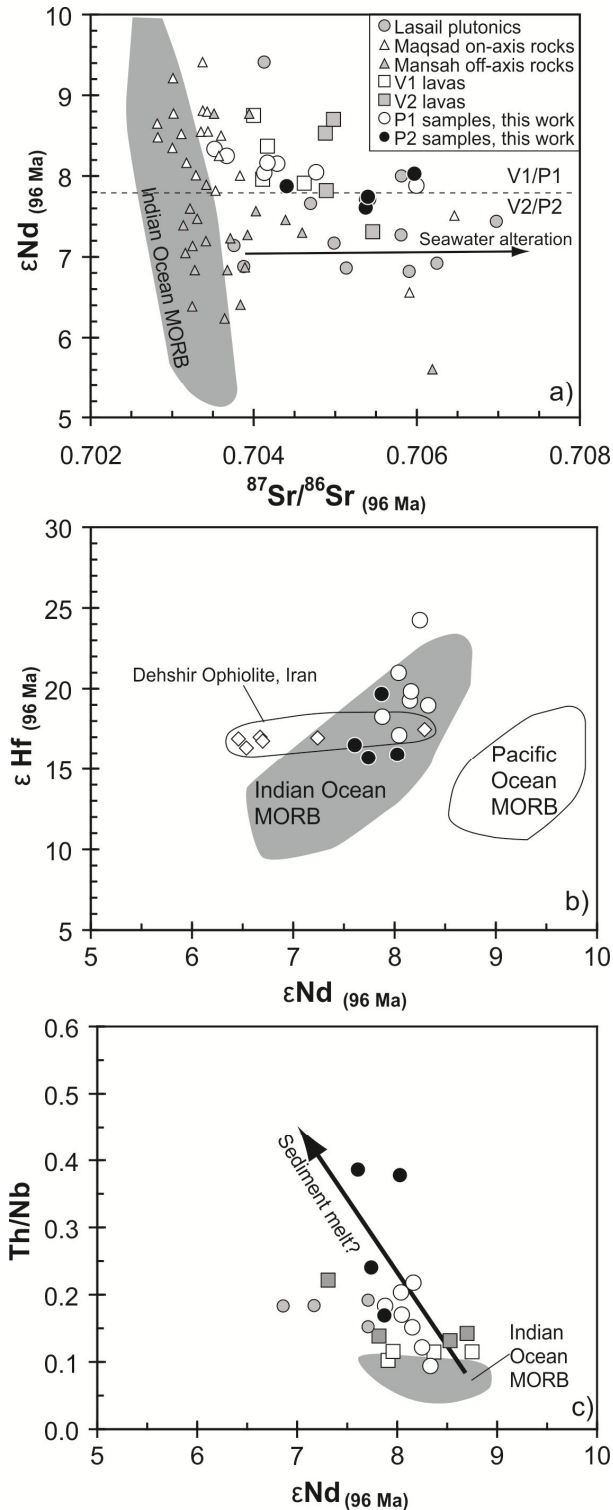


**Figure D.1.8:** Age-corrected isotope ratios of (a)  $\epsilon\text{Nd}$  versus  $^{87}\text{Sr}/^{86}\text{Sr}$ , (b)  $\epsilon\text{Hf}$  versus  $\epsilon\text{Nd}$ , and (c) Th/Nb versus  $\epsilon\text{Nd}$ . Also shown is the effect of seawater alteration on the Sr isotope composition of the rocks. MORB variations from PetDB (Lehnert et al. 2000) and other data from sources as in Fig. D.1.3 and Benoit et al. (1999).



### ***D.1.6.3. Formation of the felsic magmas***

Felsic magmas in the oceanic crust are believed to form either by fractional crystallization of mafic melts or by partial melting of hydrothermally altered (amphibolitic) mafic rocks in the crust (Brophy 2009; Koepke et al. 2007; e.g. Koepke et al. 2004). In the Oman ophiolite, felsic rocks of both the P1 and P2 groups occur as elongated intrusions with diameters ranging from tens to hundreds of metres and as dykes and veins with thicknesses ranging from few centimetres to metres. The large intrusions most likely represent frozen melt lenses in the shallow crust which are believed to be common at mid-oceanic ridge settings (Detrick et al. 1987). Felsic compositions appear to be more abundant in the plutonic rocks than in the lavas but dacitic to rhyolitic lavas were found both in the V1 and in the V2 lava groups (Alabaster et al. 1982; MacLeod et al. 2013). The continuous trends of major and trace elements with SiO<sub>2</sub> with variable MgO indicate that the felsic magmas of the V1/P1 and V2/P2 groups generally form by extensive fractional crystallization from mafic parental melts. For example, the decrease of TiO<sub>2</sub> at 4 and 2 wt.% MgO in the V1/P1 and V2/P2 rocks, respectively, most likely reflects fractional crystallization of Ti-magnetite. Alternatively, such a trend could be explained by mixing between a felsic melt with an MgO content <1 wt.% and a basaltic magma with MgO of 4 and 2 wt.%, respectively. Partial melting of mafic rocks leads to low TiO<sub>2</sub> and FeO<sup>T</sup> for melts with SiO<sub>2</sub> >60 wt.% as inferred from experimental studies (Koepke et al. 2007; Koepke et al. 2004) and such melts may mix with mafic melts in a magma chamber. However, binary mixing between end-members with similar MgO is not observed for other elements and, for example, P<sub>2</sub>O<sub>5</sub> shows a maximum content in V1/P1 rocks at about 2 wt.% MgO which marks the onset of apatite fractionation (Fig. D.1.3). We conclude that the major element trends imply fractional crystallization processes with marked changes of slope due to the onset of fractionation of different phases including olivine, clinopyroxene, plagioclase, (Ti-) magnetite, and apatite rather than binary mixing between felsic and mafic magmas. The difference of the two fractionation trends reflects different water contents and fO<sub>2</sub> in the primary magmas (MacLeod et al. 2013). Thus, the relatively dry and reducing V1/P1 melts show a stronger enrichment in FeO<sup>T</sup> than the more water-rich V2/P2 magmas.

Model calculations suggested a negative correlation of the LREEs and SiO<sub>2</sub> (>62 wt.%) for plagiogranites produced by hydrous partial melting of mid-ocean ridge gabbros (Brophy 2008; Brophy 2009; Brophy and Pu 2012; France et al. 2014). However, the two groups show no negative correlation of LREEs and SiO<sub>2</sub> (>62 wt.%) but the P1 and P2 rocks exhibit a strong increase in LREE and other incompatible elements with increasing SiO<sub>2</sub> and decreasing MgO (Fig. D.1.4b, c) supporting an origin by fractional crystallisation from a mafic magma (Brophy 2008; Brophy 2009; Brophy and Pu 2012). The relatively constant incompatible and Nd isotope ratios for rocks with highly variable MgO contents (Fig. D.1.6) are also consistent with fractional crystallization whereas much less systematic variation would be expected for binary mixing processes between melts from crustal and mantle rocks. Finally, we find systematic variations in V and Eu/Eu\* with decreasing MgO contents that indicate depletion of V and Eu in magmas with less than about 4 wt.% MgO (Figs. D.1.4 and 6). These depletions can be explained by fractional crystallization of magnetite and plagioclase, respectively, but are more difficult to reconcile with magma mixing. We conclude that the observed variation in the V1/P1 and V2/P2 rock series reflects significant fractional crystallization processes of mafic melts in the shallow

crust that can lead to the formation of large bodies of felsic melts with SiO<sub>2</sub> contents up to about 75 wt.%.

Assimilation-fractional crystallization (AFC) processes are typical for ascending magmas at oceanic spreading centres settings (e.g. Freund et al. 2013; Wanless et al. 2010) and have been proposed for Oman ophiolite plagiogranites on the basis of O isotope data in minerals like quartz and zircon (Grimes et al. 2013; Stakes and Taylor 2003). Net-veining of felsic rocks containing basaltic and gabbroic xenoliths is observed frequently (Sumail massif; Wadi Tayin massif) indicating that assimilation of wall rocks likely plays an important role during the formation of felsic magmas. Thus, although we do not find geochemical evidence for assimilation in our samples we suggest that this process also affected the felsic magmas of the Oman ophiolite.

#### ***D.1.6.4. Anatectic processes at the dyke/gabbro transition of the Wadi Tayin block***

Small plagiogranite dykes and veins with cm- to dm-thickness showing high SiO<sub>2</sub> contents which are exposed in the dyke/gabbro transition of the Wadi Tayin block near the village Ibra have been interpreted as products of hydrous partial melting of previously altered sheeted dykes, triggered by ascending axial magma chambers providing heat for high-grade contact metamorphism (pyroxene hornfels facies) culminating in anatectic processes (France et al. 2010; France et al. 2014). At several locations which were also sampled in this study (locations TA 11, 12, 13 in Fig. D.1.1 and Table D.1.ESM), France et al. (2010) discovered the presence of granoblastic two-pyroxene hornfelses which can be regarded as restites after partial melting of hydrated basalts from the sheeted dyke sequence, in accordance with other localities from gabbro/dyke transitions from fast-spreading ridges in recent oceans (e.g. Erdmann et al. 2015; Gillis 2008) or in the Troodos ophiolite (Gillis and Coogan 2002). In a recent study, France et al. (2014) analyzed the trace element composition of experimental phases produced by hydrous partial melting of altered basalt from the Oman sheeted dyke section, and applied the results to the natural hornfelses and plagiogranites of the dyke/gabbro transition of the Ibra area. They showed that the experimental products generated below 970°C match the natural lithologies, both in terms of major and trace elements: The composition of the experimental melts corresponds to the felsic veinlets, while the residual minerals of the experiments match the composition of the two-pyroxene hornfelses, implying that hydrous partial melting is an important magmatic process in the gabbro/dyke transition of fast-spreading mid-oceanic ridges.

We have only very few rocks in our sample suites from the dyke/gabbro transition near Ibra (Wadi Tayin TA11 to 13) which have SiO<sub>2</sub> contents high enough to fit with that model (SiO<sub>2</sub> >61 wt%, according to experiments of France et al.; 2010). These rocks show in their trace element patterns all those characteristics revealed experimentally by France et al. (2014): flat patterns, slight negative Sr and Eu anomalies, Zr and Hf enrichment (only for the sample with the highest SiO<sub>2</sub> content). Moreover, these samples show decreasing La concentrations with increasing SiO<sub>2</sub> implying generation via partial melting according to the systematics developed by Brophy (2009). In combination with the important observation that restitic granoblastic hornfelses exist in these outcrops, these features imply a model that these plagiogranites from the gabbro/dyke transition near Ibra can indeed be regarded as products of hydrous partial melting of dyke basalts, according to the model of France et al. (2014). Another argument for this model is provided by the Al<sub>2</sub>O<sub>3</sub> contents of these three plagiogranites, which are too elevated (up to 16.4



wt%) for a given MgO content, when comparing with modeled melt compositions resulted by fractional crystallization of hydrous MORB with respect to the compositions of the sheeted dykes from the Ibra area (MacLeod et al. 2013). As discussed in Wanless et al. (2010) and experimentally shown (Beard and Lofgren 1991; France et al. 2010), strongly enriched  $\text{Al}_2\text{O}_3$  contents in felsic rocks are typical for a hydrous partial melting origin. We suggest that relatively rare small volumes of felsic melts at the transition between the gabbros and sheeted dykes like those near Ibra are generated by partial melting of hydrothermally altered rocks. Such melts are either assimilated by larger magma bodies or may intrude into the wall rocks.

#### ***D.1.6.5. Implications for the evolution of the oceanic crust***

Felsic lavas and plutonic rocks occur along the active spreading axes of the Earth and these melts often form in shallow magma lenses at the transition between the sheeted dykes and underlying varitextured gabbros. Such melt lenses have been found especially along fast-spreading ridges (Detrick et al. 1987; Freund et al. 2013; MacLeod and Yaouancq 2000; Wanless et al. 2010). The V1/P1 rocks of the Oman ophiolite most likely represent similar magmatic processes at the relatively fast spreading axis of the Tethys Ocean. However, the presence of felsic intrusions with diameters of several 100 m and V2 composition implies that a significant part of the plutonic crust must have formed off-axis by replacing older rocks. Because the felsic V2/P2 magmas were generated largely by fractional crystallization, relatively large volumes of hydrous mafic to ultramafic intrusions must occur in the deeper crust of the Oman ophiolite, which is indeed observed (Adachi and Miyashita 2003; Benoit et al. 1999; Goodenough et al. 2010). Such massive intrusions into the oceanic crust are surprising because they require a replacement of large volumes of existing V1/P1 rocks. On the other hand, dyke swarms with V2 composition were observed (Adachi and Miyashita 2003) and indicate significant off-axis extension of the crust that could allow the emplacement of larger intrusive bodies in the crust. Several phases of dyke intrusions exist in the Oman ophiolite and are believed to have occurred in crust with ages of several millions of years and more than 100 km distant from the spreading axis (Adachi and Miyashita 2003; Nicolas et al. 2000b). Recent precise U/Pb dating of lower crustal rocks at the East Pacific Rise yielded crystallization age ranges of up to 124 kyr suggesting that intrusions may occur at least 10 km distant from the spreading axis (Rioux et al. 2012b). We suggest that extensional stress allowed the off-axis intrusion of large magma bodies into the crust of the Oman ophiolite following the formation of these magmas by fluid-induced melting above a subduction zone.

Rioux et al. (2012a, 2013) measured precise U-Pb ages of zircon from plutonic rocks (gabbros and plagiogranites) from five Oman ophiolite blocks (Fizh, Haylayn, Rustaq, Sumail, Wadi Tayin) and suggested an older group of rocks that crystallized between  $96.44 \pm 0.06$  to  $95.48 \pm 0.06$  Ma at a spreading axis, and a younger group ( $95.41 \pm 0.06$  to  $95.08 \pm 0.06$  Ma). Eight of our sample locations in the Sumail, Haylayn, Rustaq and Wadi Tayin blocks are apparently identical to the outcrops age-dated by Rioux et al. (2013) and one is similar to the location of the dated sample CWO38. We suppose therefore that our samples are of comparable ages to those dated previously. The variation of Sm/Nd ratios with age indicates that P1 intrusions occurred between 96.5 and 95.0 Ma but P2 rocks with Sm/Nd >0.35 appear to be restricted to ages of 96.0 to 95.0 Ma (Fig. D.1.9a). As noted previously by Rioux et al. (2013) rocks with ages of 96.5 to 95.5 Ma

have relatively constant  $\epsilon_{Nd}$  around 8 whereas some of the samples with ages of less than 95.5 Ma have lower Nd isotope ratios than the older rocks (Fig. D.1.9b). Thus, the variation of rock compositions with age indicates a change to magmas with higher Sm/Nd but lower Nd isotope ratios at about 96.0 Ma possibly reflecting the increasing influence of a subducting slab component. Samples with ages between 96.2 and 95.5 Ma from the Tayin block are relatively homogeneous in composition and rocks from this block do not show influence of enriched components from subduction. Thus, although the older rocks with ages of 96.5 to 96.0 Ma generally resemble MORB, the samples younger than 96.0 Ma indicate that many magmas formed from a more depleted mantle than those of the early stage and that a variable subduction influence affected this mantle. The plutonic rocks show a more complex and partly contemporaneous formation in contrast to the succession of volcanic rocks with MORB-like V1 rocks erupting during the spreading stage followed by supra-subduction-like V2 compositions in the post-spreading stage. However, some of these complexities may be due to the problems with age resolution.

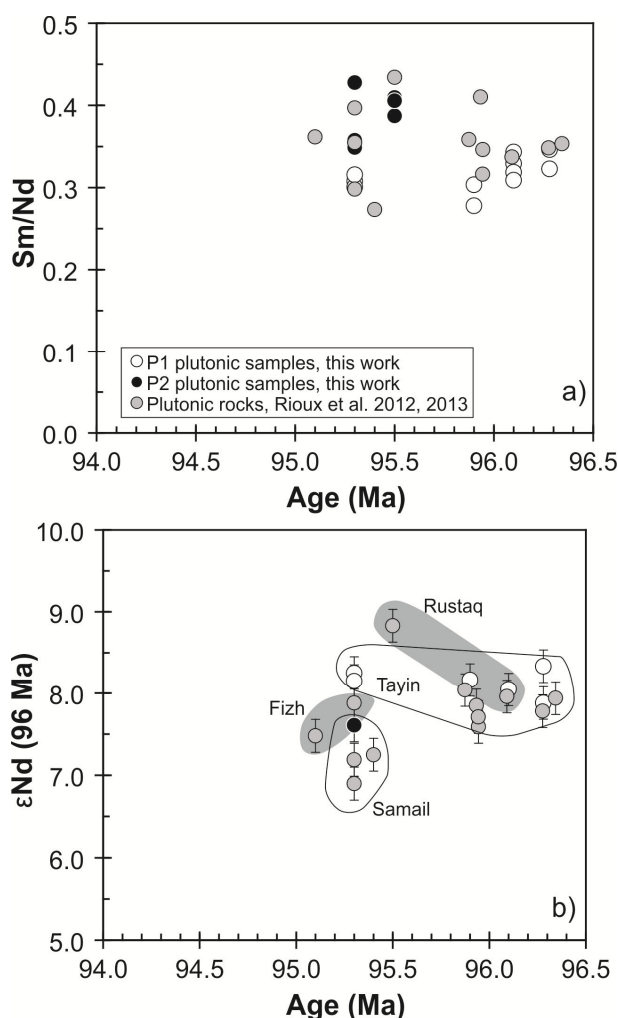


**Figure D.1.9:** (a) Sm/Nd ratio versus age and (b)  $\epsilon_{Nd}$  (96 Ma) versus age for samples from Rioux et al (2012a, b, 2013) and P1 and P2 samples from locations dated previously (estimated by comparison with Rioux et al. (2012a, b, 2013)).

#### ***D.1.6.6. Constraints on the mantle source composition and the nature of the slab component***

Mid-ocean ridge basalts usually vary significantly in Hf isotope ratios at almost constant Nd isotope ratios (Nowell et al. 1998) whereas ocean-island basalts and island-arc basalts (as well as sediments) show a correlation in Hf and Nd isotopes (Chauvel and Blichert-Toft 2001). In terms

of Nd and Hf isotopes, the Oman ophiolite P1 and P2 samples lie within the field of Indian MORB supporting an earlier suggestion of Indian-MORB-type mantle beneath the Tethys Ocean that was based on published Pb and Nd isotope data from different samples (Mahoney et al. 1998). The Oman ophiolite samples show a very steep trend to lower Hf with decreasing Nd isotope ratios that possibly reflects mixing between two source components (Fig. D.1.8a, b). The high Nd and Hf isotope ratios of the P1 group suggest a depleted MORB mantle source whereas the P2 group rocks generally show lower Hf isotope ratios suggesting that their source was slightly more enriched than that of P1 rocks. Because incompatible element composition of the P2 rocks also indicates an influence of a subduction component the relatively low Nd and Hf isotope ratios possibly reflect this slab component. In order to change the Hf isotope composition Hf must be mobilized significantly from the slab and this most likely reflects an input of melts of sediments from the subducting slab (e.g. Woodhead et al. 2001). Mixing of a melt of sediments into the Oman ophiolite mantle wedge is supported by the observed trend of Th/Nb with Nd isotopes (Fig. D.1.8c) because sediments typically have a high Th/Nb (Elliott 2003). Melts from sediments have been described from the mantle portion of the Oman ophiolite (Cox et al. 1999; Haase et al. 2015) and such melts may mix into the melts of the mantle wedge (Fig. D.1.8c). It appears plausible that some of these melts from sediments affected the hot interior of the mantle wedge where the V2/P2 magmas were forming. We conclude that the V2/P2 magmatic rocks were influenced by an enriched subduction component, most likely small amounts of melts from pelagic sediments. The addition of this component may have caused partial melting of the off-axis magmas.

### **D.1.7. Conclusions**

The new geochemical data of shallow-level intrusive rocks from the Oman ophiolite show that a P1 and P2 group of plutonic rocks can be distinguished throughout the entire ophiolite in agreement with previous findings on V1 and V2 volcanic rocks. Well-defined major element trends and Hf and Nd isotope ratio variations suggest that the crustal plagiogranites and the mafic crustal host-rocks and lavas are genetically related. Most of the felsic rocks of the plagiogranite intrusions from the Oman ophiolite formed by fractional crystallization processes from mafic melts that also occur in some intrusions. Melts of subducted sediments apparently affected an increasingly depleted mantle wedge. The V1/P1 magmas formed by decompression melting at a spreading axis with little geochemical influence of a subduction zone whereas the V2/P2 magmas show a stronger input of a slab component. This slab component appears to be a sedimentary melt such as has been found in the mantle section of the Oman ophiolite. Both plagiogranite groups occur on the whole length of the ophiolite, but the P1 group is apparently more abundant in the southern blocks than in the northern blocks. The significant volume of P2 plutonic rocks implies ongoing crustal extension that allowed the emplacement of the intrusions.

### ***Acknowledgments***

We acknowledge the help of H. Brätz and R. Klemm (both GeoZentrum Nordbayern) during trace element analyses. We thank A. Richter for patient support with electron microprobe analyses and S. Hauff (GEOMAR) for the Hf isotope analysis. C. Weinzierl is thanked for his generous helpful corrective advice. We thank the Director General of Minerals, Ministry of Commerce and Industry of the Sultanate of Oman, for allowing us to conduct field work in the

Sultanate of Oman. S. Freund thanks L. Pflug for inspiring discussions and critical questions. S. Freund was funded by DFG grant HA2568/21. Constructive reviews by G. Ceuleneer, M. Rioux and the editor O. Müntener helped to significantly improve the quality of this work.

## D.2. Melts of sediments in the mantle wedge of the Oman ophiolite

Karsten M. Haase<sup>1</sup>, Sarah Freund<sup>1</sup>, Jürgen Koepke<sup>2</sup>, Folkmar Hauff<sup>3</sup>, **Martin Erdmann**<sup>2</sup>

<sup>1</sup>GeoZentrum Nordbayern, Friedrich-Alexander Universität Erlangen-Nürnberg, Schlossgarten 5, 91054 Erlangen

<sup>2</sup>Institut für Mineralogie, Leibniz Universität Hannover, Callinstr. 3, 30167 Hannover, Germany

<sup>3</sup>GEOMAR Helmholtz Centre for Ocean Research Kiel, Wischhofstr. 1-3, 24148 Kiel, Germany

**Geology, Volume 43(4), pages 275-278, 2015**

**DOI: 10.1130/G36451.1**

### D.2.1. Abstract

The rocks in the crustal section of the Oman ophiolite show an increasing input of a subduction component with time, most likely reflecting the generation of the ophiolite above a subducting slab. Field relations, new geochemical data, and Nd-Hf isotope data for felsic to mafic intrusive rocks in the mantle harzburgite from the Haylayn block in the Oman ophiolite suggest late magmatic events in a mantle wedge shortly before obduction of the ophiolite. Incompatible element contents and low  $\epsilon_{\text{Nd}}$  and  $\epsilon_{\text{Hf}}$  of the felsic rocks exclude differentiation from mafic magmas, but are consistent with an origin by partial melting of pelagic sediments similar to leucogranites in continental collision zones. These melts apparently mixed with mafic magmas resembling enriched late-stage lavas from the ophiolite. The leucogranitic intrusions into the mantle wedge confirm the transfer of melts of sediments from the subducted plate into the mantle at subduction zones. We suggest that the enrichment of Rb, K, and Pb observed in the Oman boninites is caused by addition of melts of sediments similar to those from the Haylayn block to the boninite source in the mantle wedge.

### D.2.2. Introduction

At subduction zones, hydrous fluids and melts are transported from subducting plates into the overlying mantle wedge, causing melting of the mantle and adding a characteristic slab component to the magmas. Magmatic rocks at several subduction zones show evidence for a contribution of subducted sedimentary material and contain, for example, significant  $^{10}\text{Be}$ , high  $^{207}\text{Pb}/^{204}\text{Pb}$ , and low  $^{143}\text{Nd}/^{144}\text{Nd}$  isotopic compositions (e.g., White and Dupre, 1986; Morris and Tera, 1989). The element transport from the slab into the mantle wedge probably is accomplished by hydrous fluids or silicate melts, but the actual processes are not well understood.

The younger lavas and boninites of the Oman ophiolite show geochemical signatures implying that the ophiolite formed above a subduction zone, possibly during subduction initiation (e.g., Pearce, 2003; Ishikawa et al. 2005). Therefore the mantle portion of the Oman ophiolite probably represents a fossil mantle wedge. Incompatible element-enriched felsic sills and dikes intrude the mantle portion of the Haylayn block (Rollinson, 2014) and one of these intrusions yields a U/Pb age of ca. 95.2 Ma and a low  $\epsilon_{\text{Nd}(96\text{ Ma})}$  of -7.8 (Rioux et al. 2013). Here we propose that the

felsic intrusions in the Haylayn block mantle were formed by melts from subducted sediment, and discuss the possible consequences of the ascent of such melts into the mantle.

### **D.2.3. Geological overview**

The Oman ophiolite includes a complete section of the mantle, lower crust, sheeted dikes, and the lava units with intercalated pelagic sediments. The lava pile consists of three geochemically different groups: the early lavas and sheeted dikes resemble mid-oceanic ridge basalts (Geotimes or V1 lavas) and grade into lavas with typical subduction signatures (Lasail and Alley or V2 lavas), implying that the ophiolite formed above a subducting slab (e.g., Godard et al. 2003; MacLeod et al. 2013; Goodenough et al. 2014). The late V3 lava group is incompatible element enriched and appears to be related to off-axis volcanism. Zircon U/Pb ages of felsic plutonic rocks suggest that the ophiolite crust was generated between 96.5 and 95.5 Ma, but the youngest magmatic activity in the ophiolite was dated as ca. 94.5 Ma (Warren et al. 2005; Rioux et al. 2013). Recent models suggest that the Oman ophiolite formed either at a spreading axis obliquely intersecting a subduction zone or in a forearc shortly after initiation of subduction (e.g., Pearce, 2003; Rioux et al. 2013). Peak metamorphism of amphibolites from rock units below the Oman ophiolite occurred ca. 94.5 Ma at 770–900 °C and 1.1–1.3 GPa (Warren et al. 2005; Cowan et al. 2014). The metamorphic rocks imply that Jurassic or Triassic metabasalts were subducted to depths of >30 km during the time of formation of the ophiolite crust.

There are numerous felsic intrusions in the mantle section of the Haylayn block, several of which were sampled (Table D.2.ESM.1). Our samples OM11-HA5A to OM11-HA5P are from the same area that yielded a U/Pb zircon age of 95.2 Ma (sample 9201M01; Rioux et al. 2013). The felsic intrusions consist of large (>100 m) bodies and smaller, 2–10-m-thick sills and dikes in the serpentinitized harzburgites of the uppermost mantle portion of the ophiolite (see Figure in D.2.ESM.2). Some of these felsic intrusions at Wadi Hamaliya were previously interpreted as magmas resulting from mixing between melts from mafic and sedimentary crustal rocks and melts from mantle sources (Rollinson 2009, 2014).

### **D.2.4. Results**

The felsic Haylayn mantle intrusions comprise gray, fine- to medium-grained tonalites and granodiorites, but 3 of the 5 sample locations (HA-2, HA-3, and HA-5) contain bright white leucogranite bodies that are 1–3 m thick and as much as 10 m long (samples HA-2D, HA-3A, and HA-5Fh), frequently in the center of the intrusions (see Figure in D.2.ESM.2). Most of the felsic Haylayn intrusive rocks consist of quartz, euhedral plagioclase, and amphibole. The leucogranitic portions within the felsic intrusions contain quartz, K-feldspar, plagioclase, muscovite, and biotite crystals that are mostly anhedral, recrystallized, and foliated, the latter indicating postcrystallization plastic deformation. Zircon is observed frequently, but the intrusive rocks lack opaque phases. Plagioclase crystals in the Haylayn felsic intrusives show distinct zoning, frequently with anorthite-rich cores ( $An_{90-80}$ ) and decreasing An content ( $An_{50-40}$ ) toward the crystal rims.

With the exception of one sample from the rim of a wide dike, the intrusive rocks of the Haylayn block have  $SiO_2 > 63$  wt% and  $MgO < 6$  wt% (Fig. D.2.1; Table D.2.ESM.2). The samples follow distinct linear trends of major elements with varying MgO, whereas the V1 and V2 lavas

from the crustal portions of the northern Oman ophiolite are on trends with differing slopes. For example, the felsic intrusives in the Haylayn mantle section show positive linear trends in  $\text{FeO}^{\text{T}}$

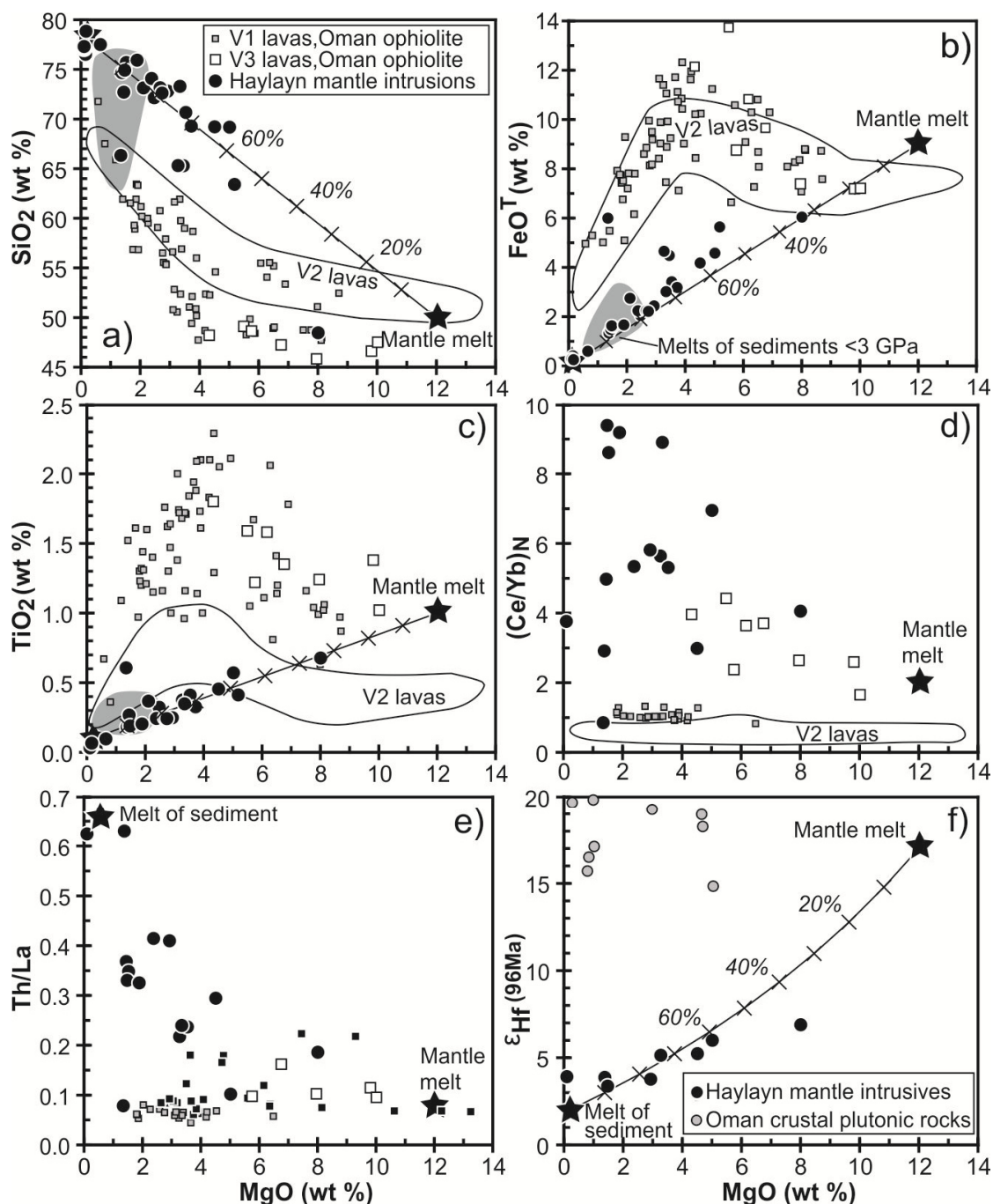


**Figure D.2.1:** Major element variations of the intrusive rocks in the mantle of the Haylayn block (Oman) compared with V1, V2 and V3 lavas (Alabaster et al. 1982; Godard et al. 2003, 2006; Lilly 2006; MacLeod et al. 2013), plutonic rocks from the crust of the Oman ophiolite (Freund 2013), and gray fields for experimentally derived sediment melts (Johnson and Plank 1999; Hermann and Spandler 2008). Mixing (tick marks in 10% increments) between a granitic melt from sediments and an assumed mafic melt with 12 wt.% MgO is shown (analytical methods and details of compositions of the mixing end-members are given in D.2.ESM.2).

and TiO<sub>2</sub> and a negative linear trend in SiO<sub>2</sub> with increasing MgO, in contrast to the trends of the V1 and V2 lavas that show distinct changes at ~3 wt% MgO (Fig. D.2.1). Some of the studied felsic intrusives have low K<sub>2</sub>O (<1 wt%), whereas others show increasing K<sub>2</sub>O, to as much as 3.8

wt%, with decreasing MgO, but in general, all samples are on the linear trends. The white Haylayn granites contain ~77 wt% SiO<sub>2</sub> and resemble leucogranites from the northern Oman ophiolite (Cox et al. 1999) and continental collision zones like the Himalaya in terms of high SiO<sub>2</sub> and K<sub>2</sub>O contents but low FeO<sup>T</sup> and TiO<sub>2</sub> contents. These Haylayn leucogranites display extreme enrichments of the fluid-mobile elements Rb, U, K, and Pb compared to the other incompatible elements (Fig. D.2.2), and closely resemble Himalayan leucogranites (Guillot and Le Fort, 1995; Guo and Wilson, 2012). The most mafic sample, OM11-HA-1C, from the rim of a felsic intrusion consists mainly of amphibole and plagioclase; it has relatively low K and Pb contents but significantly higher rare earth element (REE) concentrations compared to the SiO<sub>2</sub>-rich samples (Fig. D.2.2). The Haylayn leucogranites have higher Th/La (Fig. D.2.1) and lower Ce/Pb than the more MgO-rich intrusives. As noted elsewhere (Amri et al. 1996; Rioux et al. 2013), the felsic intrusive of the Haylayn mantle rocks have negative  $\epsilon_{\text{Nd}(96 \text{ Ma})}$  and relatively low initial  $\epsilon_{\text{Hf}(96 \text{ Ma})}$  of 3.9–6.5 (Figs. D.2.1 and D.2.3), but high initial  $^{87}\text{Sr}/^{86}\text{Sr}$  resembling pelagic sediment compositions. The samples with the lowest MgO also have the lowest  $\epsilon_{\text{Hf}(96 \text{ Ma})}$ , <4, whereas samples with MgO > 3 wt% have higher  $\epsilon_{\text{Hf}(96 \text{ Ma})}$  (Fig. D.2.1).

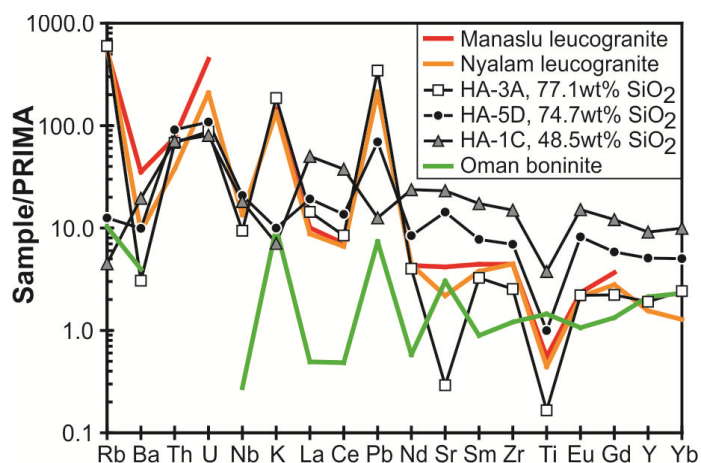


**Figure D.2.2:** Primitive mantle (PRIMA) normalized (Hofmann 1988) element patterns of a felsic, an intermediate, and the mafic end-member sample from the intrusive rocks in the mantle of the Haylayn block (Oman). The Haylayn block intrusive rocks are compared to boninite from the Oman ophiolite (Ishikawa et al. 2005) and the Manaslu (Guillot and Le Fort 1995) and Nyalam (Guo and Wilson 2012) leucogranites from the Himalaya collision zone. Note the close resemblance of the Haylayn felsic sample to the Himalaya leucogranites with distinct enrichment in the fluid mobile elements Rb, K, and Pb.

## D.2.5. Discussion

### D.2.5.1. Origin of the felsic rocks by melting of sediments

The leucogranite end members in the Haylayn mantle intrusive rocks contain biotite, muscovite, and K-feldspar, and thus differ from the felsic lavas that formed by fractional crystallization of mafic magmas in the crust of the Oman ophiolite. The major element composition of the felsic Haylayn mantle intrusives with >72 wt% SiO<sub>2</sub> closely resembles partial melts of pelagic sediments (Fig. D.2.1) at <900 °C (Johnson and Plank, 1999; Hermann and Spandler, 2008). In addition, the similarity of the incompatible element composition of the most SiO<sub>2</sub>-rich rocks to the Himalayan leucogranites and the low Nd and Hf isotope ratios (Fig. D.2.3) imply that these rocks represent partial melts of sediments. The extreme enrichment of fluid-mobile elements Rb,



K, and Pb probably reflects a large contribution of hydrous fluids to the melts that is also assumed for the Himalayan leucogranites (Guillot and Le Fort, 1995; Guo and Wilson, 2012). We conclude that the Haylayn mantle leucogranites represent partial melts of pelagic sediments from the lower plate subducting beneath the Oman ophiolite. Because garnet forms in metapelites at  $\sim 750^\circ\text{C}$  (Hermann and Spandler, 2008) and the Haylayn leucogranites have only slightly depleted heavy REEs (Fig. 2), we suggest formation of these melts at  $<750^\circ\text{C}$  and at low pressures. These melts probably formed at relatively shallow depths, similar to the Himalayan leucogranites, and intruded the mantle wedge as dikes and small intrusive bodies. Because the felsic melts crystallized and did not react significantly with the Haylayn mantle rocks, the latter must have been relatively cold and partly serpentinized. This is in agreement with models for the corner of a mantle wedge consisting of relatively cold serpentinite due to massive fluid infiltration from the subducting slab (Hyndman et al., 2000).

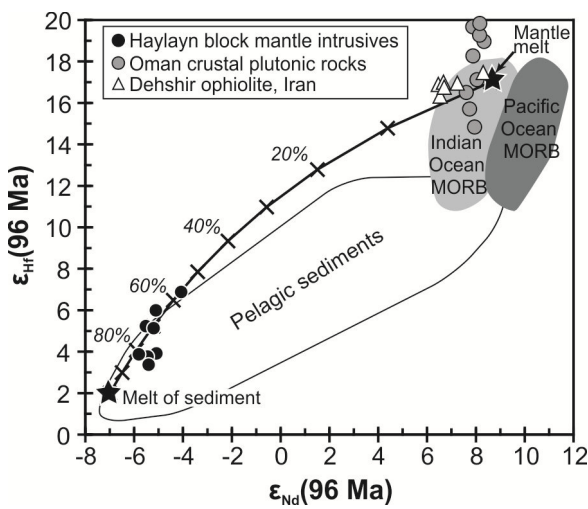


**Figure D.2.3:**  $\epsilon_{\text{Hf}}$  versus  $\epsilon_{\text{Nd}}$  at 96 Ma ago for the Haylayn (Oman) mantle intrusive rocks showing distinctly lower Hf and Nd isotope ratios compared to crustal plagiogranitic rocks from the Oman ophiolite crust (Freund 2013), MORB (Nowell et al. 1998; Chauvel and Blichert-Toft 2001), and rocks from the Dehshir ophiolite in Iran (Moghadam et al. 2012), but ratios similar to marine sediments (Vervoort et al. 1999). Potential mixing between a granitic melt from sediments and an assumed mafic melt is shown (details of the mixing end members are in the supplementary Table 2 of D.2.ESM.2).

#### D.2.5.2. Evidence for two-component mixing

The linear trends in major elements as well as the variation of Hf isotope and Th/La ratios with MgO indicate binary mixing between the sedimentary melt and an MgO-rich component (Fig. D.2.1). To explain the occurrence of granites in the Oman ophiolite mantle section, some suggested melting of volcanoclastic material or amphibolite from the metamorphic sole (Briqueu et al. 1991; Cox et al. 1999), whereas Rollinson (2009) assumed partial melting of subducted eclogite. In these models mixing between sediment and mafic rocks occurs prior to melting in the source region of the magmas. Such processes would not yield the observed linear binary mixing trends in our samples. We interpret the plagioclase with core compositions of  $\text{An}_{90-80}$  in the felsic rocks as xenocrysts from hydrous basaltic melts that mixed with the granitic melts, producing the linear major element trends. The close association of felsic, intermediate, and mafic intrusive rocks in the same intrusion also indicates mixing between melts of granitic and basaltic composition. Rollinson (2014) suggested a reaction of the granites with the ultramafic wall rocks to form intermediate rocks. However, the mafic mixing end member cannot represent assimilated host harzburgite because it must have high  $\text{TiO}_2$  and incompatible element contents (Fig. D.2.1), unlike the depleted harzburgite. Rather, the linear trends suggest that this mafic end member is a basaltic melt with a high MgO of perhaps 12 wt%, but low  $\text{SiO}_2$  and  $\text{K}_2\text{O}$ . This rock has the composition of an incompatible element-enriched basalt with a negative Nb anomaly and high Y and Yb concentrations (Fig. D.2.2). Incompatible element-enriched magmas occur in the

northern Oman ophiolite, and these so-called V3 basalts have high  $(Ce/Yb)_N$  of 1.7–4.4 and variable Nb/La of 0.8–1.0 (Godard et al. 2003; Lilly, 2006), similar to the  $(Ce/Yb)_N$  of 4.1 and Nb/La of 0.5 in sample HA-1C. Partial melts from subducted basalts (adakites) typically have low HREEs due to residual garnet (Castillo, 2012), and are thus different from the mafic Haylayn sample. However, the intrusive relation indicates that the melts formed from sediments and intruded the mantle at the same time as the late-stage enriched basalt because they mixed in the shallow mantle. The 95.2 Ma age of a granite intrusion in the Haylayn mantle (Rioux et al. 2013) implies that at least some of these felsic and mafic magmas intruded the shallow mantle <0.5 m.y. after formation of the ophiolite crust at a spreading axis.

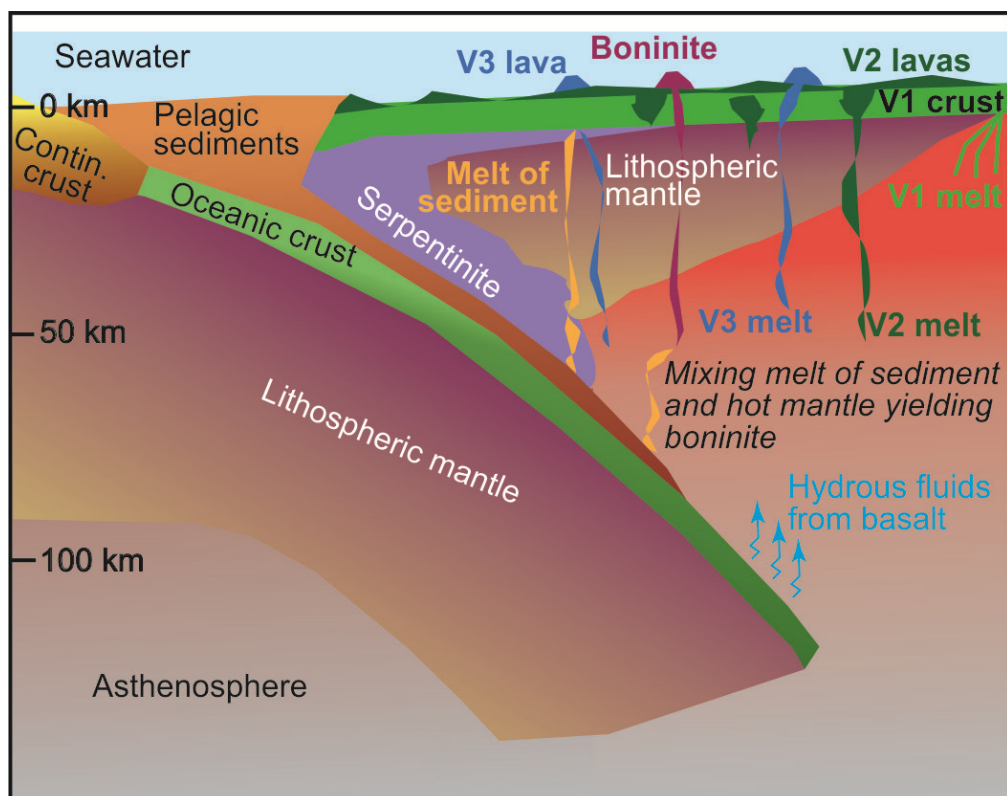


**Figure D.2.4:** Model of the formation of the Oman ophiolite during subduction of oceanic crust perhaps 1-2 Ma after spontaneous subduction began at a sedimented fracture zone (Gerya 2011). Spreading forms the V1 magmas of the crust and increasing subduction input leads to the formation of the V2 magmas containing a slab component, possibly hydrous fluids. The subducted sediments start melting at relatively shallow depths and some granitic melts intrude the cold serpentinized front of the mantle wedge where they can mix with ascending mafic magmas. Deeper melts of sediments contribute to the formation of boninite magmas in the hotter part of the mantle wedge.

### ***D.2.5.3. Implications for sediment recycling in subduction zones***

The Oman ophiolite represents the upper plate in a subduction zone ca. 95 Ma, when the felsic and mafic melts intruded the shallow mantle of the Haylayn block, and mixing between these melts formed the intermediate rocks. This mantle probably represents the tip of the mantle wedge of the former subduction zone (Fig. D.2.4) and must have been relatively cold, because it did not react with the felsic melts and intrusive boundaries are sharp. Models suggest that close to the trench the mantle wedge largely consists of serpentinite with temperatures of <800 °C (Hyndman and Peacock, 2003) and that sedimentary material rises in diapirs until it begins to melt (Behn et al. 2011). The Haylayn felsic rocks represent partial melts of sediments that crystallized in the

forearc mantle, in agreement with previous tectonic models of the Oman ophiolite. It is interesting that the boninitic lavas of the Oman ophiolite show a strong enrichment of Rb, K, and Pb, but not the light REEs, similar to the Haylayn leucogranites (Fig. D.2.2), which could thus represent the slab component affecting the boninite mantle source (Fig. D.2.4). Due to the lack of comprehensive geochemical data for Oman boninites, we cannot assess this further, but sedimentary melts have been suggested to contribute to boninite source mantle in the Cretaceous Troodos ophiolite (Cyprus) (König et al. 2010), in the Ordovician Betts Cove ophiolite (Canada) (Bédard, 1999), and in the Neoproterozoic of southern China (Zhao and Asimow, 2014). We suggest that hydrous sedimentary melts formed from the subducting plate beneath the Oman ophiolite, and these melts intruded both the cold shallow part and the hotter interior of the mantle wedge, yielding the incompatible element signature of boninite magmas (Fig. D.2.4).

#### ***D.2.5.4. Implications for the formation of the Oman ophiolite***

The Oman ophiolite may have formed due to spontaneous subduction initiation (e.g., Whattam and Stern, 2011), and a relatively deep transfer of oceanic crust is indicated by garnet amphibolites representing deeply (>30 km) subducted basaltic rocks (Cowan et al. 2014). Numerical models indicate that spontaneous subduction initiation at a fracture zone separating plates with large age difference may lead to a subduction system and the formation of a spreading axis within <2 m.y. (Gerya, 2011). These models also suggest mixing of hydrous mafic melts from the mantle wedge with melts of sediments from the surface of the subducted plate (Gerya, 2011). The presence of melts of sediments in the Oman ophiolite supports the model of spontaneous subduction initiation along a fracture zone that separates heavily sedimented old lithosphere from significantly younger lithosphere. Partial melting of these sediments generated the leucogranitic magmas that either intruded the cold serpentinized part of the mantle wedge or mixed into hot depleted parts of the mantle wedge, yielding boninitic magmas (Fig. D.2.4).

#### ***Acknowledgements***

We acknowledge the help of C. Beier, A. Richter, H. Brätz, R. Klemd, and S. Hauff during analytical work. Constructive reviews by P. Castillo, H. Rollinson, and two anonymous reviewers, as well as comments by editor B. Murphy, considerably improved the quality of this work. We gratefully acknowledge the Director General of Minerals, Ministry of Commerce and Industry of the Sultanate of Oman, for allowing us to conduct field work in the Sultanate of Oman. S. Freund thanks L. Pflug for critical reading of an earlier version. This study was funded by German Research Foundation (DFG) grant HA2568/21.

## Concluding remarks

Different hypotheses were tested experimentally during this PhD-project:

- The application of temperature cycling in a dacitic system may help to produce different textures in experiments that allow easier melt analysis with *in-situ* methods.
- Extensive crystallization at low water activity in a formerly evolved dacitic system is sufficient to generate highly evolved rocks as sampled at the oceanic crust.
- Partial melting of moderately altered basaltic dike at reduced water activity can reproduce the major and trace element composition of the natural counterparts (i.e., felsic veins and residual granoblastic dikes). Felsic melts have the potential to contaminate fresh MORB by mixing. Amphibole-rich protoliths are irrelevant for anatectic processes at the sheeted-dike rooting zone.

In order to test these various hypotheses, numerous experiments were performed with different objectives. Inspired by the study of Mills et al. (2011), the cycling technique was adopted to crystallization experiments performed at 200 MPa and varying water activities, with the goal to obtain larger melt pools and crystals in silica-rich experiments close to the solidus. Cycling the temperature with amplitudes from 20 to 50 K enlarges crystals and melt pools significantly (19 times larger clinopyroxene crystals and 69 times larger plagioclase crystals; tiny crystals in melt pools, prohibiting uncontaminated analyses, are dissolved) without affecting the phase relations or phase compositions. The experimental conditions (i.e., pressure, temperatures, redox conditions, and water activities) are applicable for phase relation studies in various magmatic systems.

The simulation of crystallization processes in a dacitic system from the fast-spreading PAR reveals that relatively low water activities ( $a_{\text{H}_2\text{O}} < 0.4$ ) can be sufficient for felsic melt generation. Especially the strong enrichment in  $\text{Al}_2\text{O}_3$  in high  $a_{\text{H}_2\text{O}}$  experiments contradicts natural observations and bulk compositions of felsic rocks are best reproduced in the melt of those experiments performed under low  $a_{\text{H}_2\text{O}}$ . Moreover, given early-stage Cl enrichment in the protolith, probably due to contamination of hydrothermally altered crust or brines, relatively high Cl contents, as observed in natural systems ( $\text{Cl} \leq 0.9 \text{ wt}\%$ ), can be reproduced in evolved melts of the crystallization experiments performed under low  $a_{\text{H}_2\text{O}}$ . The observation that highly evolved experimental melts remain  $\text{H}_2\text{O}$ -poor while they are relatively enriched in chlorine implies a decoupling between these two volatiles during crustal contamination.

The importance of reduced water activity for felsic melt generation is additionally confirmed by partial melting experiments. When simulating anatectic processes occurring at the roof of an oceanic magma chamber by using different lithologies obtained at IODP drilling Site 1256 (equatorial Pacific) as protoliths, first of all the influence of the starting material on the experimental melt composition becomes apparent. Previously performed studies (e.g., Beard and Lofgren 1991; France et al. 2010, 2014), using strongly hydrothermal altered starting material, show distinct  $\text{K}_2\text{O}$  enrichment of experimental melts. Those high values ( $\text{K}_2\text{O} \gg 0.3 \text{ wt}\%$ ) are in contrast to natural tonalites from Hole 1256D. Moderately altered basalts from Site 1256 as

protoliths lead to low  $K_2O$  concentrations in the partial melts and, thus, reproduce the natural trend. As implied by the crystallization experiments, partial melting experiments at low  $aH_2O$  are the only way to reproduce the low  $Al_2O_3$  values observed in natural anatectic veins from the dike/gabbro transition at IODP Site 1256. Moreover, residual plagioclase in experiments performed at reduced water activity are lower in anorthite content than those produced at water saturated conditions and, thus, comparable to the natural equivalents (i.e., plagioclase in residual granoblastic hornfels). However, comparatively low  $SiO_2$  values in the experimental melts (58.9 to 65.7 wt%) raise the question of whether those anatectic melts can be highly enriched in REE and other trace elements. By analyzing the experimental melts via SIMS, the resulting trace element data confirm that anatexis at low  $aH_2O$  is an important process in felsic melt generation despite relatively low  $SiO_2$ -contents.

The trace element results additionally provide a tool to track MORB contamination by assimilation of highly evolved wall rocks. However, calculations of mixing and assimilation-fractional crystallization using the experimental partial melts obtained from one protolith as contaminant/assimilant showed that anatectic melts can only be a minor contributor to the contamination process. Nevertheless, the results reveal the importance of trace elements in order to distinguish between the end-member processes of felsic melt generation (i.e., partial melting and fractional crystallization), in particular due to a new comprehensive set of bulk and mineral/melt trace element partition coefficients for different potential protoliths of anatectic processes over a large range of temperature and for different water activities. In contrast to modeling results of Brophy (2008), who aimed to decipher the end-member processes and assumed amphibole as a major phase in the residue, experiments of this study imply that partial melting can lead to continuous REE enrichment also at high  $SiO_2$  contents, at least in an amphibole free residue. The lack of amphibole in our experimental residue is in agreement with observations in two-pyroxene hornfels from IODP Site 1256 where amphibole only occurs as a secondary phase, generated by a late stage hydrothermal overprint (e.g., Zhang et al. 2014; Koepke and Goetze 2015). Thus, amphibole-rich protoliths for anatexis at the dike/gabbro transition from present day fast-spreading ridges, which are often used for chemical modeling of felsic rock suites in the oceanic crust, are probably less important.

# References

- Adachi Y, Miyashita S (2003) Geology and petrology of the plutonic complexes in the Wadi Fihz area: Multiple magmatic events and segment structure in the northern Oman ophiolite. *Geochemistry Geophysics Geosystems* 4
- Alabaster T, Pearce JA, Malpas J (1982) The volcanic stratigraphy and petrogenesis of the Oman ophiolite complex. *Contributions to Mineralogy and Petrology* 81:168-183
- Alberts R, Grimes C.B., Koepke J., Erdmann M., Kitajima K., Spicuzza M.J., Valley J.W.; 2015; High- & Low- $\delta^{18}\text{O}$  magma: Comparative study of crustal and mantle plagiogranites from the Oman ophiolite; In 2015 AGU Fall Meeting, AGU
- Aldiss DT (1981) Plagiogranites from the ocean crust and ophiolites. *Nature* 289, 577-578
- Almeev RR, Nash BP, Holtz F, Erdmann M, Cathey HE (2012) High-temperature, low-H<sub>2</sub>O Silicic Magmas of the Yellowstone Hotspot: an Experimental Study of Rhyolite from the Bruneau-Jarbridge Eruptive Center, Central Snake River Plain, USA. *Journal of Petrology* 53(9):1837-1866
- Alt JC, Laverne C, Coggon RM, Teagle DAH, Banerjee NR, Morgan S, Smith-Duque CE, Harris M, Galli L (2010) Subsurface structure of a submarine hydrothermal system in ocean crust formed at the East Pacific Rise, ODP/IODP Site 1256. *Geochemistry, Geophysics, Geosystems* 11(10):Q10010
- Amri I, Benoit M, Ceuleneer G (1996) Tectonic setting for the genesis of oceanic plagiogranites: evidence from a paleo-spreading structure in the Oman ophiolite. *Earth and Planetary Science Letters* 139:177-194
- Amri I, Ceuleneer G, Benoit M, Python M, Puga E, Targuisti K (2007) Genesis of granitoids by interaction between mantle peridotites and hydrothermal fluids in oceanic spreading setting in the Oman Ophiolite. *Geogaceta* 42:23-26
- Andersen DJ, Lindsley DH (1985) New (and final!) models for the Ti-magnetite/ilmenite geothermometer and oxygen barometer. *American Geophysical Union* 66(Abstract AGU 1985 Spring Meeting Eos Transactions):416
- Andersen DJ, Lindsley DH, Davidson PM (1993) QUILF: A pascal program to assess equilibria among Fe-Mg-Mn-Ti oxides, pyroxenes, olivine, and quartz. *Computers & Geosciences* 19(9):1333-1350
- Ayers JC, Eggler DH (1995) Partitioning of elements between silicate melt and H<sub>2</sub>O--NaCl fluids at 1.5 and 2.0 GPa pressure: Implications for mantle metasomatism. *Geochimica et Cosmochimica Acta* 59(20):4237-4246
- Bach W, Peucker-Ehrenbrink B, Hart SR, Blusztajn JS (2003) Geochemistry of hydrothermally altered oceanic crust: DSDP/ODP Hole 504B - Implications for seawater-crust exchange budgets and Sr- and Pb-isotopic evolution of the mantle. *Geochemistry, Geophysics, Geosystems* 4(3)
- Baker MB, Stolper EM (1994) Determining the composition of high-pressure mantle melts using diamond aggregates. *Geochimica et Cosmochimica Acta* 58(13):2811-2827
- Barker F (1979) *Trondhjemitic, dacitic and related rocks*. Elsevier, Amsterdam:659 pp
- Beard JS (1990) Partial melting of metabasites in the contact aureoles of gabbroic plutons in the Smartville complex, Sierra Nevada, California. The nature and origin of Cordilleran magmatism. *Geol. Soc. Am. Mem.* 174:303-313
- Beard JS (1995) Experimental, geological, and geochemical constraints on the origins of low- $\alpha$  K silicic magmas in oceanic arcs. *Journal of Geophysical Research: Solid Earth* 100(B8):15593-15600
- Beard JS, Lofgren GE (1991) Dehydration melting and water-saturated melting of basaltic and andesitic greenstones and amphibolites at 1, 3, and 6.9 kb. *Journal of Petrology* 32:365-401
- Bédard JH (1999) Petrogenesis of Boninites from the Betts Cove Ophiolite, Newfoundland, Canada: Identification of Subducted Source Components. *Journal of Petrology* 40:1853-1889
- Behn MD, Kelemen PB, Hirth G, Hacker BR, Massonne HJ (2011) Diapirs as the source of the sediment signature in arc lavas. *Nature Geoscience* 4:641-646
- Benoit M, Ceuleneer G, Polvé M (1999) The remelting of hydrothermally altered peridotite at mid-ocean ridges by intruding mantle diapirs. *Nature* 402:514-517
- Berndt J, Koepke J, Holtz FO (2005) An Experimental Investigation of the Influence of Water and Oxygen Fugacity on Differentiation of MORB at 200MPa. *Journal of Petrology* 46(1):135-167
- Berndt J, Liesbke C, Holtz F, Freise M, Nowak M, Ziegenbein D, Hurkuck W, Koepke J (2002) A combined rapid-quench and H<sub>2</sub>-membrane setup for internally heated pressure vessels: Description and application for water solubility in basaltic melts. *American Mineralogist* 87(11-12):1717-1726
- Bézos A, Humler E (2005) The Fe<sup>3+</sup>/[Sigma]Fe ratios of MORB glasses and their implications for mantle melting. *Geochimica et Cosmochimica Acta* 69(3):711-725
- Blackman DK, Ildefonse B, John BE, MacLeod CJ, Ohara Y, Miller DJ, Team IEP (2004) Oceanic core complex formation, Atlantis Massif—oceanic core complex formation, Atlantis Massif, Mid-Atlantic Ridge: drilling into the footwall and hanging wall of a tectonic exposure of deep, young oceanic lithosphere to study deformation, alteration, and melt generation. *IODP Sci. Prosp.* 304/305
- Blichert-Toft J, Chauvel C, Albarede F (1997) Separation of Hf and Lu for high-precision isotope analyses of rock samples by magnetic sector-multiple collector ICP-MS. *Contributions to Mineralogy and Petrology* 127:248-260
- Bosch D, Jamaïs M, Boudier F, Nicolas A, Dautria J-M, Agrinier P (2004) Deep and high-temperature hydrothermal circulation in the Oman ophiolite—petrological and isotopic evidence. *Journal of Petrology* 45:1181-1208
- Botcharnikov RE, Almeev RR, Koepke J, Holtz F (2008) Phase Relations and Liquid Lines of Descent in Hydrous Ferrobasalt: Implications for the Skaergaard Intrusion and Columbia River Flood Basalts. *Journal of Petrology* 49(9):1687-1727
- Botcharnikov RE, Behrens H, Holtz F, Koepke J, Sato H (2004) Sulfur and chlorine solubility in Mt. Unzen rhyodacitic melt at 850 °C and 200 MPa. *Chemical Geology* 213(1-3):207-225
- Botcharnikov RE, Holtz F, Behrens H (2007) The effect of CO<sub>2</sub> on the solubility of H<sub>2</sub>O-Cl fluids in andesitic melt. *Eur J Mineral* 19(5):671-680
- Botcharnikov RE, Koepke J, Holtz F, McCammon C, Wilke M (2005) The effect of water activity on the oxidation and structural state of Fe in a ferro-basaltic melt. *Geochimica et Cosmochimica Acta* 69(21):5071-5085
- Boudier F, Ceuleneer G, Nicolas A (1988) Shear zones, thrusts and related magmatism in the Oman ophiolite: Initiation of thrusting on an oceanic ridge. *Tectonophysics* 151:275-296
- Brey GP, Koehler T (1990) Geothermobarometry in Four-phase Lherzolites II. New Thermobarometers, and Practical Assessment of Existing Thermobarometers. *Journal of Petrology* 31(6):1353-1378
- Briqueu L, Mével C, Boudier F (1991) Sr, Nd and Pb isotopic constraints in the genesis of a calc-alkaline plutonic suite in Oman ophiolite related to the obduction process. In: Peters T, Nicolas A, Coleman RG (eds) *Ophiolite genesis and evolution of the oceanic lithosphere*, vol. Ministry of Petroleum and Minerals, Sultanate of Oman, pp 517-542
- Brophy JG (2008) A study of rare earth element (REE)-SiO<sub>2</sub> variations in felsic liquids generated by basalt fractionation and amphibolite melting: a potential test for discriminating between the two different processes. *Contributions to Mineralogy and Petrology* 156:337-357
- Brophy JG (2009) La-SiO<sub>2</sub> and Yb-SiO<sub>2</sub> systematics in mid-ocean ridge magmas: implications for the origin of oceanic plagiogranite. *Contributions to Mineralogy and Petrology* 158:99-111
- Brophy JG, Pu X (2012) Rare earth element-SiO<sub>2</sub> systematics of mid-ocean ridge plagiogranites and host gabbros from the Fournier oceanic fragment, New Brunswick, Canada: a field evaluation of some model predictions. *Contributions to Mineralogy and Petrology* 164:191-204
- Brugger C, Johnston AD, Cashman K (2003) Phase relations in silicic systems at one-atmosphere pressure. *Contributions to Mineralogy and Petrology* 146(3):356-369
- Brugger C, Hammer JE (2010) Crystal size distribution analysis of plagioclase in experimentally decompressed hydrous rhyodacite magma. *Earth and Planetary Science Letters* 300:246-254
- Burnham CW (1979) *The importance of volatile constituents*, vol. Princeton University Press,
- Burnham CW (1981) The nature of multicomponent aluminosilicate melts. *Physics and Chemistry of The Earth* 13-14:197-229
- Burnham CW (1994) Development of the Burnham model for prediction of H<sub>2</sub>O solubility in magmas. In Carroll, M. R. & Holloway, J. R. (eds) *Volatiles in Magmas*. Mineralogical Society of America and Geochemical Society, *Reviews in Mineralogy and Geochemistry* 30:123-129
- Byerly GR, Melson WG, Vogt PR (1976) Rhyodacites, andesites, ferro-basalts and ocean tholeiites from the galapagos spreading center. *Earth and Planetary Science Letters* 30(2):215-221
- Cadoux A, Scailliet B, Druitt TH, Deloué E (2014) Magma storage conditions of large Plinian eruptions of Santorini Volcano (Greece). *Journal of Petrology* 55(6):1129-1171
- Canales JP, Detrick RS, Toomey DR, Wilcock WSD (2003) Segment-scale variations in the crustal structure of 150-300 kyr old fast spreading oceanic crust (East Pacific Rise, 8°15'N-10°5'N) from wide-angle seismic refraction profiles. *Geophysical Journal International* 152(3):766-794
- Carbotte SM, Marjanović M, Carton H, Mutter JC, Canales JP, Nedimović MR, Han S, Perfit MR (2013) Fine-scale segmentation of the crustal magma reservoir beneath the East Pacific Rise. *Nature Geoscience* 6, 866-870
- Caress DW, Burnett MS, Orcutt JA (1992) Tomographic image of the axial low-velocity zone at 12°50'N on the East Pacific Rise. *Journal of Geophysical Research: Solid Earth* 97(B6):9243-9263
- Carmichael ISE, Turner FJ, Verhoogen J (1974) *Igneous petrology*, vol. McGraw-Hill, New York
- Castillo PR (2012) Adakite petrogenesis. *Lithos* 134-135:304-316

- Charlier B, Grove TL (2012) Experiments on liquid immiscibility along tholeiitic liquid lines of descent. *Contributions to Mineralogy and Petrology* 164(1):27-44.
- Charlier B, Namur O, Grove TL (2013) Compositional and kinetic controls on liquid immiscibility in ferrobasalt-rhyolite volcanic and plutonic series. *Geochimica et Cosmochimica Acta* 113(0):79-93
- Charlier B, Namur O, Toplis MJ, Schiano P, Cluzel N, Higgins MD, Vander Auwera J (2011) Large-scale silicate liquid immiscibility during differentiation of tholeiitic basalt to granite and the origin of the Daly gap. *Geology* 39:907-910
- Chauvel C, Blichert-Toft J (2001) A hafnium isotope and trace element perspective on melting of the depleted mantle. *Earth and Planetary Science Letters* 190:137-151
- Coleman RG (1977) *Ophiolites*, vol. Springer, Berlin
- Coleman RG (1981) Tectonic setting for ophiolite obduction in Oman. *Journal of Geophysical Research* 86:2497-2508
- Coleman RG, Donato MM (1979) Oceanic plagiogranite revisited. In: Barker F (ed) *Trondhjemites, dacites and related rocks*, vol. Elsevier, Amsterdam, pp 149-168
- Coleman RG, Peterman ZE (1975) Oceanic plagiogranite. *Journal of Geophysical Research* 80:1099-1108
- Coogan LA (2003) Contamination of the lower oceanic crust in the Oman ophiolite. *Geology* 31, 1065-1068
- Coogan LA (2007) The Lower Oceanic Crust. In: *Treatise on Geochemistry*, vol 3.
- Coogan LA, Gillis KM, MacLeod CJ, Thompson GM, Hékinian R (2002) Petrology and geochemistry of the lower ocean crust formed at the East Pacific Rise and exposed at Hess Deep: A synthesis and new results. *Geochemistry, Geophysics, Geosystems* 3(11):1-30.
- Coogan LA, Mitchell NC, O'Hara MJ (2003) Roof assimilation at fast spreading ridges: An investigation combining geophysical, geochemical, and field evidence. *J. Geophys. Res.* 108(B1):2002
- Coogan LA, Saunders AD, Wilson RN (2014) Aluminum-in-olivine thermometry of primitive basalts: Evidence of an anomalously hot mantle source for large igneous provinces. *Chemical Geology* 368:1-10
- Costa F, Scaillet B, Pichavant M (2004) Petrological and experimental constraints on the pre-eruption conditions of Holocene dacite from Volcán San Pedro (36 S, Chilean Andes) and the importance of sulphur in silicic subduction-related magmas. *Journal of Petrology* 45(4):855-881
- Cotsonika LA, Perfit MR, Smith MC, Kamenov G, Stakes D, Ridley WI, Wallace P (2005) Petrogenesis of Andesites and Dacites From the Southern Juan de Fuca Ridge. *Eos Trans. AGU* 86 (52)(Fall Meet. Suppl.):Abstract V13B-0551
- Cottrell E, Kelley KA (2011) The influence of magmatic differentiation on the oxidation state of Fe in a basaltic arc magma. *Earth and Planetary Science Letters* 305(3-4):270-282
- Cowan RJ, Searle MP, Waters DJ (2014) Structure of the metamorphic sole to the Oman Ophiolite, Sumeini Window and Wadi Tayyin: implications for ophiolite obduction processes. In: Rollinson HR, Searle MP, Abbasi IA, Al-Lazki A, Kindi MHA (eds) *Tectonic Evolution of the Oman Mountains*, vol 392. Geological Society, London, London, pp 155-175
- Cox J, Searle M, Pedersen R (1999) The petrogenesis of leucogranitic dykes intruding the northern Semai ophiolite, United Arab Emirates: field relationships, geochemistry and Sr/Nd isotope systematics. *Contributions to Mineralogy and Petrology* 137:267-287
- Crawford WC, Webb SC, Hildebrand JA (1999) Constraints on melt in the lower crust and Moho at the East Pacific Rise, 9°48'N, using seafloor compliance measurements. *Journal of Geophysical Research: Solid Earth* 104(B2):2923-2939
- Dall'Agnol R, Scaillet B, Pichavant M (1999) An experimental study of a lower proterozoic A-type granite from the Eastern Amazonian Craton, Brazil. *Journal of Petrology* 40(11): 1673-1698
- Danyushevsky LV, Plechov P (2011) Petrolog3: Integrated software for modeling crystallization processes. *Geochemistry, Geophysics, Geosystems* 12
- Davis J, Coleman D, Gracely J, Gaschnig R, Stearns M (2012) Magma accumulation rates and thermal histories of plutons of the Sierra Nevada batholith, CA. *Contributions to Mineralogy and Petrology*:1-17
- DePaolo DJ (1981) Trace element and isotopic effects of combined wallrock assimilation and fractional crystallization. *Earth and Planetary Science Letters* 53(2), 189-202
- Delaney JR, Kelley DS, Lilley MD, Butterfield DA, Baross JA, Wilcock WSD, Embley RW, Summit M (1998) The quantum event of oceanic crustal accretion: Impacts of diking at Mid-ocean Ridges. *Science* 281:222-230
- Detrick RS, Buhl P, Vera E, Mutter J, Orcutt J, Madsen J, Brocher T (1987) Multi-channel seismic imaging of a crustal magma chamber along the East Pacific Rise. *Nature* 326:35-41
- Devine JD, Gardner JE, Brack HP, Layne GD, Rutherford MJ (1995) Comparison of microanalytical methods for estimating H<sub>2</sub>O contents of silicic volcanic glasses. *American Mineralogist* 80(3-4):319-328
- Dick HJB, MacLeod CJ, Blum P (2015) Southwest Indian Ridge lower crust and Moho: the nature of the lower crust and Moho at slower spreading ridges (SloMo-Leg 1). *International Ocean Discovery Program Scientific Prospectus*, 360
- Dick HJB, Natland JH, Alt JC, Bach W, Bideau D, Gee JS, Haggas S, Hertogen JGH, Hirth G, Holm PM, Ildefonse B, Iturrino GJ, John BE, Kelley DS, Kikawa E, Kingdon A, LeRoux PJ, Maeda J, Meyer PS, Miller DJ, Naslund HR, Niu Y-L, Robinson PT, Snow J, Stephen RA, Trimby PW, Worm H-U, Yoshinobu A (2000) A long in situ section of the lower ocean crust: results of ODP Leg 176 drilling at the Southwest Indian Ridge. *Earth and Planetary Science Letters* 179(1):31-51
- Dick HJB, Ozawa K, Meyer PS, Niu Y, Robinson PT, Constantin M, Hebert R, Maeda J, Natland JH, Hirth JG (2002) Primary silicate mineral chemistry of a 1.5-km section of very slow spreading lower ocean crust: ODP hole 735B, Southwest Indian ridge. *Proceedings of the Ocean Drilling Program, Scientific Results*, J. Natland, H. Dick, D. Miller, RP Von Herzen, eds. Online:1-61
- Dilek Y, Furnes H (2011) Ophiolite genesis and global tectonics: Geochemical and tectonic fingerprinting of ancient oceanic lithosphere. *Geological Society of America Bulletin* 123:387-411
- Dixon S, Rutherford MJ (1979) Plagiogranites as late-stage immiscible liquids in ophiolite and mid-ocean ridge suites: an experimental study. *Earth and Planetary Science Letters* 45, 45-60
- Dixon-Spulber S, Rutherford MJ (1983) The Origin of Rhyolite and Plagiogranite in Oceanic Crust: An Experimental Study. *Journal of Petrology* 24(1):1-25
- Donhowe DP, Hartel RW (1996) Recrystallization of ice in ice cream during controlled accelerated storage. *International Dairy Journal* 6(11-12):1191-1208
- Dreyer BM, Portner RA, Clague DA, Daczko N, Castillo P, Bindeman IN (2014) The Complex History of Alarcon Rise Mid-Ocean Ridge Rhyolite Revealed through Mineral Chemistry. *Eos Trans. AGU (Fall Meet. Suppl.):Abstract #V31B-4746*
- Dunn RA, Toomey DR, Solomon SC (2000) Three-dimensional seismic structure and physical properties of the crust and shallow mantle beneath the East Pacific Rise at 9°30'N. *Journal of Geophysical Research: Solid Earth* 105(B10):23537-23555
- Eggler DH, Burnham CW (1973) Crystallization and fractionation trends in the system andesite-H<sub>2</sub>O-CO<sub>2</sub>-O<sub>2</sub> at pressures to 10 kb. *Geological Society of America Bulletin* 84(8):2517-2532
- Einaudi F, Godard M, Pezard P, Cochemé J-J, Coulon C, Brewer T, Harvey P (2003) Magmatic cycles and formation of the upper oceanic crust at spreading centers: Geochemical study of a continuous extrusive section in the Oman ophiolite. *Geochemistry Geophysics Geosystems* 4
- Elliott T (2003) Tracers of the slab. *Am. Geophys. Un. Geophys. Mon.* 138:23-45
- Erdmann M, Fischer LA, France L, Zhang C, Godard M, Koepke J (2015) Anatexis at the roof of an oceanic magma chamber at IODP Site 1256 (equatorial Pacific): an experimental study. *Contributions to Mineralogy and Petrology* 169
- Erdmann M, Koepke J (2016a) Experimental temperature cycling as a powerful tool to enlarge melt pools and crystals at magma storage conditions. *American Mineralogist* 101(4):960-969
- Erdmann M, Koepke J (2016b) Silica-rich lavas in the oceanic crust: experimental evidence for fractional crystallization under low water activity. *Contributions to Mineralogy and Petrology*, 171(10):83
- Ernewein M, Pflumio C, Whitechurch H (1988) The death of an accretion zone as evidenced by the magmatic history of the Sumail ophiolite (Oman). *Tectonophysics* 151:247-274
- Ernst WG (1976) *Petrologic phase equilibria*. San Francisco, W.H. Freeman and Co.:333
- Ernst WG, Liu JUN (1998) Experimental phase-equilibrium study of Al and Ti-contents of calcic amphibole in MORB - A semiquantitative thermobarometer. *Am. Mineral* 83:952-969
- Expedition 309/312 Scientists, 2006. Site 1256. *Proc. IODP, 309/312* 309/312, 1-549
- Fahey AJ (1998) Details of the measurement of rare earth and other trace element abundances by secondary ion mass spectrometry. *International Journal of Mass Spectrometry* 176(1):63-76
- Fahey AJ, Zimmer EK, Crozaz G, Kornacki AS (1987) Microdistributions of Mg isotopes and REE abundances in a Type A calcium-aluminum-rich inclusion from Efremovka. *Geochimica et Cosmochimica Acta* 51(12):3215-3229
- Feig S, Koepke J, Snow J (2006) Effect of water on tholeiitic basalt phase equilibria: an experimental study under oxidizing conditions. *Contributions to Mineralogy and Petrology* 152(5):611-638
- Feig S, Koepke J, Snow J (2010) Effect of oxygen fugacity and water on phase equilibria of a hydrous tholeiitic basalt. *Contributions to Mineralogy and Petrology* 160(4):551-568
- Fischer LA (2011) Experimental hydrous partial melting of gabbro: A new approach to enlarge melt pools by adding synthetic glass. BSc thesis, Gottfried Wilhelm Leibniz Universität Hannover, 56 p.
- Fischer LA, Brophy JG, Erdmann M, Koepke J (2012) Experimental hydrous partial melting of gabbro: A new approach to enlarge melt pools by adding synthetic glass. Abstract for EMPG conference 2012, Kiel
- Fischer LA, Erdmann M, France L, Wolff PE, Deloué E, Zhang C, Godard M, Koepke J (2016) Trace element evidence for anatexis at oceanic magma chamber roofs and the role of partial melts for contamination of fresh MORB. *Lithos* 260:1-8
- Flagler PA, Spray JG (1991) Generation of plagiogranite by amphibolite anatexis in oceanic shear zones. *Geology* 19(1):70-73

- Foley S, Tiepolo M, Vannucci R (2002) Growth of early continental crust controlled by melting of amphibolite in subduction zones. *Nature* 417(6891):837-840
- Fornari DJ, Perfit MR, Malahoff A, Embley R (1983) Geochemical studies of abyssal lavas recovered by DSRV Alvin from Eastern Galapagos Rift, Inca Transform, and Ecuador Rift: 1. Major element variations in natural glasses and spatial distribution of lavas. *Journal of Geophysical Research: Solid Earth* 88(B12):10519-10529
- France L, Ildefonse B, Koepke J (2009) Interactions between magma and hydrothermal system in Oman ophiolite and in IODP Hole 1256D: Fossilization of a dynamic melt lens at fast spreading ridges. *Geochem. Geophys. Geosyst.* 10(10):Q10019
- France L, Ildefonse B, Koepke J (2013) Hydrous magmatism triggered by assimilation of hydrothermally altered rocks in fossil oceanic crust (northern Oman ophiolite). *Geochemistry, Geophysics, Geosystems* 14(8):2598-2614
- France L, Koepke J, Ildefonse B, Cichy S, Deschamps F (2010) Hydrous partial melting in the sheeted dike complex at fast spreading ridges: experimental and natural observations. *Contributions to Mineralogy and Petrology* 160(5):683-704
- France L, Koepke J, MacLeod CJ, Ildefonse B, Godard M, Deloule E (2014) Contamination of MORB by anatexis of magma chamber roof rocks: Constraints from a geochemical study of experimental melts and associated residues. *Lithos* 202-203:120-137
- Freund S (2014) The generation of felsic magmas in the oceanic crust: assimilation-fractional crystallization processes versus re-melting of the crust. Dissertation, Friedrich-Alexander-Universität Erlangen-Nürnberg, 152 p.
- Freund S, Beier C, Krumm S, Haase KM (2013) Oxygen isotope evidence for the formation of andesitic-dacitic magmas from the fast-spreading Pacific-Antarctic Rise by assimilation-fractional crystallization. *Chemical Geology* 347:271-283
- Freund S, Haase KM, Keith M, Beier C, Garbe-Schönberg D (2014) Constraints on the formation of geochemically variable plagiogranite intrusions in the Troodos Ophiolite, Cyprus. *Contributions to Mineralogy and Petrology* 167
- Gaetani GA, Grove TL, Bryan WB (1993) The influence of water on the petrogenesis of subduction-related igneous rocks. *Nature* 365: 332-334
- Gale A, Dalton CA, Langmuir CH, Su Y, Schilling J-G (2013) The mean composition of ocean ridge basalts. *Geochemistry, Geophysics, Geosystems* 14(3):489-518
- Gao S, Liu X, Yuan H, Hattendorf B, Günther D, Chen L, Hu S (2002) Determination of forty two major and trace elements in USGS and NIST SRM glasses by Laser Ablation-Inductively Coupled Plasma-Mass Spectrometry. *Geostandards Newsletter* 26(2):181-196
- Geist D, Howard KA, Larson P (1995) The Generation of Oceanic Rhyolites by Crystal Fractionation: the Basalt-Rhyolite Association at Volcán Alcedo, Galápagos Archipelago. *J. Petrology* 36(4):965-982
- Gerya TV (2011) Intra-oceanic subduction zones, in Brown D., and Ryan PD, eds., *Arc-continent collision*: Berlin, Springer Verlag, p. 23-51
- Ghiorso MS, Sack RO (1995) Chemical mass transfer in magmatic processes IV. A revised and internally consistent thermodynamic model for the interpolation and extrapolation of liquid-solid equilibria in magmatic systems at elevated temperatures and pressures. *Contributions to Mineralogy and Petrology* 119(2):197-212
- Gillis KM (2008) The roof of an axial magma chamber: A hornfelsic heat exchanger. *Geology* 36:299-302
- Gillis KM, Coogan LA (2002) Anatectic migmatites from the roof of an ocean ridge magma chamber. *Journal of Petrology* 43:2075-2095
- Gillis KM, Roberts MD (1999) Cracking at the magma-hydrothermal transition: evidence from the Troodos Ophiolite, Cyprus. *Earth and Planetary Science Letters* 169:227-244
- Gillis KM, Robinson PT (1988) Distribution of alteration zones in the upper oceanic crust. *Geology* 16:262-266
- Giordano D, Russell JK, Dingwell DB (2008) Viscosity of magmatic liquids: A model. *Earth and Planetary Science Letters* 271(1-4):123-134
- Gladney ES, O'Malley BT, Roelands I, Gills TE (1987) Compilation of Elemental Concentration Data for NBS Clinical, Biological, Geological, and Environmental Standard Reference Materials. National Bureau of Standards (U.S.) NBS Special Publication 260-111:547
- Godard M, Bosch D, Einaudi F (2006) A MORB source for low-Ti magmatism in the Semail ophiolite. *Chemical Geology* 234:58-78
- Godard M, Dautria J-M, Perrin M (2003) Geochemical variability of the Oman ophiolite lavas: Relationship with spatial distribution and paleomagnetic directions. *Geochemistry Geophysics Geosystems* 4
- Goodenough KM, Styles MT, Schofield D, Thomas RJ, Crowley QC, Lilly RM, McKervey J, Stephenson D, Carney JN (2010) Architecture of the Oman - UAE ophiolite: evidence for a multi-phase magmatic history. *Arab. J. Geosc.* 3:439-458
- Goodenough KM, Thomas RJ, Styles MT, Schofield DI, MacLeod CJ (2014) Records of ocean growth and destruction in the Oman-UAE ophiolite. *Elements* 10:109-114
- Gregory RT, Taylor HP (1981) An oxygen isotope profile in a section of Cretaceous oceanic crust, Semail ophiolite, Oman.; Evidence for  $\delta^{18}\text{O}$  buffering of the oceans by deep (>5 km) seawater-hydrothermal circulation at mid-ocean ridges. *Journal of Geophysical Research* 86:2737-2755
- Grimes CB, John BE, Cheadle MJ, Wooden JL (2008) Protracted construction of gabbroic crust at a slow spreading ridge: Constraints from 206Pb/238U zircon ages from Atlantis Massif and IODP Hole U1309D (30°N, MAR). *Geochemistry, Geophysics, Geosystems* 9
- Grimes CB, Ushikubo T, Kozdon R, Valley JW (2013) Perspectives on the origin of plagiogranite in ophiolites from oxygen isotopes in zircon. *Lithos* 179(0):48-66
- Grove TL, Bence AE (1979) Crystallization kinetics in a multiply saturated basalt magma - an experimental study of Luna 24 ferrobasalt. *Lunar and Planetary Science Conference* 1:439-478
- Grimes CB, Ushikubo T, John BE, Valley JW (2011) Uniformly mantle-like  $\delta^{18}\text{O}$  in zircons from oceanic plagiogranites and gabbros. *Contributions to Mineralogy and Petrology* 161:13-33
- Grimes CB, Ushikubo T, Kozdon R, Valley JW (2013) Perspectives on the origin of plagiogranite in ophiolites from oxygen isotopes in zircon. *Lithos* 179:48-66
- Guillot S, Le Fort P (1995) Geochemical constraints on the bimodal origin of High Himalayan leucogranites. *Lithos* 35:221-234.
- Guo Z, Wilson M (2012) The Himalayan leucogranites: Constraints on the nature of their crustal source region and geodynamic setting. *Gondwana Research* 22:360-376
- Haase KM, Freund S, Koepke J, Hauff F, Erdmann M (2015) Melts of sediments in the mantle wedge of the Oman ophiolite. *Geology* 43:275-278
- Haase KM, Stroncik N, Garbe-Schönberg D, Stoffers P (2006) Formation of island arc dacite magmas by extreme crystal fractionation: An example from Brothers Seamount, Kermadec island arc (SW Pacific). *Journal of Volcanology and Geothermal Research* 152(3-4):316-330
- Haase KM, Stroncik NA, Hekinian R, Stoffers P (2005) Nb-depleted andesites from the Pacific-Antarctic Rise as analogs for early continental crust. *Geology* 33(12):921-924
- Hamilton DL, Burnham CW, Osborn EF (1964) The solubility of water and effects of oxygen fugacity and water content on crystallization in mafic magmas. *Journal of Petrology* 5(1):21-39
- Hanghøj K, Kelemen PB, Hassler D, Godard M (2010) Composition and genesis of depleted mantle peridotites from the Wadi Tayin Massif, Oman Ophiolite; Major and trace element geochemistry, and Os isotope and PGE systematics. *Journal of Petrology* 51:201-227
- Hedenquist JW, Lowenstern JB (1994) The role of magmas in the formation of hydrothermal ore deposits. *Nature* 370(6490):519-527
- Hekinian R, Stoffers P, Ackermann D, Révillon S, Maia M, Bohn M (1999) Ridge-hotspot interaction: the Pacific-Antarctic Ridge and the foundation seamounts. *Marine Geology* 160(3-4):199-223
- Hellebrand E, Snow JE, Hoppe P, Hofmann AW (2002) Garnet-field melting and late-stage refertilization in 'residual' abyssal peridotites from the Central Indian Ridge. *Journal of Petrology* 43(12):2305-2338
- Helz RT (1973) Phase Relations of Basalts in their Melting Range at  $\text{PH}_2\text{O} = 5 \text{ kb}$  as a Function of Oxygen Fugacity: Part I. Mafic Phases. *Journal of Petrology* 14(2):249-302
- Hermann J, Spandler CJ (2008) Sediment Melts at Sub-arc Depths: an Experimental Study. *Journal of Petrology* 49:717-740.
- Hofmann AW (1988) Chemical differentiation of the Earth: the relationship between mantle, continental crust, and oceanic crust. *Earth and Planetary Science Letters* 90:297-314
- Holland T, Blundy J (1994) Non-ideal interactions in calcic amphiboles and their bearing on amphibole-plagioclase thermometry. *Contributions to Mineralogy and Petrology* 116(4):433-447
- Holloway JR, Burnham C (1972) Melting relations of basalt with equilibrium water pressure less than total pressure. *Journal of Petrology* 13:1-29
- Holloway JR, Dixon JE, Pawley AR (1992) An internally heated, rapid-quench, high-pressure vessel. *American Mineralogist* 77(5-6):643-646
- Holtz F, Johannes W, Tamic N, Behrens H (2001) Maximum and minimum water contents of granitic melts generated in the crust: a reevaluation and implications. *Lithos* 56(1):1-14
- Holtz F, Pichavant M, Barbey P, Johannes W (1992) Effects of  $\text{H}_2\text{O}$  on liquidus phase relations in the haplogranite system at 2 and 5 kbar. *American Mineralogist* 77(11-12):1223-1241
- Holtz F, Sato H, Lewis J, Behrens H, Nakada S (2005) Experimental petrology of the 1991-1995 Unzen dacite, Japan. Part I: phase relations, phase composition and pre-eruptive conditions. *Journal of Petrology* 46(2):319-337
- Huppert HE, Sparks RSJ (1988) The Generation of Granitic Magmas by Intrusion of Basalt into Continental Crust. *Journal of Petrology* 29(3):599-624
- Hyndman RD, Peacock SM (2003) Serpentinization of the forearc mantle. *Earth and Planetary Science Letters* 212:417-432
- Ila P, Frey FA (2000) Trace Element Analysis of USGS Standards AGV2, BCR2, BHVO2, DTS2 and GSP2 by INAA. *Journal of Radioanalytical and Nuclear Chemistry* 244(3):599-602



- Ishikawa T, Fujisawa S, Nagaishi K, Masuda T (2005) Trace element characteristics of the fluid liberated from amphibolite-facies slab: Inference from the metamorphic sole beneath the Oman ophiolite and implication for boninite genesis. *Earth and Planetary Science Letters* 240:355-377
- Ishikawa T, Nagaishi K, Umino S (2002) Boninitic volcanism in the Oman ophiolite: Implications for thermal condition during transition from spreading ridge to arc. *Geology* 30:899-902
- Jambon A, Déruelle B, Dreibus G, Pineau F (1995) Chlorine and bromine abundance in MORB: the contrasting behaviour of the Mid-Atlantic Ridge and East Pacific Rise and implications for chlorine geodynamic cycle. *Chemical Geology* 126(2):101-117
- Johannes W, Holtz F (1996) *Petrogenesis and Experimental Petrology of Granitic Rocks*. Springer Verlag, Heidelberg
- Johannes W, Koepke J (2001) Incomplete reaction of plagioclase in experimental dehydration melting of amphibolite. *Australian Journal of Earth Sciences: An International Geoscience Journal of the Geological Society of Australia* 48(4):581 – 590
- Johnson MC, Plank T (1999) Dehydration and melting experiments constrain the fate of subducted sediments. *Geochemistry Geophysics Geosystems* 1
- Juster TC, Grove TL, Perfit MR (1989) Experimental Constraints on the Generation of FeTi Basalts, Andesites, and Rhyodacites at the Galapagos Spreading Center, 85°W and 95°W. *J. Geophys. Res.* 94(B7):9251-9274
- Juteau T, Ernewein M, Reuber I, Whitechurch H, Dahl R (1988) Duality of magmatism in the plutonic sequence of the Sumail Nappe, Oman. *Tectonophysics* 151:107-135
- Kawahata H, Nohara M, Ishizuka H, Hasebe S, Chiba H (2001) Sr isotope geochemistry and hydrothermal alteration of the Oman ophiolite. *Journal of Geophysical Research* 106(B6):11083
- Kawamoto T (1996) Experimental constraints on differentiation and H<sub>2</sub>O abundance of calc-alkaline magmas. *Earth and Planetary Science Letters* 144(3-4):577-589
- Kendrick MA, Arculus R, Burnard P, Honda M (2013) Quantifying brine assimilation by submarine magmas: Examples from the Galápagos Spreading Centre and Lau Basin. *Geochimica et Cosmochimica Acta* 123: 150-165
- Kepler H (1996) Constraints from partitioning experiments on the composition of subduction-zone fluids. *Nature* 380(6571):237-240
- Kirkpatrick RJ (1977) Nucleation and growth of plagioclase, Makaopuhi and Alae lava lakes, Kilauea Volcano, Hawaii. *Geological Society of America Bulletin* 88(1):78-84
- Klein EM (2003) Geochemistry of the igneous ocean crust, in: Rudnick, R.L. (Ed.), *Treatise on Geochemistry*. The Crust. pp. 433–463
- Koepke J, Berndt J, Bussy F (2003) An experimental study on the shallow-level migmatization of ferrogabbros from the Fuerteventura Basal Complex, Canary Islands. *Lithos* 69(3-4):105-125
- Koepke J, Berndt J, Feig ST, Holtz F (2007) The formation of SiO<sub>2</sub>-rich melts within the deep oceanic crust by hydrous partial melting of gabbros. *Contributions to Mineralogy and Petrology* 153:67-84
- Koepke J, Berndt J, Horn I, Fahle J, Wolff PE (2014) Partial melting of oceanic gabbro triggered by migrating water-rich fluids: a prime example from the Oman Ophiolite. *Geological Society, London, Special Publications* 392(1):195-212
- Koepke J, Christie DM, Dziony W, Holtz F, Lattard D, MacLennan J, Park S, Scheibner B, Yamasaki T, Yamazaki S (2008) Petrography of the dike-gabbro transition at IODP Site 1256 (equatorial Pacific): The evolution of the granoblastic dikes. *Geochem. Geophys. Geosyst.* 9(7):Q07009
- Koepke J, Feig S, Snow J (2005a) Late stage magmatic evolution of oceanic gabbros as a result of hydrous partial melting: Evidence from the Ocean Drilling Program (ODP) Leg 153 drilling at the Mid-Atlantic Ridge. *Geochem. Geophys. Geosyst.* 6(2):Q02001
- Koepke J, Feig S, Snow J (2005b) Hydrous partial melting within the lower oceanic crust. *Terra Nova* 17(3):286-291
- Koepke J, Feig S, Snow J, Freise M (2004) Petrogenesis of oceanic plagiogranites by partial melting of gabbros: an experimental study. *Contributions to Mineralogy and Petrology* 146(4):414-432
- Koepke J, France L, Müller T, Faure F, Goetze N, Dziony W, Ildefonse B (2011) Gabbros from IODP Site 1256, equatorial Pacific: Insight into axial magma chamber processes at fast spreading ocean ridges. *Geochem. Geophys. Geosyst.* 12(9):Q09014
- Koepke J, Goetze N (2015) Data report: Microanalytical and geothermometric investigations on granoblastic dikes from the gabbro-dike transition from Hole 1256D (IODP Expedition 335, East Pacific Rise). In Teagle, D.A.H., Ildefonse, B., Blum, P., and the Expedition 335 Scientists, Proc. IODP, 335. Integrated Ocean Drilling Program Management International, Inc., Tokyo. doi:10.2204/iodp.proc.335.201.2015
- Koepke J, Schoenborn S, Oelze M, Wittmann H, Feig ST, Hellebrand E, Boudier F, Schoenberg R (2009) Petrogenesis of crustal wehrlites in the Oman ophiolite: Experiments and natural rocks. *Geochem. Geophys. Geosyst.* 10(10):Q10002
- König S, Münker C, Schuth S, Luguët A, Hoffmann JE, Kuduon J (2010) Boninites as windows into trace element mobility in subduction zones. *Geochimica et Cosmochimica Acta* 74: 684-704
- Kusano Y, Adachi Y, Miyashita S, Umino S (2012) Lava accretion system around mid-ocean ridges: Volcanic stratigraphy in the Wadi Fizh area, northern Oman ophiolite. *Geochemistry Geophysics Geosystems* 13
- Lamoureux GI, Ildefonse B, Mainprice D (1999) Modelling the seismic properties of fast-spreading ridge crustal Low-Velocity Zones: insights from Oman gabbro textures. *Tectonophysics* 312(2-4):283-301
- Lehnert K, Su Y, Langmuir CH, Sarbas B, Nohl U (2000) A global geochemical database structure for rocks. *Geochemistry Geophysics Geosystems* 1
- Le Bas MJ, Streckeisen AL (1991) The IUGS systematics of igneous rocks. *Journal of the Geological Society of London* 148:825-834
- Le Roux PJ, Shirey SB, Hauri EH, Perfit MR, Bender JF (2006) The effects of variable sources, processes and contaminants on the composition of northern EPR MORB (8-10°N and 12-14°N): Evidence from volatiles (H<sub>2</sub>O, CO<sub>2</sub>, S) and halogens (F, Cl). *Earth and Planetary Science Letters* 251, 209–231
- Lilly RM (2006) The magmatic evolution and crustal accretion of the Northern Oman-United Arab Emirates ophiolite. Dissertation, Cardiff University, 202 p.
- Lippard SJ, Shelton AW, Gass IG (1986) The ophiolite of northern Oman, vol. Blackwell, Oxford, p 178
- Lissenberg CJ, MacLeod CJ, Howard KA, Godard M (2013) Pervasive reactive melt migration through fast-spreading lower oceanic crust (Hess Deep, equatorial Pacific Ocean). *Earth and Planetary Science Letters* 361, 436–447
- Lissenberg CJ, Rioux M, Shimizu N, Bowring SA, Mével C (2009) Zircon dating of oceanic crustal accretion. *Science* 323:1048-1050
- Lister CRB (1974) On the Penetration of Water into Hot Rock. *Geophysical Journal International* 39(3):465-509
- Lowell RP, Burnell DK (1991) Mathematical modeling of conductive heat transfer from a freezing, convecting magma chamber to a single-pass hydrothermal system: Implications for seafloor black smokers. *Earth and Planetary Science Letters* 104(1):59-69.
- MacLeod CJ, Lissenberg CJ, Bibby LE (2013) "Moist MORB" axial magmatism in the Oman ophiolite: The evidence against a mid-ocean ridge origin. *Geology* 41:459-462
- MacLeod CJ, Rothery DA (1992) Ridge axial segmentation in the Oman ophiolite: evidence from along-strike variations in the sheeted dyke complex. *Geological Society, London, Special Publications* 60(1):39-63.
- MacLeod CJ, Yaouancq G (2000) A fossil melt lens in the Oman ophiolite: Implications for magma chamber processes at fast spreading ridges. *Earth and Planetary Science Letters* 176:357-373
- Mahoney JJ, Frei R, Tejada MLG, Mo XX, Leat PT, Nägler TF (1998) Tracing the Indian Ocean mantle domain through time: Isotopic results from old West Indian, East Tethyan, and South Pacific seafloor. *Journal of Petrology* 39:1285-1306
- Marjanovic M, Carbotte SM, Carton H, Nedimovic MR, Mutter JC, Canales JP (2014) A multi-sill magma plumbing system beneath the axis of the East Pacific Rise. *Nature Geoscience* 7:825-829
- Marsh BD, Gunnarson B, Congdon R, Carmody R (1991) Hawaiian basalt and Icelandic rhyolite: indicators of differentiation and partial melting. *Geologische Rundschau* 80:481-510
- Martel C, Pichavant M, Bourdier JL, Traineau H, Holtz F, Scaillet B (1998) Magma storage conditions and control of eruption regime in silicic volcanoes: experimental evidence from Mt. Pelée. *Earth and Planetary Science Letters* 156(1-2):89-99
- Martin E, Martin H, Sigmarrson O (2008) Could Iceland be a modern analogue for the Earth's early continental crust? *Terra Nova* 20(6):463-468
- Martin D, Griffiths R, Campbell I (1987) Compositional and thermal convection in magma chambers. *Contributions to Mineralogy and Petrology* 96(4):465-475
- McBirney AR (2008) Comments on: "Liquid Immiscibility and the Evolution of Basaltic Magma" *Journal of Petrology* 48, 2187-2210. *Journal of Petrology* 49(12):2169-2170
- McBirney AR, Nakamura Y (1974) Immiscibility in late-stage magmas of the Skaergaard intrusion. *Carnegie Institution of Washington Yearbook* 73:348-352
- McCaig AM, Harris M (2012) Hydrothermal circulation and the dike-gabbro transition in the detachment mode of slow seafloor spreading. *Geology* 40(4):367-370
- McKenzie D, O'Nions RK (1991) Partial melt distributions from inversion of rare Earth element concentrations. *Journal of Petrology* 32, 1021-1091
- Meurer WP, Gee JS (2002) Evidence for the protracted construction of slow-spread oceanic crust by small magmatic injections. *Earth and Planetary Science Letters* 201:45-55
- Mibe K, Fujii T, Yasuda A (1998) Connectivity of aqueous fluids in the Earth's upper mantle. *Geophysical Research Letters* 25:1233-1236
- Michael PJ, Chase R (1987) The influence of primary magma composition, H<sub>2</sub>O and pressure on mid-ocean ridge basalt differentiation. *Contributions to Mineralogy and Petrology* 96(2):245-263
- Michael PJ, Cornell WC (1998) Influence of spreading rate and magma supply on crystallization and assimilation beneath mid-ocean ridges: Evidence from chlorine and major element chemistry of mid-ocean ridge basalts. *J. Geophys. Res.* 103(B8):18325-18356

- Michael PJ, Schilling J-G (1989) Chlorine in mid-ocean ridge magmas: Evidence for assimilation of seawater-influenced components. *Geochimica et Cosmochimica Acta* 53(12):3131-3143
- Mills R, Glazner A (2013) Experimental study on the effects of temperature cycling on coarsening of plagioclase and olivine in an alkali basalt. *Contributions to Mineralogy and Petrology*:1-15
- Mills RD, Glazner AF (2011) Experimental evidence for coarsening of crystals and bubbles during thermal cycling of mafic and silicic magmas. *Goldschmidt Conference Abstracts: Mineralogical Magazine* 75:1475
- Mills RD, Ratner JJ, Glazner AF (2011) Experimental evidence for crystal coarsening and fabric development during temperature cycling. *Geology* 39(12):1139-1142
- Moghadam HS, Stern RJ, Kimura J-I, Hirahara Y, Senda R, Miyazaki T (2012) Hf-Nd isotope constraints on the origin of Dehshir Ophiolite, Central Iran. *The Island Arc* 21:202-214
- Morgan VI GB, London D (2005) Effect of current density on the electron microprobe analysis of alkali aluminosilicate glasses *American Mineralogist* 90:1131-1138
- Morris J, Tera F (1989) 10Be and 9Be in mineral separates and whole rocks from volcanic arcs; implications for sediment subduction. *Geochimica et Cosmochimica Acta* 53:3197-3206
- Morse SA (2008) Compositional Convection Trumps Silicate Liquid Immiscibility in Layered Intrusions: a Discussion of "Liquid immiscibility and the evolution of basaltic magma" by Veksler et al., *Journal of Petrology* 48, 2187-2210. *Journal of Petrology* 49(12):2157-2168
- Müller T, Koepke J, Garbe-Schönberg CD, Dietrich M, Bauer U, Wolff PE (accepted) Anatomy of a frozen axial melt lens from a fast-spreading paleo-ridge (Wadi Gideah, Oman ophiolite). *Lithos*, accepted with minor revisions
- Nakajima K, Arima M (1998) Melting experiments on hydrous low-K tholeiite: Implications for the genesis of tonalitic crust in the Izu-Bonin-Mariana arc. *Island Arc* 7(3):359-373
- Naslund HR (1986) Disequilibrium partial melting and rheomorphic layer formation in the contact aureole of the Basistoppen sill, East Greenland. *Contributions to Mineralogy and Petrology* 93(3):359-367
- Natland JH, Dick HJB (2009) Paired melt lenses at the East Pacific Rise and the pattern of melt flow through the gabbroic layer at a fast-spreading ridge. *Lithos* 112(1-2):73-86
- Natland JH, Meyer PS, Dick HJB, Bloomer SH (1991) 4. Magmatic oxides and sulfides in gabbroic rocks from Hole 735B and the later development of the liquid line of descent, in: Von Herzen, R.P., Robinson, P.T. (Eds.), *Proceedings of the Ocean Drilling Program, Scientific Results*
- Nicolas A, Boudier F (1991) Rooting of the Sheeted Dike Complex in the Oman Ophiolite. In: Peters T, Nicolas A, Coleman RG (eds) *Ophiolite Genesis and Evolution of the Oceanic Lithosphere*, vol 5. Springer Netherlands, pp 39-54
- Nicolas A, Boudier F, Ildefonse B, Ball E (2000a) Accretion of Oman and United Arab Emirates ophiolite - Discussion of a new structural map. *Marine Geophysical Research* 21:147-179
- Nicolas A, Boudier F, Koepke J, France L, Ildefonse B, Mevel C (2008) Root zone of the sheeted dike complex in the Oman ophiolite. *Geochem. Geophys. Geosyst.* 9(5):Q05001
- Nicolas A, Ceuleneer G, Boudier F, Misseri M (1988) Structural mapping in the Oman ophiolites: Mantle diapirism along an oceanic ridge. *Tectonophysics* 151(1-4):27-56
- Nicolas A, Ildefonse B, Boudier F, Lenoir X, Ismail WB (2000b) Dike distribution in the Oman-United Arab Emirates ophiolite. *Marine Geophysical Researches* 21:269-287
- Nicolas A, Reuber I, Benn K (1988) A new magma chamber model based on structural studies in the Oman ophiolite. *Tectonophysics* 151:87-105
- Niu Y, Gilmore T, Mackie S, Greig A, Bach W (2002) Mineral chemistry, whole-rock compositions, and petrogenesis of leg 176: Data and discussion, in: Natland, J.H., Dick, H.J.B., Miller, D.J., Von Herzen, R.P. (Eds.), *Proc. ODP, Sci. Results*. pp. 1-60
- Nowell GM, Kempton PD, Noble SR, Fitton JG, Saunders AD, Mahoney JJ, Taylor RN (1998) High precision Hf isotope measurements of MORB and OIB by thermal ionisation mass spectrometry: insights into the depleted mantle. *Chemical Geology* 149:211-233
- O'Neill HSC, Jenner FE (2012) The global pattern of trace-element distributions in ocean floor basalts. *Nature* 491, 698-704
- Pallister JS (1981) Structure of the sheeted dyke complex of the Samail ophiolite near Ibra, Oman. *Journal of Geophysical Research* 86:2661-2672
- Parat F, Holtz F, Feig S (2008) Pre-eruptive Conditions of the Huerto Andesite (Fish Canyon System, San Juan Volcanic Field, Colorado): Influence of Volatiles (C-O-H-S) on Phase Equilibria and Mineral Composition. *Journal of Petrology* 49(5):911-935
- Pearce JA (2003) Supra-subduction zone ophiolites: The search for modern analogues. In: Dilek Y, Newcomb S (eds) *Ophiolite concept and the evolution of geological thought*, vol 373. *Geol. Soc. Am. Spec. Paper*, Boulder, Colorado, pp 269-293
- Pearce JA, Alabaster T, Shelton AW, Searle MP (1981) The Oman ophiolite as a Cretaceous arc-basin complex: evidence and implications. *Philosophical Transactions of the Royal Society of London A* 300:299-317
- Pearce NJG, Perkins WT, Westgate JA, Gorton MP, Jackson SE, Neal CR, Chenevry SP (1997) A compilation of new and published major and trace element data for NIST SRM 610 and NIST SRM 612 glass reference materials. *Geostandards Newsletters* 21:115-144
- Perfit MR, Fornari DJ (1983) Geochemical studies of abyssal lavas recovered by DSRV Alvin from Eastern Galapagos Rift, Inca Transform, and Ecuador Rift: 2. Phase chemistry and crystallization history. *Journal of Geophysical Research: Solid Earth* 88(B12):10530-10550
- Perfit MR, Fornari DJ, Malahotf A, Embley R (1983) Geochemical studies of abyssal lavas recovered from eastern Galapagos Rift, Inca transform, and Ecuador Rift: 3. Trace element abundances and petrogenesis. *Journal of Geophysical Research* 88: 10-551
- Perfit MR, Ridley WI, Jonasson IR (1999) Geologic, petrologic and geochemical relationships between magmatism and massive sulfide mineralization along the eastern Galapagos Spreading Center. Volcanic-associated massive sulfide deposits, in *Reviews in Economic Geology*, eds. C.T. Barrie and M.D. Hannington, V. 8, 75-100.
- Perfit MR, Schmitt AK, Ridley WI, Rubin KH, Valley JW (2008) Petrogenesis of dacites from the southern Juan de Fuca Ridge. *Geochimica et Cosmochimica Acta Supplement* 72:736
- Peters T, Kamber BS (1994) Peraluminous potassium-rich granitoids in the Semail ophiolite. *Contributions to Mineralogy and Petrology* 118:229-238
- Philpotts AR (1979) Silicate liquid immiscibility in tholeiitic basalts. *Journal of Petrology* 20(1):99-118
- Philpotts AR (1982) Compositions of immiscible liquids in volcanic rocks. *Contributions to Mineralogy and Petrology* 80(3):201-218
- Phipps Morgan J, Harding A, Orcutt J, Kent G, Chen YJ (1994) An observational and theoretical synthesis of magma chamber geometry and crustal genesis along a mid-ocean ridge spreading center. In: Ryan MP (ed) *Magmatic systems*, vol. Academic Press, San Diego, pp 139-178
- Pichavant M, Costa F, Burgisser A, Scaillet B, Martel C, Poussineau S (2007) Equilibration scales in silicic to intermediate magmas—implications for experimental studies. *Journal of Petrology* 48(10): 1955-1972
- Pitzer KS, Sterner SM (1995) Equations of state valid continuously from zero to extreme pressures with H<sub>2</sub>O and CO<sub>2</sub> as examples. *International Journal of Thermophysics* 16(2):511-518
- Prowatke S, Klemme S (2006) Trace element partitioning between apatite and silicate melts. *Geochimica et Cosmochimica Acta* 70(17):4513-4527
- Pupier E, Duchene S, Toplis M (2008) Experimental quantification of plagioclase crystal size distribution during cooling of a basaltic liquid. *Contributions to Mineralogy and Petrology* 155(5):555-570
- Purdy GM, Kong LSL, Christeson GL, Solomon SC (1992) Relationship between spreading rate and the seismic structure of mid-ocean ridges. *Nature* 355(6363):815-817
- Python M, Ceuleneer G (2003) Nature and distribution of dykes and related melt migration structures in the mantle section of the Oman ophiolite. *Geochemistry, Geophysics, Geosystems* 4(7)
- Raczek I, Jochum KP, Hofmann AW (2003) Neodymium and Strontium Isotope Data for USGS Reference Materials BCR-1, BCR-2, BHVO-1, BHVO-2, AGV-1, AGV-2, GSP-1, GSP-2 and Eight MPI-DING Reference Glasses. *Geostandards Newsletter* 27(2):173-179
- Randolph AD, Larson MA, Larson ADRA (1971) *Theory of Particulate Processes*. Academic Press, New York, pp 111-126
- Rapp RP (1995) Amphibole-out phase boundary in partially melted metabasalt, its control over liquid fraction and composition, and source permeability. *Journal of Geophysical Research: Solid Earth* 100, 15601-15610
- Rioux M, Bowring S, Kelemen PB, Gordon S, Dudas F, Miller R (2012a) Rapid crustal accretion and magma assimilation in the Oman-U.A.E. ophiolite: High precision U-Pb zircon geochronology of the gabbroic crust. *Journal of Geophysical Research* 117
- Rioux M, Bowring S, Kelemen PB, Gordon S, Miller R, Dudas F (2013) Tectonic development of the Samail ophiolite: High precision U-Pb zircon geochronology and Sm-Nd isotopic constraints on crustal growth and emplacement. *Journal of Geophysical Research* 118:2085-2101
- Rioux M, Lissenberg CJ, McLean NM, Bowring SA, MacLeod CJ, Hellebrand E, Shimizu N (2012b) Protracted timescales of lower crustal growth at the fast-spreading East Pacific Rise. *Nature Geoscience* 5:275-278
- Rollinson HR (2008) Ophiolitic trondhjemites: a possible analogue for Hadean felsic 'crust'. *Terra Nova* 20(5):364-369
- Rollinson HR (2009) New models for the genesis of plagiogranites in the Oman ophiolite. *Lithos* 112:603-614
- Rollinson H (2014) Plagiogranites from the mantle section of the Oman Ophiolite: models for early crustal evolution. In Rollinson, H, Searle MP, Abbasi IA, Al-Lazki A, and Kindi MHA, eds., *Tectonic evolution of the Oman Mountains*, Volume 392: London, Geological Society of London, Special Publication, p. 247-261
- Rollinson HR (2015) Slab and sediment melting during subduction initiation: granitoid dykes from the mantle section of the Oman ophiolite. *Contributions to Mineralogy and Petrology* 170

- Rothery DA (1983) The base of a sheeted dyke complex, Oman ophiolite: implications for magma chambers at oceanic spreading axes. *Journal of the Geological Society* 140(2):287-296
- Roux J, Lefevre A (1992) A fast-quench device for internally heated pressure vessels. *European Journal of Mineralogy* 4(2):279-281
- Rubin KH, Sinton JM (2007) Inferences on mid-ocean ridge thermal and magmatic structure from MORB compositions. *Earth and Planetary Science Letters*, 260(1), 257-276
- Rudnick RL, Gao S, Heinrich DH, Karl KT (2003) Composition of the Continental Crust. In: *Treatise on Geochemistry*, vol. Pergamon, Oxford, pp 1-64
- Rutherford MJ, Devine JD (2003) Magmatic Conditions and Magma Ascent as Indicated by Hornblende Phase Equilibria and Reactions in the 1995-2002 Soufrière Hills Magma. *Journal of Petrology* 44(8):1433-1453
- Sato H (1978) Segregation vesicles and immiscible liquid droplets in ocean-floor basalt of Hole 396B, IPOD/DSDP Leg 46. Initial reports of the deep sea drilling project 46:283-291
- Sawyer EW (1991) Disequilibrium Melting and the Rate of Melt-Residuum Separation During Migmatization of Mafic Rocks from the Grenville Front, Quebec. *Journal of Petrology* 32(4):701-738
- Scaillet B, Evans BW (1999) The 15 June 1991 eruption of Mount Pinatubo. I. Phase equilibria and pre-eruption P-T-fO<sub>2</sub>-fH<sub>2</sub>O conditions of the dacite magma. *Journal of Petrology* 40(3):381-411.
- Scaillet B, Pichavant M, Roux J (1995) Experimental Crystallization of Leucogranite Magmas. *Journal of Petrology* 36(3):663-705
- Scaillet B, Pichavant M, Roux J, Humbert G, Lefevre A (1992) Improvements of the Shaw membrane technique for measurement and control of f H<sub>2</sub> at high temperatures and pressures. *American Mineralogist* 77(5-6):647-655
- Schmitt AK, Perfit MR, Rubin KH, Stockli DF, Smith MC, Cotsonika LA, Zellmer GF, Ridley WI, Lovera OM (2011) Rapid cooling rates at an active mid-ocean ridge from zircon thermochronology. *Earth and Planetary Science Letters* 302(3): 349-358
- Schneider CA, Rasband WS, Eliceiri KW (2012) NIH Image to ImageJ: 25 years of image analysis. *Nat Meth* 9(7):671-675
- Schulz R, Klemd R, Brätz H (2006) Host rock compositional controls on zircon trace element signatures in metabasites from the Austroalpine basement. *Geochimica et Cosmochimica Acta* 70:697-710
- Schwab RG, Küstner D (1981) Die Gleichgewichtsfugazitäten technologisch und petrologisch wichtiger Sauerstoffpuffer. *Neues Jahrb. Mineral. Abh.* 140:111-142
- Severs MJ, Beard JS, Fedele L, Hanchar JM, Mutchler SR, Bodnar RJ (2009) Partitioning behavior of trace elements between dacitic melt and plagioclase, orthopyroxene, and clinopyroxene based on laser ablation ICPMS analysis of silicate melt inclusions. *Geochimica et Cosmochimica Acta* 73(7):2123-2141
- Shaw HR, Wones DR (1964) Fugacity coefficients for hydrogen gas between 0 degrees and 1000 degrees C, for pressures to 3000 atm. *Am J Sci* 262(7):918-929
- Silantyev SA, Koepke J, Ariskin AA, Anosova MO, Krasnova EA, Dubinina EO, Suhr G (2014) Geochemical nature and age of the plagiogranite-gabbro-norite association of the oceanic core complex of the Mid-Atlantic ridge at 5°10'S. *Petrology* 22(2):109-127
- Sinton JM, Detrick RS (1992) Mid-Ocean Ridge Magma Chambers. *J. Geophys. Res.* 97(B1):197-216
- Smith IEM, Worthington TJ, Stewart RB, Price RC, Gamble JA (2003) Felsic volcanism in the Kermadec arc, SW Pacific: crustal recycling in an oceanic setting. *Geological Society, London, Special Publications* 219(1):99-118
- Smithies RH, Champion DC, Van Kranendonk MJ (2009) Formation of Paleoproterozoic continental crust through infracrustal melting of enriched basalt. *Earth and Planetary Science Letters* 281(3-4):298-306
- Stakes DS, Perfit MR, Tivey MA, Caress DW, Ramirez TM, Maher N. (2006) The Cleft revealed: Geologic, magnetic, and morphologic evidence for construction of upper oceanic crust along the southern Juan de Fuca Ridge. *Geochemistry, Geophysics, Geosystems*, 7(4)
- Stakes DS, Taylor HP (2003) Oxygen isotope and chemical studies on the origin of large plagiogranite bodies in northern Oman, and their relationship to the overlying massive sulphide deposits. In: Dilek Y, Robinson PT (eds) *Ophiolites in Earth history*, vol 218. *Geol. Soc. Spec. Publ.*, London, pp 315-351
- Stelling J, Botcharnikov RE, Beermann O, Nowak M (2008) Solubility of H<sub>2</sub>O- and chlorine-bearing fluids in basaltic melt of Mount Etna at T=1050-1250°C and P=200 MPa, vol 256. Elsevier, Oxford, ROYAUME-UNI, p 9
- Stormer JC, Jr. (1983) The effects of recalculation on estimates of temperature and oxygen fugacity from analyses of multicomponent iron-titanium oxides. *American Mineralogist* 68:586-594
- Strnad L, Mihaljevic M, Sebek O (2005) Laser Ablation and Solution ICP-MS Determination of Rare Earth Elements in USGS BIR-1G, BHVO-2G and BCR-2G Glass Reference Materials. *Geostandards and Geoanalytical Research* 29(3):303-314
- Sun SS, McDonough WF (1989) Chemical and isotopic systematics of oceanic basalts: implications for mantle composition and processes. *Geological Society, London, Special Publications* 42(1):313-345
- Sun WD, Binns RA, Fan AC, Kamenetsky VS, Wysoczanski R, Wei GJ, Hu YH, Arculus RJ (2007) Chlorine in submarine volcanic glasses from the eastern Manus basin. *Geochimica et Cosmochimica Acta* 71, 1542-1552
- Taylor SR, McLennan SM (1985) The continental crust, its composition and evolution: an examination of the geochemical record preserved in sedimentary rocks / Stuart Ross Taylor, Scott M. McLennan, vol. Blackwell Scientific Publications, Oxford; Melbourne
- Teagle DAH, Alt JC, Umino S, Miyashita S, Banerjee NR, Wilson DS, and the Expedition 309/312 Scientists (2006) Proc. IODP, 309/312. Integrated Ocean Drilling Program, Management International, Inc., Washington, DC
- Teagle DAH, Ildefonse B, Blum P, the Expedition 335 scientists (2012) Proceedings IODP, 335: Tokyo, Integrated Ocean Drilling Program Management International, Inc.
- Thayer TP (1977) Some implications of sheeted dike swarms in ophiolitic complexes. *Geotectonics* 11:419-426
- Tilton GR, Hopson CA, Wright JE (1981) Uranium-lead isotopic ages of the Semail ophiolite, Oman, with applications to Tethyan ocean ridge tectonics. *Journal of Geophysical Research* 86:2763-2776
- Toplis MJ, Carroll MR (1995) An Experimental Study of the Influence of Oxygen Fugacity on Fe-Ti Oxide Stability, Phase Relations, and Mineral/Melt Equilibria in Ferro-Basaltic Systems. *Journal of Petrology* 36(5):1137-1170
- Toplis MJ, Carroll MR (1996) Differentiation of ferro-basaltic magmas under conditions open and closed to oxygen: implications for the Skaergaard intrusion and other natural systems. *Journal of Petrology* 37(4):837-858
- Tsuchiya N, Shibata T, Yoshikawa M, Adachi Y, Miyashita S, Adachi T, Nakano N, Osanai Y (2013) Petrology of Lasail plutonic complex, northern Oman ophiolite, Oman: An example of arc-like magmatism associated with ophiolite detachment. *Lithos* 156-159:120-138
- Umino S, Miyashita S, Hotta F, Adachi Y (2003) Along-strike variation of the sheeted dike complex in the Oman Ophiolite: Insights into subaxial ridge segment structures and the magma plumbing system. *Geochemistry Geophysics Geosystems* 4
- Vanko DA (1986) High-chlorine amphiboles from oceanic rocks; product of highly-saline hydrothermal fluids? *American Mineralogist* 71(1-2):51-59
- Van der Zwan FM, Devey CW, Augustin N, Almeev RR, Bantan RA, Basaham A (2015) Hydrothermal activity at the ultraslow- to slow-spreading Red Sea Rift traced by chlorine in basalt. *Chemical Geology* 405, 63-81
- Veksler IV, Dorfman AM, Borisov AA, Wirth R, Dingwell DB (2007) Liquid Immiscibility and the Evolution of Basaltic Magma. *Journal of Petrology* 48(11):2187-2210
- Vera EE, Mutter JC, Buhl P, Orcutt JA, Harding AJ, Kappus ME, Detrick RS, Brocher TM (1990) The structure of 0- to 0.2-m.y.-old oceanic crust at 9°N on the East Pacific Rise from expanded spread profiles. *Journal of Geophysical Research: Solid Earth* 95(B10):15529-15556
- Vervoort JD, Patchett PJ, Blichert-Toft J, Albarede F (1999) Relationship between Lu-Hf and Sm - Nd isotopic systems in the global sedimentary system. *Earth and Planetary Science Letters* 168:79-99
- Wanless VD, Perfit MR, Ridley WI, Klein EM (2010) Dacite petrogenesis on Mid-ocean ridges: Evidence for oceanic crustal melting and assimilation. *Journal of Petrology* 51:2377-2410
- Wanless VD, Perfit MR, Ridley WI, Wallace PJ, Grimes CB, Klein EM (2011) Volatile abundances and oxygen isotopes in basaltic to dacitic lavas on mid-ocean ridges: The role of assimilation at spreading centers. *Chemical Geology* 287(1-2):54-65
- Wanless VD, Shaw AM (2012) Lower crustal crystallization and melt evolution at mid-ocean ridges. *Nature Geoscience* 5:651-655
- Warren CJ, Parrish RR, Searle MP, Waters DJ (2003) Dating the subduction of the Arabian continental margin beneath the Semail ophiolite, Oman. *Geology* 31:889-892
- Warren CJ, Parrish RR, Waters DJ, Searle MP (2005) Dating the geologic history of Oman's Semail ophiolite: insights from U-Pb geochronology. *Contributions to Mineralogy and Petrology* 150:403-422
- Werts KR (2012) Phase chemistry and petrogenesis of dacitic lavas from the southern Juan de Fuca Ridge. A thesis presented to the graduate school of the University of Florida in partial fulfillment of the requirements for the degree of Master of Science, 86 p.
- Whattam SA, Stern RJ (2011) The 'subduction initiation rule': a key for linking ophiolites, intra-oceanic forearcs, and subduction initiation. *Contributions to Mineralogy and Petrology* 162:1031-1045.
- White WM, Dupre B (1986) Sediment subduction and magma genesis in the Lesser Antilles: Isotopic and trace element constraints. *Journal of Geophysical Research* 91:5927-5941
- Wilson DS (1996) Fastest known spreading on the Miocene Cocos-Pacific Plate Boundary. *Geophysical Research Letters* 23(21):3003-3006

- Wilson DS, Teagle DAH, Alt JC, Banerjee NR, Umino S, Miyashita S, Acton GD, Anma R, Barr SR, Belghoul A, Carlot J, Christie DM, Coggon RM, Cooper KM, Cordier C, Crispini L, Durand SR, Einaudi F, Galli L, Gao Y, Geldmacher J, Gilbert LA, Hayman NW, Herrero-Bervera E, Hirano N, Holter S, Ingle S, Jiang S, Kalberkamp U, Kerneklian M, Koepke J, Laverne C, Vasquez HLL, Maclennan J, Morgan S, Neo N, Nichols HJ, Park S-H, Reichow MK, Sakuyama T, Sano T, Sandwell R, Scheibner B, Smith-Duque CE, Swift SA, Tartarotti P, Tikku AA, Tominaga M, Veloso EA, Yamasaki T, Yamazaki S, Ziegler C (2006) Drilling to Gabbro in Intact Ocean Crust. *Science* 312(5776):1016-1020
- Wilson SA (1997) Data Compilation for USGS Reference Material BHVO-2, Hawaiian Basalt. US Geological Survey Open-File Report 2-3
- Wolf M, Wyllie P (1994) Dehydration-melting of amphibolite at 10 kbar: the effects of temperature and time. *Contributions to Mineralogy and Petrology* 115(4):369-383
- Wolff PE, Koepke J, Feig ST (2013) The reaction mechanism of fluid-induced partial melting of gabbro in the oceanic crust. *European Journal of Mineralogy* 25(3):279-298
- Woodhead JD, Hergt JM, Davidson JP, Eggins SM (2001) Hafnium isotope evidence for 'conservative' element mobility during subduction zone processes. *Earth and Planetary Science Letters* 192:331-346
- Wright TJ, Sigmundsson F, Pagli C, M. Belachew IJH, Brandsdottir B, Keir D, Pedersen R, Ayele A, Ebinger C, Einarsson P, Lewi E, Calais E (2012) Geophysical constraints on the dynamics of spreading centres from rifting episodes on land. *Nature Geoscience* 5:242-250
- Yamasaki T, Maeda J, Mizuta T (2006) Geochemical evidence in clinopyroxenes from gabbroic sequence for two distinct magmatisms in the Oman ophiolite. *Earth and Planetary Science Letters* 251:52-65
- Zhang C, Koepke J, Kirchner C, Goetze N, Behrens H (2014) Rapid hydrothermal cooling above the axial melt lens at fast-spreading mid-ocean ridge. *Sci. Rep.* 4
- Zhao JH, Asimow PD (2014) Neoproterozoic boninite-series rocks in South China: A depleted mantle source modified by sediment-derived melt. *Chemical Geology* 388:98-111

# Curriculum Vitae

## ■ Personal details

---

Dipl.-Geow. Martin Erdmann  
m.erdmann@mineralogie.uni-hannover.de  
\*23.05.1985 in Nienburg/Weser, German citizenship

## ■ Work experience

---

Since Jan 2015	<b>Research assistant</b> Federal Institute for Geosciences and Natural Resources (BGR), Hannover, Germany
Sep 2014 – Dec 2014	<b>Student assistant</b> Institut for Mineralogy, Leibniz Universität Hannover, Germany
Dec 2010 – Aug 2014	<b>Research assistant</b> Institut for Mineralogy, Leibniz Universität Hannover, Germany

## ■ Education

---

Since Dec 2010	<b>PhD-student</b> Dissertation: “Felsic melts in the oceanic crust: an experimental study on their generation, phase equilibria, and trace element partitioning” at the Leibniz Universität Hannover, Germany in Cooperation with Centre de Recherches Pétrographiques et Géochimiques (CRPG), Nancy, France
Oct 2005 – Nov 2010	<b>Studies of geosciences</b> Leibniz Universität Hannover, Germany Thesis: “The role of redox conditions in genesis of Yellowstone hotspot rhyolites” Qualification: Dipl.-Geow. (M.Sc. equivalent)
Aug 1997 – Jul 2004	<b>Abitur</b> Albert-Schweitzer-Schule Nienburg, Germany, Gymnasium Qualification: Abitur (A-level equivalent)

# List of Publications

## ■ Journals

---

### 2016

**Erdmann M.**, France L., Fischer L.A., Deloule E., Koepke J.; submitted to *Chemical Geology*; Trace elements in anatectic products at the roof of mid-ocean ridge magma chambers: an experimental study

**Erdmann M.**, Koepke J.; 2016; Silica-rich lavas in the oceanic crust: Experimental evidence for fractional crystallization under low water activity; *Contrib Mineral Petrol*, 171(10), 83

Fischer L.A., **Erdmann M.**, Wolff P.E., France L., Deloule E., Koepke J.; 2016; Trace element evidence for anatexis at oceanic magma chamber roofs and the role of partial melts as for contamination of fresh MORB; *Lithos* 260, 1-8

**Erdmann M.**, Koepke J.; 2016; Experimental temperature cycling as a powerful tool to enlarge melt pools and crystals at magma storage conditions; *American Mineralogist*, 101(4), 960-969

Haase K.M., Freund S., Beier C., Koepke J., **Erdmann M.**, Hauff F.; 2016; Constraints on the magmatic evolution of the oceanic crust from plagiogranite intrusion in the Oman ophiolite; *Contrib Mineral Petrol*, 171(5), 1-16

### 2015

**Erdmann M.**, Fischer L.A., France L., Zhang C., Godard M., Koepke J.; 2015; Anatexis at the roof of an oceanic magma chamber at IODP Site 1256 (equatorial Pacific): an experimental study; *Contrib Mineral Petrol*, 169(4), 1-28

Haase K.M., Freund S., Koepke J., Hauff V., **Erdmann M.**; 2015: Melts of sediments in the mantle wedge of the Oman ophiolite; *Geology*, 43(4), 275-278

### 2014

Dultz S., Boy J., Dupont C., Halisch M., Behrens H., Welsch A.-M., **Erdmann M.**, Cramm S., Hensch G., and Deubener J.; 2014: Alteration of a submarine basaltic glass under environmental conditions conducive for microorganisms: Growth patterns of the microbial community and mechanism of palagonite formation; *Geomicrobiology Journal*, 31(9), 813-834

### 2012

Almeev R., Bolte T., Nash B., Holtz F., **Erdmann M.**, Cathey H.; 2012; High-temperature, low H<sub>2</sub>O Silicic Magmas of the Yellowstone Hotspot: an Experimental Study of Rhyolite from the Bruneau-Jarbidge Eruptive Center, Central Snake River Plain, USA; *Journal of Petrology*, 53(9), 1837-1866

## ■ Conference Abstracts

---

### 2016

**Erdmann M.**, Szurlies M., Wilken H.; 2016; Innovative technologies for exploration and mining of polymetallic ore deposits in Germany – the funding measure r<sup>4</sup> of the BMBF; Abstract and poster for 1<sup>st</sup> GOOD Meeting on the Geology of Ore Deposits, Freiberg

### 2015

Alberts R., Grimes C.B., Koepke J., **Erdmann M.**, Kitajima K., Spicuzza M.J., Valley J.W.; 2015; High- & Low- $\delta^{18}\text{O}$  magma: Comparative study of crustal and mantle plagiogranites from the Oman ophiolite; Abstract and poster (V21A-3011) for AGU Fall Meeting 2015, San Francisco

### 2013

**Erdmann M.**, Fischer L.A., France L., Deloule E., Koepke J.; 2013; Felsic melt generation at the MOR magma chamber roof: Trace element evidence of experimental hydrous partial melts for anatectic processes at the East-Pacific Rise; Abstract and poster (V31A-2677) for AGU Fall Meeting 2013, San Francisco

Fischer L.A., **Erdmann M.**, France L., Deloule E., Koepke J.; 2013; Generation of felsic melts within fast-spreading oceanic crust: Experimental partial melting of hydrothermally altered sheeted dike; Abstract and poster (V31A-2675) for AGU Fall Meeting 2013, San Francisco

**Erdmann M.**, Fischer L.A., France L., Deloule E., and Koepke J.; 2013; Trace element contents of experimental hydrous partial melts from the MOR magma chamber roof: evidence for crustal contamination and felsic melt generation; Abstract and oral presentation for DMG Joint Meeting, Tübingen, 2013

**Erdmann M.**, Koepke J.; 2013; Temperature cycling as a powerful tool to enlarge melt pools and crystals in experiments; Abstract and poster for DMG Joint Meeting, Tübingen, 2013

Fischer L.A., **Erdmann M.**, France L., Deloule E., Koepke J.; 2013; Experimental study on hydrous partial melting of hydrothermally altered dolerite: Generation of felsic melts within fast-spreading oceanic crust; Abstract and poster for DMG Joint Meeting, Tübingen, 2013

Freund S., **Erdmann M.**, Koepke J., Hauff F., Haase K.M.; 2013; Crustal evolution and petrogenesis of silicic plutonic rocks within the Oman ophiolite – petrological and geochemical investigations; Abstract and poster for Goldschmidt Conference, Florence, 2013

**Erdmann M.**, Fischer L.A., France L., Freund S., Koepke J.; 2013; Hydrous partial melting at the dike/gabbro transition at fast-spreading ridges - an experimental study; Abstract and oral presentation for IODP 335 2nd post-cruise meeting, Corsica, 2013

Dierick M., France L., **Erdmann M.**, Koepke J., and the IODP Expedition 335 Scientific party, 2013; Magma chamber processes at IODP 1256D Hole: A highly detailed petrological and geochemical study of upper oceanic crust; Abstract and oral presentation for IODP 335 2nd post-cruise meeting, Corsica, 2013

## 2012

**Erdmann M.**, Freund S., Haase K.M., Koepke J.; 2012; Application of techniques to enlarge melt pools and crystals in crystallization experiments: A case study in an andesitic system from the Pacific-Antarctic Rise; European Mineralogical Conference, Vol. 1, EMC2012-303, 2012

**Erdmann, M.**, Koepke, J., Freund, S.; 2012; Phase relations and distribution coefficients for evolved lavas from the Pacific-Antarctic Rise; Abstract and poster for EMPG conference 2012, Kiel

Fischer L.A., Brophy J.G., **Erdmann M.**, Koepke J.; 2012; Experimental hydrous partial melting of gabbro: A new approach to enlarge melt pools by adding synthetic glass; Abstract and poster for EMPG conference 2012, Kiel

**Erdmann M.**, Freund S., Fischer L., Haase K.M., Koepke J.; 2011; Plagiogranites in the Oman ophiolite: a key to understand the formation of SiO<sub>2</sub>-rich magmas within fast-spreading oceanic crust; Abstract and poster for Oman conference 2012, Muscat

## 2011

Bolte T., **Erdmann M.**, Nash B., Cathey H.E., Almeev R., Holtz F.; 2011; Preliminary estimates on magma storage conditions of the Heise volcanic field, Snake River Plain; Abstract and poster for Goldschmidt conference 2011, Prag

## 2010

**Erdmann M.**, Sehlke A., Behrens H., Avaré G., Whittington A.G.; 2010; The viscosity of hydrous rhyodacitic melts; Abstract and poster for EMPG conference 2010, Toulouse

Bolte T., **Erdmann M.**, Sehlke A., Nash B., Almeev R., Holtz F.; 2010; Preliminary estimates on pre-eruptive magma conditions at the Heise volcanic field, Snake River Plain, Idaho, western USA; Abstract and poster for DMG conference 2010, Muenster